

**DYNAMIC MOLECULAR CONTROL OF NANOPARTICLE  
BUILDING BLOCK ASSEMBLY**

**Stefan Borsley**

**A Thesis Submitted for the Degree of PhD  
at the  
University of St Andrews**



**2016**

**Full metadata for this item is available in  
St Andrews Research Repository  
at:**

**<http://research-repository.st-andrews.ac.uk/>**

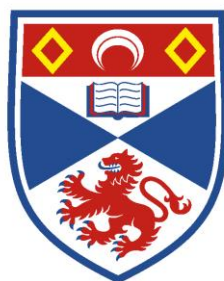
**Please use this identifier to cite or link to this item:**

**<http://hdl.handle.net/10023/9317>**

**This item is protected by original copyright**

# Dynamic Molecular Control of Nanoparticle Building Block Assembly

by  
Stefan Borsley



University of  
St Andrews

This Thesis is submitted in partial fulfilment  
for the degree of Doctor of Philosophy  
at the  
University of St Andrews

September 2015

**1. Candidate's declarations:**

I, Stefan Borsley, hereby certify that this thesis, which is approximately 45000 words in length, has been written by me, and that it is the record of work carried out by me, or principally by myself in collaboration with others as acknowledged, and that it has not been submitted in any previous application for a higher degree.

I was admitted as a research student in September 2011 and as a candidate for the degree of PhD in September 2015; the higher study for which this is a record was carried out in the University of St Andrews between 2011 and 2015.

Date 25/09/2015 signature of candidate .....

**2. Supervisor's declaration:**

I hereby certify that the candidate has fulfilled the conditions of the Resolution and Regulations appropriate for the degree of PhD in the University of St Andrews and that the candidate is qualified to submit this thesis in application for that degree.

Date 25/09/2015 signature of supervisor .....

**3. Permission for publication: (to be signed by both candidate and supervisor)**

In submitting this thesis to the University of St Andrews I understand that I am giving permission for it to be made available for use in accordance with the regulations of the University Library for the time being in force, subject to any copyright vested in the work not being affected thereby. I also understand that the title and the abstract will be published, and that a copy of the work may be made and supplied to any bona fide library or research worker, that my thesis will be electronically accessible for personal or research use unless exempt by award of an embargo as requested below, and that the library has the right to migrate my thesis into new electronic forms as required to ensure continued access to the thesis. I have obtained any third-party copyright permissions that may be required in order to allow such access and migration, or have requested the appropriate embargo below.

The following is an agreed request by candidate and supervisor regarding the publication of this thesis:

**PRINTED COPY**

- a) No embargo on print copy

**ELECTRONIC COPY**

- a) No embargo on electronic copy

Date 25/09/2015

Signature of candidate .....

Signature of supervisor .....

## Table of contents

<b>ABSTRACT</b>	<b>VI</b>
<b>ACKNOWLEDGEMENTS</b>	<b>VIII</b>
<b>ABBREVIATIONS</b>	<b>X</b>
<b>CHAPTER 1: INTRODUCTION</b>	<b>1</b>
1.1 Nanoparticle functional materials	1
1.2 Gold nanoparticles: Structure and properties	2
1.3 Synthesis of gold nanoparticles	3
1.3.1 Electrostatic stabilisation: The Turkevich–Frens synthesis	4
1.3.2 Steric stabilisation: The Brust–Schiffrin two-phase synthesis	6
1.3.3 Steric stabilisation: The Stucky synthesis and other one-phase syntheses	8
1.4 Nanoparticle characterisation	12
1.4.1 Nuclear magnetic resonance for characterisation of nanoparticle-bound molecules	14
1.5 Nanoparticle functionalisation	15
1.6 Nanoparticle assembly	17
1.6.1 Assembly of nanoparticles using covalent bonds	18
1.6.2 Noncovalent nanoparticle assembly	19
1.7 Dynamic covalent chemistry for nanoparticle functionalisation and assembly	23
1.7.1 An introduction to dynamic covalent chemistry	23
1.7.2 Dynamic covalent chemistry on nanoparticles	25
1.8 Outlook and aims	33
<b>CHAPTER 2: SYNTHESIS AND CHARACTERISATION OF FUNCTIONALISED GOLD NANOPARTICLES</b>	<b>35</b>
2.1 Introduction	36
2.2 Investigating the ligand scope of nanoparticle synthesis	39
2.3 Size control of nanoparticles by varying the rate of reductant addition	46
2.4 Mechanism of size-controlled nanoparticle synthesis	54
2.5 Molecular-level characterisation of boronic acid-coated nanoparticles	56
2.6 Conclusions and future work	62
<b>CHAPTER 3: REVERSIBLE BORONIC ESTER FORMATION ON NANOPARTICLE-BOUND MONOLAYERS</b>	<b>65</b>
3.1 Introduction	66
3.1.1 Dynamic boronic ester exchange	68
3.2 Scope of binding partners for boronic acids	70

3.3	Boronic ester formation on nanoparticles	80
3.4	Reversible boronic ester formation on nanoparticles	83
3.5	Quantifying boronic ester formation on nanoparticles	86
3.6	Conclusions and future work	90
	<b>CHAPTER 4: BORONIC ESTER-MEDIATED NANOPARTICLE ASSEMBLY</b>	<b>93</b>
4.1	Introduction	94
4.2	Design of boronic ester-mediated nanoparticle assembly	97
4.3	Boronic ester-mediated nanoparticle assembly	99
4.4	Reversible boronic ester-mediated nanoparticle assembly: Disassembly	108
4.5	Mechanism of boronic ester-mediated nanoparticle assembly	110
4.6	Analysis and molecular-level control of assembly morphology	113
4.7	Towards reconfigurable nanoparticle assemblies	120
4.8	Conclusions and future work	121
	<b>CHAPTER 5: NONCOVALENT PLANET–SATELLITE NANOPARTICLE ASSEMBLY</b>	<b>124</b>
5.1	Introduction	126
5.2	Synthesis and characterisation of planet–satellite assemblies	128
5.3	Colloidal stability of planet–satellite assemblies	138
5.4	Probing the planet–satellite interaction	144
5.5	Modifying the ‘planet’ nanoparticle	149
5.6	Planet–satellite assemblies for surface-enhanced Raman spectroscopy	152
5.7	Conclusions and future work	155
	<b>CHAPTER 6: GENERAL CONCLUSIONS</b>	<b>159</b>
	<b>CHAPTER 7: EXPERIMENTAL AND SYNTHETIC PROCEDURES</b>	<b>163</b>
7.1	General experimental procedures	163
7.2	Synthesis of organic compounds	165
7.3	Nanoparticle synthesis and characterisation	187
7.3.1	Synthesis and characterisation of ligand-functionalised nanoparticles	187
7.3.2	Synthesis and characterisation of citrate-stabilised nanoparticles	201
7.4	NMR experiments	205
7.4.1	$T_1$ measurements	206
7.4.2	Single-point measurement of association constants	206

7.4.3	Titration	209
<b>7.5</b>	<b>Boronic ester-mediated nanoparticle assembly</b>	<b>211</b>
7.5.1	Stability of AuNP-7	211
7.5.2	Interparticle distance modelling	211
7.5.3	Fractal dimension determination	212
	<b>REFERENCES</b>	<b>213</b>

# Abstract

Nanoparticles have generated much excitement as a result of their often unique properties, inherently dependent on nanoparticle material, shape and size. Virtually all conceivable nanoparticle applications will require excellent control over how nanoparticles are assembled and linked to other components. When several nanoparticles are brought together, the assembly structure is crucial in determining their newly emergent properties. However, the synthetic chemistry techniques required to control nanoparticle functionalisation and assembly are still under-developed, with complex biological or supramolecular systems being the current best approaches. There remains a need for simple, generalisable strategies for molecular-level control over nanoparticle functionalisation and assembly. This thesis presents the development of a toolkit of nanoparticle building blocks, which may be assembled in a predictable and controlled way, governed by simple and easily optimised abiotic molecular systems.

Efficient, size-controlled, direct synthesis of functionalised gold nanoparticle building blocks with control over size and dispersity is developed.  $^{19}\text{F}$  NMR spectroscopy studies provide a fundamental understanding of the implications of confinement at the nanoparticle surface for molecular reactivity. Two self-assembly strategies, each resulting in structures of high order and predictability, are presented. First, the reversible nature of dynamic covalent boronic ester formation is exploited to induce reversible nanoparticle self-assembly. Links between molecular details and resulting morphology are demonstrated and rationalised. A second strategy exploits multivalent non-covalent interactions, resulting in 'planet-satellite' structures displaying high order, stability and predictability.

This thesis demonstrates that relatively simple molecular systems present a viable, and ultimately more flexible, alternative to existing methods of directing precise, predictable control of nanoparticle functionalisation and assembly. Advancing a molecular-level understanding of the underlying processes

enables a high level of control. Future application of this molecular approach to dynamic nanomaterial control will lead to more complex and sophisticated nanostructures, helping nanotechnology progress towards its undoubtedly revolutionary full potential.

# Acknowledgements

I knew I wanted to do a PhD ever since I started my undergraduate degree, however, at that time, I had no idea what a nanoparticle was, or how interesting research on nanoparticles might be. Under the excellent supervision of Dr Euan Kay, I have found the work I have done during my PhD not only thoroughly interesting and challenging but also immensely enjoyable. To reach the present stage, I have relied on the help of many people, and although I will do my best to remember as many of you as possible by name, I fear that the sheer number of people who I need to thank will make that impossible.

It is my great privilege and pleasure to start by thanking Euan. Since the first day of my PhD, Euan has encouraged me to think for myself, design my experiments, and shape the direction of my PhD. This would not have been possible had it not been for his continued support, both academic and pastoral. Euan, thank you so much for inviting me to do a PhD with you, and putting up with me! Your enthusiasm and passion for science has been contagious; that rush of excitement when an experiment works! Similarly, thank you for your encouragement and support when things didn't work. Thank you for all the help and opportunities you have provided for me during my PhD and introducing me to such an exciting topic.

Staying with academia, I am pleased to thank a number of other people in the department without whom this thesis would not have been possible. To Mrs Melanja Smith and Dr Tomas Lebl, thank you for the efficient and immensely friendly running of the NMR facilities – I hope I didn't cause too many machine errors! To Mr Ross Blackley, thank you so much for your help with TEM and SEM. I still don't know what some of the buttons do, but thank you so much for your patience with me every time I had problems with the TEM. Thanks also to Dr Caroline Botting, Dr Sally Shirran, Dr Matthew Fuszard and Mrs Caroline Hornsburg for mass spectroscopy, Dr Lorna Eades for ICP-OES and Dr Steven Aisala for collaboration in Glasgow on Raman spectroscopy. Also a brief note to thank Dr Ian Watt, who supervised my final-year undergraduate project at the University of Manchester, who's influence nurtured my interest in supramolecular chemistry.

I next thank the people in the lab, the poor souls who have had to endure my company, my chatter, my music and my insistence that I be left alone when there was a test match to listen to! Tamara, thank you for always being there with so much help and discussion, but above all thank you for your friendship, both inside and outside the lab. The past four years would not have been anywhere near as easy or enjoyable (or filled with so much good food!) without it. Dr William Edwards (Will), it has been a pleasure having you around, always great for a chat, be it

about chemistry or not (I'm so glad there was another cricket fan in the lab!), and thank you for all the stimulating discussion. Leonardo, Flavio, Will, Nicolas, David and Josh, thank you all for making the lab environment such a pleasant and fun place to be! Looking a little further down the corridor, I must single out Dr Neil Keddie. Neil, you were always great for a chat, immensely helpful when discussing chemistry, and just good fun when discussing other things. I'm sure I'm not the first to also thank you for being so friendly and helpful with all those little practical things that everyone seems to forget about how difficult or time consuming they were. Frida, Stephen and Maciek, thank you for being such good friends and thanks for all the trips to the Highlands!

Beyond my academic circle, I must, first and foremost, thank my parents. You have always supported and encouraged me through my PhD; you have been there for me through the good times and the bad times. I probably don't ever say enough how much I appreciate it. It is a joy and pride to have parents such as you, who have supported me over the past four years, encouraged me and always been there for me. I must also thank my mum for proofreading my thesis. Despite not understanding much of it, you have been an immense help, and certainly helped me to write much more gooder.

Last but not least, my warm thanks go to all the other people who have made my time in St Andrews so enjoyable. Sophie, Riccardo, Axel, Tanya, Rodrigo, Rudy and Graziella, to name but a few more friends from the neighbouring labs. The badminton club's Andy, Mike, Dave, Toma, Rob, Caroline, Gavin and Donald – thank you for such enjoyable and competitive Tuesday evenings! The cricket team's Dom, Stan, Pat, Angus, Phil, Tom, James, Ross, Josh, Graham, Francis, Alyn, Lewis, Dave and others – thank you for allowing me to embarrass myself on (and off) the cricket field in your company. You have always provided a delightful way for me to spend a sunny (who am I kidding, it's Scotland...) Sunday afternoon, enjoying the game and relaxing from all the hard work.

The knowledge, skills, friends, experience and memories I have gained during my PhD will stay with me for the rest of my life. I think I will remain forever interested in my work, and am sure that in the dim and distant future, I will still be excited to hear about the latest developments in the world of nanoparticle building blocks. Thank you Euan and all!

# Abbreviations

A	Absorbance
Ar	Aryl
(Au)NP(s)	(Gold) nanoparticle(s)
d	Diameter or doublet or deuterated
dd	Doublet of doublets
D1	Delay time
$\delta$	Chemical shift
DCC	Dynamic covalent chemistry
DLS	Dynamic light scattering
DMF	<i>N,N</i> -Dimethylformamide
DMSO	Dimethyl sulfoxide
DNA	Deoxyribonucleic acid
$\epsilon$	Molar extinction coefficient
EDC( $\cdot$ HCl)	1-Ethyl-3-(3-dimethylaminopropyl)carbodiimide (hydrochloride)
Eq.	Equivalent
EI	Electron impact
ES	Electrospray ionisation
Et	Ethyl
g	Grams
h	Hour
HRMS	High resolution mass spectrometry
HONt	Hydroxybenzotriazole
ICP-OES	Inductively coupled plasma optical emission spectrometry
IS	Internal standard
<i>J</i>	Coupling constant
$K_a$	Equilibrium constant
lit.	Literature

Me	Methyl
(M)Hz	(Mega)hertz
m	Multiplet
min	Minute
(m)M	(Milli)molar
$\mu$ M	Micromolar
M.p.	Melting point
Ms	Mesyl
nM	Nanomolar
NADH	Nicotinamide adenine dinucleotide
NMR	Nuclear magnetic resonance
Ph	Phenyl
$pK_a$	Acid dissociation constant
ppm	Parts per million
RNA	Ribonucleic acid
RT	Room temperature
s	Second or singlet
SPR	Surface plasmon resonance
t	Time or triplet
$T_1$	Spin-lattice relaxation time
$T_2$	Spin-spin relaxation time
TBAB	<i>tert</i> -Butylamine borane complex
TEM	Transmission electron microscopy
THF	Tetrahydrofuran
TLC	Thin layer chromatography
TOAB	Tetraoctylammonium bromide
Trt	Trityl
UV-vis	Ultraviolet-visible
v	Volume

# Chapter 1: Introduction

## 1.1 Nanoparticle functional materials

Nanoparticle research has attracted a great deal of interest, with thousands of publications in the last two decades.<sup>1,2</sup> Nanoparticles are neither bulk materials nor individual atoms or molecules, and, as such, they have a number of interesting and unique properties.<sup>1,3</sup> These properties can relate to the nanoparticle size, size quantum effects or surface-dependent properties.<sup>4</sup> The unique optical,<sup>1,2,5-7</sup> magnetic<sup>8,9</sup> and electronic<sup>10-12</sup> properties of gold nanoparticles, have already resulted in a number of potential applications in electronics,<sup>13,14</sup> sensing,<sup>15</sup> catalysis<sup>16-19</sup> and drug delivery.<sup>20,21</sup>

Molecules have long been covalently linked to form bulk materials, for example polymer materials are now widespread. However, the assembly of nanoparticles to form a bulk material is still in its infancy.<sup>22,23</sup> While there have been a number of advances in both the preparation of nanomaterials<sup>17</sup> and in the synthesis of complex molecules over the past several decades,<sup>24</sup> there is currently no general strategy for creating materials combining both molecule and nanoparticle components.

## 1.2 Gold nanoparticles: Structure and properties

Nanoparticles can be formed from a range of materials, including gold, silver and platinum, metal oxides, carbon nanomaterials and semiconductor materials to give quantum dots.<sup>25</sup> However, gold nanoparticles are generally regarded as the most widespread and easiest to work with,<sup>1</sup> and have the advantage of being non-toxic, which is relevant to potential biological applications. The work in this thesis will focus on gold nanoparticles.

The structure of a gold nanoparticle is a metal core, generally of between 1–100 nm in diameter. This metal core must be stabilised in order to prevent uncontrolled aggregation of nanoparticles in solution. Gold nanoparticle stabilisation can be achieved either electrostatically<sup>8,9</sup> or sterically,<sup>26</sup> or through a combination of the two. Electrostatic stabilisation is achieved through electrostatic repulsion of an adsorbed charged inorganic or organic species. Steric stabilisation may be achieved by the formation of a self-assembled monolayer of organic ligands on the nanoparticle surface (**Figure 1.1**). These ligands may be bound strongly to the gold surface through a strong gold-thiol bond.<sup>27</sup>

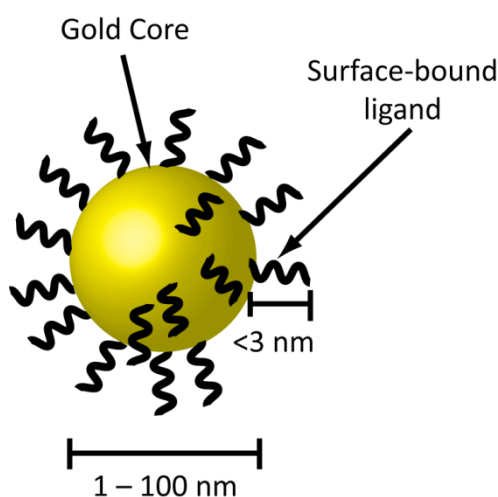


**Figure 1.1** Schematic representation of the structure of a gold nanoparticle stabilised by surface-bound ligands.

Gold nanoparticles have been shown to have a number of unique properties, for example surface plasmon resonance (SPR).<sup>28</sup> For gold nanoparticles in the

range of 2–100 nm, this SPR, which arises from the collective oscillation of electrons on the nanoparticles, gives rise to a deep red colour for gold nanoparticle solutions of this size range. Additionally, gold nanoparticles have been shown to have significant catalytic activity in a number of reactions, for example gold nanoparticle-catalysed oxidation of carbon monoxide.<sup>29</sup>

The organic ligands which stabilise the nanoparticle may be functionalised impart new properties/reactivity to the nanoparticle. The demand for functionalised nanoparticles is driven by the possibility of using organic chemistry in the nanoparticle-ligand monolayer to control nanoparticle properties and behaviour (see **Section 1.5**). Therefore, developing generalisable strategies for the synthesis of monodisperse nanoparticles, coated with functional ligands, is of crucial importance. Furthermore, as ever more sophisticated ligands are employed for nanoparticle synthesis, developing a rational control and understanding of factors that influence nanoparticle size presents a further challenge.

### **1.3 Synthesis of gold nanoparticles**

There are a large number of methods for creating gold nanoparticles: grinding methods, gas-phase methods and liquid-phase methods.<sup>30</sup> Grinding methods involve the physical breaking up of bulk gold into smaller fragments, ultimately down to the nanoparticle scale.<sup>31</sup> While this is a relatively cheap and easy method, it produces low quality polydisperse nanoparticles with poor size control. Gas-phase methods provide high quality nanoparticles but the high temperature (> 500 °C) and the fact that the result is non-functionalised nanoparticles mean that this method is not suitable for routine use.<sup>32</sup> By far the most common approach to synthesising gold nanoparticles is by solution-phase methods. The product of solution-phase syntheses are surface-functionalised nanoparticles which can allow a good control over their size and have reasonably low dispersities.

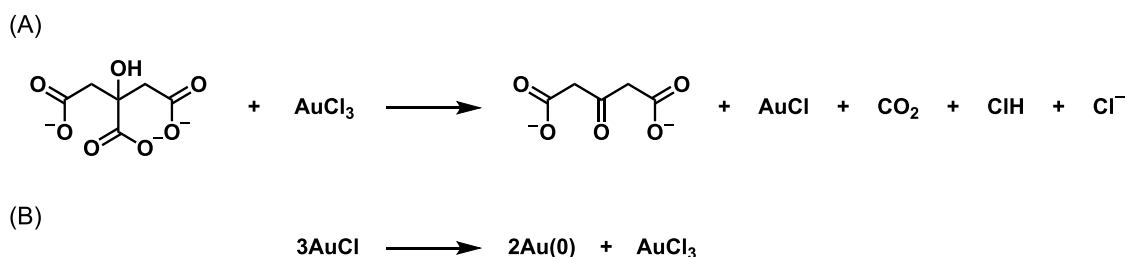
Nearly all unique nanoparticle properties are size-dependent. Therefore, achieving near-monodisperse samples of nanoparticles, and being able to fine-tune the nanoparticle size, is a key consideration in the use of nanoparticles for assembly into bulk materials, as well as for many other applications. The production of near-monodisperse nanoparticles would ensure that the average number of ligands per functionalised nanoparticle can be accurately estimated and controlled, and would reduce the distribution of size-dependent properties. There are a number of post-synthesis treatments which can decrease the size distribution of a nanoparticle solution, such as centrifugation,<sup>33</sup> which separates nanoparticles according to size, and thermal annealing,<sup>34</sup> which improves the dispersity of a sample by the inter-particle transfer of metal atoms. However, it is more desirable, easier and less wasteful to produce a narrower size distribution during the synthesis.

In general, solution-phase gold nanoparticle synthesis involves a source of gold (which is a salt), commonly gold(III) chloride or chloroauric acid, being reduced to colloidal gold(0). Solution-phase nanoparticle formation can be divided into two distinct processes: nucleation and growth.<sup>7,35,36</sup> Bonds in the metal precursor are broken and the solvate shells are removed in the endothermic nucleation process. This is followed by an exothermic growth process, where the particles grow, releasing the enthalpy of formation for the solid. Subsequently, in the absence of any stabilisers, particle aggregation will progress exothermically too, as overall surface area is reduced. A stabilising agent prevents the formation of colloidal aggregates. This stabilisation may be electrostatic or steric.

### **1.3.1 Electrostatic stabilisation: The Turkevich–Frens synthesis**

The most widespread synthesis of charge-stabilised nanoparticles is the Turkevich–Frens method,<sup>8,37</sup> which produces citrate-stabilised gold nanoparticles, which are colloidally stable in water. This method is often used for producing commercial supplies of colloidal gold. The synthesis uses sodium citrate as both the reducing agent and the charge-stabiliser in this high-

temperature synthesis. Although the mechanistic details of the stabilising role of citrate are still contested, it is known that the citrate reduces gold(III) to gold(I), in the process itself being oxidised to dicarboxyacetone (**Scheme 1.1A**). This is followed by a disproportionation of the gold(I) species<sup>38,39</sup> (**Scheme 1.1B**).



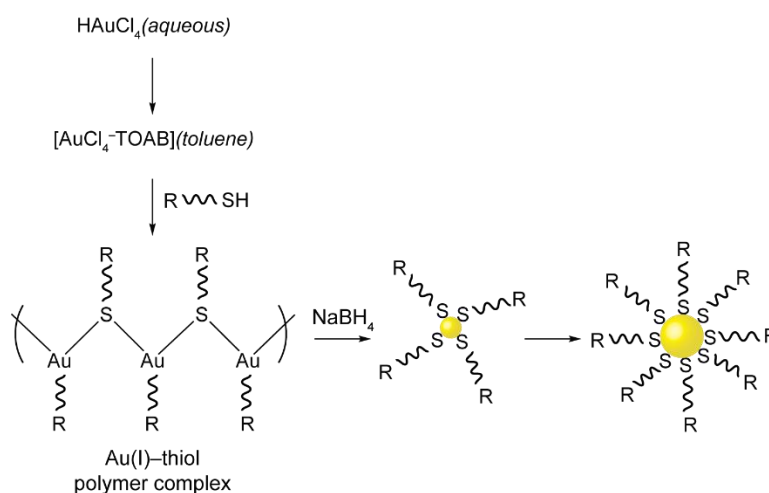
**Scheme 1.1** Mechanism for the reduction of gold(III) in the citrate synthesis of gold nanoparticles. **(A)** Reduction of gold(III) to gold(I). **(B)** Disproportionation of gold(I) to gold(III) and gold(0).<sup>38,39</sup>

Temperature and citrate concentration may be varied in order to give access to nanoparticles in the size range of 10–150 nm in diameter. Nanoparticle sizes are generally reported as average diameter of the size distribution, with one standard deviation quoted as the size dispersity. Nanoparticles synthesised by this citrate method often have high dispersities of > 30%,<sup>40</sup> especially for larger nanoparticles. As well as the problems with high size dispersities of nanoparticles produced by this method, the citrate stabilisation of the nanoparticles means that an organic ligand must subsequently be introduced to allow post-synthetic chemical modification of the nanoparticle properties. This can often induce a loss of colloidal stability. Even when the nanoparticles remain stable upon addition of an organic thiol ligand, complete removal of the charge-stabilisers is difficult. Furthermore, electrostatic stabilisation requires nanoparticles to be handled at very low concentrations and the nanoparticles are very susceptible to changes in ionic strength and pH.<sup>41</sup> Therefore direct synthetic routes to ligand-stabilised nanoparticles are highly desirable.

### 1.3.2 Steric stabilisation: The Brust–Schiffrin two-phase synthesis

One of the most widely used solution-phase methods for producing gold nanoparticles is the Brust–Schiffrin method.<sup>26</sup> This uses a biphasic system with tetraoctylammonium bromide (TOAB) as both a stabilising agent and a phase transfer catalyst, and, with sodium borohydride, as the reducing agent in the presence of an alkanethiol (most commonly dodecanethiol), to produce alkanethiol-coated nanoparticles in the organic phase.<sup>13</sup>

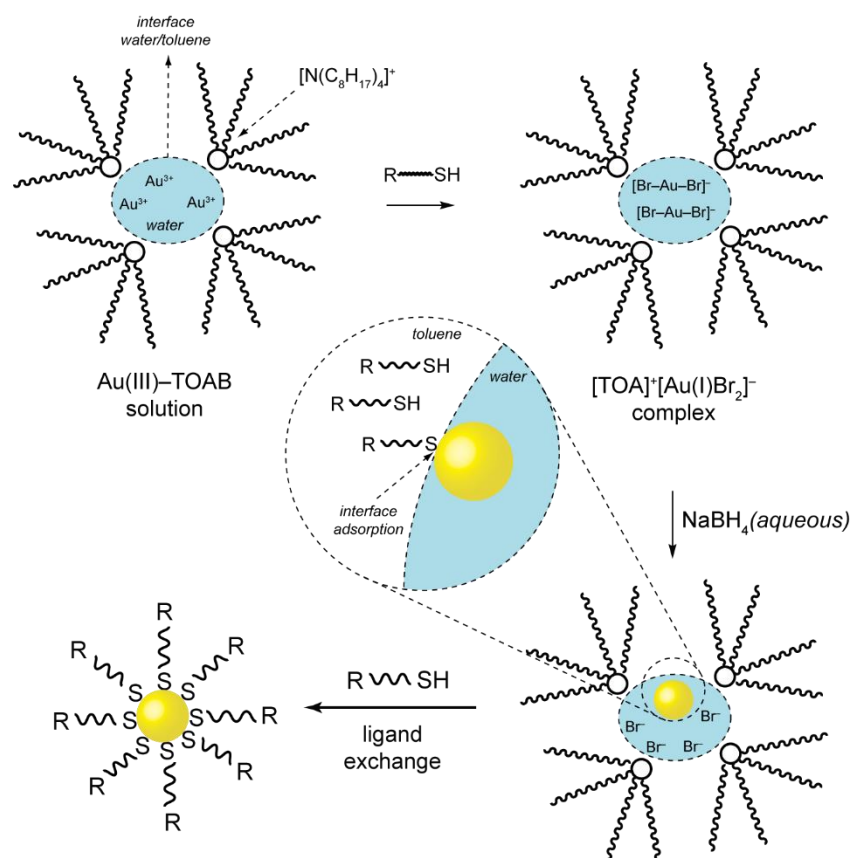
The mechanistic details of the process are debated. It has been proposed by Murray<sup>13</sup> that initially, gold(III) is transferred from the aqueous phase to the organic phase by the TOAB. Subsequently, Murray proposes the formation of a gold(I)-thiol polymer, which is then reduced to form nanoparticles (**Scheme 1.2**).



**Scheme 1.2** General mechanism of the Brust–Schiffrin gold nanoparticle synthesis as proposed by Murray.<sup>13</sup> Murray proposed that following transfer of gold(III) from the aqueous to organic phases, a gold(I)-thiol polymer forms prior to reduction to gold(0) and nanoparticle formation using sodium borohydride.

However, while agreeing with the presence of gold(I) in the initial stages of the synthesis, more recent investigations into the mechanism of the Brust–Schiffrin nanoparticle synthesis by Tong<sup>42</sup> and Lennox<sup>14</sup> have found no evidence for the existence of a gold(I)-thiol polymer, failing to observe any stretching vibration for a Au–S bond by Raman Spectroscopy. Instead a vibration corresponding to a  $[\text{Au(I)-Br}_2]^-$  species was observed. It was rationalised that the gold(III) was

being reduced to gold(I) by the thiol, which itself was oxidised to a disulfide. In addition, Tong observed by  $^1\text{H}$  NMR spectroscopy a large downfield shift of the water peak. It was proposed that the initial stages of the Brust–Schiffrin mechanism proceed through the formation of a  $[\text{TOA}]^+[\text{Au}(\text{I})\text{Br}_2]^-$  complex within inverse micelles in the organic phase (**Scheme 1.3**). Addition of the reducing agent,  $\text{NaBH}_4$ , reduces the gold(I) to gold(0), giving rise to nanoparticles stabilised by the TOAB, which are subsequently coated with the thiol.



**Scheme 1.3** General mechanism of the Brust–Schiffrin gold nanoparticle synthesis as proposed by Tong.<sup>42</sup> Tong proposed that gold(III) present in inverse micelles forms a gold(I)  $[\text{Au}(\text{I})\text{Br}_2]^-$  complex, before being reduced to gold(0) and forming nanoparticles, which are functionalised with thiols at the toluene/water interface.

The Brust–Schiffrin synthesis has a number of advantages over previous nanoparticle syntheses, producing thermal- and air-stable ligand-stabilised nanoparticles under ambient conditions. The Brust–Schiffrin method is widely used to produce gold nanoparticles due to the ease and operational simplicity in producing small ( $< 5$  nm) nanoparticles. However, it is limited due to the

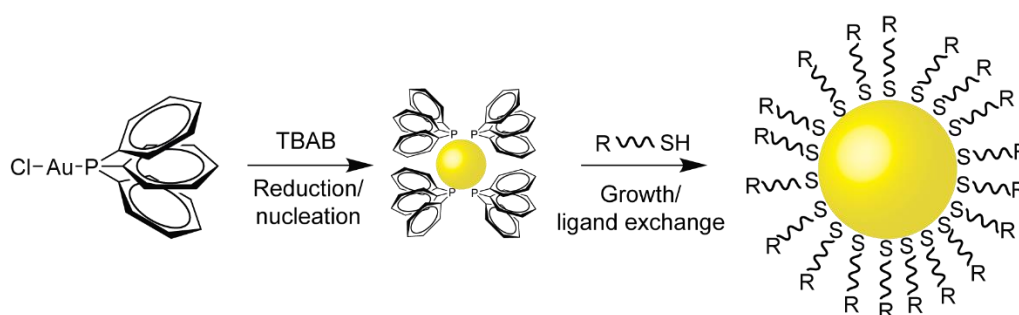
relatively high polydispersity of nanoparticles that it produces (> 15%). Despite a number of modifications to the original method over the past nineteen years since its publication, achieving polydispersities of below 10% has not been possible.<sup>43–46</sup>

### 1.3.3 Steric stabilisation: The Stucky synthesis and other one-phase syntheses

As an alternative to the two-phase Brust–Schiffrin method, a number of single-phase syntheses have been developed. An advantage of one-phase methods over two-phase methods is that nucleation and growth can occur throughout the solution, rather than only at the interface between the phases, which in addition to eliminating the need for a phase transfer agent, affords a more uniform nucleation and growth of nanoparticles, leading to narrower size distributions. A wide range of solvents have been used, particularly benzene or chloroform, or a mixture of the two.<sup>18</sup>

A single-phase synthesis using gold(I) in the form of triphenylphosphine gold chloride, developed by Stucky,<sup>18</sup> gives rise to nanoparticles with generally narrow size distributions (< 15%). Stucky uses a mild borane reducing agent, *tert*-butyl ammonium borane complex (TBAB) to reduce gold(0) in the presence of a thiol ligand. Lee<sup>19</sup> investigated the mechanism of the Stucky synthesis. Lee's investigations tried to ascertain what factors contributed to the narrow size distribution reported, < 5% for 5.9 nm dodecanethiol-coated nanoparticles synthesised in benzene. Initially, the gold source, gold(I) versus gold(III), was investigated. Replacing the triphenylphosphine gold chloride with chloroauric acid and TOAB as a phase transfer agent (required because chloroauric acid is insoluble in toluene) in the Stucky synthesis led to the formation of polydisperse nanoparticles between 1.7–2.7 nm. Addition of TOAB to a synthesis starting from triphenylphosphine gold chloride had essentially no effect on the nanoparticle size or distribution, with near monodisperse 6.0 nm nanoparticles obtained. Lee reasoned that the triphenylphosphine was important in stabilising the nanoparticles in the initial stages of the synthesis. While phosphine ligands are known to coordinate to gold nanoparticles,<sup>47</sup> and are commonly used in the

preparation of atomically precise gold clusters, syntheses using a gold(III) salt with a phosphine additive or a gold(I) salt without a phosphine ligand were not attempted. However, in the absence of a thiol ligand, small ( $\approx 1$  nm), polydisperse triphenylphosphine-stabilised nanoparticles were obtained, leading to a proposed mechanism of the initial formation of triphenylphosphine-stabilised particles, followed by growth to thiol-stabilised nanoparticles (**Scheme 1.4**).



**Scheme 1.4** Proposed mechanism for the Stucky synthesis of gold nanoparticles. Initial formation of triphenylphosphine-stabilised clusters is followed by growth to give thiol-coated nanoparticles.<sup>18,19</sup>

Nanoparticle size and dispersity in the Stucky synthesis is determined by the growth phase, as demonstrated in a study where the nanoparticle size and dispersity were found to be insensitive to the initial particle size and dispersity.<sup>36</sup> At time-points early in the synthesis, after a short growth phase, bimodal distributions are observed.<sup>48</sup> As the growth period is extended, the particle size distribution tends to monomodal distributions. This growth period has been shown by real-time solution-phase transmission electron microscopy (TEM) to proceed by monomer attachment and particle coalescence.<sup>49</sup> These mechanistic investigations indicate that developing good control over the length of the growth period of the nanoparticle synthesis can give rise to larger, less disperse nanoparticles.

In contrast to the Brust–Schiffrin method, Stucky’s method uses *tert*-butylamine borane complex (TBAB) as the reducing agent. TBAB has a significantly weaker

reduction potential than sodium borohydride. A number of reducing agents have been employed in gold nanoparticle syntheses, ranging from reducing agents with a high reduction potential, such as sodium borohydride,<sup>26</sup> hydrazine or tetrakis(hydroxyl-methyl)phosphonium chloride,<sup>50</sup> to ones with low reduction potential, such as *tert*-butylamine borane complex,<sup>18</sup> ascorbic acid<sup>51</sup> or oleylamine.<sup>52,53</sup> The reducing agent may reflect whether the nucleation or growth process is more responsible for controlling the nanoparticle size distribution in a particular synthesis. Nucleation-controlled syntheses rely on an instantaneous nucleation event for obtaining narrow nanoparticle size distributions. While reduction potential is not necessarily linked to the kinetics of the reduction, a reducing agent with a high reduction potential is desirable, for nucleation-controlled syntheses in order to promote simultaneous, instantaneous nucleation. For growth-controlled syntheses, mild reducing agents produce well temporally-defined nucleation events which may give rise to a wide distribution of particle sizes, which can then grow by monomer attachment and particle coalescence.

Alkanethiols are most commonly used as ligands for gold nanoparticle synthesis. The chain lengths may vary widely from about three carbons to sixteen carbons. A detailed study of varying chain length in the Stucky synthesis<sup>18</sup> by Lee<sup>19</sup> showed a slight trend for smaller nanoparticles at shorter chain lengths for synthesis in benzene, although upon changing the solvent to chloroform, the trend was no longer observed. Alkyl chain length does not appear to have any effect on the size dispersity of nanoparticles that are produced (approx. 10%–15%). Ligands other than alkanethiols have also been explored for nanoparticle synthesis. Disulfides act in a similar way to alkanethiols, and may be substituted in the synthesis of nanoparticles, because the disulfide bond is readily reduced under the synthesis conditions.<sup>54</sup> Amines are a weaker ligand for gold than thiols. The use of amine ligands by Peng<sup>43</sup> in a one-phase synthesis produced less polydisperse nanoparticles than when the synthesis was carried out in the presence of alkanethiols. The use of a weaker, more labile ligand is suggested to be favourable for the synthesis of monodisperse nanoparticles as the stronger ligands limit the activity of the initial nucleated species. Sun<sup>55</sup> developed another synthesis of amine-coated

nanoparticles, using TBAB, tetrachloroauric acid and a large excess of amine ligand to obtain nanoparticles with low (< 10%) dispersities; however, thiols were not compared under the same conditions.

A comparison of the different syntheses reveals much contradictory evidence across different nanoparticle syntheses over what factors influence particle size and dispersity. For example, in the Stucky synthesis<sup>18</sup> increasing the temperature leads to the synthesis of larger nanoparticles, whereas in the Sun synthesis<sup>55</sup> the opposite effect is observed. There is a lack of generalisable understanding over what factors and conditions influence nanoparticle size and dispersity. The lack of generally applicable understanding across different methods of nanoparticle synthesis may be a reflection of whether control over nanoparticle size and size distribution in each particular synthesis is dominated by the nucleation or the growth process.

A number of factors, such as temperature or solvent, may affect nanoparticle size and size distribution of a synthesis. Generalisations about what conditions control particle size are hard to draw. Even simply changing alkanethiol chain-length can lead to unpredictable results. Hexanethiol-coated nanoparticles synthesised by the Stucky method in benzene ( $3.4 \pm 0.4$  nm) were smaller than hexadecanethiol-coated nanoparticles ( $4.9 \pm 0.5$  nm) synthesised in the same conditions, whereas repeating the synthesis in chloroform resulted in larger hexanethiol-coated nanoparticles ( $2.5 \pm 0.5$  nm) than hexadecanethiol-coated nanoparticles ( $1.8 \pm 0.3$  nm).<sup>19</sup>

Introducing chemical functionality into the ligand design (see **Section 1.5**) can also significantly affect nanoparticle size and size dispersity. Direct synthesis of nanoparticles with functionalised ligands is an underdeveloped area of research. A comparative study of functionalised ligands was conducted by Shumaker-Parry.<sup>56</sup> Shumaker-Parry developed a one-phase synthesis<sup>57</sup> similar to the Stucky synthesis, substituting 9-borabicyclo- [3.3.1]nonane (9-BBN) as a mild reducing agent. Direct synthesis of nanoparticles coated with a range of alkanethiols, functionalised with an acid, amine or azide was reported. The size

and size dispersity of the nanoparticles depends on what ligand is used, in an apparently unpredictable way (**Figure 1.2**).

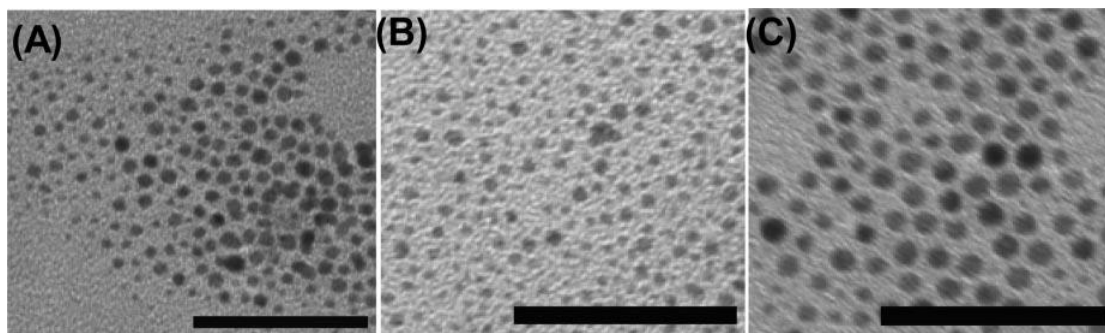


**Figure 1.2** TEM images of nanoparticles coated with in (A) 11-mercaptoundecanoic acid, (B) 11-mercaptoundecanamide, and (C) 11-azidoundecane-1-thiol. Scale bars are 40 nm. Figure reproduced from **ref. 56**.

## 1.4 Nanoparticle characterisation

Gold nanoparticles, consisting of an inorganic metal core coated with an organic ligand monolayer present a number of challenges regarding their characterisation. Both the inorganic and organic parts of the construct must be characterised. The gold core defines the shape and size of the nanoparticle, and determines its optical properties. The organic ligands commonly define nanoparticle solubility and reactivity, and ideally should be characterised with the same level of atomic precision routinely applied to organic molecules. In addition, nanoparticle samples are inherently polydisperse, a feature which can be statistically assessed, most simply and routinely by simply reporting the average size and standard deviation of the sample size. Variations in size and size dispersity between batches of identically functionalised nanoparticles present an additional challenge. A wide array of experimental techniques have been applied to characterisation of nanoparticles; however, only techniques used extensively in this thesis are covered here.

Nanoparticle sizes are most commonly characterised through transmission electron microscopy<sup>58</sup> (TEM), which allows direct visualisation of nanoparticles with sub-nanometer resolution. Nanoparticle diameters can be measured by

means of imaging software programs. Microscopy is a sampling technique and therefore, for an accurate representation of a sample, many images must be obtained, but even doing so, only a tiny fraction of the total sample is examined. TEM is limited by a narrow depth of focus and does not give any information about the ligand monolayer of a nanoparticle. Furthermore, TEM generally requires dried nanoparticle samples, and thus the resulting image is not representative of a colloidal dispersion of the nanoparticles.<sup>58</sup>

Dynamic light scattering provides an ensemble technique for analysis of colloidal dispersions.<sup>59</sup> By detecting the scattering of light from particles in solution, information about the random motion of particles is obtained and may be used to calculate diffusion coefficients. For spherical particles, the radius may be calculated, but the radius obtained is the solvodynamic radius, which includes the solvation shell of the nanoparticle as well as the core radius and the ligand. This radius is therefore highly dependent on ligand packing and solvent–ligand interaction. Dynamic light scattering is highly sensitive to nanoparticle shape and dispersity, and cannot compete with transmission electron microscopy in the amount of detail it provides about a nanoparticle sample size and size distribution.

UV-vis spectroscopy provides another tool widely used for characterising gold nanoparticles. The surface plasmon resonance (SPR), which arises from the collective oscillation of conduction band electrons at the nanoparticle surface, is responsible for the deep red colour of gold nanoparticles. The SPR of a nanoparticle can be measured by UV-vis spectroscopy, and is characterised by a broad absorption band at around 520 nm for gold nanoparticles in the 2–20 nm range. The exact position of the SPR band is related to nanoparticle sample size and size dispersity, as well as other factors such as the ligand shell and the solvent. In general, the SPR band for smaller nanoparticles is blue-shifted and decreases in intensity.<sup>1</sup> Changes in the core structure or colloidal stability of a nanoparticle sample will result in a change in the SPR band, which may be monitored by UV-vis spectroscopy.

The methods outlined above provide information about the inorganic core of the nanoparticle. In order to characterise the organic ligand, techniques such as IR spectroscopy and elemental analysis are employed. IR spectroscopy can give qualitative information about the structure of ligands. Elemental analysis in particular can provide accurate quantitative information about the composition of a nanoparticle. Inductively coupled plasma atomic emission spectroscopy (ICP-OES) is an elemental analysis technique that can be used to quantitatively detect emissions from excited states of elements. From the absolute concentration of elements such as gold, sulfur and boron, information about nanoparticle structure may be calculated. The most detailed structural information about nanoparticle-bound ligands comes from NMR spectroscopy.

#### **1.4.1 Nuclear magnetic resonance for characterisation of nanoparticle-bound molecules**

NMR spectroscopy, which is routinely used to characterise molecules in solution and to follow the dynamics of solution-phase molecular and supramolecular systems can also be used to for the *in-situ* non-destructive analysis of colloidal dispersions of ligand-functionalised nanoparticles. Unfortunately, the NMR analysis of nanoparticle-bound molecules is significantly more challenging than of freely dissolved molecules for a number of reasons.<sup>38,60,61</sup> First, inhomogeneity of the nanoparticle surface means that ligands are situated within different microenvironments, an effect that is more pronounced for nuclei close to the nanoparticle surface, which is reflected in a distribution of chemical shifts. Secondly, the dense packing of ligands in the nanoparticle monolayer means that degrees of molecular motion are severely restricted, particularly close to the nanoparticle surface, resulting in broad resonances. Thirdly, fast spin–spin ( $T_2$ ) relaxation times result from the slow tumbling of nanoparticles in solution due to their large size (relative to freely dissolved molecules). As the half-height peak width is inversely proportional to  $T_2$  times, this leads to inherently broad signals. A combination of these factors results in very broad resonances observed for nanoparticle-bound species.

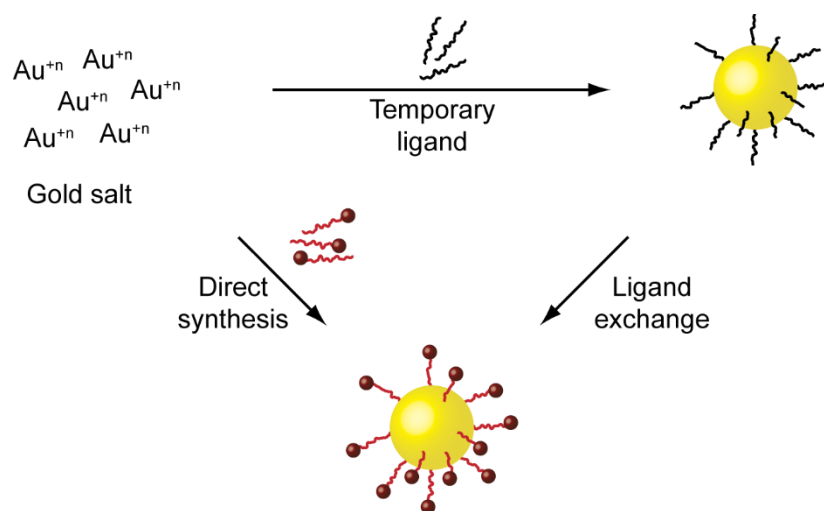
For a typical colloidal dispersion of nanoparticles, the concentration of organic ligands is intrinsically low (< 5 mM). This, coupled with the broad nature of signals obtained by NMR spectroscopy, makes obtaining detailed structural information about nanoparticle-bound species extremely challenging, with resonances well over 1 ppm wide not uncommon.  $^1\text{H}$  NMR spectroscopy badly suffers from the broad nature of signals due to the narrow chemical shift range. Furthermore, organic ligands generally have a large number of proton resonances, so signals often overlap.<sup>38,40,60</sup>  $^{13}\text{C}$  NMR offers a much wider range of chemical shifts; however,  $^{13}\text{C}$  NMR spectroscopy is insensitive due to the low relative abundance of  $^{13}\text{C}$  ( $\approx 1\%$ ), and therefore acquisition of  $^{13}\text{C}$  NMR spectra of nanoparticle-bound ligands is very time-consuming,<sup>60</sup> or requires costly and synthetically demanding preparation of  $^{13}\text{C}$ -enriched ligands.  $^{19}\text{F}$  NMR spectroscopy combines a high sensitivity with a wide range of chemical shifts, making it an attractive method of studying nanoparticle-bound systems. However, many ligands do not contain many fluorine atoms, so detailed structural information can be hard to obtain.<sup>60</sup>

Despite the significant challenges facing molecular-level characterisation of inherently dilute, heterogeneous and polydisperse nanoparticle systems, the variety of analytical tools provide the opportunity to fully elucidate molecular details of nanoparticle-bound molecules. The ability to characterise nanoparticles and nanoparticle-bound processes well is crucial for determining the link between phenomenological behaviour and structural detail, and ultimately developing rational control over nanoparticle functionalisation and assembly.

## 1.5 Nanoparticle functionalisation

The properties of ligands on the nanoparticle surface play a major role in determining the chemical properties of nanoparticles, such as reactivity and solubility. Two of the most common ligand designs are based on alkanethiols<sup>26</sup> or oligoethylene glycol spacers,<sup>62,63</sup> which can, respectively, contribute to

nanoparticle solubility in apolar or polar solvents (including water). Apart from modifying the solubility, ligands may have functional groups attached at their termini. Nanoparticles may be functionalised with ligands in two ways, either by synthesising the nanoparticle directly functionalised in the desired ligand or by exchanging the desired ligand onto a pre-formed nanoparticle in place of a sacrificial ligand<sup>64–66</sup> (or charge-stabiliser) (**Scheme 1.5**).



**Scheme 1.5** General scheme illustrating the two main approaches to nanoparticle functionalisation. Direct synthesis involves synthesis of the nanoparticle directly coated with a ligand bearing the desired functionality. Ligand exchange involves substituting on a ligand bearing the desired functionality in place of a sacrificial ligand.

Both direct synthesis and ligand exchange offer a number of advantages and disadvantages. Direct synthesis offers quick, efficient routes to functionalised nanoparticles, but the ligand stability must be compatible with the reducing environment of the synthesis conditions. Furthermore, the size and size dispersity of the nanoparticles depend on what ligand is used, in an apparently unpredictable way<sup>56</sup> (**Section 1.3, Figure 1.2**). Ligand exchange can give access to nanoparticles coated with a variety of ligands starting from the same nanoparticle batch; however, there is evidence for the transfer of not only ligands but also gold between nanoparticles during ligand exchange, so nanoparticles may not necessarily have the same size and size distribution after ligand exchange as before. Achieving complete ligand exchange can be

difficult<sup>66,69</sup> and requires a large excess of the incoming ligand to ensure full displacement of the sacrificial ligand, which can lead to problems in nanoparticle purification after ligand exchange. The details of the mechanism of ligand exchange are not fully understood, with differences for specific nanoparticle–ligand combinations, and even different behaviour between batches with different sample histories.<sup>66</sup> In many cases the efficiency of ligand exchange can be greatly improved by displacing a weaker ligand (non-thiol or short alkyl thiol) with a stronger-binding ligand.<sup>43</sup>

There are a number of post-synthetic methods for the modification of ligands and hence nanoparticle properties. Charge-switching,<sup>70,71</sup> host–guest complexation,<sup>72–75</sup> molecular switches,<sup>76–78</sup> irreversible covalent reactions<sup>79,80</sup> and reversible covalent reactions<sup>81,82</sup> offer routes to modifying nanoparticle properties, adding functionality or interfacing the nanoparticles with other components, be they molecular, other nanoparticles or surfaces.

## 1.6 Nanoparticle assembly

Nanoparticle assembly is a key area of nanoparticle research. Interfacing two or more nanoparticles with each other offers the potential to access emergent properties,<sup>83–86</sup> which could be harnessed to create new devices and materials. If the spacing, alignment and relative orientation of nanoparticles can be controlled, the way will be paved for a number of sophisticated applications. A number of approaches to the assembly of nanoparticles have been reported. Broadly speaking, nanoparticle assembly methods may be divided into two categories: assembly through covalent interactions and assembly through noncovalent interactions.

### 1.6.1 Assembly of nanoparticles using covalent bonds

Covalently-linked nanoparticle assembly strategies offer a number of attractive features. Covalent bonds are generally very stable, and can offer access to robust assemblies. A vast array of literature in the field of organic chemistry has developed numerous covalent bond-forming reactions, with a huge range of structural diversity. Each bond-forming reaction tends to occur between two functional groups of just a few atoms, which can therefore be incorporated within a molecule of virtually any size or complexity.

Linking nanoparticles covalently has been used for assembly of both discrete nanoparticle structures<sup>87–90</sup> and extended nanoparticle assemblies.<sup>91–95</sup> Covalent nanoparticle assembly can most simply be achieved through linking nanoparticles with a di-thiol linker molecule.<sup>90,91</sup> Such assembly strategies rely on the formation of strong gold–sulfur bonds, and result in nanoparticles linked directly to each other. This kind of assembly strategy has also been applied to amine linkers,<sup>94,95</sup> where the amine interacts with the gold surface. Directly linked covalent assemblies such as these are characterised by short inter-particle distances, which are generally controlled by the length of the linker molecule, and may as such be fine-tuned by the molecular design of the linker.<sup>90</sup> However, the structures formed are generally not highly ordered, and controlling the structure of the nanoparticle assembly in a sophisticated manner is generally not possible. Although these nanoparticle assemblies formed with ditopic linkers are covalently linked, no covalent bonds are formed in the process and, instead, the gold–thiol or gold–amine bond formation drives the assembly. Although such reactions are effectively ligand-exchange reactions, which are often reversible,<sup>64–66</sup> these systems generally produce structures which rapidly precipitate, making the nanoparticle assembly an irreversible process.

Nanoparticles have also been assembled through the formation of a covalent bond between the ligands of two differently functionalised nanoparticles. For example, click-chemistry between an azide and an alkyne has been used to generate discrete nanoparticle ‘planet–satellite’ assemblies,<sup>87</sup> however, uniform

structures are not generated. The limited control over nanoparticle assembly, observed for covalently-linked structures, arises from the kinetic control of such reactions. When nanoparticles are assembled irreversibly, ‘errors’ in the assembly structure cannot be corrected.

### 1.6.2 Noncovalent nanoparticle assembly

Thermodynamically-controlled processes offer the opportunity for ‘error correcting’, stimuli-responsive systems. A system under thermodynamic control will tend towards the energy minimum. For example, as illustrated by **Figure 1.3**, while **A** may initially be converted to **C**, for a system under thermodynamic control, **C** may be converted back to **A**, which may in turn be converted to **B**, which is the thermodynamic product of the system, at the energy minimum. This is despite the transition barrier from **A** to **C** ( $\Delta G_{AC}^\ddagger$ ) having a lower energy than the barrier from **A** to **B** ( $\Delta G_{AB}^\ddagger$ ), so long as there is sufficient energy in the system to surmount all the activation barriers. A system under kinetic control is more likely to go from **A** to **C** than **A** to **B**, as ( $\Delta G_{AC}^\ddagger$ ) is lower than ( $\Delta G_{AB}^\ddagger$ ). In a more complex system with a large number of local minima, a system truly under thermodynamic control will tend towards the global minimum, analogous to finding the global minimum of an energy surface in a Monte Carlo simulation. However, in a kinetically-controlled system, it is not possible to go back from the products to the starting material (under the same conditions), making the system irreversible.

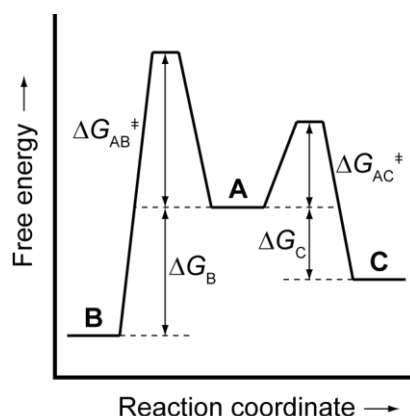


**Figure 1.3** Free energy profile illustrating the conversion of **A** to **B** under thermodynamic control or **A** to **C** under kinetic control.

A wide range of noncovalent approaches to nanoparticle assembly have been reported, using hydrogen bonding,<sup>96</sup> halogen bonding,<sup>97</sup> electrostatic interactions<sup>98–100</sup> and dipole–dipole interactions.<sup>92</sup> Reversibility has been demonstrated for a number of these systems. Host–guest interactions, such as between a macrocyclic host and an appropriate guest are among the most successful noncovalent approaches to nanoparticle assembly.<sup>98,101,102</sup> Nanoparticles functionalised with a crown ether-macrocyclic host are assembled through addition of a guest capable of binding to two hosts, which can bridge two nanoparticles, inducing their assembly.<sup>101</sup> This process may be inhibited by the addition of a competing guest which can only bind a single host, demonstrating the stimuli-responsive nature of the system. Similar host–guest systems have been developed for the reversible synthesis of discrete nanoparticle assemblies.<sup>98</sup> Additionally, polymer-supported guests have been used in a similar system in order to direct the nanoparticle assembly.<sup>96</sup> However, these relatively weak intermolecular interactions tend to produce kinetically labile assemblies, leading to disordered aggregates at long time-periods as the system precipitates, forming a kinetically trapped aggregate.

In the ultimate expression of the noncovalent approach, oligonucleotide-functionalised nanoparticles have been assembled under fully thermodynamic control to produce crystalline nanoparticle arrays with molecular control over crystal lattice structure.<sup>72</sup> Oligonucleotide-based nanoparticle assembly approaches exploit the particularly strong hydrogen bonding effect arising from the multiple hydrogen bonds between complementary oligonucleotides. Pioneered by Mirkin<sup>103</sup> and Alivisatos.<sup>104</sup> Mirkin<sup>103</sup> coated relatively large (13 nm) nanoparticles with non-complementary oligonucleotides. Upon the addition of a complementary oligonucleotide linker strand, strong hydrogen bonds were formed between the complementary base pairs (**Figure 1.4A**), leading to the reversible formation of aggregates, which could be broken up by raising the temperature of the system. Alivisatos's<sup>104</sup> approach used much smaller nanoparticles (1.4 nm), attaching single strands of oligonucleotides to the nanoparticles, leading to the formation of discrete two- or three-nanoparticle

'colloidal molecules' (**Figure 1.4B**), again, assembled by complementary base-pairing between the oligonucleotides.

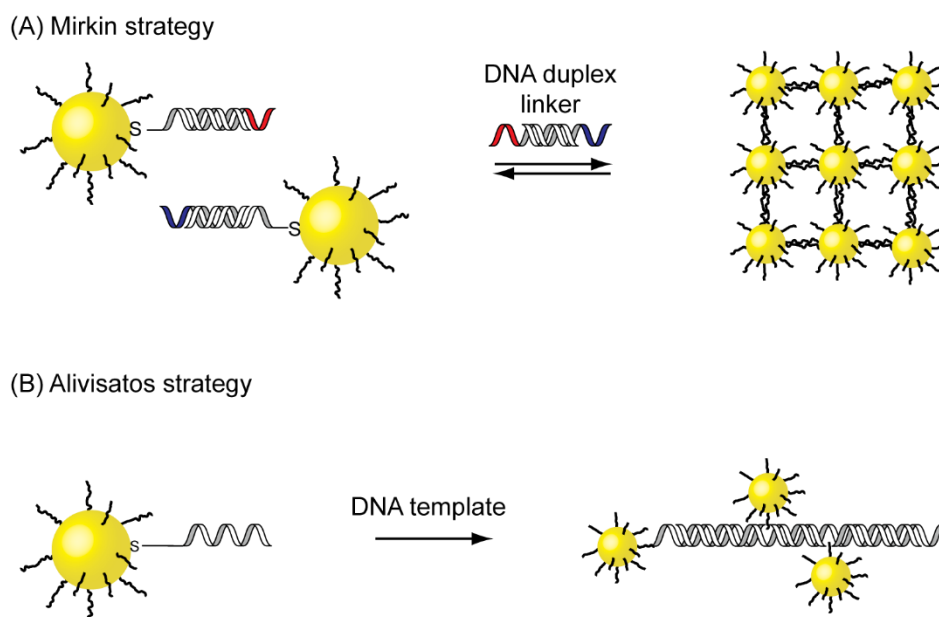


**Figure 1.4** Assembly of nanoparticles driven by oligonucleotide hybridisation. (A) Nanoparticles functionalised with non-complementary oligonucleotides assemble upon the addition of a complementary DNA linker strand.<sup>103</sup> (B) Oligonucleotide-functionalised nanoparticles assembled to form discrete 'colloidal molecules' upon the addition of a single-strand template.<sup>104</sup>

The level of control achieved in oligonucleotide-based nanoparticle assembly systems comes from the thermodynamic control. Indeed, the level of control is such that oligonucleotide-based approaches are the only current approaches to the synthesis of three-dimensional crystalline nanoparticle assemblies with independent control over packing structure and nanoparticle size and shape. Ordered crystalline face-centred-cubic and body-centred-cubic crystal nanoparticle assemblies have since been formed using oligonucleotide linkers. Mirkin<sup>105,106</sup> and Gang<sup>107</sup> independently developed systems using DNA-based linkers, which could produce thermodynamically-stable long-range ordered structures. The reversibility of such systems allows the initial random aggregation to be error-corrected, and, over time, oligonucleotide-linked crystalline lattices form (**Figure 1.5**). These lattices form as they are more thermodynamically stable structures than the initial random assembly, which is a local energy minimum, rather than a global energy minimum of the system.

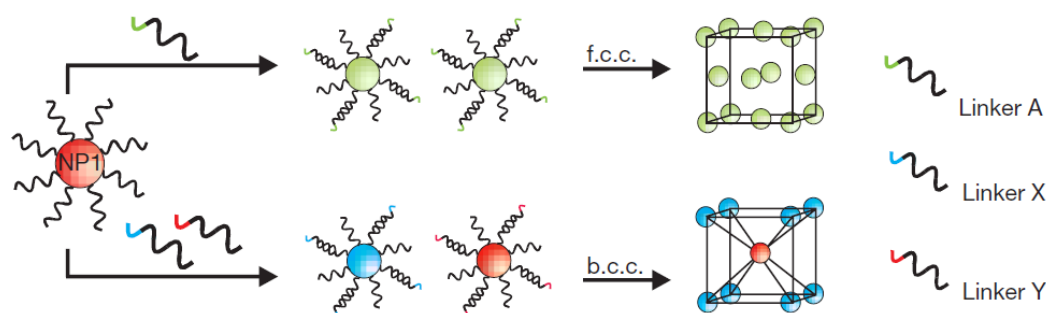


**Figure 1.5** Ordered nanoparticle assemblies linked by oligonucleotide strands. The reversible nature of the aggregation process allows an ordered thermodynamically-stable crystalline lattice to be formed. The nanoparticle crystal packing arises from the oligonucleotide linker used. (Figure taken from ref. 105.)

A remarkable aspect of oligonucleotide-assembled crystalline nanoparticle lattices is that both face-centred-cubic (f.c.c.) and body-centred-cubic (b.c.c.) nanoparticle lattices may be achieved using the same nanoparticles, modifying the sequence or the length of the oligonucleotide linker. This level of molecular control over nanoparticle assembly is unprecedented. By contrast, nanoparticle superlattices formed either by careful drying of nanoparticle samples or electrostatic interactions form closely-packed assemblies where the packing arrangement is intrinsically linked to the size(s) of the nanoparticle building blocks.<sup>108–112</sup> More recently, many more oligonucleotide-linked crystal lattices have been accessed<sup>72,105,113–116</sup> along with a sophisticated understanding of a number of factors such as nanoparticle size, curvature and oligonucleotide binding strength.<sup>117,118</sup>

Such a sophisticated level of control over nanoparticle assembly as has been achieved by oligonucleotide approaches has yielded significant medical and biological applications.<sup>119</sup> Using the binding affinity of nanoparticle-bound oligonucleotides, fluorescence-based sensing of biologically relevant molecules such as mRNA<sup>120</sup> and adenosine triphosphate<sup>121</sup> have been developed, as well as colorimetric detection of cancer cells.<sup>122</sup>

While oligonucleotide-based approaches to nanoparticle assembly have yielded unprecedented levels of control, there are a number of drawbacks. Although

inter-particle distances may be controlled by changing the length of the oligonucleotide linker, relatively long linkers<sup>123–125</sup> are required for DNA hybridisation, rendering very short inter-particle distances inaccessible. Furthermore, discrete ‘colloidal molecules’ formed by oligonucleotide-based nanoparticle assembly must be purified, either by electrophoresis<sup>126</sup> or by differential centrifugation.<sup>89,127,128</sup> Double-stranded DNA hybrids display chemical and structural stability only in a relatively narrow range of conditions (for example solvent, pH, temperature, and buffer concentrations). As such oligonucleotide-based assemblies are stable only within a narrow range of conditions. Furthermore, the complexity of the biomolecules employed makes *in-situ* molecular-level characterisation of these structures very challenging.

## 1.7 Dynamic covalent chemistry for nanoparticle functionalisation and assembly

### 1.7.1 An introduction to dynamic covalent chemistry

Dynamic covalent chemistry (DCC) is a powerful concept for the thermodynamic self-assembly of complex structures which can then be made kinetically stable by the application of an external stimulus.<sup>129</sup> Dynamic covalent reactions are characterised by being reversible under thermodynamic control, allowing a system to equilibrate to a distribution of products characterised by their thermodynamic stability. To be suitable for use in dynamic covalent chemistry, a covalent bond-forming reaction must be reversible on a reasonable timescale and it should be possible to ‘freeze’ the system to prevent re-equilibration of the desired products once formed. There are a number of suitable reactions for this, as shown in **Table 1.1**.<sup>129</sup>

**Table 1.1** A selection of reversible covalent reactions employed in dynamic covalent processes.<sup>129</sup>

<b>C=N exchange</b>					
Transimination	$R_1\text{-CH=N-R}_2$	+	$R_3\text{-CH=N-R}_4$	$\xrightleftharpoons{\text{Acid}}$	$R_1\text{-CH=N-R}_4$ + $R_3\text{-CH=N-R}_2$
Hydrazone exchange	$R_1\text{-CH=N-NH-R}_2$	+	$R_3\text{-CH=N-NH-R}_4$	$\xrightleftharpoons{\text{Acid}}$	$R_1\text{-CH=N-NH-R}_4$ + $R_3\text{-CH=N-NH-R}_2$
Oxime exchange	$R_1\text{-CH=N-O-R}_2$	+	$R_3\text{-CH=N-O-R}_4$	$\xrightleftharpoons{\text{Acid}}$	$R_1\text{-CH=N-O-R}_4$ + $R_3\text{-CH=N-O-R}_2$
<b>Acyl exchange</b>					
Transesterification	$R_1\text{-C(=O)-O-R}_2$	+	$R_3\text{-C(=O)-O-R}_4$	$\xrightleftharpoons{\text{Base}}$	$R_1\text{-C(=O)-O-R}_4$ + $R_3\text{-C(=O)-O-R}_2$
Transtioesterification	$R_1\text{-C(=O)-S-R}_2$	+	$R_3\text{-C(=O)-S-R}_4$	$\xrightleftharpoons{\text{Base}}$	$R_1\text{-C(=O)-S-R}_4$ + $R_3\text{-C(=O)-S-R}_2$
Transamidation	$R_1\text{-C(=O)-NH-R}_2$	+	$R_3\text{-C(=O)-NH-R}_4$	$\xrightleftharpoons{\text{Protease or metal}}$	$R_1\text{-C(=O)-NH-R}_4$ + $R_3\text{-C(=O)-NH-R}_2$
Michael-addition	$R_1\text{-CH=CH-C(=O)-R}_2$	+	$R_3\text{-SH}$	$\xrightleftharpoons{\text{Base}}$	$R_1\text{-CH(R}_3\text{)-CH}_2\text{-C(=O)-R}_2$
<b>Other exchange</b>					
Disulfide exchange	$R_1\text{-S-S-R}_2$	+	$R_3\text{-S-S-R}_4$	$\xrightleftharpoons{\text{R-S}^-}$	$R_1\text{-S-S-R}_4$ + $R_3\text{-S-S-R}_2$
Olefin metathesis	$R_1\text{-CH=CH-R}_2$	+	$R_3\text{-CH=CH-R}_4$	$\xrightleftharpoons{\text{Grubbs catalyst}}$	$R_1\text{-CH=CH-R}_4$ + $R_3\text{-CH=CH-R}_2$
Boronic ester exchange	$R_1\text{-B(O-R}_2\text{)(O-R}_3\text{)(O-R}_4\text{)(O-R}_5\text{)}$	+	$\text{HO-C(R}_6\text{)(R}_7\text{)-OH-C(R}_8\text{)(R}_9\text{)-OH}$	$\xrightleftharpoons{\text{Base}}$	$R_1\text{-B(O-R}_6\text{)(O-R}_7\text{)(O-R}_8\text{)(O-R}_9\text{)}$ + $\text{HO-C(R}_2\text{)(R}_3\text{)-OH-C(R}_4\text{)(R}_5\text{)-OH}$
Acetal exchange	$R_1\text{-C(OR)(OR)-R}_2$	+	$R_3\text{-C(OR')(OR')-R}_4$	$\xrightleftharpoons{\text{Acid}}$	$R_1\text{-C(OR')(OR')-R}_2$ + $R_3\text{-C(OR)(OR)-R}_4$
Dies-Alder	$\text{Cyclopentadiene-C(R}_1\text{)=C(R}_2\text{)}$	+	$\text{C=C(R}_3\text{)(R}_4\text{)-C(R}_3\text{)(R}_4\text{)-C(R}_3\text{)(R}_4\text{)}$	$\xrightleftharpoons{\hspace{1cm}}$	$\text{Bicyclo[2.2.1]heptane-C(R}_1\text{)(R}_2\text{)-C(R}_3\text{)(R}_4\text{)-C(R}_3\text{)(R}_4\text{)-C(R}_3\text{)(R}_4\text{)}$

Dynamic covalent chemistry has attracted a large amount of interest and has found numerous applications in, for example, self-assembly, molecular recognition, drug discovery and systems chemistry.<sup>130–134</sup> Boronic ester formation (which is the focus of **Chapters 3** and **4** of this thesis) involves the reaction of a boronic acid with a 1,2- or 1,3-diol (**Chapter 3.1**).<sup>135–137</sup> Boronic ester formation is a rapid process, which can operate in aqueous conditions, making it particularly attractive for a number of applications, and in particular has been successfully employed for the synthesis of covalent organic frameworks<sup>138–141</sup> by self-assembly, sugar binding<sup>142,143</sup> and numerous sensing applications.<sup>144–146</sup>

### 1.7.2 Dynamic covalent chemistry on nanoparticles

Dynamic covalent chemistry is particularly attractive as a means of nanoparticle functionalisation and assembly because it offers a combination of the reversibility and stimuli-responsiveness displayed by noncovalent interactions with the stability and structural diversity of covalent chemistry. Dynamic covalent chemistry has the potential to deliver a diverse range of nanoparticle-bound systems, offering precise and reconfigurable control. However, nanoparticle-bound dynamic covalent chemistry is in its infancy.

Nanoparticle-bound hydrazones and imines have been used for peptide sensing,<sup>147</sup> bioimaging,<sup>148</sup> antibacterial applications<sup>149</sup> and drug delivery systems for anti-cancer drugs.<sup>150–154</sup> The majority of these applications operate under pseudo-irreversible conditions, and are essentially indistinguishable from irreversible covalent bond-forming or bond-breaking reactions. Sensing and bioimaging have been reported through the use of aldehyde-functionalised quantum dots. Conjugation of a hydrazide derivative peptide to the nanoparticle through hydrazone bond formation induces nanoparticle aggregation, which can be detected through fluorescence.<sup>147</sup> A small number of drug delivery applications involve both bond formation and bond breaking, although these

processes are, again, carried out under pseudo-irreversible conditions. Nanoparticles are conjugated to the drug, and hydrolysis of the hydrazone bond under acidic conditions leads to the release of the drug. In any of these systems, not only are the dynamic features of the chemistry not exploited but also the molecular details of the covalent bond-forming or bond-breaking process are not addressed; thus, the evidence for covalent bond formation or bond breaking is purely phenomenological, derived from the uptake or release of cargo by the nanoparticle.

While there are a number of examples of the use of nanoparticle-bound boronic ester exchange, particularly for the sensing of sugars,<sup>155–157</sup> proteins/peptides<sup>157–169</sup> and other biologically relevant materials,<sup>170–174</sup> and for drug delivery,<sup>175–177</sup> these systems operate in a dynamic fashion, with boronic ester-formation or hydrolysis used in an irreversible manner. The use of nanoparticle-bound boronic ester formation for sensing is a particularly attractive application, due to the prevalence of 1,2-diols in biologically relevant molecules, for example sugars and glycoproteins. Three examples presented here (**Figure 1.6**) report the use of boronic ester formation for the conjugation and detection of biomolecules.

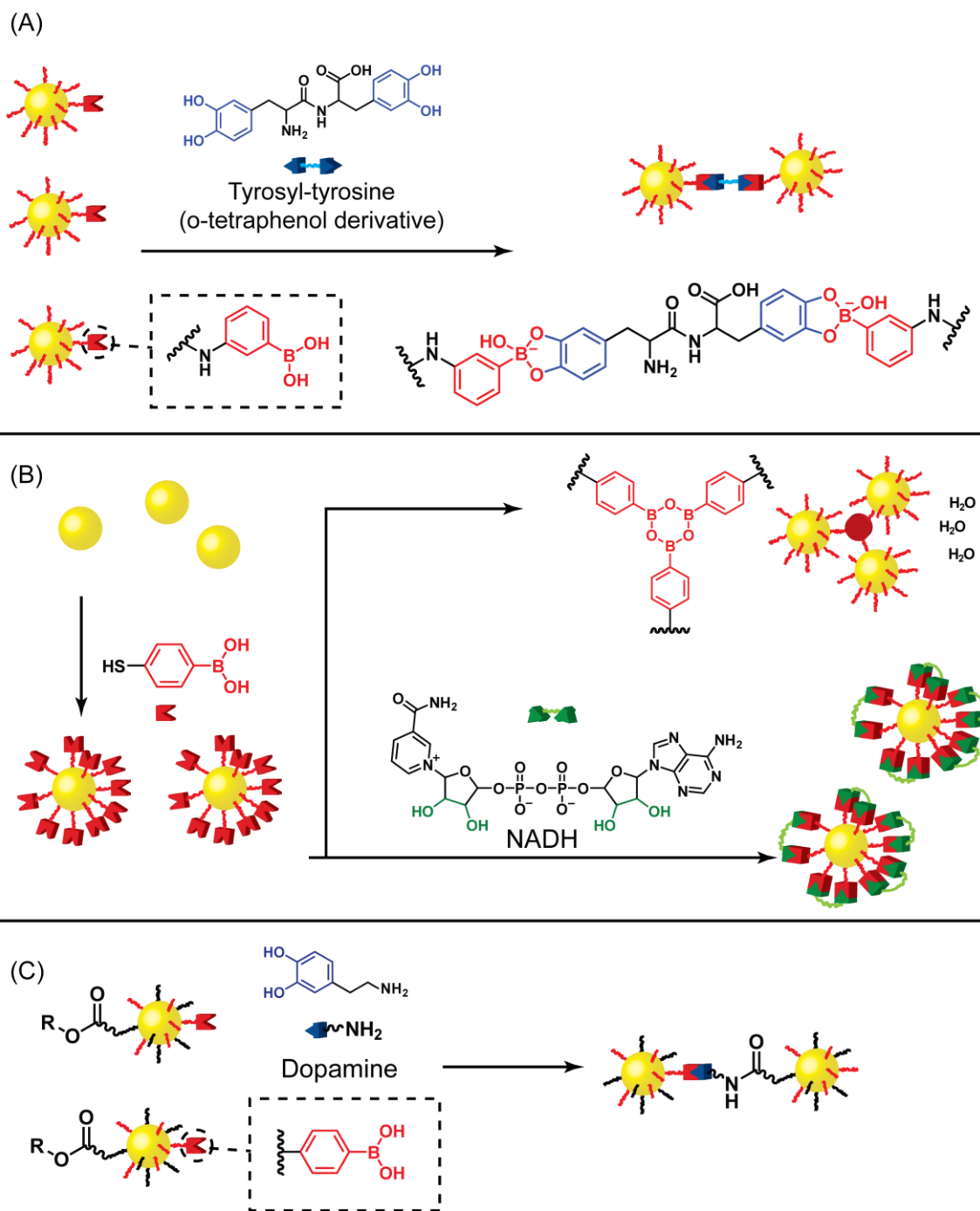


**Figure 1.6** Schematic representation of the use of nanoparticle-bound boronic acids for sensing of (A) peptides<sup>173</sup> (B) NADH<sup>171</sup> and (C) dopamine.<sup>174</sup> The presence of the analyte induces (or prevents in (B)) nanoparticle aggregation, which can be detected by a decrease in the UV absorption or colorimetrically due to SPR coupling.

The first example<sup>173</sup> (**Figure 1.6A**) reports the detection of the o-tetraphenol derivative of the dipeptide tyrosyl-tyrosine. 13 nm citrate-stabilised

nanoparticles are functionalised sequentially with mercaptoundecanoic acid, by means of a ligand-exchange reaction, and then with aminophenylboronic acid, by an EDC-mediated peptide coupling with the carboxylic acid. However, no evidence of the molecular structure of the functionalised nanoparticles is provided at any stage, with slight change in the UV-vis spectra of the nanoparticles providing the only evidence of a change in the nanoparticle monolayer. Upon addition of the *o*-tetraphenol tyrosyl-tyrosine derivative, the nanoparticle UV-vis absorbance decreases; however, surprisingly, no shift in  $\lambda_{\text{max}}$  (SPR) (as a result of plasmon coupling between nanoparticles in close proximity) is observed. The decrease in absorbance is attributed to the precipitation of nanoparticles from solution. TEM images show signs of nanoparticle aggregation, but there is no evidence of the molecular process that causes the aggregation. No reversibility in the system is reported and the authors do not attempt to resuspend the nanoparticle aggregates.

The second example<sup>171</sup> (**Figure 1.6B**) reports the use of nanoparticle-bound boronic ester formation for the detection of NADH (nicotinamide adenine dinucleotide). An aqueous solution of 13 nm citrate-stabilised nanoparticles is mixed with mercaptophenylboronic acid. Upon mixing, a colour change from red to blue is observed. UV-vis analysis of the solution indicates a shift in the  $\lambda_{\text{max}}$  (SPR), indicating nanoparticle aggregation. The authors suggest that the nanoparticles are functionalised with the boronic acid by means of a strong gold–thiol bond, and subsequently aggregate due to the formation of inter-nanoparticle 6-membered boroxane rings. This is a surprising conclusion, as boroxane formation is an equilibrium process, which releases three molecules of water for each boroxane formed, so it is expected to be highly disfavoured in an aqueous environment. If the citrate-functionalised nanoparticles are mixed with NADH prior to addition of mercaptophenylboronic acid, no nanoparticle aggregation is seen. The authors suggest that the absence of nanoparticle aggregation is due to the formation of boronic esters between the 1,2-diols on the NADH and the nanoparticle–boronic acids, preventing boroxane formation. However, other than not observing nanoparticle aggregation in the presence of NADH, there is no other evidence for this conclusion.

A third sensing example<sup>174</sup> (**Figure 1.6C**) reports the use of nanoparticles functionalised with a boronic acid and an activated acid for the detection of dopamine. Citrate-stabilised nanoparticles are functionalised with a mixture of boronic acid and succinimidyl ester. X-ray photoemission spectroscopy indicates the presence of sulfur, nitrogen and boron on the functionalised nanoparticles, although more detailed molecular analysis of the monolayer composition is not reported. Upon addition of dopamine, the solution changes colour from red to blue, and a shift is observed in the  $\lambda_{\max}$  (SPR), indicating nanoparticle aggregation. The authors attribute the nanoparticle aggregation to the formation of amides and boronic esters, which covalently link the nanoparticles, although no further evidence of this process is provided.

In none of the examples of nanoparticle-bound boronic ester formation discussed above is the reversibility of this process is demonstrated. Furthermore, there is a lack of any molecular-level characterisation, and the evidence for boronic ester formation is purely phenomenological.

The molecular details of reversible nanoparticle-bound covalent bond-formation processes have been examined more thoroughly in only two cases. One is a template-driven dynamic covalent nanoparticle functionalisation, recently reported by Otto.<sup>82</sup> Gold nanoparticles functionalised with a mixed monolayer of aldehyde and ammonium-terminated ligands were combined in water with an excess of aromatic amines, capable of forming imines with the nanoparticle-bound aldehydes (**Figure 1.7**). HPLC analysis of the aqueous mixture showed that negligible amounts of imines were formed. Addition of short DNA template, which could intercalate the amines, resulted in a change in the amine product distribution by HPLC analysis, indicating the uptake of imines by the nanoparticles. The uptake of amines in the presence of the DNA template indicated that amines were intercalated by the DNA template, allowing cooperative imine formation with the nanoparticle-bound aldehydes. A control experiment using nanoparticles lacking aldehyde functionality resulted in a very limited amine uptake. The nanoparticles could be separated and amines

displaced from the aldehydes by the addition of a hydroxylamine to form an oxime. The resulting amine product distribution could be analysed and was shown to be dependent on the base pair sequence of the DNA template. This system clearly exploits the reversibility of imine covalent bond formation. However, despite the strong evidence for the formation of nanoparticle-bound imines, there is no direct molecular-level characterisation of the nanoparticle-bound dynamic covalent bond.

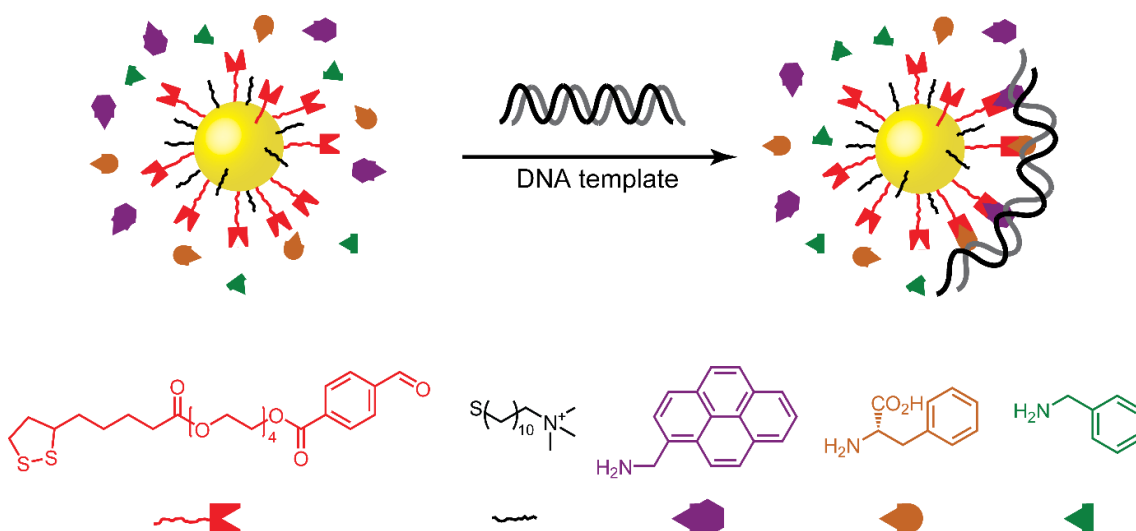


**Figure 1.7** Template-driven dynamic covalent imine formation with nanoparticle-bound aldehydes.<sup>82</sup> Negligible imine formation is observed in the absence of the DNA template. The DNA template allows cooperative imines formation, with the resulting product distribution dependent on the DNA base pair sequence.

The current best-characterised and most well-understood example of dynamic covalent chemistry on nanoparticle monolayers comes from the Kay group.<sup>81</sup> Dynamic covalent hydrazone exchange was investigated at the molecular level. Nanoparticles functionalised with a fluorinated hydrazone-terminated ligand were modified by addition of an alternative fluorinated aldehyde (**Figure 1.8A**). Hydrazone exchange on the nanoparticle monolayer occurred under acidic conditions and was observed directly by <sup>19</sup>F NMR spectroscopy, which allowed for the direct quantitative detection of nanoparticle-bound species. The

hydrazone exchange was shown to be reversible and the kinetics of the exchange were monitored and found to be slower than with a corresponding molecular model, an effect that can be attributed to the increased steric crowding on nanoparticle monolayers, as seen previously for irreversible covalent reactions.<sup>40</sup> The detailed molecular understanding developed of dynamic covalent hydrazone exchange was subsequently applied to fine-tuning the nanoparticle solubility properties. The solubility of the nanoparticles could be freely and completely reversibly modulated, simply by exchanging the desired aldehyde onto the nanoparticle–ligand monolayer (**Figure 1.8B**).

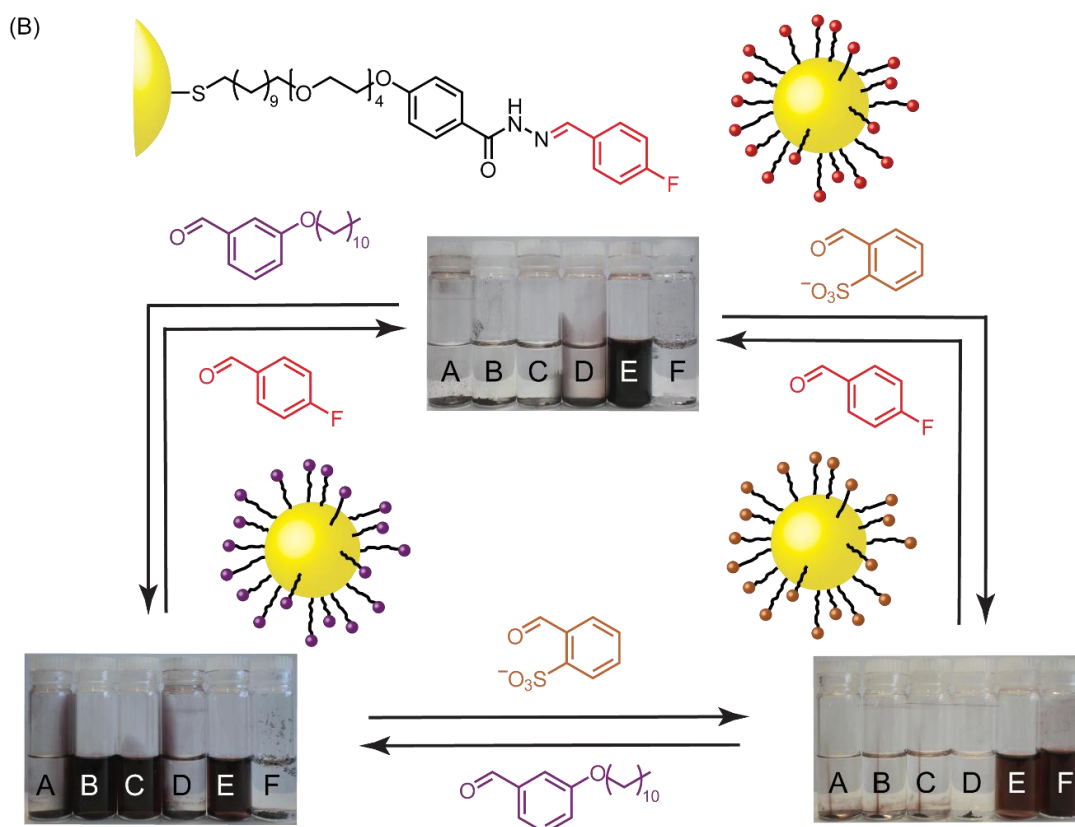
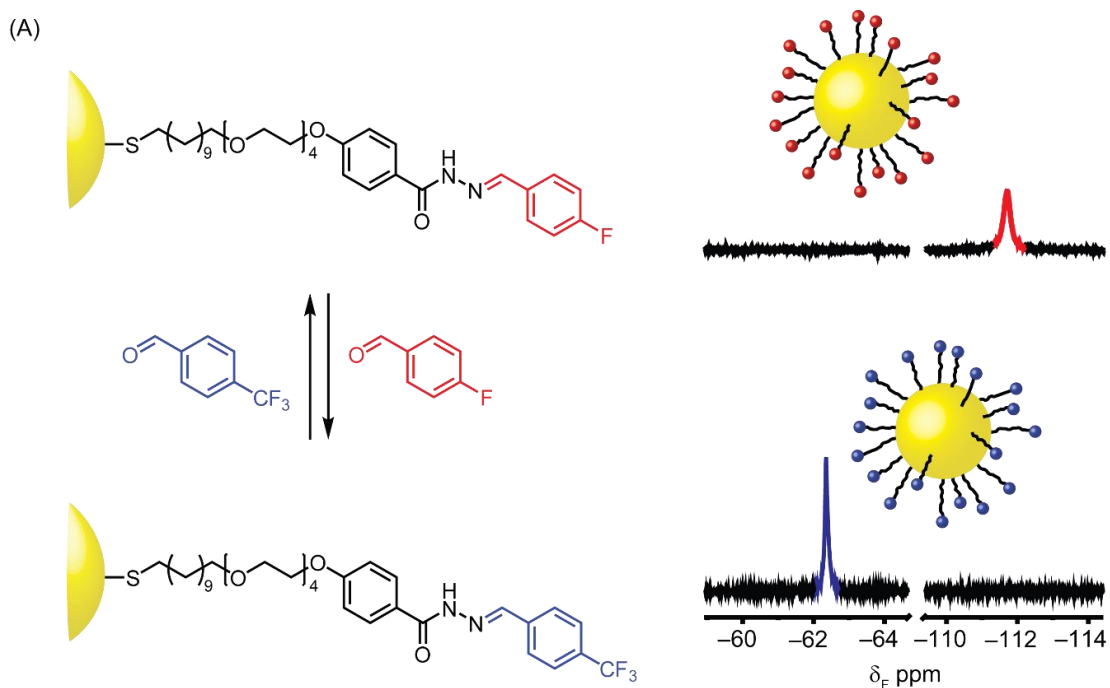


**Figure 1.8** Nanoparticle-bound dynamic covalent hydrazone exchange.<sup>81</sup> (A) Direct, observation of the dynamic covalent exchange between two fluorinated hydrazones by  $^{19}\text{F}$  NMR spectroscopy (DMF- $d_7$ , 475.5 MHz, 295 K). (B) Fully reversible dynamic covalent modification of a nanoparticle solubility by hydrazone exchange. Solvents: **A** = hexane, **B** = chloroform, **C** = tetrahydrofuran, **D** = methanol, **E** = *N,N*-dimethylformamide, **F** = water.

## 1.8 Outlook and aims

Tremendous advances in the control of nanoparticle synthesis over the past two decades have generated much excitement as a result of the often unique properties observed on the nanoscale. These properties are inherently dependent on nanoparticle material, shape and size. However, challenges remain in the size-controlled synthesis of functionalised nanoparticles. Although virtually all conceivable nanoparticle applications require excellent control over how nanoparticles are assembled and linked to other components, the synthetic chemistry techniques required to control nanoparticle functionalisation and assembly are still underdeveloped, with complex biological or supramolecular systems currently constituting the best approaches. There remains an unmet need for simple and generalisable strategies for molecular-level control over nanoparticle functionalisation and assembly.

The development of a toolkit of nanoparticle building blocks which may be assembled in a predictable and controlled way, governed by simple and easily optimised abiotic molecular systems is highly desirable. A full understanding of the molecular implications of transferring well-established chemistry to a nanoparticle-bound monolayer will be crucial for the rational design of nanoparticle assembly. The aim of this thesis is to demonstrate that relatively simple molecular systems present a viable, and ultimately more flexible, alternative to the existing methods of directing precise and predictable control of nanoparticle building blocks. However, in order to achieve this, significant challenges must be addressed at all stages, including nanoparticle synthesis, purification and *in-situ* structural characterisation of nanoparticle-bound molecules.

The synthesis of functionalised nanoparticles will be investigated with a view to developing general strategies for the synthesis of a wide range of nanoparticle

building blocks, with narrow size distributions and well-defined control over nanoparticle size.

Dynamic covalent-chemistry offers an attractive means of combining the reversibility and stimuli-responsiveness of thermodynamically-controlled noncovalent approaches to nanoparticle assembly with the kinetic stability and structural diversity of covalent chemistry. To this end, dynamic covalent boronic ester formation on boronic acid-coated nanoparticles and molecular-level investigation by NMR spectroscopy to provide direct evidence of the details of the dynamic covalent exchange process will be discussed.

The ultimate goal of this thesis is to apply boronic ester formation to the reversible covalent assembly of nanoparticles. Molecular-level understanding will help provide a link between the phenomenological behaviour of dynamic covalently assembled nanoparticles and the structural details, with the ultimate view to producing a generalisable strategy for the controlled and predictable dynamic covalent assembly of nanoparticle building blocks.

# Chapter 2: Synthesis and characterisation of functionalised gold nanoparticles

This chapter reports the synthesis of gold nanoparticles functionalised with a monolayer of organic ligands. A one-phase synthesis is explored for the synthesis of a range of functionalised nanoparticles, and shown to be suitable for synthesising nanoparticles bearing a range of functionalities and displaying a range of solvent compatibilities, from a polar organic solvents to water. The size distributions obtained for all functionalised ligands remain below 15%.

Size control for the synthesis of a range of functionalised nanoparticles is demonstrated through controlling the rate of addition of the reducing agent. Slow addition of the reductant over two hours results in the formation of nanoparticles larger than identically functionalised nanoparticles synthesised under the same conditions but with instant reductant addition. Using this slow addition method, nanoparticle size could be varied for all functionalised nanoparticles tested, with increases in nanoparticle size of around 2 nm for two cases, and over 7 nm for alkyl-tetra(ethyleneglycol)-coated nanoparticles.

Molecular level characterisation of boronic acid-coated nanoparticles revealed degradation of the ligand during the synthesis, resulting in nanoparticles functionalised in a mixed mono-layer of the desired boronic acid ligand and an unknown species. The unknown ligand was identified as the corresponding phenol, which was formed by a peroxide-induced oxidation of the boronic acid during the nanoparticle synthesis. This oxidation reaction could be suppressed by the addition of an anti-oxidant scavenger to the synthesis. The ligand composition of boronic acid-coated nanoparticles was investigated and the concentration of boronic acids was accurately determined.

## 2.1 Introduction

While developing the synthetic chemistry for linking nanoparticles to other components is crucial for establishing a sophisticated and precise molecular control over nanomaterials, synthetic techniques for producing functionalised nanoparticle building blocks themselves remain underdeveloped. Nanoparticle synthesis is key to all subsequent development of functionality. As with traditional complex molecular systems which exhibit self-assembly, nanoscale systems must be carefully designed and synthesised, bearing the correct functionality to achieve the desired control. Nanoparticles bearing chemically useful ligands must first be produced, before chemical control of a nanosystem can be established. Unlike molecular systems, there are two further complications which must be considered when designing and synthesising nanomaterials; firstly, the size of the particle must be considered, and secondly, the size distribution of functional nanoparticles. The size (and shape) of nanoparticles is crucial for determining nanomaterial properties. Therefore, a fully flexible synthetic nanochemistry requires independent control over nanoparticle material, size, shape and surface-bound functionality.

The larger the particle, the greater the surface area (scaling as a square of the particle radius) and therefore the more ligands per particle. This has significant implications for multivalent interactions between particles. Increasing the particle size also leads to a decrease in the curvature of the nanoparticle surface, or, as particles are not truly spheres, leads to a decrease in the ratio of edges and vertices to faces for ligand binding<sup>178</sup> (**Figure 2.1**). This change in ligand environment may in turn affect the reactivity of surface-bound molecules.

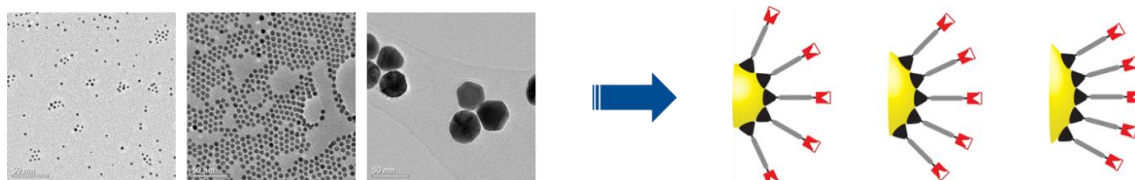


**Figure 2.1** Schematic representation of the effect of changing nanoparticle diameter on the ligand packing as a result of the decreased curvature of the nanoparticle surface as the radius increases.

Nanoparticle size dispersity is a phenomenon which may be likened to polydispersity of polymer chain lengths. The inherent size distribution of any real nanoparticle sample means that all assertions about particle behaviour in fact correspond to a statistical measure of a range of particles. For the majority of applications, and of importance to developing an accurate understanding of molecular interactions with nanoscale systems, as narrow a size distribution as possible is desirable. A high size dispersity can lead to outlying particles dominating the observed behaviour of the population.

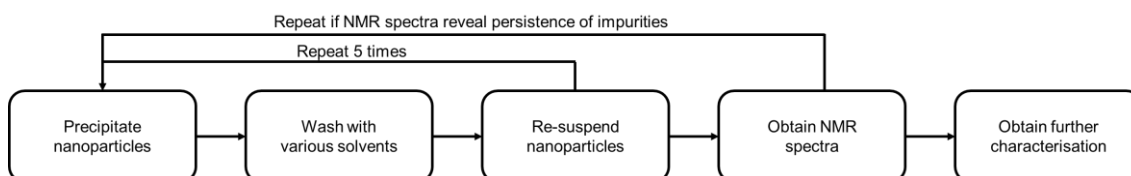
The importance of particle size and size distribution is highlighted by the vast array of literature concerning nanoparticle synthesis (**Chapter 1.3**), with demand for size-controlled syntheses with an ever-narrower size distribution fuelling research in the area. As nanoparticles (particularly gold nanoparticles, discussed in the remainder of the chapter) are presented with ever more industrial applications, a further important consideration is the operational complexity of nanoparticle synthesis methods, with operationally complex and time-consuming syntheses, unsurprisingly, less desirable. Furthermore, in general, syntheses are reported for a specific ligand, and while the nanoparticle size may often be tuned for that ligand, general synthetic approaches to the synthesis of nanoparticles across a wide size range (with control over size) and with different ligand types have not yet been developed<sup>56</sup> (**Chapter 1.3.3**).

Although dispersities of around 10% are now commonplace for nanoparticle syntheses,<sup>18,26,43,55,57</sup> such synthetic techniques relate almost exclusively to nanoparticles functionalised only with simple, alkanethiol ligands. Indeed, even such simple changes as varying alkyl chain length may result in unpredictable effects on both nanoparticle size and dispersity (**Chapter 1.3.3**).<sup>19</sup> More complex variation of ligand functionality often results in markedly different results,<sup>56</sup> with unpredictable sizes and generally a loss of control over sample size dispersity.<sup>55</sup> Functionalisation of nanoparticles may be achieved by ligand exchange (**Chapter 1.5**), first synthesising a simple, alkanethiol nanoparticle and then exchanging this alkanethiol for the desired functional ligand.<sup>64–66,179</sup> However, such procedures are time-consuming, require multiple operational steps, and do not guarantee complete surface coverage with the new ligand.<sup>179</sup>

Furthermore, ligand exchange has been shown to result in not only transfer of ligands, but also movement of metal atoms,<sup>67</sup> often resulting in ripening processes<sup>68</sup> that can lead to changes in both the size and the dispersity of nanoparticles. Therefore, direct synthetic routes to functionalised nanoparticles, with a high degree of size control, are highly desirable.

The one-step single-phase method developed by Stucky and co-workers<sup>18</sup> (see **Chapter 1.3.3**) presents an attractive starting point for expanding the scope of gold nanoparticles syntheses. The reported dispersities are generally low, and a variety of solvents have been shown to be compatible with synthesis of dodecanethiol-coated nanoparticles.<sup>18,19</sup> A wide range of solvent compatibilities for nanoparticle synthesis is of great importance when considering diversifying the synthesis for a wide variety of ligands and functionalities, as the nanoparticle solvent compatibility will change, and nanoparticles must be kept in colloidal suspension in order to achieve a narrow size distribution during their synthesis.

Following nanoparticle synthesis, the nanoparticles must be purified to remove excess unbound-ligand and other impurities, and the purity must be assessed. Nanoparticles are generally purified by a precipitation-washing procedure (**Scheme 2.1**). Nanoparticles are suspended in a suitable solvent and precipitated with a non-solvent. The precipitate is washed and the process is repeated. Nanoparticle purity is evaluated in the first instance by NMR spectroscopy. Once the nanoparticles are clean by NMR spectroscopy, further characterisation such as TEM, UV and ICP-OES is obtained.



**Scheme 2.1** Scheme representing the process of nanoparticle purification.

## 2.2 Investigating the ligand scope of nanoparticle synthesis

The Stucky synthesis involves mixing a gold(I) salt (triphenylphosphine gold chloride **E1**) with a borane reducing agent (*tert*-butylamine borane complex (TBAB)) in the presence of either a thiol or disulfide ligand. In general, the synthesis is carried out at an elevated temperature for an hour, followed by stirring at room temperature. Nanoparticles are subsequently purified by precipitation and washing with appropriate solvents. This procedure is employed throughout all functionalised nanoparticle syntheses presented in this theses. All sizes reported are after purification. The synthetic details are outlined in **Chapter 7.3.1**.

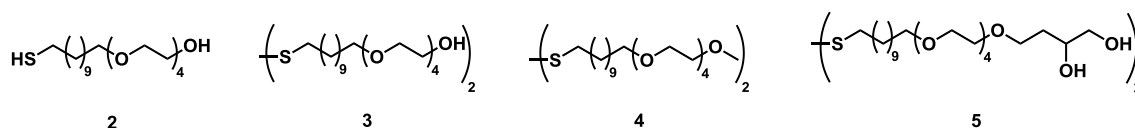


**Figure 2.2** Structure of a range of alkyl-tetra(ethyleneglycol) derived ligands employed for the synthesis of water-soluble nanoparticles.

Initially, water-soluble nanoparticles were selected as a synthetic target, due to their biological significance and due to the significant structural difference between the required ligands and traditional alkanethiol ligands. A range of alkyl-tetra(ethyleneglycol) derived ligands were synthesised (**Figure 2.2**). Employing identical conditions ( $[Au] = 10 \text{ mM}$ ,  $[thiol] = 12 \text{ mM}$ ,  $[TBAB] = 100 \text{ mM}$ ,  $\text{CHCl}_3$ ,  $55 \text{ }^\circ\text{C}$ ) to those reported by Stucky,<sup>18</sup> a nanoparticle synthesis was attempted substituting dodecanethiol (as reported by Stucky) for alkyl-PEG thiol **2**. Although initially all components were fully dissolved, as the synthesis proceeded, a black precipitate was observed. This suggests that as the nanoparticles grew, the alkyl portion of the ligand became inaccessible to solvent, meaning that only the hydrophilic PEG portion was oriented towards the bulk solvent, resulting in a loss of colloidal stability. A variety of solvent systems were investigated, and a 1:1 v/v mixture of THF and acetonitrile was found to be optimal, being sufficiently non-polar to dissolve the reagents, in particular the highly non-polar triphenylphosphine gold chloride, while

sufficiently polar to maintain colloidal stability of the nanoparticles, even at the relatively high concentrations ( $[Au] = 10 \text{ mM}$ ) employed.

The nanoparticles obtained were found to have a diameter of  $4.38 \pm 0.60 \text{ nm}$ , maintaining an acceptably narrow size distribution of 14% (**Figure 2.3**). Starting from disulfide **3** rather than thiol **2**, maintaining the same molar ratio in terms of sulfur atoms, resulted in no significant change in either nanoparticle size or distribution (**Chapter 7.3.1**).

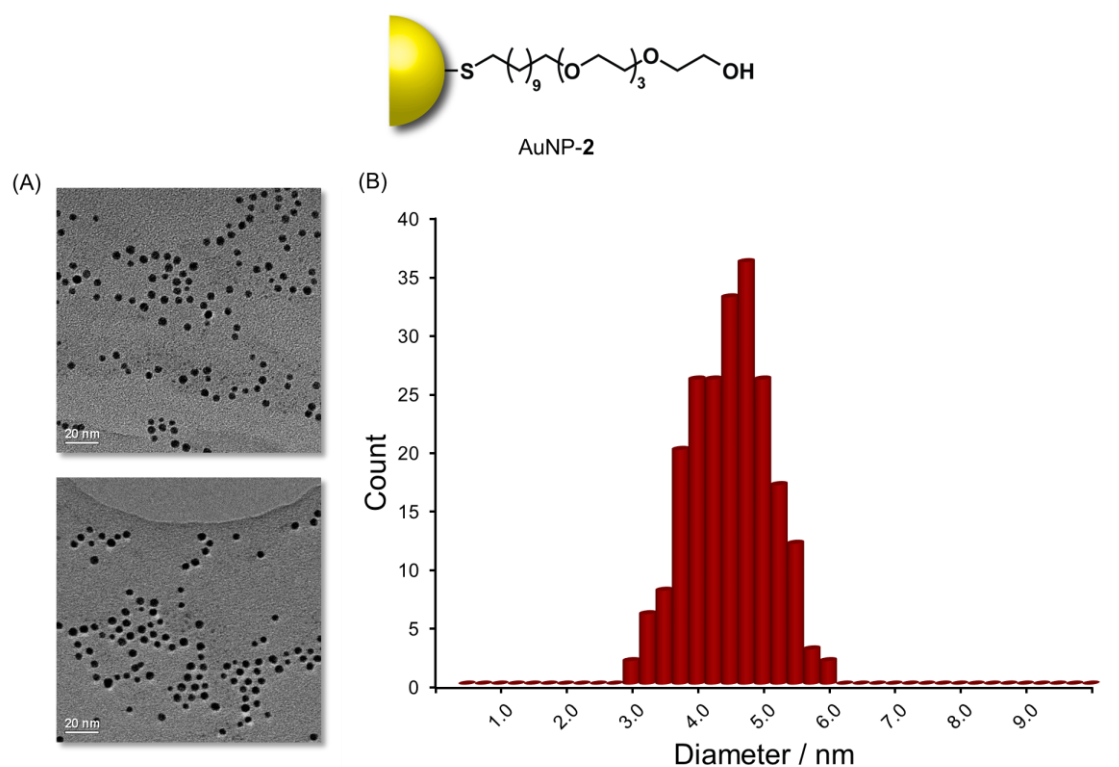


**Figure 2.3** (A) TEM images of AuNP-2 and (B) histogram of size distribution of nanoparticles as found through analysis of TEM images. AuNP-2 were found to have a size of  $4.38 \pm 0.60 \text{ nm}$ , constituting a dispersity of 14%.

Other ligands containing the alkyl-tetra(ethyleneglycol) motif, **4** and **5**, were prepared, with a view to diversifying the range of examples of water soluble nanoparticles that could be synthesised. The synthesis was carried out in 1:1 v/v mixture of THF and acetonitrile. Nanoparticles with a narrow size distribution were obtained in both cases, with a size of  $4.23 \pm 0.65 \text{ nm}$  for AuNP-4 (**Figure 2.4**) and  $5.73 \pm 0.85 \text{ nm}$  for AuNP-5 (**Figure 2.5**).

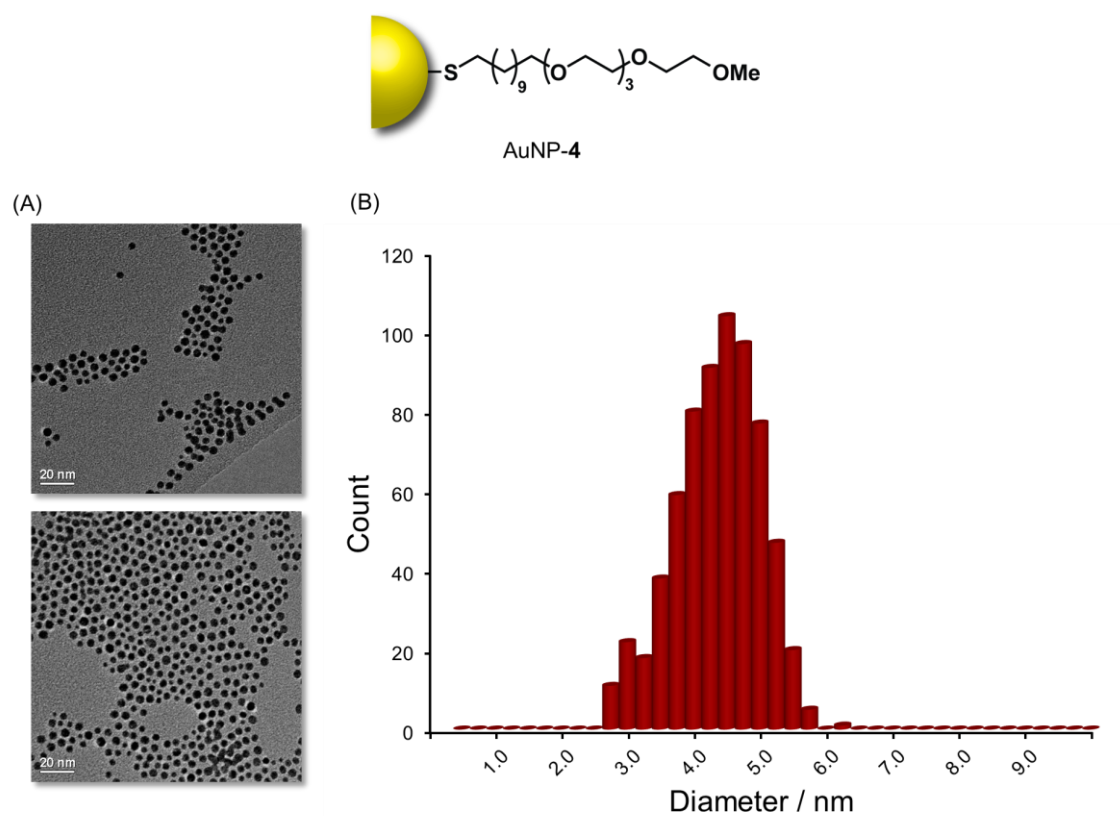


**Figure 2.4** (A) TEM images of AuNP-4 and (B) histogram of size distribution of nanoparticles as found through analysis of TEM images. AuNP-4 were found to have a size of  $4.23 \pm 0.65$  nm, constituting a dispersity of 15%.

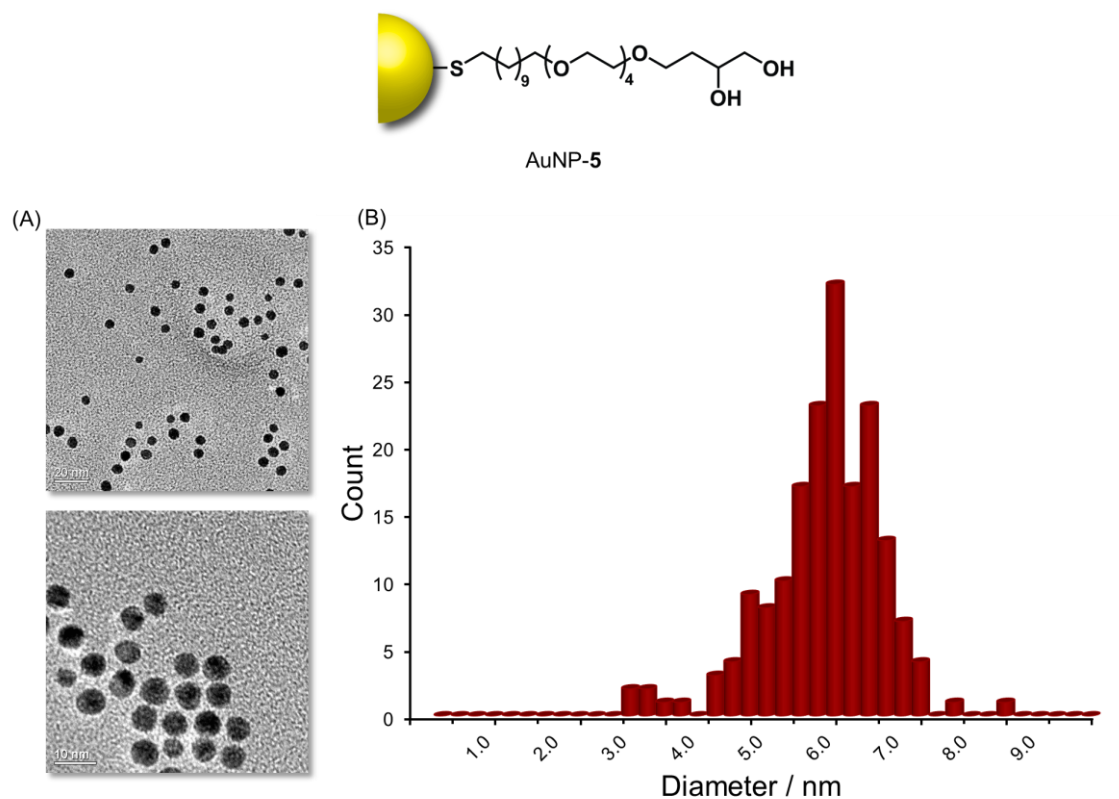


**Figure 2.5** (A) TEM images of AuNP-5 and (B) histogram of size distribution of nanoparticles as found through analysis of TEM images. AuNP-5 were found to have a size of  $5.73 \pm 0.85$  nm, constituting a dispersity of 15%.

Further exploration of the ligand scope for the synthesis aimed to introduce other complex functional groups. Amides were identified as a synthetically relevant target due to the commercial availability of 11-mercaptoundecanoic acid, which can be easily coupled to an amine to introduce a wide diversity of functionality (**Figure 2.6**). Fluorine-labelled benzamide **6** was synthesised as a model compound for exploring the compatibility of the amide functionality with the synthetic procedure. The fluorine tag was introduced to allow product analysis by  $^{19}\text{F}$  NMR spectroscopy.  $^{19}\text{F}$  NMR spectroscopy, with its high sensitivity and large chemical shift scale serves as a good diagnostic tool for confirming ligand structural integrity in the nanoparticle products (**Chapter 1.4.1**). By trying a range of solvents for the synthesis, a suitable solvent mixture (THF/MeOH, 10:1 v/v) was determined for the synthesis of nanoparticles functionalised with **6**. The nanoparticles obtained with fluorinated ligand **6** had a narrow size dispersity ( $3.86 \pm 0.39$  nm) (**Figure 2.7**) but could not be fully purified by simple washing processes, due to the similarity in solubility of the

nanoparticles and the disulfide. However, the nanoparticles could be purified by gel-permeation chromatography.

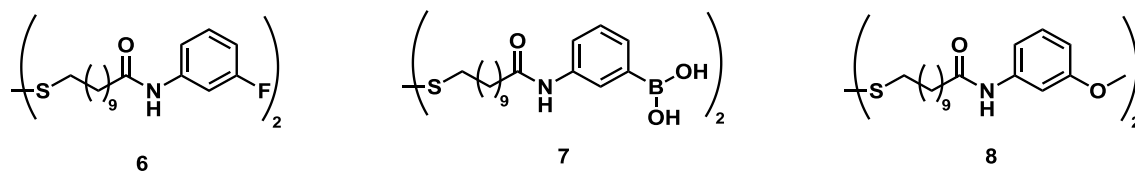


**Figure 2.6** Structure of a range of benzamide ligands employed for the synthesis of nanoparticles.

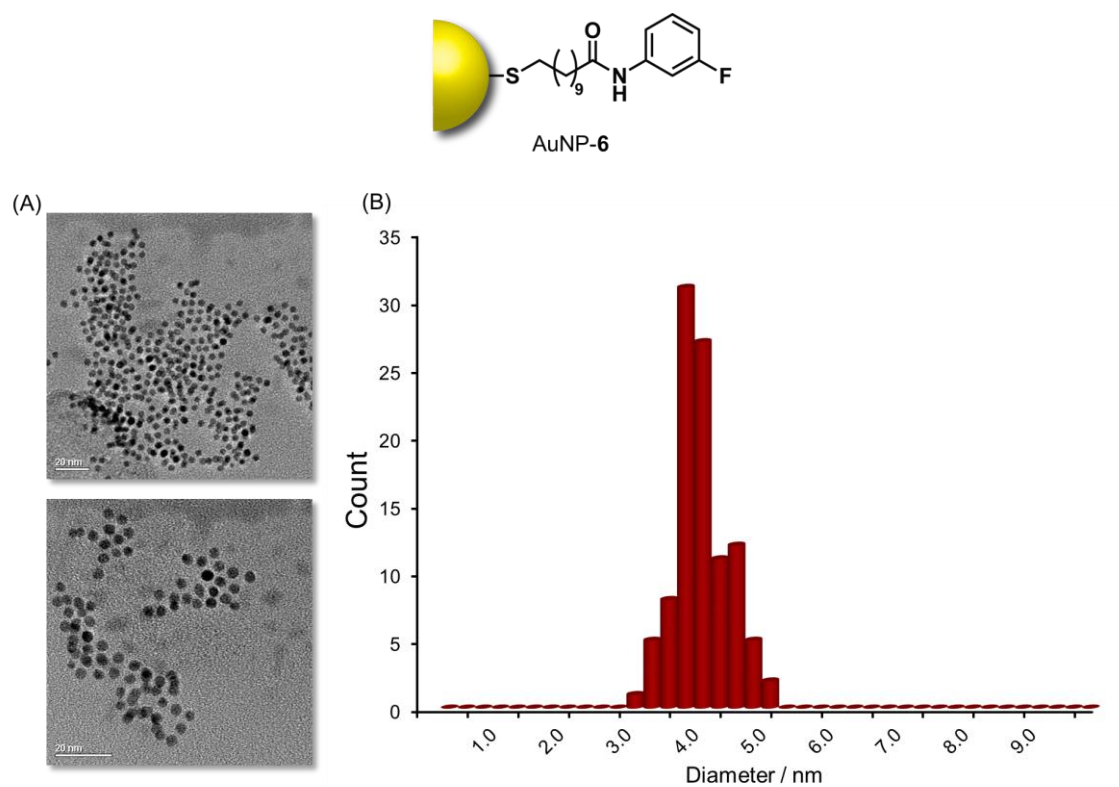


**Figure 2.7** (A) TEM images of AuNP-6 and (B) histogram of size distribution of nanoparticles as found through analysis of TEM images. AuNP-6 were found to have a size of  $3.86 \pm 0.39$  nm, constituting a dispersity of 10%.

A <sup>19</sup>F NMR spectrum of AuNP-6 (Figure 2.8) showed only a single, broad peak, indicating the presence of only one fluorinated species bound to the nanoparticle. Indeed, upon treatment of the nanoparticle sample with iodine, to strip the ligand off the nanoparticle, the subsequent spectra were identical to

the spectra of the disulfide, indicating that the nanoparticle synthesis was compatible with the presence of amide functionality (**Figure 8**).

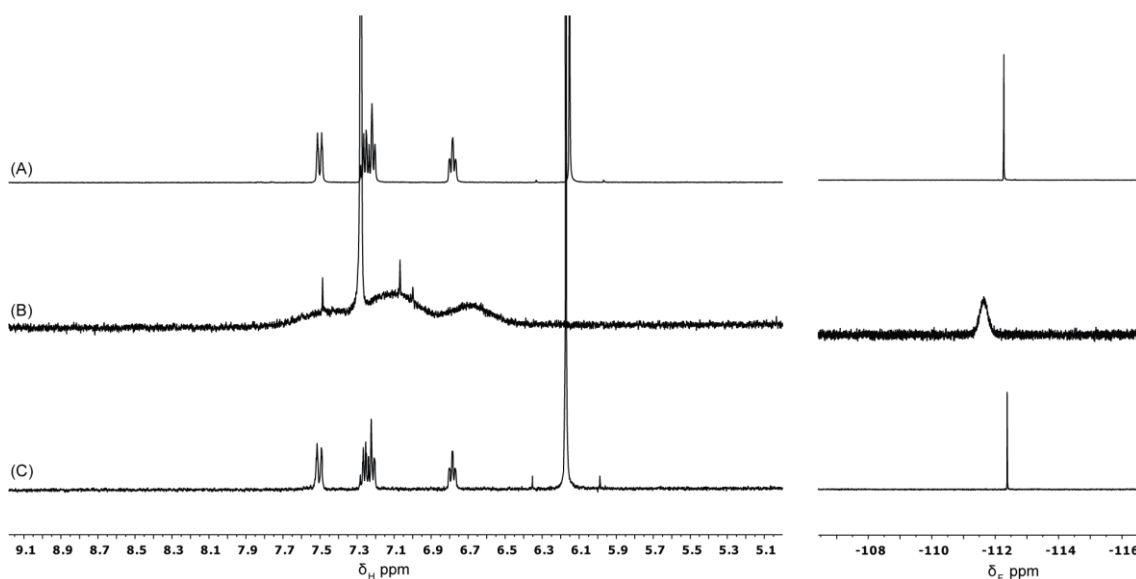


**Figure 2.8** Partial  $^1\text{H}$  (500.1 MHz, 295 K) and  $^{19}\text{F}$  NMR spectra (470.5 MHz, 295 K) of (A) fluorine-tagged disulfide **6** ( $\text{CDCl}_3$ ), (B) AuNP-6 ( $\text{CD}_3\text{OD}$ ) and (C) AuNP-6 after treatment with iodine ( $\text{CDCl}_3$ ).

Two further ligands bearing amide functionality were synthesised. Boronic acid ligand **7** was designed to allow dynamic covalent boronic ester formation on nanoparticles coated with this ligand to be investigated (**Chapters 3** and **4**). Methyl ether ligand **8** was designed as a structurally similar ligand to **7**. For nanoparticle synthesis with both **7** and **8**, THF/MeOH, 10:1 v/v was found to be an appropriate solvent mixture. Boronic acid-coated AuNP-**7** and methyl ether-coated AuNP-**7** were obtained with similar sizes:  $3.10 \pm 0.42$  nm for boronic acid-coated AuNP-**7** (**Figure 2.9**) and  $3.48 \pm 0.49$  nm for methyl ether-coated AuNP-**8** (**Figure 2.10**).

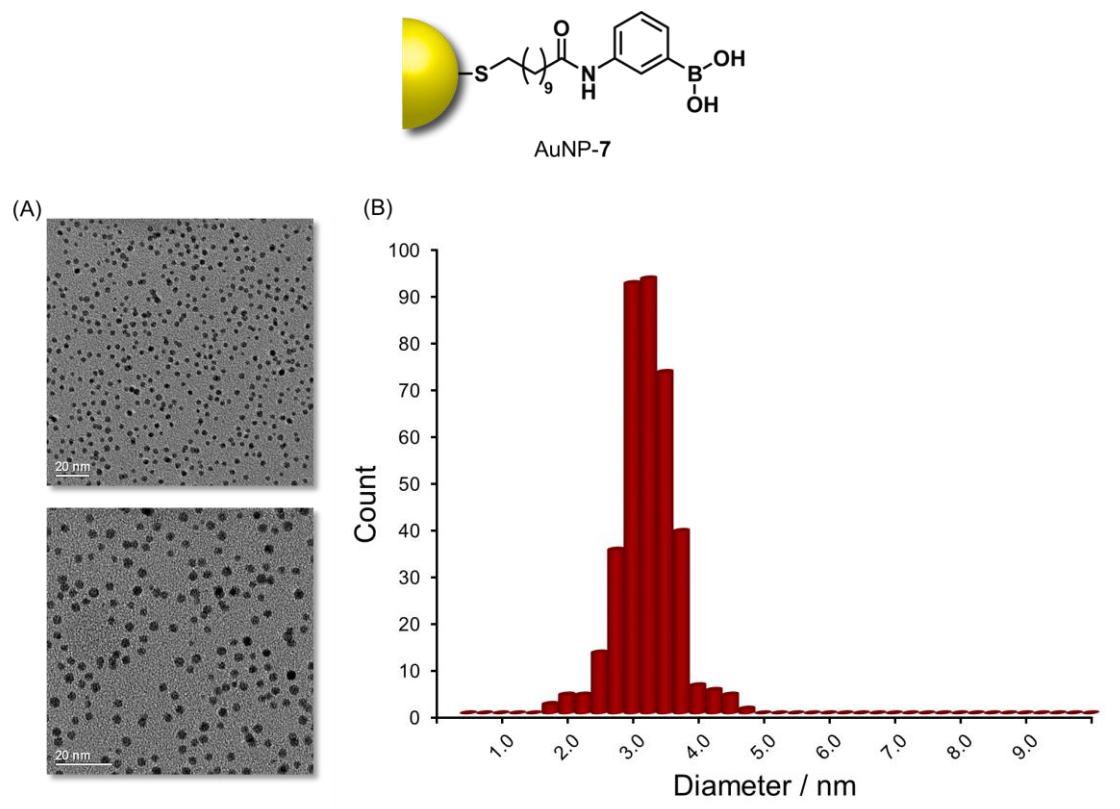


**Figure 2.9** (A) TEM images of AuNP-7 and (B) histogram of nanoparticle size distribution as found through analysis of several images. AuNP-7 were found to have a size of  $3.10 \pm 0.42$  nm, constituting a dispersity of 13%.

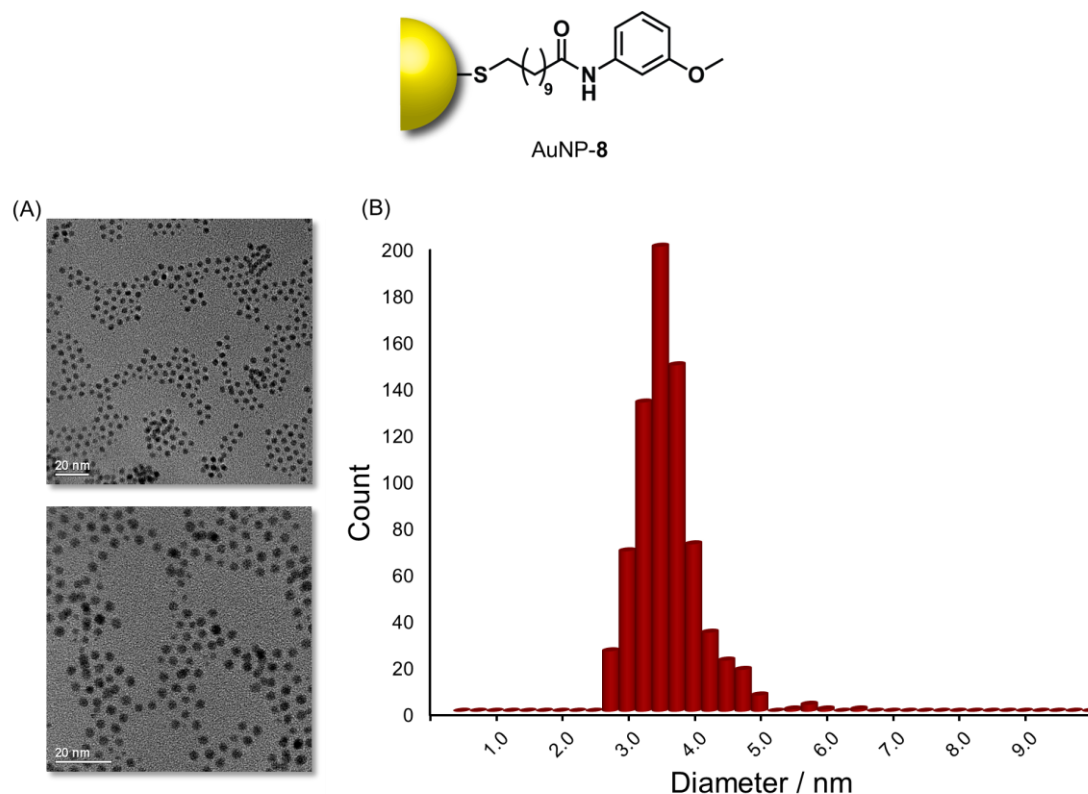


**Figure 2.10** (A) TEM images of AuNP-8 and (B) histogram of nanoparticle size distribution as found through analysis of several images. AuNP-8 were found to have a size of  $3.48 \pm 0.49$  nm, constituting a dispersity of 14%.

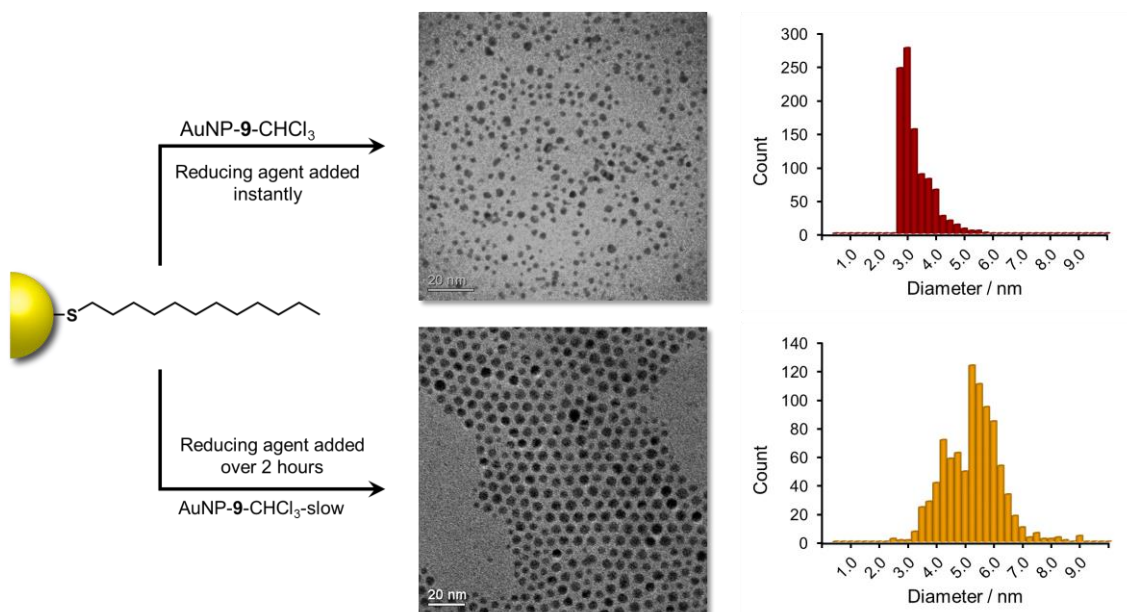
### 2.3 Size control of nanoparticles by varying the rate of reductant addition

The wide range of ligands and functionalities employed here illustrates the versatility of this synthetic approach. Impressively low dispersities ( $< 15\%$ ) were maintained for all nanoparticles prepared. However, there is currently no way of predicting the particle size. With the tetra(ethyleneglycol) ligands generally producing larger nanoparticles ( $\approx 5$  nm) than the benzamide-functionalised nanoparticles ( $\approx 3.5$  nm). This size distinction may be due to the different solvent mixtures employed. The influence of solvent on nanoparticle size is well illustrated by Stucky's results,<sup>18</sup> where dodecanethiol-coated nanoparticles are synthesised in chloroform and benzene, giving sizes of  $3.5 \pm 0.3$  nm and  $6.2 \pm 0.3$  nm, respectively. Although there is a clear effect on nanoparticle size in relation to solvent, the influence of solvent choice on nanoparticle size is poorly understood, and employing solvent choice as a predictable control of

nanoparticle size is not possible when moving beyond well-documented dodecanethiol-coated nanoparticles.

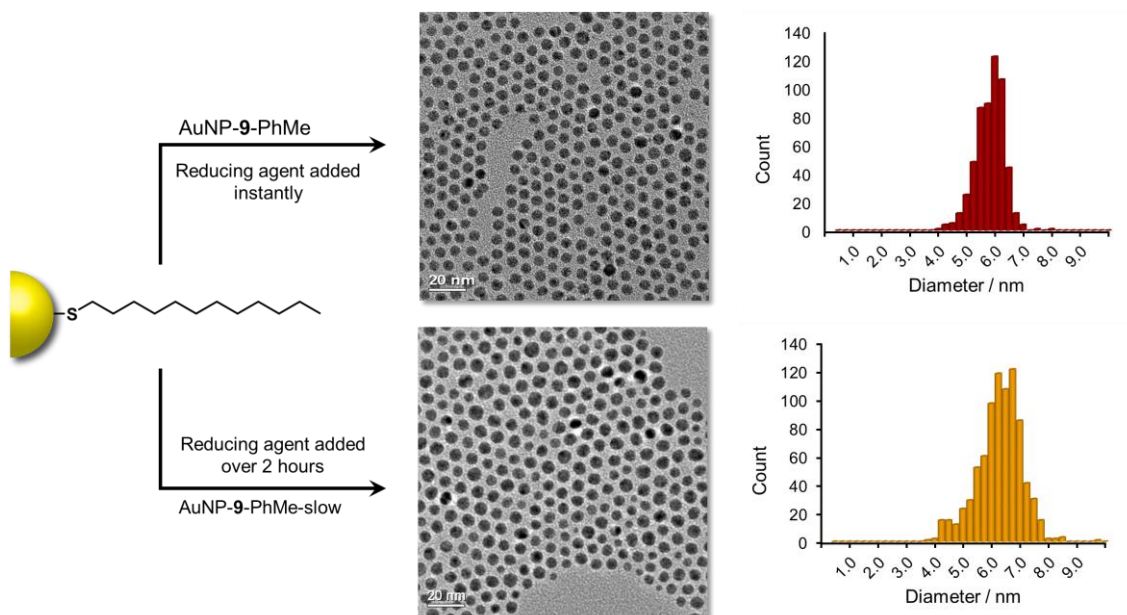
Nanoparticle sizes were determined by TEM microscopy. Nanoparticle sizes were measured automatically using the ImageJ software (see experimental **Chapter 7.1** for details). There are a number of sources of error in such measurements. The image must be properly focused to allow precise nanoparticle sizing. The image must be thresholded before particles can be measured, so the image must be of a suitable contrast to allow this. A minimum of five images, containing several hundred nanoparticles are used to improve the statistical representation of the sample. While parameters for minimum particle size and circularity may be adjusted in order to prevent mistaken identification and measurement of single nanoparticles (e.g noise from the grid or overlapping nanoparticles), manually selecting each nanoparticle to be measured may be more accurate. Because of the inherent polydisperse nature of nanoparticle samples and the potential errors from the images, it can be difficult to compare nanoparticle size distributions and verify the differences between them. Repeated measurements of nanoparticle sizes could allow for the application of t-tests in order to statistically estimate the differences between size distributions.

It was found that controlling the rate of addition of the reducing agent, TBAB, influenced the size of the particles. As demonstrated by Stucky, synthesis of dodecanethiol (**9**)-coated nanoparticles in chloroform gives rise to small nanoparticles ( $3.5 \pm 0.3$  nm). Replicating this synthesis, originally reported by Stucky, gave nanoparticles of  $3.14 \pm 0.55$  nm (18%) (AuNP-**9**-CHCl<sub>3</sub>), in good agreement with the reported size. In the original conditions, the reducing agent is added as a solid powder. Maintaining the same conditions otherwise, but adding the TBAB as a solution over a period of two hours, gave rise to a significant increase in the particle size to  $5.14 \pm 0.95$  nm (18%) (AuNP-**9**-CHCl<sub>3</sub>-slow) (**Figure 2.11**).



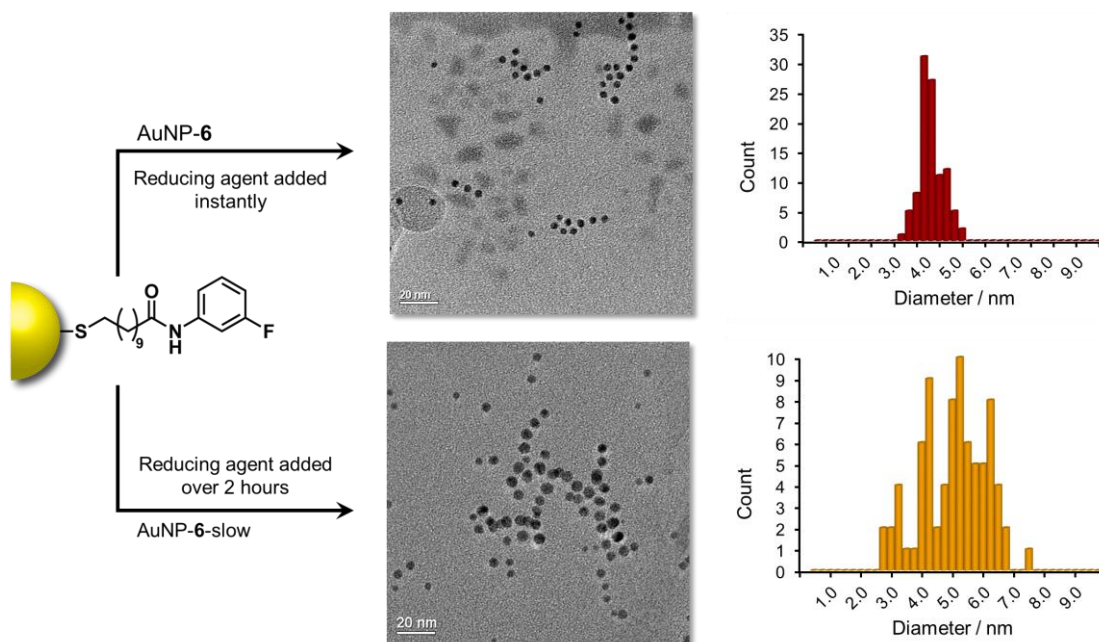
**Figure 2.11** TEM images of AuNP-9-CHCl<sub>3</sub> and AuNP-9-CHCl<sub>3</sub>-slow and histograms of nanoparticle size distribution. AuNP-9-CHCl<sub>3</sub> were found to have a size of  $3.14 \pm 0.55$  nm, constituting a dispersity of 18%. AuNP-9-CHCl<sub>3</sub>-slow were found to have a size of  $5.14 \pm 0.95$  nm, constituting a dispersity of 18%.

Slow reducing agent addition was also investigated for the preparation of dodecanethiol-coated nanoparticles in toluene. Instant addition of the reducing agent gave nanoparticles (AuNP-9-PhMe) of  $5.70 \pm 0.51$  nm (9%), with a slight increase to  $6.17 \pm 0.77$  nm (12%) (AuNP-9-PhMe-slow) (**Figure 2.12**) upon slow addition of the reducing agent. The increase here is much less appreciable, and it may be that the initial large size of the nanoparticles in toluene limits the amount that the particle size may be increased through the slow addition of the reducing agent, as dodecanthiol may not be a long enough ligand to provide colloidal stability for larger nanoparticles.



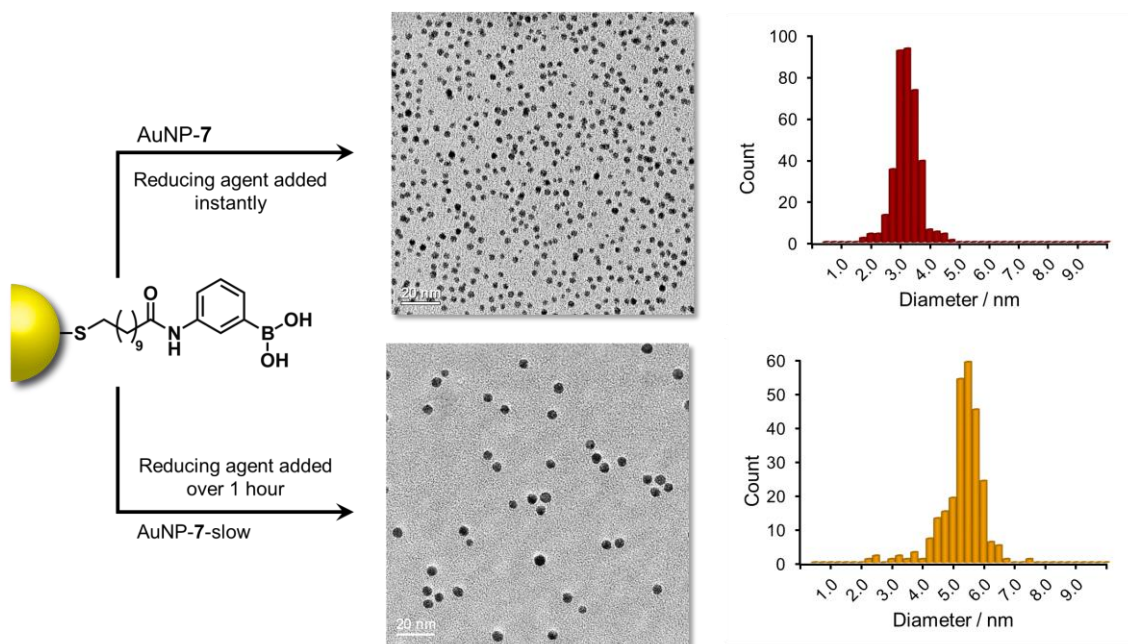
**Figure 2.12** TEM images of toluene syntheses of AuNP-9-PhMe and AuNP-9-PhMe-slow and histograms of nanoparticle size distribution. AuNP-9-PhMe were found to have a size of  $5.70 \pm 0.51$  nm, constituting a dispersity of 9%. AuNP-9-PhMe-slow were found to have a size of  $6.17 \pm 0.77$  nm, constituting a dispersity of 12%.

Although in the case of dodecanethiol-coated nanoparticles the larger sizes seen from the slow addition of the reducing agent in chloroform may be achieved simply by changing the solvent to toluene, this is only possible as the nanoparticles are not limited in solubility to a narrow range of solvents. Other, more complex ligands, such as fluorinated ligand **6** or boronic acid ligand **7** have much more limited solubility, both for the ligand and for the resulting nanoparticles. In such cases, it may not be possible to change the solvent in order to change the nanoparticle size. It is therefore desirable to have a predictable, generally applicable way of varying the nanoparticle size.



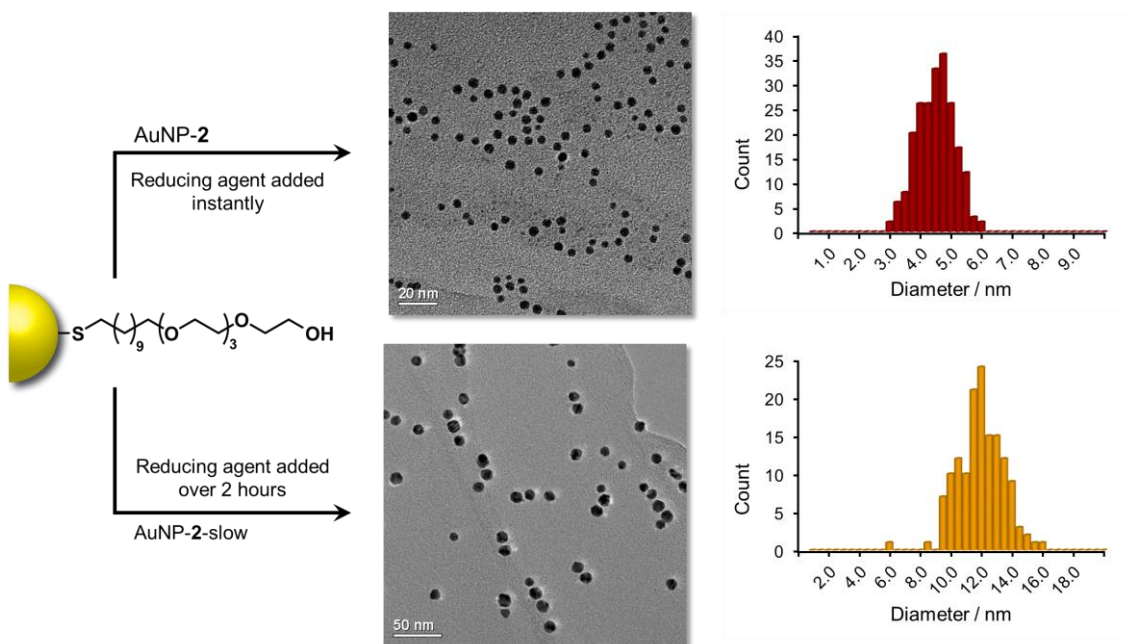
**Figure 2.13** TEM images of syntheses of fluorinated AuNP-6 and AuNP-6-slow and histograms of nanoparticle size distribution. AuNP-6 were found to have a size of  $3.86 \pm 0.39$  nm, constituting a dispersity of 10%. AuNP-6-slow were found to have a size of  $4.64 \pm 1.05$  nm, constituting a dispersity of 21%.

Slow addition of reducing agent during the preparation of both benzamide AuNP-6 and AuNP-7 was also attempted. Slow addition of the reducing agent for synthesis of nanoparticles coated with fluorine-tagged ligand **6** gave AuNP-6-slow as  $4.64 \pm 1.05$  nm (21%), a slight increase over the AuNP-6 ( $3.86 \pm 0.39$  nm) (**Figure 2.13**). Although the size does increase upon slow reductant addition, in this case a significant increase in the nanoparticle dispersity is observed, with the size distribution looking broad, and potentially bimodal, with maxima around both 4 nm and 5 nm. As previously discussed (**Chapter 1.3**), bimodal particle distributions are often associated with the early stages of the aggregative growth phase of a nanoparticle synthesis, indicating that optimisation of the conditions, in particular a longer synthesis period, may improve this dispersity.



**Figure 2.14** TEM images of syntheses of boronic acid-coated AuNP-7 and AuNP-7-slow and histograms of nanoparticle size distribution. AuNP-7 were found to have a size of  $3.10 \pm 0.42$  nm, constituting a dispersity of 13%. AuNP-7-slow were found to have a size of  $4.95 \pm 0.66$  nm, constituting a dispersity of 13%.

Slow addition of the reducing agent for synthesis of nanoparticles coated with boronic acid ligand **7** gave AuNP-7-slow as  $4.95 \pm 0.66$  nm (13%), compared to AuNP-7 ( $3.10 \pm 0.42$  nm) (**Figure 2.14**). Here, the slow addition had a large effect on the nanoparticle size, increasing the average size by almost 2 nm, while the size distribution was unaffected. It should be noted that for boronic acid-coated AuNP-7-slow, the reducing agent was added over only one hour, while in the other slow addition experiments described so far, the addition was performed over two hours. This is because in a two-hour addition experiment, with ligand **7**, the nanoparticles became colloidally unstable.

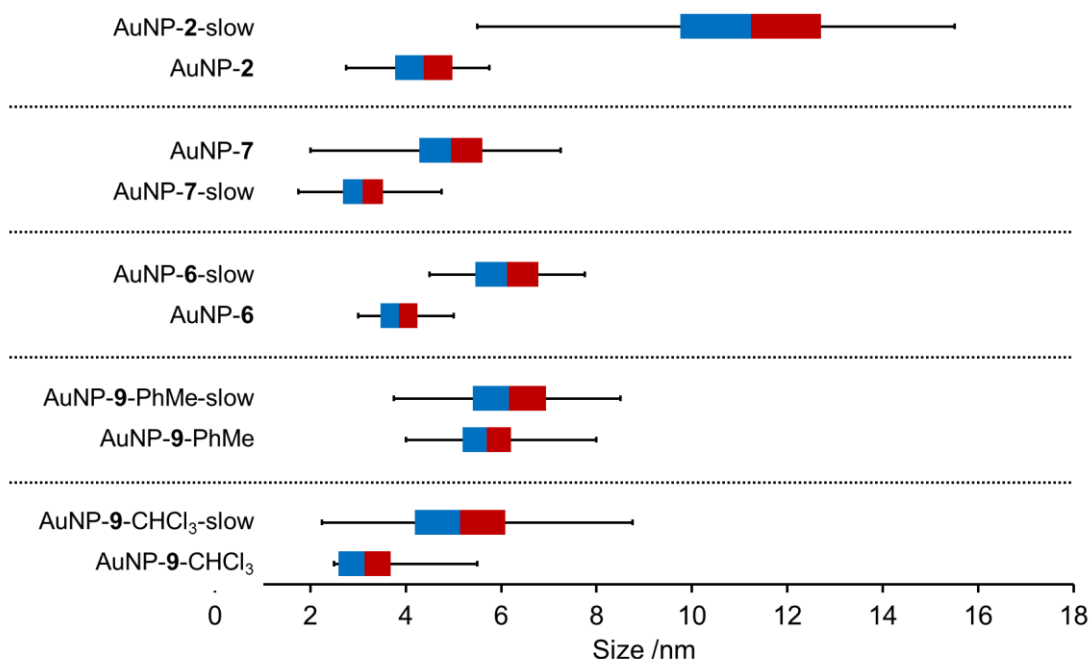


**Figure 2.15** TEM images of syntheses of alkyl-tetra(ethyleneglycol) AuNP-2 and AuNP-2-slow and histograms of nanoparticle size distribution. AuNP-2 were found to have a size of  $4.38 \pm 0.60$  nm, constituting a dispersity of 14%. AuNP-2-slow were found to have a size of  $11.23 \pm 1.48$  nm, constituting a dispersity of 13%.

Finally, slow addition of the reducing agent was carried out for the synthesis of water-soluble nanoparticles, coated with alkanethiol-tetra(ethyleneglycol) **2** to give AuNP-2-slow as  $11.23 \pm 1.48$  nm (13%), compared to AuNP-2 ( $4.38 \pm 0.60$  nm) (**Figure 2.15**). For synthesis with ligand **2**, nanoparticles of more than double the diameter were obtained upon slow addition of the reducing agent. The size distribution was unaffected.

**Table 2.1** Summary of the results of slow addition of the reducing agent with a range of ligands.

Ligand	NP diameter / nm (instant reductant addition)	NP diameter / nm (two-hour reductant addition)
Dodecanethiol <b>9</b> (CHCl <sub>3</sub> )	3.14 ± 0.55 (18%)	5.14 ± 0.95 (18%)
Dodecanethiol <b>9</b> (PhMe)	5.70 ± 0.51 (9%)	6.17 ± 0.77 (12%)
Fluorine labelled amide <b>6</b>	3.86 ± 0.39 (10%)	4.64 ± 1.05 (21%)
Boronic acid <b>7</b>	3.10 ± 0.42 (13%)	4.95 ± 0.66 <sup>a</sup> (13%)
Alkyl-tetra(ethyleneglycol) <b>2</b>	4.38 ± 0.60 (14%)	11.23 ± 1.48 (13%)

<sup>a</sup> Reductant was added over one hour in this case**Figure 2.16** Summary of the results of slow addition of the reducing agent with a range of ligands represented as a box and whisker diagram. The smallest and largest nanoparticles measured are represented by the whiskers and the box represents one standard deviation of the distribution around the mean.

The results of all slow addition experiments are summarised in **Table 2.1** and **Figure 2.16**. An increase in the average nanoparticle size upon slow reductant addition was observed in all cases. With the exception of AuNP-6, nanoparticle dispersity did not increase significantly with slow reductant addition. Although the size of nanoparticles obtained with instant reductant addition cannot be predicted, and the extent of increase in nanoparticle size upon slow reductant addition cannot be predicted, nevertheless, slower reductant addition rates offer a general ligand-non-specific means to control the size of functionalised nanoparticles.

## 2.4 Mechanism of size-controlled nanoparticle synthesis

As discussed in **Chapter 1.3**, the size and size distribution in the Stucky synthesis is likely primarily controlled by aggregative growth,<sup>36</sup> and therefore does not rely on an initial narrow particle distribution during particle nucleation. In this case, therefore, a fast nucleation event is not necessary to maintain a narrow particle size distribution. This explains why, in general, no appreciable increase in the particle size distribution is observed as a result of the slow addition syntheses, where the nucleation occurs over a long period, as with a two-hour addition of 10 equivalents of reducing agent, it is not until after 12 minutes that 1 equivalent of reducing agent has been added. It should be noted that each borane may accept up to three electrons, so while there are 10 equivalents of reducing agent when counting molecules, when considering electrons, there are far more equivalents.

The increased size observed in the slow addition method may also be rationalised by considering the aggregative growth method. Under normal conditions, where the reducing agent is added quickly, the synthesis can mechanistically be distinguished into two different stages: nucleation and growth. Nucleation is generally much faster than growth. Under instant addition of reductant, the nucleation event is fast, and there is very little overlap between

the nucleation and growth phases of the synthesis (**Figure 2.17A**). Under slow addition conditions, the absence of sufficient reducing agent in the early parts of the synthesis (first 10–20 minutes) means that the nucleation event occurs over a much longer time period, more similar to the aggregative growth phase. This leads to significant overlap between the two stages. Initially some nucleation occurs, creating initial clusters that may then grow by an aggregative growth mechanism. However, as these clusters grow, more nucleation occurs, providing more small clusters. Aggregative growth may then proceed further, through monomer attachment and particle coalescence,<sup>49</sup> further growing the larger particles at the expense of smaller clusters (**Figure 2.17B**). This can be viewed as an *in situ* seeded growth process.

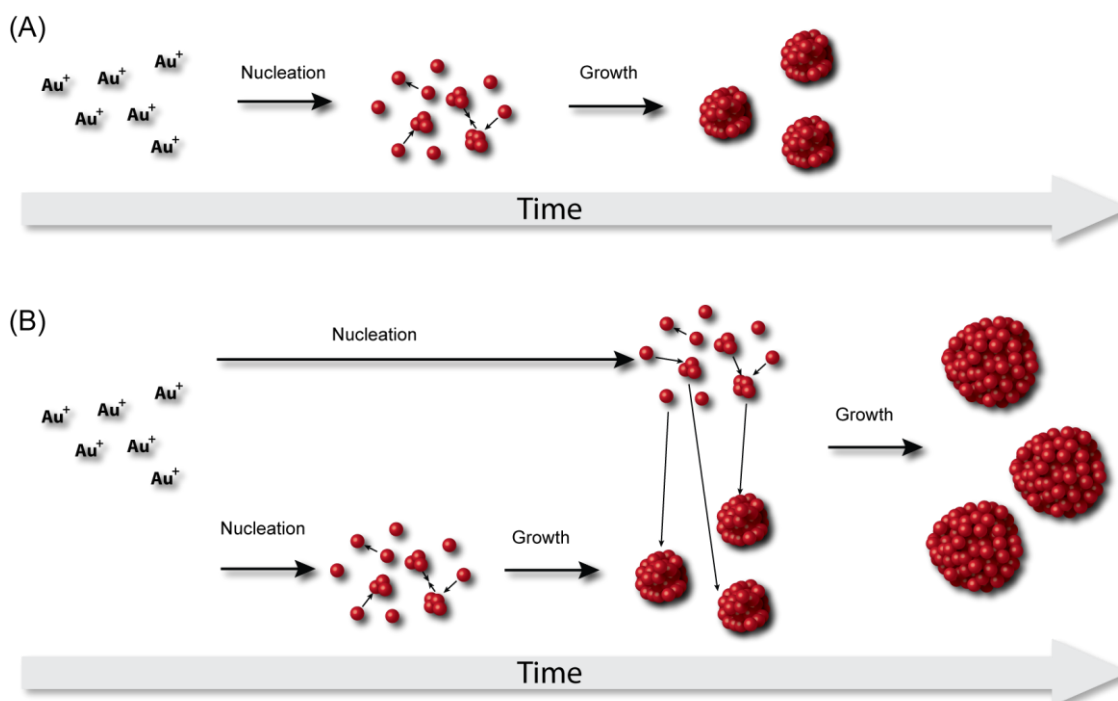


**Figure 2.17** Schematic representation of the mechanism of the Stucky nanoparticle synthesis under conditions of instant addition of the reducing agent (**A**) and slow addition of the reducing agent (**B**). Under instant addition conditions (**A**), the nucleation phase is much faster than the growth phase, and there is very little overlap between the two phases. Under slow addition conditions (**B**), the nucleation phase is much slower, leading to significant overlap between the two phases, resulting in larger nanoparticles.

Although these initial results do not provide a full understanding of the influence of the rate of addition of reducing agent on nanoparticle size, some general conclusions begin to emerge. Slower addition of the reducing agent can lead to

an increase in the nanoparticle size, with increases in mean diameter of over 6 nm observed. The nanoparticles produced under slow addition generally have dispersities similar to nanoparticles of the same ligand produced under instant addition conditions. Although the lower limit of the size seems to be determined by the solvent mixture and the ligand used, and the upper size limit may be determined by colloidal stability of the nanoparticles in a given solvent, this method nonetheless provides a way of modifying nanoparticle size, and has been shown to be generally applicable to nanoparticles of different functionality and solubility.

Nanoparticles of different sizes are highly desirable for a number of applications. Nanoparticle assembly is one area where nanoparticle size is crucial. A set of nanoparticle building blocks should ideally allow selection of nanoparticle size, independent of the chemistry to be employed in assembly. The functionality imparted by the ligands determines the chemistry which may be used to assemble nanoparticle building blocks, as such it is imperative to control and characterise not only nanoparticle size, but also the organic ligand. **Chapters 3 and 4** will focus on boronic acid-coated AuNP-7, so rigorous characterisation of these nanoparticles is required.

## **2.5 Molecular-level characterisation of boronic acid-coated nanoparticles**

An important consideration of nanoparticles which usually need not be considered when making small molecules is batch-to-batch variability. For example, an organic chemist synthesising a molecule might expect to get the same molecule in > 99% purity each time he or she makes it. When synthesising a nanoparticle, while the nanoparticles may also be obtained in high purity, each batch of nanoparticles will have a slightly different size and size distribution. Due to fluctuations not only in nanoparticle size and size distribution between batches but also in sample purity, careful characterisation of each individual batch of nanoparticles is required. As the surface area of a

sphere varies as a square of the radius, small changes in the nanoparticle diameter translate to a significant difference in the number of ligands per mass of nanoparticles.

As with all nanoparticles synthesised in this thesis, following the synthesis of AuNP-7, the nanoparticles were purified by washing away excess ligand and other molecular impurities. The ligand component of AuNP-7 was then characterised by NMR spectroscopy, in addition to characterisation of the nanoparticle core by TEM and UV-vis spectroscopy. NMR spectroscopy of nanoparticle-bound molecules typically produces very broad, weak signals. As the bulk of nanoparticle mass is contained in the NMR silent metal core, ligand concentrations of nanoparticle colloidal dispersions are inherently low. The broad signals are due to both the long spin–spin relaxation times and the inherent dispersity of ligand environments (**Chapter 1.4.1**).<sup>38–60</sup> This can be seen in the  $^1\text{H}$  NMR spectrum of AuNP-7 (**Figure 2.18**).

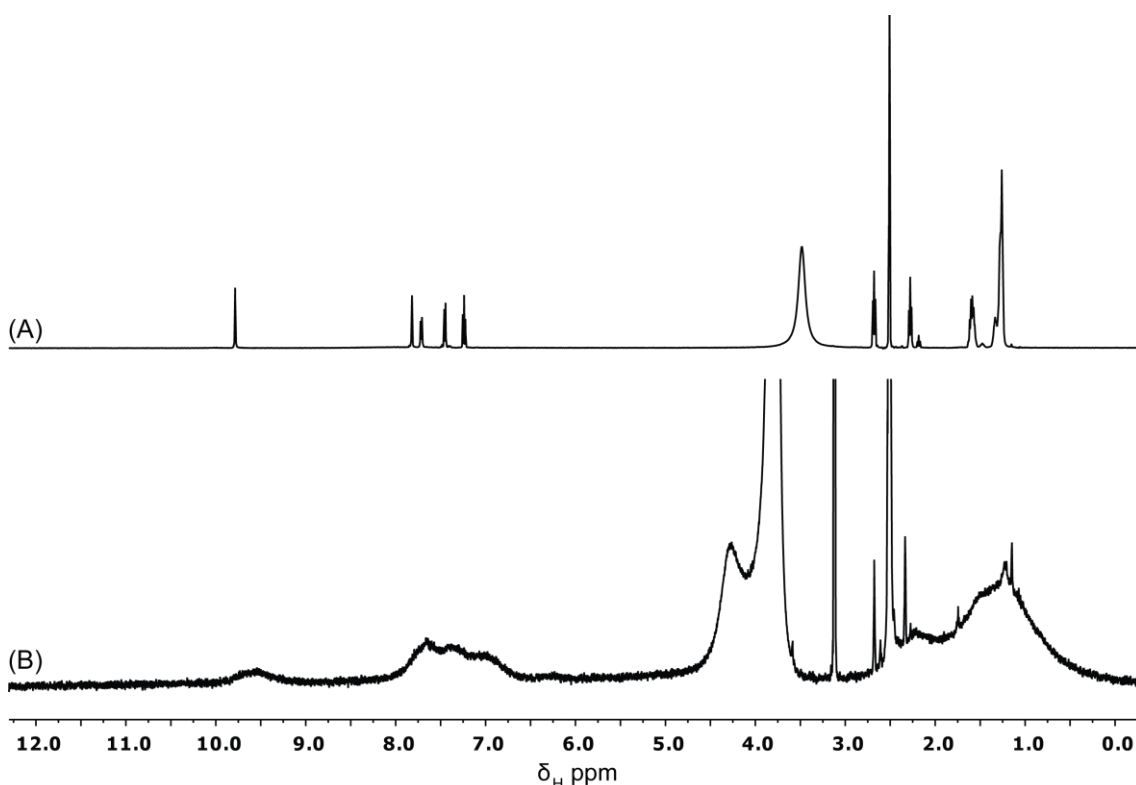


**Figure 2.18**  $^1\text{H}$  NMR spectra (DMSO-*d*6/ $\text{H}_2\text{O}$ , 99:1, 400.1 MHz, 298 K) of (A) boronic acid disulfide ligand **7** and (B) boronic acid-coated AuNP-7.

The reducing environment of the nanoparticle synthesis may cause ligand decomposition or other side reactions. However, the poor resolution of NMR spectra of nanoparticle-bound monolayers usually means that it is not possible to assess the ligand purity *in situ*. A solution to this is to remove the ligand from the surface. This may be done by displacing the ligand with a competing ligand in a place-exchange reaction.<sup>65</sup> However, this has the potential to lead to the formation of mixed disulfides, which may complicate analysis. A more common approach is to remove the ligands through a destructive ‘ligand strip’ procedure, employing either cyanide or more commonly iodine to oxidatively remove the ligands, allowing analysis of the resulting disulfide species by standard solution-phase analytical techniques.

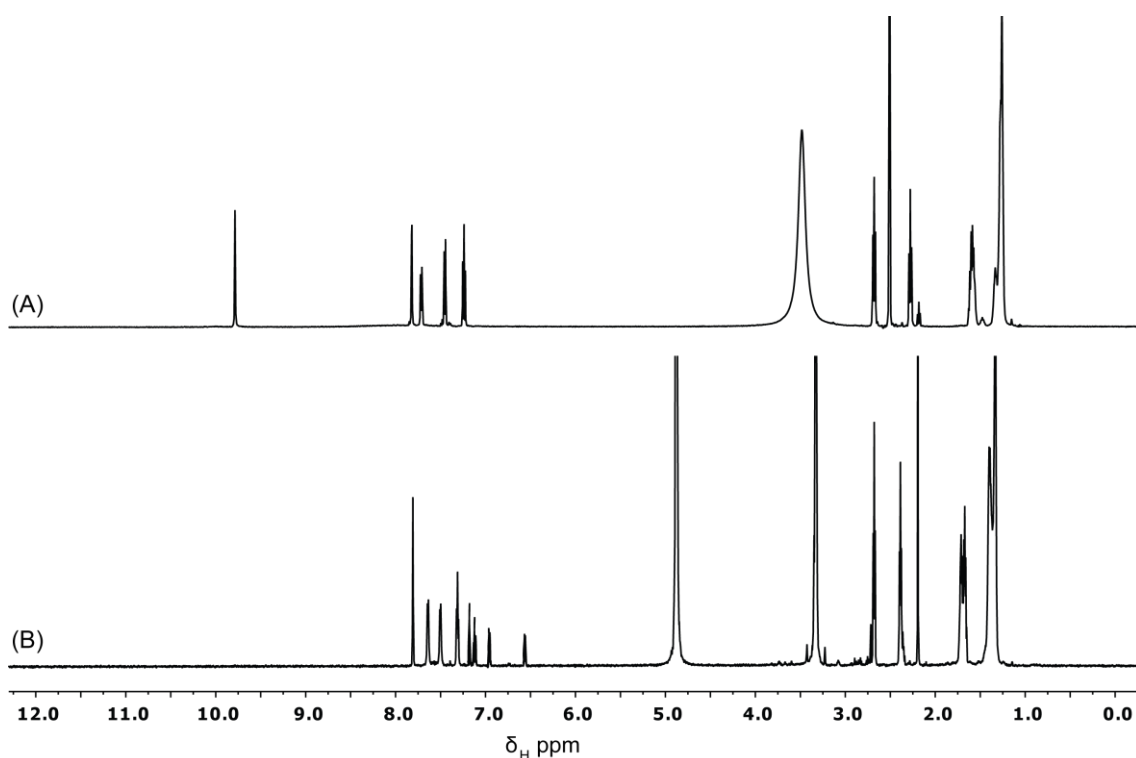


**Figure 2.19**  $^1\text{H}$  NMR spectra (DMSO- $d_6$ /D $_2$ O, 99:1, 500.1 MHz, 298 K) of (A) boronic acid disulfide ligand **7** and (B) boronic acid-coated AuNP-**7a** and iodine.

The first batch of nanoparticles was designated AuNP-**7a** (nanoparticle size:  $3.10 \pm 0.42$  nm). Adding a small amount of iodine to a colloidal suspension of

AuNP-7a revealed that in addition to the expected boronic acid, a second, unknown species was observed (**Figure 2.19**). Boronic acid ligand **7** was treated with iodine to ensure that the unknown species was not formed during the ligand strip. Boronic acid ligand **7** was inert towards iodine, suggesting that the second ligand was formed during the synthesis or purification processes. Iodine ligand stripping of fluorinated AuNP-7 revealed only the presence of the expected ligand **7**, suggesting that the side reaction seen with boronic acid-coated AuNP-7a was specific to the boronic acid functionality. Model boronic acid **10** was treated with 10 equivalents of TBAB and the boronic acid was found to be stable to reduction (**Figure 2.20**).

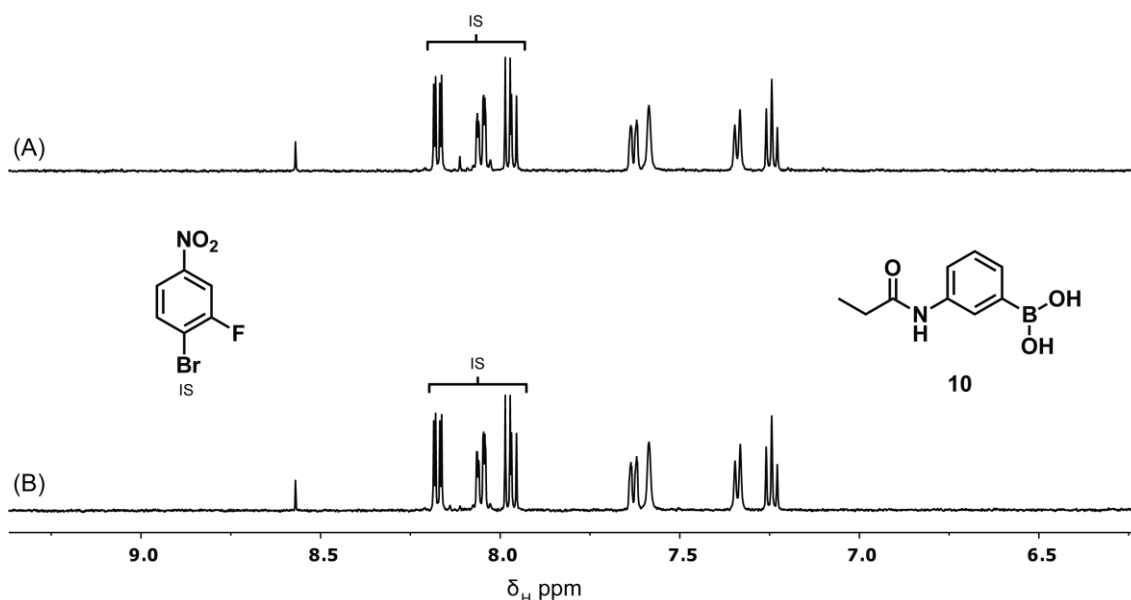


**Figure 2.20** Partial  $^1\text{H}$  NMR spectra ( $\text{CD}_3\text{OD}$ , 500.1 MHz, 298 K) of (A) boronic acid model compound ligand **7** and internal standard (3-fluoro-4-bromonitrobenzene **IS**), (B) boronic acid model compound ligand **7** and internal standard (3-fluoro-4-bromonitrobenzene **IS**) and iodine.

A well-known reaction of boronic acids is their oxidation to the corresponding phenol upon treatment with hydrogen peroxide<sup>180,181</sup> by an ionic mechanism. The solvent used for the synthesis of AuNP-7a is THF/MeOH, 10:1. THF is known to be unstable, decomposing to form peroxides. As such, THF is often supplied with a stabiliser, such as butylated hydroxytoluene (BHT). Therefore, it is possible that the boronic acid was being oxidised by peroxides formed in the THF during the synthesis or purification.

Boronic acid ligand **7** was treated with hydrogen peroxide, to form the corresponding phenol. The resulting NMR shifts matched the species observed in the ligand strip spectra from AuNP-**7a**, confirming the identity of the side product as phenol **11** (**Figure 2.21**). This was further confirmed from mass spectrometry (electrospray<sup>-</sup>) of a ligand strip sample, which revealed a species of mass 615.33, corresponding to [11-H]<sup>-</sup>.

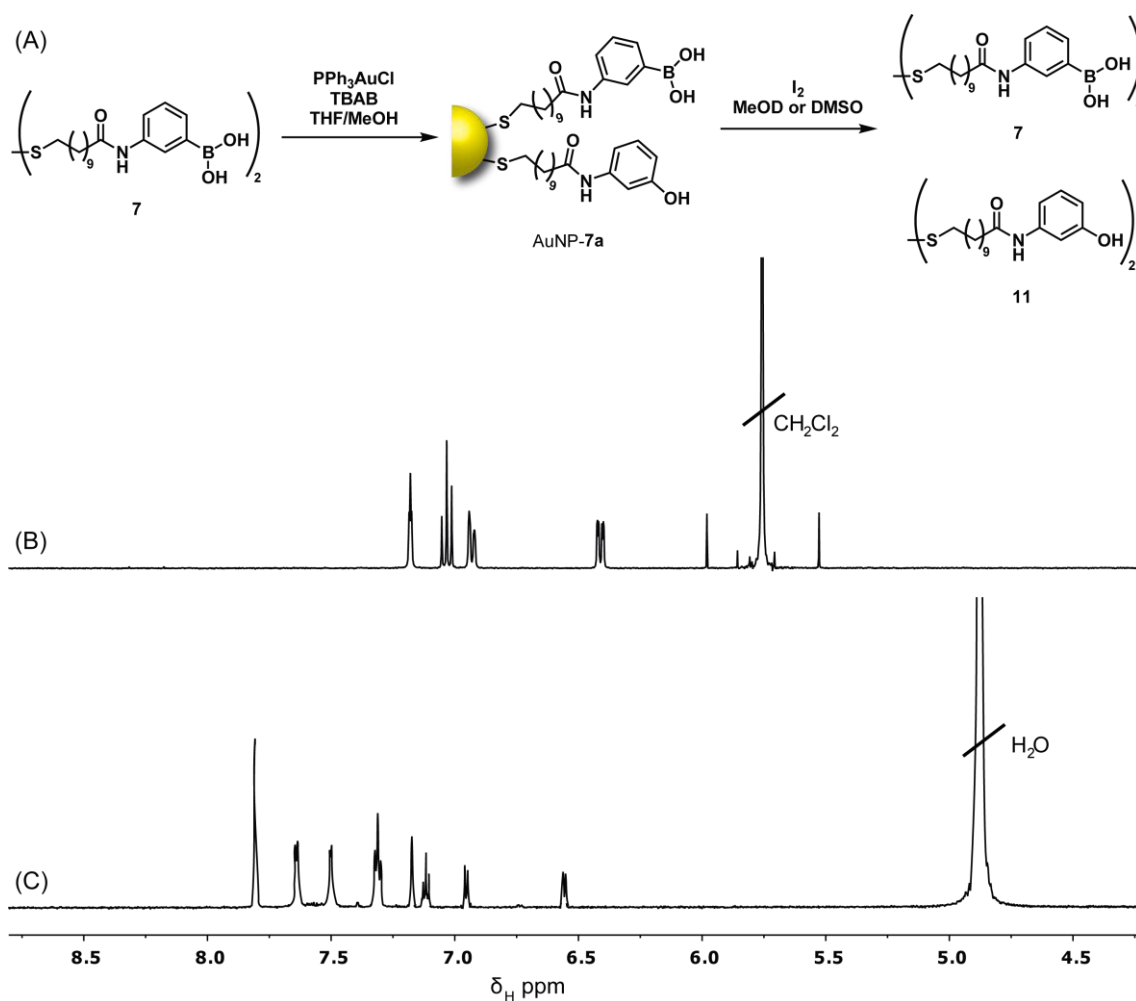


**Figure 2.21** (A) Representation of the nanoparticle synthesis, causing oxidative decomposition of the boronic acid ligand to form the phenol derivative, and the subsequent ligand strip. N.B. the ligand strip may give rise to the mixed disulfide as well as the two compounds shown. (B) Partial <sup>1</sup>H NMR spectra (DMSO-*d*<sub>6</sub>, 500.1 MHz, 298 K) of phenol **11**. (C) Partial <sup>1</sup>H NMR spectra (DMSO-*d*<sub>6</sub>/D<sub>2</sub>O, 99:1, 500.1 MHz, 298 K) of AuNP-**7a** and iodine.

The use of gold nanoparticles has been well documented for the catalysis of a number of oxidation reactions, for example aldehyde oxidation,<sup>182–184</sup> and as catalysts for hydrogen peroxide synthesis from molecular oxygen. It is possible that in this system, peroxide formation from THF is promoted by nanoparticles. Having established the identity of the side product, two questions arose: Could the nanoparticle ligand composition be determined? Could the side reaction be eradicated, or at least reduced?

Colloidal suspensions of AuNP-7a could be obtained only in protic solvents, or in mixtures containing a protic solvent. Therefore the presence of an additional nanoparticle-bound alcohol is unlikely to interfere with any reactivity of the remaining boronic acid ligands. Thus, if the nanoparticles are rigorously characterised, that quantitative investigation of dynamic boronic ester formation should still be possible, despite the presence of the oxidised ligand.

Elemental analysis of AuNP-7a by inductively coupled plasma atomic emission spectroscopy (ICP-OES) allowed the determination of the composition of gold, sulfur and boron in the sample. From the sulfur-to-boron ratio, the percentage of oxidised ligand could be determined. AuNP-7a had a gold-to-sulfur-to-boron ratio of 6.47:1.00:0.61 (**Chapter 7.3.1, Table 7.1**), indicating that 61% of the ligands remained unoxidised. Furthermore, from the absolute concentrations, it was possible to calculate a ‘molar mass’ of 2777 g mol<sup>-1</sup> for each boronic acid, by dividing the absolute total mass of the nanoparticle sample analysed by the number of moles of boron detected. Given this data, the nanoparticles could be used in quantitative measurements now despite the presence of a mixed monolayer of 61% boronic acid and 39% phenol. AuNP-7a were used for all experiments in **Chapter 4**.

Although the extent of oxidation can be quantified, it is desirable to suppress the reaction to afford nanoparticles solely coated with boronic acid ligand **7**. As the THF is the proposed source of peroxides, syntheses of AuNP-7 were attempted in other solvents, 10% MeOH in PhMe, CHCl<sub>3</sub> or MeCN. However, nanoparticles were not obtained in syntheses attempted in any of these solvents. Instead, the synthesis was carried out as before, in THF/MeOH, 10:1,

but with the addition of 15 mM BHT to the THF used for both the synthesis and purification of nanoparticles, to give AuNP-7b. AuNP-7b were found to have a size of  $3.41 \pm 0.43$  nm (13%), similar to AuNP-7a. Treating a colloidal suspension of AuNP-7b with iodine to remove the ligands revealed that almost no oxidation to the phenol had occurred (**Figure 2.22**). Elemental analysis by ICP-OES confirmed this, revealing a gold-to-sulfur-to-boron ratio of 7.26:1.00:0.97 (**Chapter 7.3.1, Table 7.2**). A 'molar mass' of  $1907 \text{ g mol}^{-1}$  for each boronic acid was calculated. AuNP-7b was used for the quantitative experiments in **Chapter 3.5**.

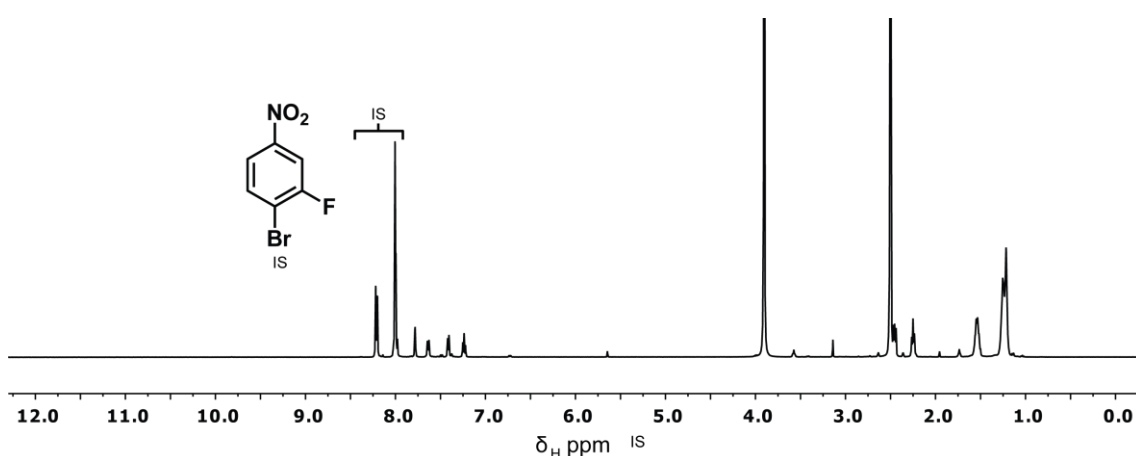


**Figure 2.22**  $^1\text{H}$  NMR spectra (DMSO-*d*<sub>6</sub>/D<sub>2</sub>O, 99:1, 500.1 MHz, 295 K) of AuNP-7b and internal standard (3-fluoro-4-bromonitrobenzene **IS**) and iodine.

## 2.6 Conclusions and future work

The functionality provided by the nanoparticle-bound ligand monolayer offers a way of controlling nanoparticle properties and reactivity. Synthetic routes to access functionalised nanoparticles are crucial for the development of nanoparticle applications. A one-phase synthesis of nanoparticles employing a mild reducing agent has been shown to be compatible with the synthesis of functionalised nanoparticles exhibiting a range of solvent compatibilities and containing a range of functional groups. Narrow size distributions of < 15% were obtained for all ligands, by contrast to existing methods, for which nanoparticle size distributions vary significantly between different ligands.

Nanoparticle size could be controlled by the rate at which the reductant was added to the synthesis. Adding the reductant as a solution slowly, over two hours, resulted in the formation of larger nanoparticles. This method of size control was found to be applicable to all ligands tested, providing a simple and general way of varying nanoparticle size without changing the ligand functionality. The largest difference was seen for alkyl-tetra(ethyleneglycol) ligand **2**, where the size of nanoparticles synthesised by adding the reductant over two hours was  $11.23 \pm 1.48$  nm, compared to nanoparticles of  $4.38 \pm 0.60$  nm synthesised by instant reductant addition. Crucially, in all but one case, the size distribution of nanoparticles produced by slow reductant addition remained similar to the corresponding nanoparticles synthesised by instant reduction addition.

The formation of larger nanoparticles by slow addition of the reductant was rationalised in terms of a nucleation–growth model. Slow addition results in nucleation over a longer time period, meaning that nuclei formed at early time points may grow at the expense of nuclei formed at later time points, resulting in an overall larger nanoparticle population.

Developing general strategies for the size-controlled synthesis of functionalised nanoparticles is crucial for their subsequent application. In addition to controlling the nanoparticle core size and dispersity, it is also necessary to assess the organic molecular ligand. Molecular level characterisation of AuNP-**7a** revealed the presence of an unknown ligand on the nanoparticle surface, in addition to the expected boronic acid **7**. The ligand was identified as the corresponding phenol, produced by the peroxide-induced oxidation of the boronic acid. The oxidation was suppressed by the addition of BHT to act as a scavenger. The extent of oxidation was assessed by a combination of ICP-OES elemental analysis and NMR spectroscopy, allowing detailed quantification of the nanoparticle composition.

The general strategy for the size-controlled synthesis of a range of functionalised nanoparticles developed in this chapter, combined with

molecular-level characterisation of the resulting nanoparticles, promises easier access to nanoparticle building blocks. Ready access to functionalised nanoparticle building blocks presents exciting opportunities for further developing the chemistry to control their functionalisation and assembly.

# Chapter 3:

## Reversible boronic ester formation on nanoparticle-bound monolayers

This chapter focuses on the reversible formation of boronic esters on nanoparticle-bound boronic acids with a number of binding partners, seeking to investigate the fundamental differences in reactivity between nanoparticle-bound boronic acids and boronic acids in solution.

Boronic ester formation between a model boronic acid and a number of binding partners is quantitatively observed by  $^{19}\text{F}$  NMR spectroscopy. Subsequently, boronic ester formation is investigated on boronic acid-coated nanoparticles prepared in **Chapter 2**. Initially, boronic ester formation is demonstrated qualitatively and observed directly by  $^{19}\text{F}$  NMR spectroscopy. The reversibility and cyclability of this dynamic covalent process is then demonstrated. Quantitative  $^{19}\text{F}$  NMR spectroscopy allows determination of association constants, which are found to be significantly different to the association constants seen with the corresponding model boronic acid. This difference in reactivity is partially attributed to steric implications of boronic ester formation in a molecular monolayer.

The differences observed between the nanoparticle-bound boronic ester formation and monomeric solution-phase boronic esters demonstrate the importance of considering the fundamentals of reactivity in nanoparticle-bound systems, in order to exploit their full potential.

*I gratefully acknowledge the contribution of Rebecca Spicer to this chapter, who synthesised compounds **15**, **16** and **17** and carried out titration experiments with salicylic acid and its derivatives to provide data for **Figures 3.7**, **3.8** and **3.9** during her Honours Project (Sept 2014 – April 2015).*



reversibility of boronic ester formation on nanoparticle-bound monolayers has not been confirmed (**Chapter 1.7.2**).

A key aspect of applying dynamic covalent chemistry to the functionalisation of nanoparticles is to develop a detailed understanding of the process. NMR spectroscopy and other spectroscopic techniques can be employed to directly observe dynamic covalent processes at the molecular level. While dynamic processes, such as boronic ester formation and exchange, have been well documented,<sup>129</sup> transferring dynamic covalent chemistry to a nanoparticle-bound molecular monolayer may have a profound effect on the reactivity and behaviour of dynamic covalent reactions. Understanding differences in reactivity of nanoparticle-bound dynamic covalent processes is crucial for developing a predictable method for controlling nanoparticle functionalisation. The ability to study the molecular details of boronic ester formation on nanoparticles provides direct evidence of the chemistry which may be employed for functionalisation of nanoparticles, rather than relying on purely phenomenological evidence of the process.

This chapter presents detailed investigations of the dynamic covalent reactivity of boronic acid functionalised AuNP-7 (**Figure 3.2**), the synthesis and the characterisation of which were discussed in **Chapter 2**.

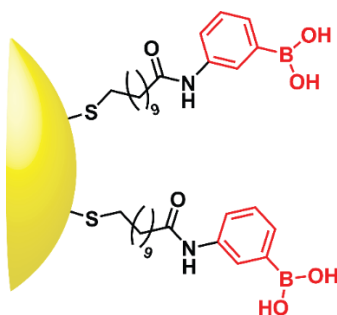
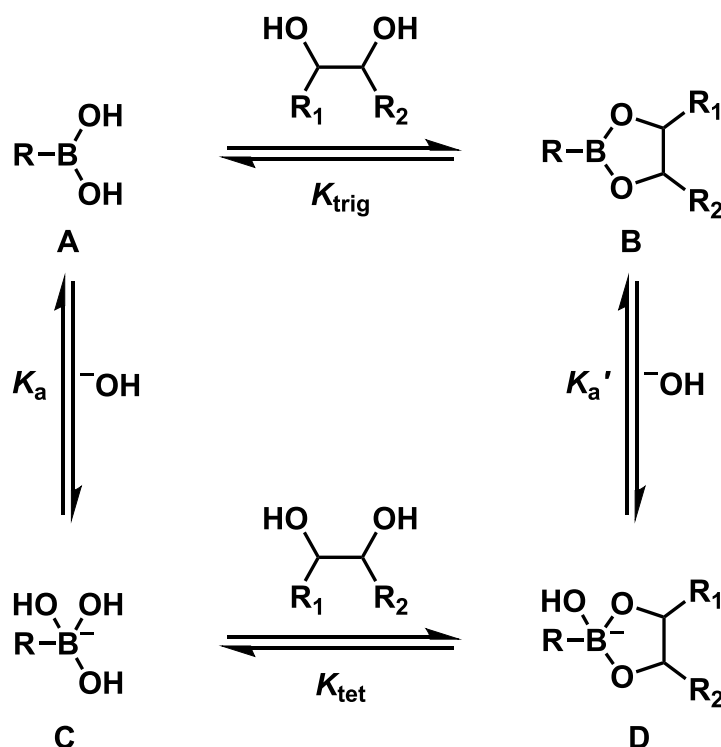


**Figure 3.2** Boronic acid functionalised gold nanoparticles (AuNP-7).

### 3.1.1 Dynamic boronic ester exchange

Boronic esters are an example of a dynamic covalent bond formed under thermodynamic control between a boronic acid and typically a *cis*-1,2-diol.<sup>135–137</sup> The equilibrium relationship between boronic acid and boronic ester is more complicated than many other dynamic covalent bonds, as both the boronic acid and the boronic ester may be either trigonal or tetrahedral around boron (**Scheme 3.1**). This reactivity arises from the electron deficient nature of boron, making it a very strong Lewis acid. With only 6 electrons, boron possesses an empty p orbital into which electron density may be donated. In aprotic environments, in the absence of any Lewis bases, boronic acids will exist as trigonal, neutral species (**Scheme 3.1, A**). Under such conditions, boronic ester formation is possible, leading to formation of trigonal boronic ester **B** and two molecules of water. The equilibrium ( $K_{\text{trig}}$ ) may be shifted in favour of boronic ester **B** by removal of water from the system, which, according to Le Châtelier's Principle, will promote formation of **B** as the system tries to produce more water. However, in protic solvents, the Lewis acidity of a typical boronic acid is such that it will interact with the weakly Lewis basic solvent, giving rise to tetrahedral negatively charged boronate acid **C**, again an equilibrium process ( $K_{\text{a}}$ ). The equilibrium between trigonal and tetrahedral boron may be strongly shifted towards the tetrahedral species by adding a much stronger Lewis base, such as an amine, in order to push the equilibrium fully towards tetrahedral species. The tetrahedral boronate acid species may also react with a 1,2-diol to form boronate ester **D**; once again this is an equilibrium process ( $K_{\text{tet}}$ ). Completing the cycle, tetrahedral boronate ester species **D** is also in equilibrium with trigonal boronic ester species **B**. All four equilibria are very fast, which means that while boronate ester formation may be thermodynamically highly favoured, the products are generally very kinetically labile. Despite the rapid equilibration, the exchange processes between **C** and **D** (and **A** and **B**) are often slow on the NMR timescale, allowing for direct observation of product distributions by NMR spectroscopy of an equilibrium mixture.



**Scheme 3.1** Equilibria governing the reaction of boronic acids with 1,2-diols. The presence of a Lewis base (in the scheme denoted  $\text{OH}^-$  for simplicity) gives rise to formation of tetrahedral boronate species, governed by the ionisation constants  $K_a$  and  $K_a'$ , respectively.  $K_{\text{trig}}$  and  $K_{\text{tet}}$  are equilibrium constants for the reaction of trigonal boronic acid **A** and tetrahedral boronate acid **C** to form trigonal boronic ester **B** and tetrahedral boronate ester **D**, respectively.

With the exception of a few extremely weakly binding diols, the  $\text{p}K_a$  values of boronic acids (**A**) are 2–4 units higher than the  $\text{p}K_a'$  values of boronic esters (**B**). The increased  $\text{p}K_a$  values are due to distortion at the boron upon diol binding, causing the empty p-orbital to become more  $\text{sp}^3$ -like in character, lowering the energy and hence increasing the Lewis acidity of the boron.<sup>143</sup> Therefore,  $K_{\text{tet}}$  is generally 2–4 orders of magnitude greater than  $K_{\text{trig}}$  as  $K_a K_{\text{tet}} = K_a' K_{\text{trig}}$  must hold true.<sup>142</sup> In general, raising the pH above the  $\text{p}K_a$  of the boronic acid leads to an enhancement in boronic ester formation. However, this scheme is an oversimplification of the true situation in most cases due to the strong Lewis acidic character of the boronic acid, which allows it to form a number of weak complexes with various reaction constituents. There are a number of further complicating factors, for example when the diol has a  $\text{p}K_a$  value of a magnitude similar to (or lower than) that of the boronic acid, which leads to separate equilibria for the protonated and deprotonated diol species.

Furthermore, factors such as solvent, buffer constituents and concentrations are known to affect boronic ester stability, but the exact relationships are not well understood.

### 3.2 Scope of binding partners for boronic acids

Boronic ester formation is not limited to *cis*-1,2-diols. Any alcohols may react to form boronate esters but, due to chelate cooperativity, the formation is generally significantly more favoured where a cyclic structure can be formed.<sup>142</sup> 1,2-Diols, such as those found in sugars, are by far the most widely investigated binding partner for boronic acids, with much work carried out on developing boronate acid systems for sugar sensing.<sup>142,143</sup>

Where the geometry of the diol is pre-organised for boronate acid binding, such as in 1,2-dihydroxybenzenes or some sugars, the association is stronger because ester formation is less entropically disfavoured, as no conformational freedom is lost. However, boronate ester formation is also observed with 1,3-diols<sup>187</sup> and  $\alpha$ -amino acids,<sup>188</sup> leading to the formation of boronate esters with a 6-membered ring. In the case of  $\alpha$ -amino acids as the binding partner, a B–N bond is formed in place of one of the B–O bonds. For the purpose of this thesis, the tetrahedral cyclic complex between a boronic acid and any binding partner will be referred to as a boronate ester, regardless of whether B–O or B–N bonds are formed. 1,2-Dihydroxybenzenes (catechols) generally bind strongly. The rigidity of the catechol structure means that no conformational freedom is lost upon binding to a boronic acid. However, the  $pK_a$  of 1,2-dihydroxybenzene is 9.45,<sup>189</sup> and depending on other substituents present on the benzene ring, the  $pK_a$  value may be lowered further, bringing it to a value similar to that of the boronic acid. Therefore partial deprotonation of the catechol may occur, complicating the interaction.

Salicylic acids are another class of binding partner that have long been known to bind boronic acids, but boronic acid–salicylic acid binding has not been

extensively investigated.<sup>190–192</sup> Salicylic acids are attractive binding partners for boronate acids because, unlike the 6-membered cyclic complexes formed by 1,3-diols and  $\alpha$ -amino acids, they are pre-organised for chelate binding. Additionally, a number of salicylic acid derivatives, including salicylamide<sup>192</sup> and salicylhydroxamic acid,<sup>193–196</sup> have been reported to also bind to boronate esters, presenting an attractive class of aromatic molecules, which may be structurally similar, but display significantly different binding. This provides the potential for a set of binding partners with differing affinity, which could ultimately prove useful in developing a versatile and tuneable nanoparticle functionalisation strategy.

### 3.3 Model compound studies

Surprisingly, detailed comparative studies of a set of structurally similar aromatic binding partners for molecular boronic acids are absent from the literature. A series of structurally related binding partners were selected for investigation (**Figure 3.3, 12–17**).

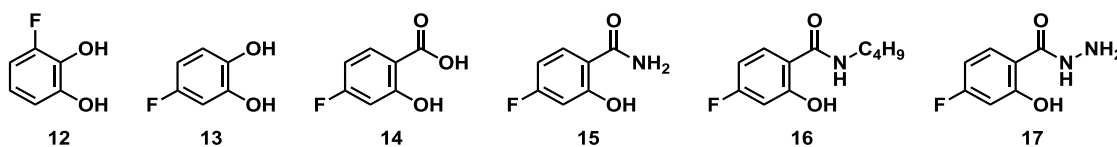
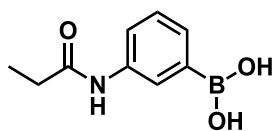


**Figure 3.3** A selection of structurally similar aromatic binding partners which were investigated with respect to their boronic acid binding. All compounds contain a fluorine tag to permit <sup>19</sup>F NMR analysis.

Fluorocatechols **12** and **13** were selected as two binding partners which both form 5-membered rings upon binding, allowing for investigation of the differing effect of electronics. The series of 4-substituted binding partners, 4-fluorocatechol **13**, 4-fluorosalicylic acid **14** and its amide and hydrazide derivatives, **15–17**, provides a second set of binding partners that lack the highly acidic proton of the parent acid.



10

**Figure 3.4** The structure of boronic acid **10**, synthesised for investigation of its binding with a variety of fluorinated binding partners.

Boronic acid **10** (**Figure 3.4**) was designed as an isoelectric molecular model of nanoparticle-bound boronic acid AuNP-7 (**Chapter 2.5**). Boronic acid **10** was synthesised by an EDC-mediated peptide coupling of 3-aminophenylboronic acid with propionic acid. Boronic acid **10** was used for studies with the fluorinated binding partners.

A mixture of model boronic acid **10** with either fluorocatechol **12** or **13** ( $[\mathbf{10}] \approx [\mathbf{12}]$  or  $[\mathbf{13}] \approx 5$  mM) in the presence of 14 eq. *N,N*-diisopropylethylamine and an internal standard (3-fluoro-4-bromonitrobenzene), in CD<sub>3</sub>OD, produced <sup>19</sup>F NMR spectra displaying three well-resolved resonances. By comparison with reference spectra of **12** or **13** under the same conditions, all peaks could be assigned as internal standard, unbound fluorocatechol or boronate ester (**Figure 3.5**). The amine base is necessary to convert the boron to its tetrahedral form, acting as a strong Lewis base. In the absence of the base, no formation of boronic esters was observed.

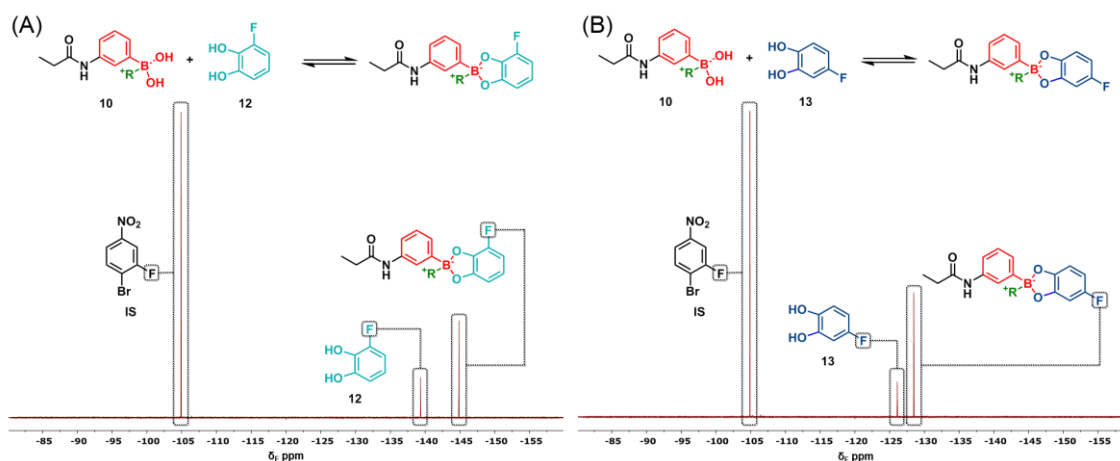


**Figure 3.5**  $^{19}\text{F}$  NMR spectra ( $\text{CD}_3\text{OD}$ , 470.5 MHz, 295 K) of model boronic esters formed with (A) 3-fluorocatechol **12** and (B) 4-fluorocatechol **13**. Distinct resonances for catechol and ester can be seen in both cases, indicating that, despite the rapid equilibration, the system is in slow exchange on the NMR timescale. ( $[\mathbf{12}]/[\mathbf{13}] \approx [\mathbf{10}] \approx 5$  mM,  $N,N$ -diisopropylethylamine = 500 mM)

Over time, additional small peaks appeared in the  $^{19}\text{F}$  NMR spectra. These were believed to arise from oxidative decomposition of the fluorocatechols.  $N,N$ -Diisopropylethylamine, the base employed in these initial experiments, has a  $\text{p}K_{\text{a}}$  (in water) of 10.78,<sup>197</sup> which is significantly higher than the  $\text{p}K_{\text{a}}$  of most catechols (about 9.5). Specifically,  $\text{p}K_{\text{a}}$  values for 3-fluorocatechol **13** and 4-fluorocatechol **12** (in 40% dioxane/water) are 9.8 and 10.1, respectively.<sup>198</sup> The high extent of deprotonation of the catechol leads to rapid and irreversible oxidation to the corresponding ortho-quinone,<sup>199</sup> followed by further decomposition reactions. An alternative base, with a lower  $\text{p}K_{\text{a}}$  was expected to eliminate, or at least slow down, the oxidation of the catechol.  $N$ -Methylmorpholine was selected, which has a  $\text{p}K_{\text{a}}$  of 7.41.<sup>200</sup> Use of the weaker base did indeed result in no detectable oxidation products by  $^{19}\text{F}$  NMR spectroscopy, although a slight colour change from colourless to yellow was still noted after standing for over a week, suggesting that oxidation was occurring, although much more slowly. Boronate ester formation experiments employing  $N$ -methylmorpholine resulted in very similar NMR spectra, indicating the continued formation of boronate esters under the employed experimental conditions (**Figure 3.6A**).

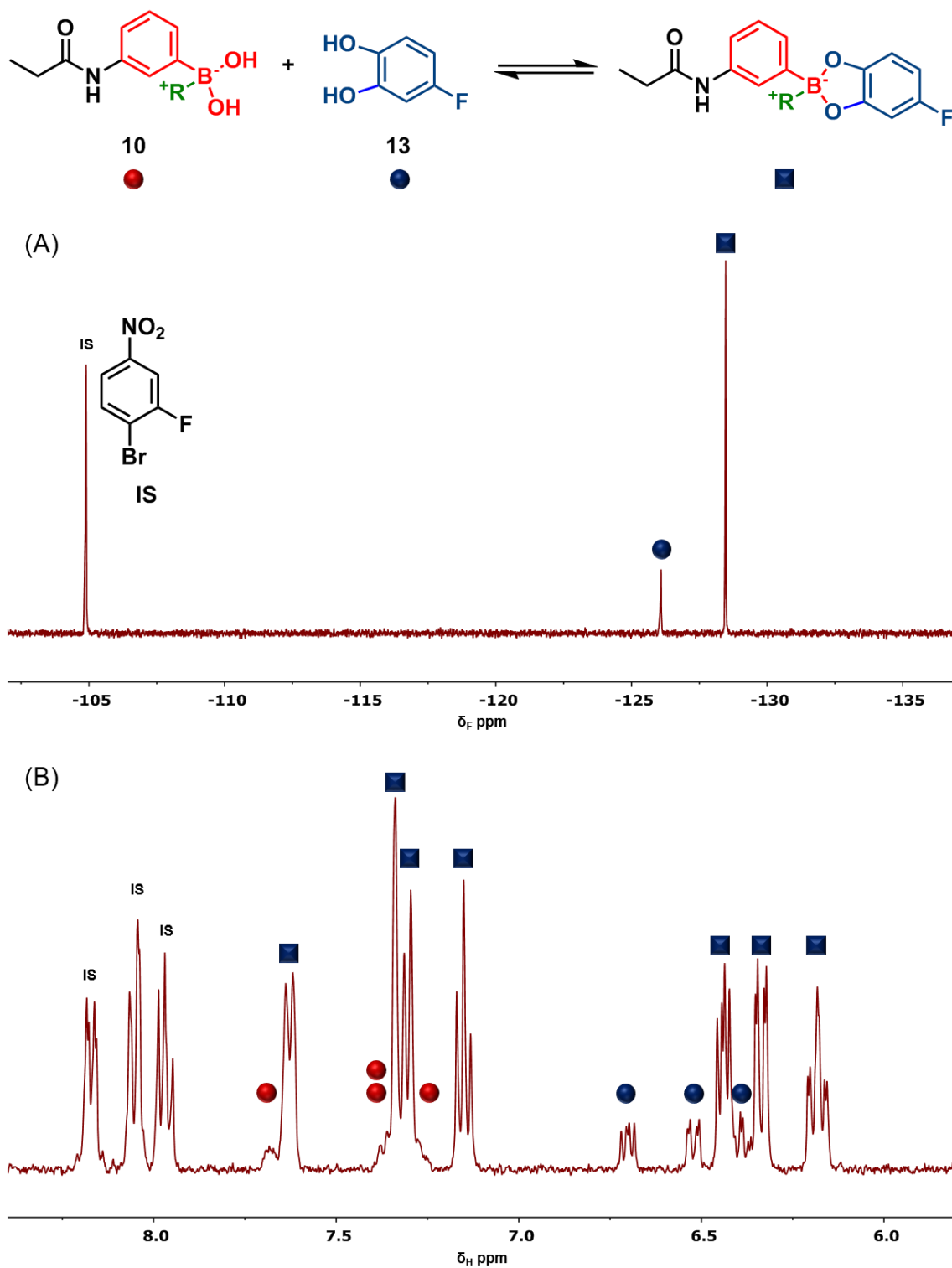


**Figure 3.6** Boronic acid **10** and 4-fluorocatechol **13** ( $[\mathbf{10}] \approx [\mathbf{13}] \approx 5$  mM) in the presence of 100 eq. *N*-methylmorpholine and an internal standard (3-fluoro-4-bromonitrobenzene **IS**), in CD<sub>3</sub>OD. (A) Partial  $^{19}\text{F}$  NMR spectrum (CD<sub>3</sub>OD, 470.5 MHz, 295 K) and (B) Partial  $^1\text{H}$  NMR spectrum (CD<sub>3</sub>OD, 500.1 MHz, 295 K). Resonances in both the fluorine and proton spectra have been assigned to the components, and derived concentrations show good agreement between the two nuclei.

Despite the larger number of signals present in the equilibrium  $^1\text{H}$  NMR spectrum, full assignment was possible and found to agree with the conclusions drawn from the  $^{19}\text{F}$  NMR spectra (**Figure 3.6B**).

The same experimental procedure was followed for salicylic acid derivatives **14–17**. In each experiment, a mixture of model boronic acid **10** with salicylic acid derivative (1:1  $\approx$  5 mM) in the presence of 100 eq. *N*-methylmorpholine and an internal standard (3-fluoro-4-bromonitrobenzene), in  $\text{CD}_3\text{OD}$ , was prepared and analysed by  $^1\text{H}$  and  $^{19}\text{F}$  NMR spectroscopy.

$^{19}\text{F}$  NMR spectra obtained with boronic acid **10** and either 4-fluorosalicylic acid **14** or 4-fluorosalicylamide **15** showed three peaks corresponding to the internal standard, unbound salicylic acid or salicylamide derivative and boronate ester (**Figure 3.7A,B**). When secondary amide, *n*-butylsalicylamide **16** was used as the binding partner, no formation of boronate ester was observed and the spectrum displayed only two peaks, corresponding to the internal standard and the unbound amide (**Figure 3.7C**). While formation of boronic esters with secondary amides have been observed<sup>192</sup> in aqueous buffered conditions, the extent of formation is much lower than in the case of primary amides. It is likely that for the aryl boronic acid used here, the sterics are too prohibitive to allow boronic ester formation. In the case of hydrazide **17**, two major peaks and a number of minor peaks were observed. The minor peaks increased in intensity over time, suggesting decomposition of the hydrazide. No peak corresponding to unbound hydrazide could be seen, and the other major peak is assumed to correspond to the boronate ester (**Figure 3.7D**).

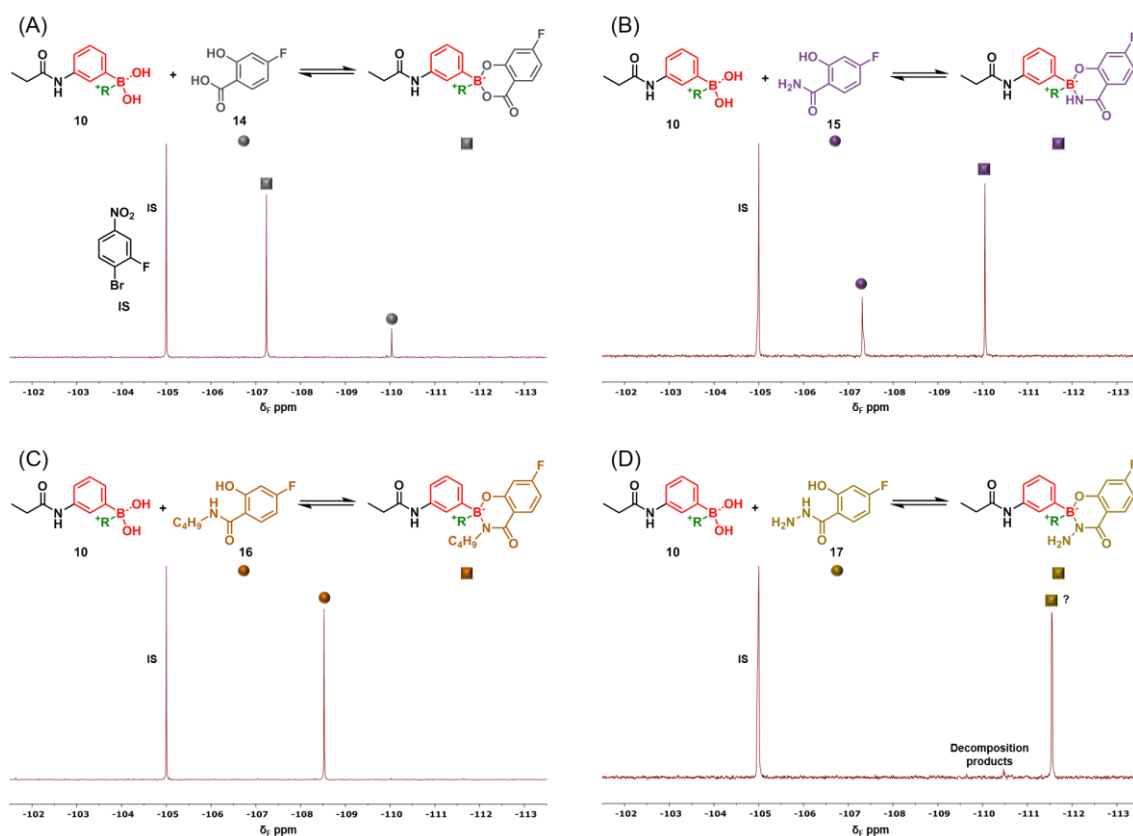


**Figure 3.7** Boronate ester formation with salicylic acid derivatives. Boronic acid **10** and salicylic acid derivative (**10** = salicylic acid derivative  $\approx 5$  mM) in the presence of 100 eq. *N*-methylmorpholine and an internal standard (3-fluoro-4-bromonitrobenzene), ( $\text{CD}_3\text{OD}$ , 470.5 MHz, 295 K). **(A)** Salicylic acid **14**: both free acid and boronate ester are observed. **(B)** Salicylamide **15**: both free amide and boronate ester are observed. **(C)** *n*-Butylsalicylamide **16**: only free amide is observed. **(D)** Salicylhydrazide **17**: one major peak (tentatively assigned as boronate ester) is observed, in addition to minor decomposition products which increase over time.

Following full assignment of the  $^{19}\text{F}$  NMR spectra for all binding partners, association constants ( $K_a$ ) for the binding of each partner with **10** were determined. As each complex is in slow exchange on the NMR timescale, equilibrium concentrations of fluorinated species by integration relative to the internal standard could be measured. Spin–lattice relaxation times ( $T_1$ ) were measured for all species using an inversion recovery method. The internal standard had the longest  $T_1$  time (3.8 s), and a 20 s delay was determined as sufficient for quantitative  $^{19}\text{F}$  NMR measurements (**Chapter 7.4.1**).

In a typical experiment to determine association constants, a mixture of model boronic acid **10** with binding partner ( $[\mathbf{10}] \approx [\text{binding partner}] \approx 5$  mM) and an internal standard (3-fluoro-4-bromonitrobenzene) was dissolved in  $\text{CD}_3\text{OD}$ .

Quantitative  $^{19}\text{F}$  and  $^1\text{H}$  NMR spectra were obtained and the initial concentration of boronic acid **10** and binding partner were accurately determined relative to the internal standard. Before the addition of base, no boronic ester formation was observed, however, small downfield shifts (most notably  $\approx -0.1$  ppm for salicylic acid **14**) indicated formation of weak, fast-exchange complexes. Subsequently, 100 eq. *N*-methylmorpholine was added to the mixture, leading to boronate ester formation.  $^1\text{H}$  and  $^{19}\text{F}$  NMR spectra were recorded within two minutes and were not observed to change after this time (with the exception of decomposition in the case of hydrazide **17**). The equilibrium concentration of boronate ester was measured relative to the internal standard, and equilibrium concentrations of boronic acid and unbound binding partner were determined from this measurement and the starting concentrations.

Association constants for both fluorocatechols **12** and **13**, 4-fluorosalicylic acid **14** and 4-fluorosalicylamide **15** with boronic acid **10** were determined using this method, with at least three replicates (**Table 3.1**).

**Table 3.1** Summary of association constants ( $K_a$ ) determined for interaction of binding partners **12–15** with boronic acid **10** in  $\text{CD}_3\text{OD}$  with 100 eq. of *N*-methylmorpholine, and association constants ( $K_{\text{base}}$ ) for the interaction between the binding partner and *N*-methylmorpholine. Errors quoted are the standard deviation of three or more repeats.

Binding partner	$K_{\text{base}} / \text{M}^{-1}$	$K_a / \text{M}^{-1}$
3-Fluorocatechol <b>12</b>	—	$1990 \pm 200$ (10%)
4-Fluorocatechol <b>13</b>	—	$3420 \pm 720$ (21%)
4-Fluorosalicylic acid <b>14</b>	$840 \pm 84$	$2500 \pm 310$ (12%)
4-Fluorosalicylamide <b>15</b>	$9 \pm 1$	$480 \pm 40$ (8%)

The association constants show that 4-fluorocatechol **13** binds more strongly than 3-fluorocatechol **12**. Of the 4-substituted compounds, catechol **13** binds slightly more strongly than acid **14**, both of which bind significantly more

strongly than amide **15**. The stronger binding of the acid over the amide was attributed to the lower  $pK_a$  of the most acidic proton. Titrations against a Lewis base (*N*-methylmorpholine) were performed with these compounds in order to determine the association constant between the binding partner and the base (**Figure 3.8**), denoted as  $K_{\text{base}}$ . The change in the  $^{19}\text{F}$  resonance position of the binding partner is effectively a measure of the extent of deprotonation of the most acidic proton: the acid proton of the salicylic acid and the phenol proton for the amide and catechol. Fitting the data to a 1:1 binding isotherm gave  $K_{\text{base}}$  values of  $840\text{ M}^{-1}$  for the acid and  $9\text{ M}^{-1}$  for the amide (**Table 3.1**). No shift in the position of the  $^{19}\text{F}$  resonance of 4-fluorocatechol **13** was observed upon addition of *N*-methylmorpholine.

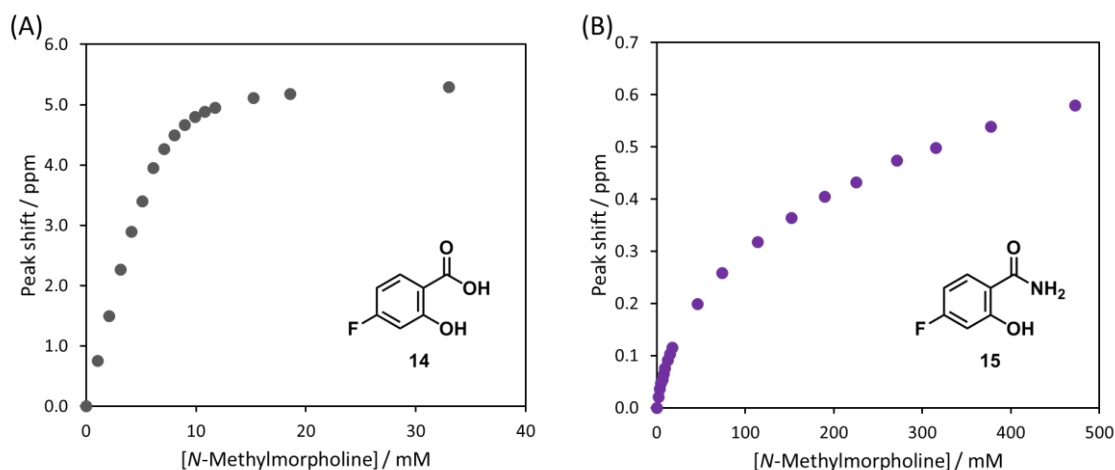


**Figure 3.8** Titration curves where the concentration of *N*-methylmorpholine was increased ( $\text{CD}_3\text{OD}$ , 470.5 MHz, 295 K) in the presence of 4-fluorosalic acid **14** (A) and 4-fluorosalic amide **15** (B). The data was fitted to a 1:1 binding isotherm to give a value for  $K_{\text{base}}$ .

At 4 eq. of base, salicylic acid **14** was fully deprotonated (**Figure 3.8A**). Therefore, under the boronic ester formation conditions employed, in the presence of 100 eq. of base, only the deprotonated form of the acid was present. To further investigate the implications of the deprotonation of salicylic acid **14**, *N*-methylmorpholine was titrated into a 1:1 solution (5 mM) of salicylic acid **14** and boronic acid **10** (**Figure 3.9A**). As the concentration of base increased, so did the proportion of bound species, until the concentration of boronic ester present remained constant at 4 eq. and higher, giving an association constant for boronate ester formation of  $2700\text{ M}^{-1}$ , the same as

seen in the single-point experiments at 100 eq. of base. This indicates that the deprotonated salicylic acid is the dominant species in binding to the boronic acid. The deprotonated binding partner is a stronger Lewis base, hence the stronger complexation.

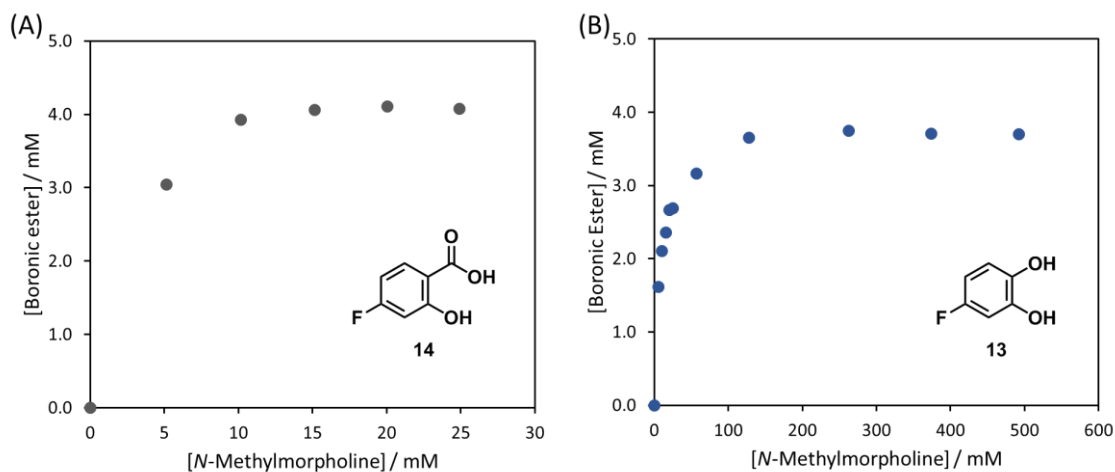


**Figure 3.9** The dependence of boronic ester formation on concentration of *N*-methylmorpholine for boronic acid **10** in the presence of (A) 4-fluorosalicylic acid **14** and (B) 4-fluorocatechol **13** ( $10 \approx 14/13 \approx 5$  mM) ( $\text{CD}_3\text{OD}$ , 470.5 MHz, 295 K).

Although no shift in the  $^{19}\text{F}$  resonance of 4-fluorocatechol **13** was observed upon addition of base, the extent of boronate ester formation was highly dependent on the concentration of base added (**Figure 3.9B**). As the concentration of base increased, so did the concentration of boronic ester. This can be attributed not to deprotonation of the catechol phenol proton, but to Lewis acid–base interaction between *N*-methylmorpholine and the boronic acid and ester species. At approximately 200 eq. of base, the concentration of boronic ester remained constant. This indicates that, for the catechol binding partners at the concentration of base employed in formation experiments (100 eq.), the base concentration is crucial for determining the  $K_a$  value, and variations in this concentration will be reflected in the extent of binding.

All of the binding partners investigated (**Figure 3.3, 12–17**), except for secondary amide **16**, were found to form boronic esters with boronic acid **10** under basic conditions. The class of salicylic acid derivative compounds – acid

**14**, amide **15** and hydrazide **17** – displayed significantly different association constants, although hydrazide **17** showed significant decomposition and was not investigated further. The stronger binding of the acid reflected its greater interaction with the base. Together, catechols **12** and **13**, acid **14** and amide **15** provide a series of aromatic binding partners for boronic ester formation, with a range of association constants, offering potential for the controlled functionalisation of boronic acid-coated nanoparticles.

### 3.3 Boronic ester formation on nanoparticles

Upon transitioning from molecular boronic acids to nanoparticle-bound boronic acids, establishing whether moving to the nanoparticle-bound environment has a significant impact on boronic ester formation is crucial: Does boronic ester formation still occur, and is the process still under thermodynamic control? Boronic acid-coated AuNP-**7a** ( $d \approx 3$  nm) (**Figure 3.10**), the synthesis and characterisation of which were discussed in **Chapter 2**, were used to investigate nanoparticle-bound boronic ester formation. The solubility limitations of these nanoparticles meant that all solution-phase boronic ester dynamic covalent chemistry using these nanoparticles required working in at least 5%–10% of a polar protic solvent. As with the model molecular work, all experiments were conducted in methanol.

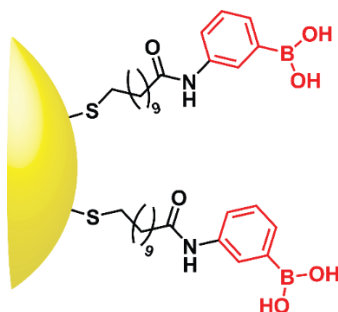


**Figure 3.10**

Boronic acid functionalised gold nanoparticles (AuNP-7).

AuNP-**7a** and either 3- or 4-fluorocatechol **12** or **13** were dissolved in CD<sub>3</sub>OD in the presence of an internal standard. As with the model boronic acid **10**, <sup>19</sup>F NMR spectroscopy at this stage revealed only two peaks, corresponding to the internal standard and the unbound catechol, indicating that no boronic ester formation was occurring. Upon addition of a Lewis base (*N,N*-diisopropylethylamine or *N*-methylmorpholine), a third peak appeared in the spectra (**Figure 3.11**). The chemical shift of the new peak was similar to the boronic ester resonance determined for the molecular model (**Figure 3.5**), however, the nanoparticle-bound boronic ester peak showed significant broadening. The broadness is characteristic of nanoparticle-bound species (**Chapter 1.4.1**). Proton NMR spectra (**Chapter 7.4, Figure 7.11**) showed the appearance of broad peaks; however, these peaks overlapped with other nanoparticle-bound aromatic peaks and are hidden under the unbound catechol.

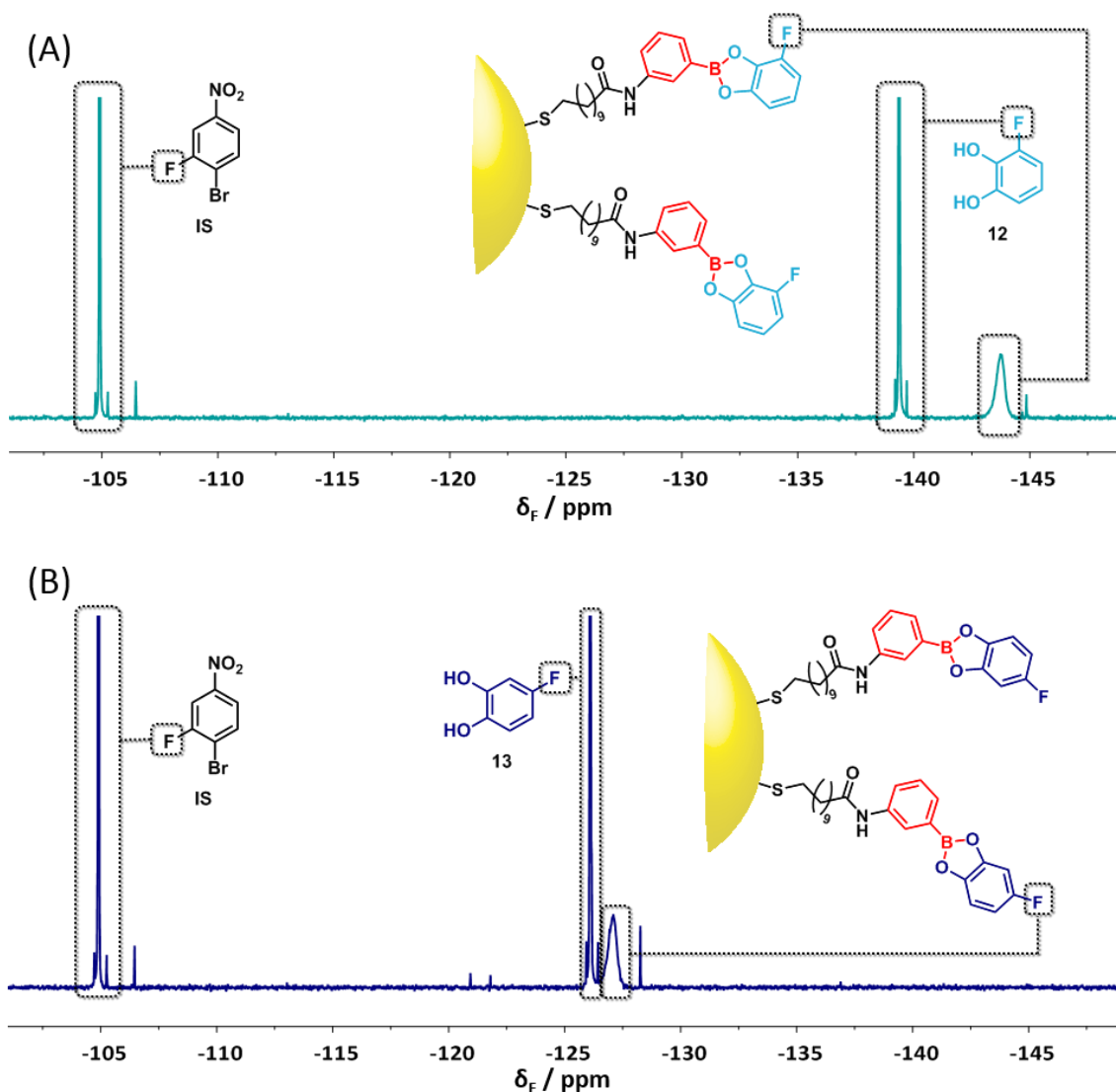


**Figure 3.11** Partial  $^{19}\text{F}$  NMR spectra ( $\text{CD}_3\text{OD}$ , 470.5 MHz, 295 K) of nanoparticle-bound boronic esters formed with (A) 3-fluorocatechol **12** and (B) 4-fluorocatechol **13**. Distinct resonances for catechol and ester can be seen in both cases. The presence of two distinct resonances indicates that despite the rapid equilibration, the system is in slow exchange on the NMR timescale.

The facile, direct observation of boronic ester formation on nanoparticles by  $^{19}\text{F}$  NMR spectroscopy provides a powerful means for studying the dynamic covalent process. Whereas other reported nanoparticle–molecule conjugation processes often rely only on phenomenological evidence for the conjugation event,<sup>94</sup> here direct evidence of the bond formation is provided, demonstrating the molecular details of the conjugation process with increased confidence.

$T_1$  relaxation times for the two nanoparticle-bound boronic esters were measured using an inversion recovery method. As for the molecular species,

the internal standard remained the species with the longest relaxation time (3.8 s) (**Chapter 7.4.1**). The nanoparticle-bound esters had shorter relaxation times than the molecular models in both cases. Having determined the  $T_1$  values, the correct delay could be applied throughout subsequent NMR spectroscopic analysis in order to ensure quantitative measurements.

### 3.4 Reversible boronic ester formation on nanoparticles

Although initial qualitative experiments confirmed that boronic ester formation was occurring on nanoparticle-bound monolayers, thermodynamic control of the process in such an unusual environment had not yet been demonstrated. Combination of fluorocatechols **12** and **13** with AuNP-**7a** afforded a system of mixed nanoparticle-bound boronic esters through which the thermodynamically controlled equilibrium process was investigated. A solution of AuNP-**7a** (10 mM) and *N,N*-diisopropylethylamine (70 mM) was prepared in the presence of an internal standard. (When referring to nanoparticles, all concentrations reported are in terms of the nanoparticle-bound species.) The solution was divided in half and 15 mM of 3-fluorocatechol **12** was added to one half, and 15 mM of 4-fluorocatechol **13** was added to the other half, leading to formation of the corresponding ester (**Figure 3.12A** and **B**). Subsequent addition of 15 mM of the alternative catechol to each sample created two samples that contained both 3- and 4-fluorocatechol **12** and **13** (**Figure 3.12C**). The concentrations of all species added to both samples were identical, differing only in the order of addition of the two catechols. The resulting NMR spectra from both samples were found to be identical, indicating that the two systems had equilibrated to the same state. The identical product distribution, independent of the order of addition, confirmed the thermodynamic control and reversibility of the nanoparticle-bound boronic ester formation.

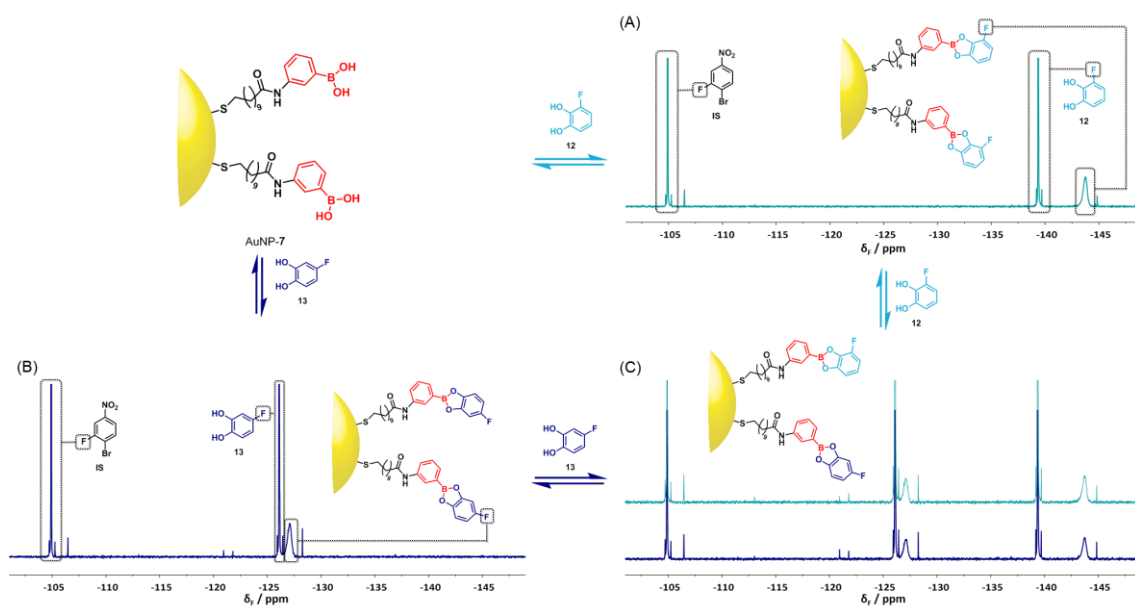


**Figure 3.12** Confirmation of thermodynamically-controlled nanoparticle-bound boronic ester formation. Partial  $^{19}\text{F}$  NMR spectra ( $\text{CD}_3\text{OD}$ , 470.5 MHz, 295 K) indicating boronic ester formation on (A) addition of 3-fluorocatechol **12** to AuNP-7a or (B) addition of 4-fluorocatechol **13** to AuNP-7a. (C) Addition of the alternative catechol to reach identical component concentrations in each sample yielded identical mixtures of nanoparticle-bound boronic esters, irrespective of the route taken. Final component concentrations: AuNP-7a<sub>0</sub> 10 mM, 3-fluorocatechol<sub>0</sub> **12** 15 mM and 4-fluorocatechol<sub>0</sub> **13** 15 mM.

Further confirmation of the reversibility of the system was provided by alternative addition of increasing amounts of 3-fluorocatechol **12** and 4-fluorocatechol **13** to a sample containing AuNP-7a (5 mM), and *N,N*-diisopropylethylamine (70 mM) in the presence of an internal standard (5 mM).  $^{19}\text{F}$  NMR spectroscopy again allowed the equilibrium product distribution to be monitored. The effect of the molar ratio of total 3-fluorocatechol **12** to 4-fluorocatechol **13** was observed by  $^{19}\text{F}$  NMR to affect the ratio of the nanoparticle-bound ester. Each catechol was alternately added until the final total concentration of catechol was 1 M, with the molar ratio changing after each addition to favour either catechol (**Figure 3.13**). The broad peaks arising from nanoparticle-bound boronate ester species seen in the spectra in **Figure 3.13** appear to have a slightly unusual shape, and it is perhaps possible to say that they are almost doublets. However, it is likely that this phenomenon has arisen as an artefact in this particular experiment, as it is not seen in any other spectra of nanoparticle-bound boronate esters (for example **Figure 3.12**).

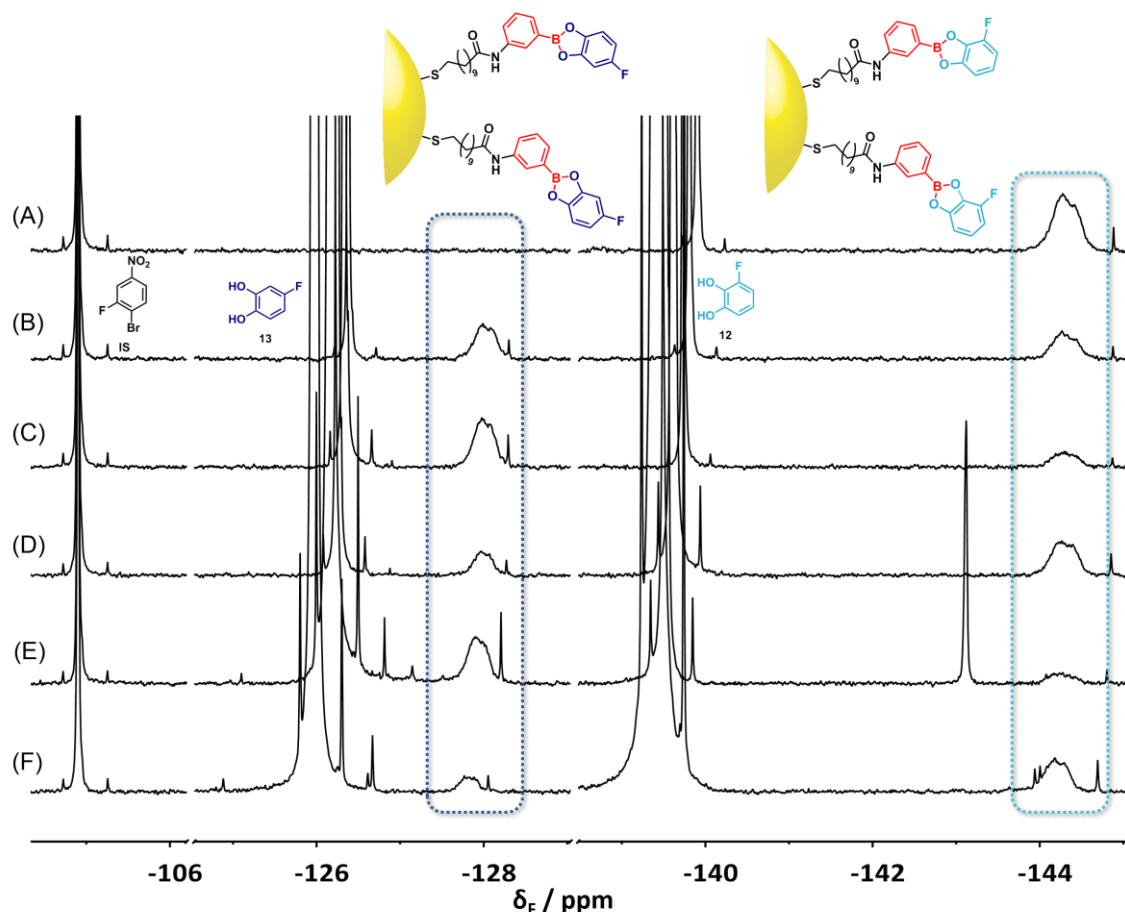


**Figure 3.13** Partial  $^{19}\text{F}$  NMR spectra ( $\text{CD}_3\text{OD}$ , 470.5 MHz, 295 K) of a sample containing nanoparticle-bound boronic acid ( $\approx 5$  mM) and *N,N*-diisopropylethylamine (70 mM). 3-Fluorocatechol **12** and 4-fluorocatechol **13** were increasingly added to the sample as follows: **(A)** 3-fluoro **12** (17.1 mM), 4-fluoro **13** (0.00 mM), **(B)** 3-fluoro **12** (17.1 mM), 4-fluoro **13** (15.6 mM), **(C)** 3-fluoro **12** (17.1 mM), 4-fluoro **13** (38.6 mM), **(D)** 3-fluoro **12** (82.3 mM), 4-fluoro **13** (38.6 mM), **(E)** 3-fluoro **12** (82.3 mM), 4-fluoro **13** (259 mM), **(F)** 3-fluoro **12** (736 mM), 4-fluoro **13** (259 mM). The small sharp peaks downfield of the nanoparticle peak correspond to a small amount of unbound ligand that dissociated over time. In all experiments this amounted to  $< 1\%$ . The sharp peak at  $-143$  ppm in spectrum **(E)** is due to an impurity/decomposition product of the catechol.

The molar ratio of the catechols is reflected in the relative concentrations of each ester. The resulting concentrations of each nanoparticle-bound ester were measured by integration relative to an internal standard. While the total concentration of catechol increased, the total ester concentration remained constant (as nanoparticle concentration remained constant). The lack of change in ester concentration indicated that all available boronic acids were bound after the first addition of catechol (3 eq.). Plotting the molar excess of the catechol

and the molar excess of the ester reveals that the equilibrium position is reflected in the resulting ester ratio.

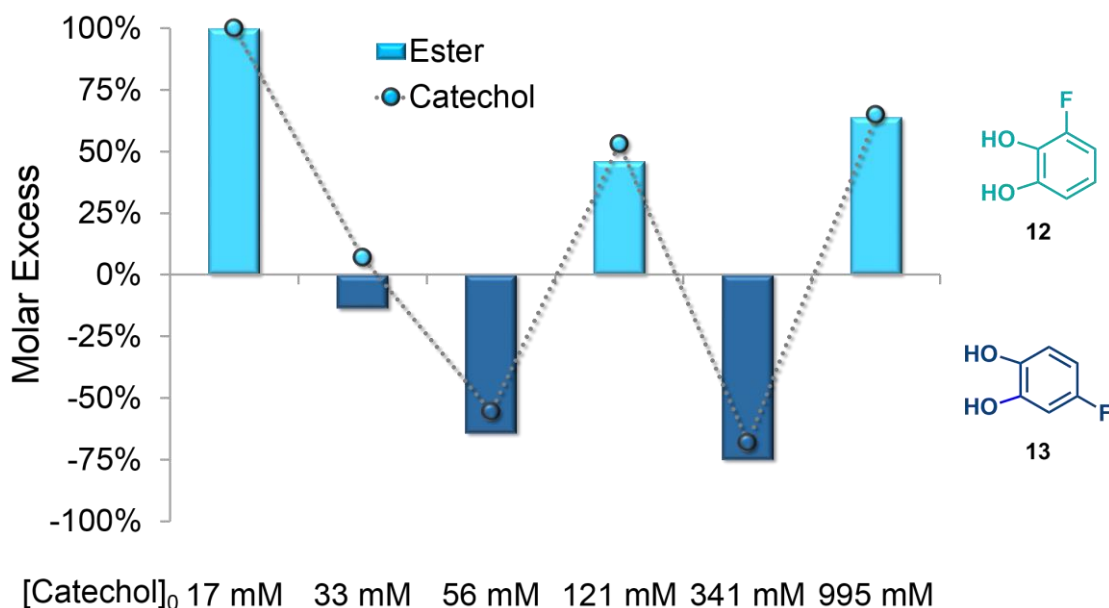


**Figure 3.14** Graph showing the molar excess of total catechol added (dots) and the molar excess of nanoparticle-bound ester observed (bars). Data in the top half of the graph (light blue) reflects an excess of 3-fluorocatechol **12** and its corresponding nanoparticle-bound ester, and the lower half of the graph (dark blue) represents an excess of 4-fluorocatechol **13** and its corresponding nanoparticle-bound ester. While the total concentration of catechol increased, the total concentration of ester remained constant. (Conditions are the same as for **Figure 3.13**).

Closer inspection of the data revealed that the molar excess of ester always lies slightly more towards the 4-fluoro ester than the molar excess of catechol. This suggests that 4-fluorocatechol **13** binds more strongly to nanoparticle-bound boronic acids than 3-fluorocatechol **12**, as is seen with molecular model boronic acid **10**.

### 3.5 Quantifying boronic ester formation on nanoparticles

The binding constants of molecular species (fluorocatechols **12** and **13**, and fluorosalicylic acid **14** with nanoparticle-bound boronic acids could be determined by  $^{19}\text{F}$  NMR spectroscopy. In a typical experiment to determine

association constants, a mixture of AuNP-**7b** with binding partner ( $[\text{AuNP-7b}] = [\text{binding partner}] \approx 5 \text{ mM}$ ) and internal standard (3-fluoro-4-bromonitrobenzene) was suspended in  $\text{CD}_3\text{OD}$ . Addition of 100 eq. *N*-methylmorpholine led to boronate ester formation, which was observed by  $^{19}\text{F}$  NMR spectroscopy. The equilibrium concentration of boronate ester and unbound binding partner was measured relative to the internal standard, and the equilibrium concentrations of boronic acid and unbound binding partner were determined from this measurement.

**Table 3.2** Summary of association constants ( $K_a$ ) determined for interaction of binding partners **12**, **13** and **14** with nanoparticle-bound boronic acid AuNP-**7b** and model boronic acid **10** in  $\text{CD}_3\text{OD}$  with 100 eq. of *N*-methylmorpholine. Errors quoted are the standard deviation of three repeats.

Binding partner	AuNP- <b>7b</b> $K_a / \text{M}^{-1}$	Model boronic acid <b>10</b> $K_a / \text{M}^{-1}$ <sup>a</sup>
3-Fluorocatechol <b>12</b>	1260 ± 130 (10%)	1990 ± 200 (10%)
4-Fluorocatechol <b>13</b>	610 ± 40 (7%)	3420 ± 720 (21%)
4-Fluorosalicylic acid <b>14</b>	400 ± 60 (15%)	2500 ± 310 (12%)

<sup>a</sup> Values reproduced from **Table 3.1**.

Two key observations can be made from these results. First, the association constants for binding with nanoparticle-bound boronic acids are lower than with model boronic acid **10** (although in the case of 3-fluorocatechol **12** the difference is relatively small). Secondly, the relative order of binding affinities for the two fluorocatechol regioisomers is swapped for the nanoparticle-bound case: 4-fluorocatechol **13** binds less strongly than 3-fluorocatechol **12**. This is in opposition to the observed trends in the reversibility/cyclability experiment (**Chapter 3.4**), where 3-fluorocatechol **12** binds less strongly to nanoparticle-bound boronic acids than 4-fluorocatechol **13**. It must be noted that the absolute values should be viewed cautiously, due to the inherent difficulty of quantifying the concentration of nanoparticle-bound species. Peak areas determined by

integrating the broad nanoparticle-bound species can vary significantly depending on phasing of the spectra and the degree of baseline correction. This variation is reduced as the peak intensity increases. Attempts to measure association constants with early batches of AuNP-7, where a high percentage of the boronic acid had oxidised to the corresponding phenol (**Chapter 2.5**), did not yield reproducible results. Nonetheless, utilising less oxidised AuNP-7b (**Chapter 2.5**) allowed use of higher boronic acid concentrations, and gave more reproducible results. The results strongly indicate that binding is significantly weaker with nanoparticle-bound boronic acids than with the model boronic acid.

This difference could be due to limitations in the accessibility of the nanoparticle-bound boronic acids. The boronic acids form a tightly packed monolayer on the nanoparticle surface. In order to bind the binding partner, each boronic acid also requires coordination of a Lewis base, in this case *N*-methylmorpholine. The steric implications of trying to attach a binding partner and base at all sites may simply be too demanding, and only a certain percentage of the available boronic acids may be bound (**Figure 3.15**).

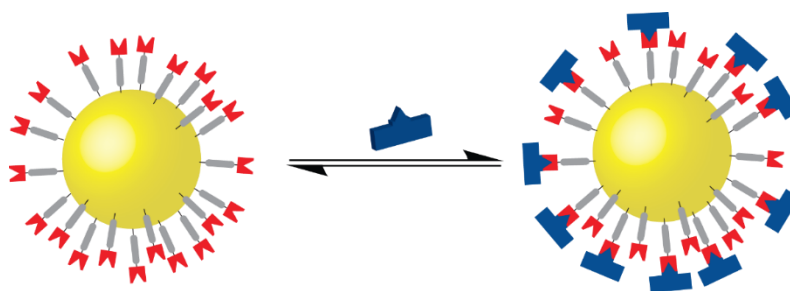


**Figure 3.15** Schematic representation of the equilibrium binding of an exchangeable unit to a nanoparticle. The steric bulk of the exchangeable unit makes complete binding of all boronic acids impossible. Binding saturation, therefore, is defined as binding of all accessible boronic acids, as opposed to all boronic acids.

Experiments were carried out in order to determine the total boronic ester concentration upon saturation of the nanoparticle with approximately 10 eq. of each binding partner. Preliminary titration curves (**Chapter 7.4.3, Figure 7.13**) indicated that this was sufficient to achieve saturation of available boronic acids.

The boronic ester concentration was once again determined by  $^{19}\text{F}$  NMR relative to an internal standard. The results (**Table 3.3**) indicate that for 4-fluorocatechol **13** and 4-fluorosalisyllic acid **14**, the binding partner formed boronic esters with approximately 65% of the total nanoparticle-bound boronic acids. For 3-fluorocatechol **12** this value was significantly higher, at 85%. The results show that even for these small binding partners, not all nanoparticle-bound boronic acids are accessible. This indicates a negative cooperative binding effect: the concentration of boronic ester increases, the subsequent association constants are effectively decreased (to zero once saturation binding is reached). As the single-point binding constants were measured under conditions near-saturation binding, this effective decrease in association constant is significantly reflected in the observed  $K_a$  value.

**Table 3.3** Summary of the percentage of boronic esters formed with nanoparticle-boronic acid AuNP-7b at saturation with binding partners **12**, **13** and **14**.

Binding partner	Percentage of accessible boronic acids
3-Fluorocatechol <b>12</b>	85%
4-Fluorocatechol <b>13</b>	65%
4-Fluorosalisyllic acid <b>14</b>	64%

At concentrations significantly lower than the saturation boronic ester concentrations, the observed  $K_a$  value may more closely match that observed with model boronic acid **10**. The inherently broad, weak spectra obtained from NMR spectra of nanoparticle-bound species make obtaining reliable data challenging at low nanoparticle concentrations; however, having now optimised access to high quality nanoparticle samples (**Chapter 2.5**) this could be revisited. Other techniques, such as isothermal titration calorimetry or titration and fitting to a Langmuir-type binding isotherm that has a packing coefficient as a fitting parameter may provide further details of this phenomenon.

This difference between the accessibility of boronic acids with 3-fluorocatechol **12** and 4-fluorocatechol **13** is striking, and hard to rationalise, as structurally the two compounds are of very similar size and shape. However, the difference does explain why a reversal in the  $K_a$  values is seen, with the lower accessibility of 4-fluorocatechol **13** over 3-fluorocatechol **12** resulting in a greater decrease in the apparent association constants relative to the model compound.

While the observed association constants may be rationalised in terms of the number of accessible boronic acids, the preference for binding 4-fluorocatechol **13** over 3-fluorocatechol **12** in the reversibility/cyclability experiment (**Chapter 3.4**) cannot be explained by this simple model. However, as the parameters affecting the number of accessible boronic acids are not understood even for a single binding catechol, it is possible that for in a mixed system the accessibility is affected differently for both catechols, therefore the product distribution reflects the individual binding events, as in the model system.

### 3.6 Conclusions and future work

Reversible boronic ester formation provides the opportunity for rapid, stimuli-responsive tuning of nanoparticle properties. Base-driven boronic ester formation in protic media has been investigated by  $^{19}\text{F}$  NMR spectroscopy with a range of fluorinated binding partners with model boronic acid **10**. Salicylic acid **14** and its derivatives were explored as a class of structurally similar binding partners, with significantly different binding affinities.

Boronic ester formation was demonstrated on nanoparticle-bound boronic acid AuNP-7.  $^{19}\text{F}$  NMR spectroscopy allowed direct observation of the boronic ester formation. In a system containing two binding partners, fluorocatechols **12** and **13**, boronic esters formed with both catechols was directly observed by  $^{19}\text{F}$  NMR spectroscopy. The equilibrium product distribution was shown to be independent of the order of addition, indicating thermodynamic control over

boronic ester formation on nanoparticle monolayers. The reversibility and cyclability of the process was further demonstrated through changing the molar excess of fluorocatechols **12** and **13**, which resulted in a change in the molar excess of the corresponding ester. Closer inspection of the data suggested that 3-fluorocatechol **12** binds to the nanoparticles more strongly than 4-fluorocatechol **13**, contrary to the association constants for the binding to model compound **10**.

Despite the broad resonances associated with nanoparticle-bound species,  $^{19}\text{F}$  NMR spectroscopy could be used quantitatively to determine association constants for binding partners with AuNP-**7b**. The association constants were lower for all of the binding partners with AuNP-**7b** than with model boronic acid **10**. The association constants also confirmed that 3-fluorocatechol **12** bound more strongly to AuNP-**7b** than 4-fluorocatechol **13**, a reversal of the trend seen for binding with model boronic acid **10**. This surprising result indicates a significant difference between binding to a nanoparticle-bound monolayer and to a free molecule in solution. A factor contributing to this difference was identified in the number of accessible boronic acids. A negative cooperative binding effect upon nanoparticle-bound boronic ester formation means that, as the concentration of boronic ester increases, the subsequent association constants are effectively decreased (to zero once saturation binding is reached). This effect was more pronounced for 4-fluorocatechol **13** than 3-fluorocatechol **12**, where fewer boronic esters could be formed. That such a small structural change results in a reversal of binding affinity between of the two catechols is quite unexpected, and has substantial implications, not only for boronic ester formation on nanoparticle monolayers, but for monolayer reactivity in general.

Boronic ester formation has been demonstrated as a dynamic covalent process suitable for the reversible post-synthetic functionalisation of nanoparticles. Boronic ester formation is apparently weaker on nanoparticle-bound boronic acids than model boronic acids in solution, an effect which can be at least partially explained by the steric limitations in the number of accessible boronic acids. However, substantial further investigation is necessary to fully

understand the implications of nanoparticle-monolayer confinement on boronic ester formation, with a view to the rational design of nanoscale systems.

# Chapter 4:

## Boronic ester-mediated nanoparticle assembly

This chapter seeks to apply dynamic covalent boronic ester formation to the assembly of boronic acid-coated nanoparticles. A bis-catechol linker molecule, capable of bridging boronic acid-coated nanoparticles through boronic ester formation, is synthesised and combined with boronic acid-coated nanoparticles at a range of concentrations. Nanoparticles precipitation is observed after mixing the nanoparticles and the linker and the resultant aggregates are visualised by transmission electron microscopy (TEM). A range of different morphologies is observed depending on nanoparticle-to-linker ratio, providing the first indications of molecular influence on assembly morphology in dynamic covalent systems. Control experiments ruled out a non-specific interaction between the linker and the nanoparticles. Although the assemblies precipitate, and are thus kinetically trapped, the nanoparticles are linked through dynamic covalent boronic esters, and this is exploited for the disassembly of the aggregates by addition of a competing catechol. Full disassembly is observed.

The assembly morphology is quantified through a fractal parameter, revealing a minimum fractal dimension of the observed morphology at intermediate linker concentrations. The observed morphologies are rationalised in terms of diffusion limited or reaction limited particle aggregation kinetics. Chemical changes in the linker structure demonstrate the link between molecular input and assembly morphology further, demonstrating in turn, for the first time, molecular control over dynamic covalently-linked nanoparticle assemblies.

## 4.1 Introduction

The vision of a bottom–up approach to sophisticated nanodevices laid out by Richard Feynman in his seminal 1956 lecture “There’s Plenty of Room at the Bottom” has provided an inspiration for much research in the field of nanoscience. The past twenty years have seen an explosion in research in nanotechnology, with ever more sophisticated chemistry offering easier access to and better control of nanomaterials, and technology improvements allowing for better characterisation and understanding of these materials. The unique properties of nanoparticles have suggested numerous optical, medical and electronic applications,<sup>1,2</sup> to name but a few. However, ever more sophisticated applications will require excellent control over how nanoparticles are assembled and linked to other components.

Sophisticated macroscopic machines are made up of many components, or building blocks. For example, a car is made up of numerous components, which are assembled to produce a car. Of course, it is not simply a case of sticking the components together to create the car, but the relative orientation of the components is also crucial to determining the assembly properties – a car will not work if the wheels are on the roof. Likewise, at the molecular level, where atoms may be considered as building blocks, the relative orientation of building blocks is again crucial to determining the assembly (molecular) properties. When considering nanoscale building blocks, such as gold nanoparticles, the same is true. A general strategy for controlling nanoparticle assembly structure, and therefore the emergent properties, irrespective of the underlying nanoparticle material, size or shape, is highly desirable.

It is not only the nature of the building blocks, for example shape and size, but also the relative orientation of particles that will determine many emergent properties. In the macroscopic case of building machines, such as a car, components can be mechanically directed into the desired assembly. With atoms, the well-understood rules of chemical reactivity can be employed to precisely generate sophisticated structures. However, as structural size and complexity increases, the limitations of this approach become apparent,

providing one of the central motivations for the development of supramolecular self-assembly strategies. While STM<sup>201</sup> and AFM<sup>202,203</sup> techniques may be used to manipulate the position of a single nanoparticle on a surface, such mechanical assembly is not yet a practical assembly technique. Ultimately, control over nanoparticles and nanoparticle assembly in a bottom-up sense must come from exploiting supramolecular chemistry concepts. Chemical control over nanoparticles allowing for their precise assembly and interaction with other components will provide ready access to sophisticated structures, expanding the applications of nanotechnology to materials, machines and devices comprising of multiple nanoparticle components.

Assembling multiple nanoparticle components with control over all structural aspects is the long-term goal of research into nanoparticle assembly. However, before the sophistication of multiple component assemblies is realised, assembling just one nanoparticle component leads to new emergent properties (for example, plasmonic or electronic behaviour for metal nanoparticle materials), which can critically depend on the packing arrangement/assembly morphology.<sup>204–207</sup> This type of simpler level of control is the immediate challenge which will be explored in this chapter.

Nanoparticles have been assembled by the formation of covalent bonds between ligands on the surface of two types of nanoparticles. Such assemblies generally use structurally simple molecules to form covalently-linked networks<sup>94</sup> or discrete<sup>90</sup> assemblies (**Chapter 1.6.1**). Stable, covalently-linked assemblies are formed under kinetic control. All-covalent nanoparticle assemblies have so far failed to match the level of sophistication achieved by noncovalent assemblies. In the ultimate expression of this approach, oligonucleotide-functionalised nanoparticles have been assembled under fully thermodynamic control to produce crystalline nanoparticle arrays with molecular control over crystal lattice structure (**Chapter 1.6.2**). However, noncovalent assemblies frequently rely on biological molecules, such as DNA, which are difficult to work with and stable only under a narrow range of conditions. Alternatively, noncovalent approaches may rely on complex nonbiomolecular host-guest architectures, which are often synthetically difficult to access and yet still mostly

fail to match the capabilities of the DNA-based approach. Dynamic covalent chemistry combines the stability of all-covalent approaches with the reversibility offered by noncovalent systems, yet using relatively simple, well-defined and readily variable nonbiomolecular structures.

The molecular synthetic simplicity and structural diversity offered by dynamic covalent chemistry allows for the potential to finely tune the molecular design of the system, potentially providing a means of affecting the assembly structure. Molecular design has been shown to affect assembly structure in both kinetically controlled all-covalent and thermodynamically controlled noncovalent systems. Most simply, covalent techniques have achieved control over inter-particle distance using bis-thiol linkers<sup>90</sup> of differing length. However, covalent approaches have had limited success in rationally controlling assembly structure.<sup>94</sup> The molecular design of noncovalent approaches has been shown to control assembly structure, for example inter-particle distance.<sup>208–210</sup> Most notably, oligonucleotide-based crystalline nanoparticle assemblies can be formed as either fcc or bcc crystal lattices depending on the design of the oligonucleotide linker<sup>72</sup> (**Chapter 1.6.2**). It is therefore reasonable to investigate the potential for molecular control over nanoparticle assembly in dynamic covalent systems.

The reversibility of dynamic covalent chemistry also offers the opportunity for creating dynamically reconfigurable assemblies, where nanoparticles can be assembled and disassembled, and allow for assembly of the same nanoparticle building blocks into different assembly structures. Reversible nanoparticle assembly has been demonstrated with a number of noncovalent systems. Oligonucleotide-linked assembly has shown reversibility and cyclability of nanoparticle assembly.<sup>103</sup> Likewise, reversibility has been demonstrated using some synthetic host–guest systems.<sup>102</sup> In a small number of exceptional examples, reconfiguration of nanoparticle assemblies has also been demonstrated. Oligonucleotide-directed crystalline assemblies are initially assembled as amorphous assemblies, before annealing reconfigures the assembly to the crystalline lattice structure.<sup>103,211</sup> Oligonucleotide-linked

assemblies have also been reconfigured between crystalline states by addition of a molecular (oligonucleotide) stimulus.<sup>125</sup>

Dynamic covalent structures offer the opportunity for detailed synthetic control over molecular structure of covalent nanoparticle assemblies. The reversible nature of dynamic covalent bonds derived from their thermodynamic control presents the opportunity for error correcting, stimuli-responsive reversible and even reconfigurable nanoparticle assembly systems. Furthermore, changes in the molecular structure may result in structural changes of the assembly morphology, ultimately offering the potential for predictable molecular control of nanoparticle assembly.

## 4.2 Design of boronic ester-mediated nanoparticle assembly

Boronic ester-mediated assemblies are perhaps most commonly associated with covalent organic frameworks.<sup>138–141</sup> Trigonal boronic ester linkages between catechols and boronic acids are employed for the self-assembly of extended, highly ordered organic structures under thermodynamic control. As discussed in **Chapter 2.5**, the solubility of boronic acid-coated AuNP-7a (**Figure 4.1**) is limited to protic solvents, under which conditions boronic ester species exist mostly in their tetrahedral boronate ester form. It was proposed that boronic acid-coated nanoparticles could be assembled by combination of boronic acid-coated nanoparticles with a ditopic molecular linker (**Figure 4.2A**). An alternative approach would be to functionalise a second nanoparticle with catechols or other complementary functionality (**Figure 4.2B**).

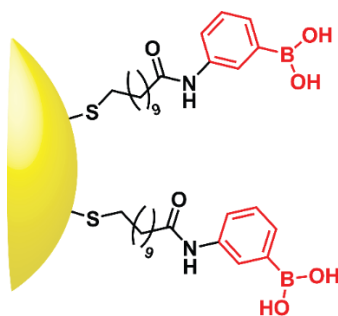


**Figure 4.1** Boronic acid-functionalised gold nanoparticles (AuNP-7).

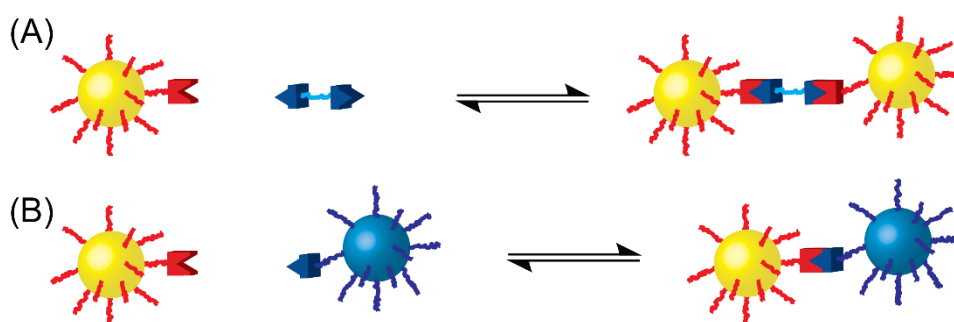


**Figure 4.2** Schematic representation of alternative approaches to the assembly of dynamic covalent nanoparticles. (A) Assembly with a ditopic linker. (B) Assembly between complementary nanoparticles. Nanoparticles are fully coated with reactive ligands but, for clarity, only one reactive site per nanoparticle is shown.

Here, investigation of boronic ester-mediated nanoparticle assembly employing a series of ditopic linker molecules is presented (**Figure 4.2A**). Initial investigations focused on linker **18** (**Figure 4.3**). This bis-catechol linker, based on a dopamine molecule, has a number of attractive features. It is structurally simple, readily accessible, relatively small and the two catechol groups are electronically independent of each other.

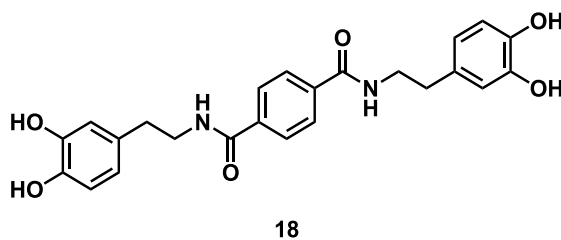


**Figure 4.3** Structure of flexible catechol linker **18**.

### 4.3 Boronic ester-mediated nanoparticle assembly

Suspending AuNP-7a ( $0.1 \text{ mg mL}^{-1}$ ,  $0.036 \text{ mM}$  in terms of boronic acids), in MeOH gives a red translucent colloidal solution. This concentration of nanoparticles is suitable for UV-vis measurements, with a  $\lambda_{\text{max}}$  (SPR) of about  $0.4$ , and UV-vis monitoring has shown that the solution remains stable for longer than one month (see experimental **Chapter 7.5.1**), with visual monitoring indicating this stability extends to over a year. A colloidal solution of AuNP-7a ( $0.1 \text{ mg mL}^{-1}$ ) in MeOH containing *N*-methylmorpholine ( $10 \text{ }\mu\text{L mL}^{-1}$ ,  $105 \text{ mM}$ ) is also stable. As discussed in **Chapter 3**, basic conditions, such as these, can lead to boronate ester formation if a suitable binding partner is present. Addition of a ditopic catechol linker **18**, capable of bridging boronic acid groups on two nanoparticles, led to the gradual appearance of a black nanoparticle precipitate, and an eventual loss of all red colour from solution (**Figure 4.4**). The red colour indicates that the nanoparticles are in solution, and no precipitate is visible. The right vial contains flexible catechol linker **18** ( $0.55 \text{ mM}$ ), the nanoparticles have precipitated from solution.

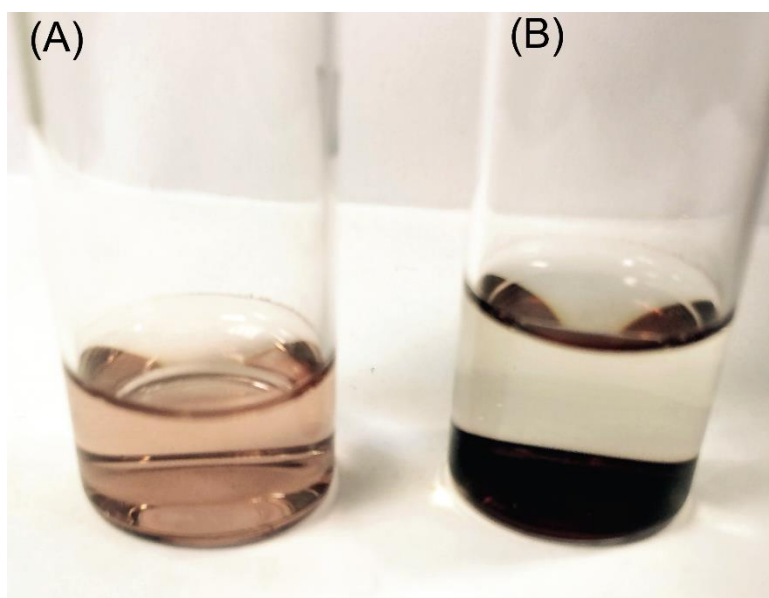


**Figure 4.4** Photograph showing colloidal dispersions of AuNP-7a ( $0.1 \text{ mg mL}^{-1}$ ) in MeOH containing *N*-methylmorpholine ( $1\% \text{ v/v}$ ,  $105 \text{ mM}$ ) after 28 days in the absence (A) and the presence (B) of linker **18** ( $0.55 \text{ mM}$ ).

Unlike many systems exhibiting nanoparticle assembly, this system does not exhibit a shift in the position of the nanoparticle SPR band of the nanoparticles. This is because the nanoparticles are too small and the inter-particle distances are too big to allow plasmonic coupling (**Chapter 7.5.2, Figure 7.15**).<sup>23,212</sup> However, the precipitation upon addition of a ditopic linker under conditions expected to give rise to boronate ester formation supports the hypothesis of boronate ester-linked nanoparticle assembly.

The equilibrium constant for the binding of the catechol group in linker **18** with model boronic ester **10** was measured as 900 M<sup>-1</sup> by NMR spectroscopy (**Chapter 7.4.1, Table 7.6**). This corresponds to a  $K_d$  of approximately 1 mM. Limitations of nanoparticle colloidal solubility and practical considerations of the transmission electron microscopy (TEM) and UV-vis analysis of assembly samples necessitate that low nanoparticle concentrations are used, such that the concentration of boronic acid is much lower than  $K_d$ , so the expectation is that an excess of linker will be required to produce significant quantities of boronic esters.

The concentration of boronic ester can be predicted using the measured  $K_a$  value for any given nanoparticle and linker stoichiometry using **Equation 4.1**; however, this is only a rough approximation. The  $K_a$  values for model compound have been shown to be significantly lower on nanoparticle-bound boronic acids than with molecular model compound (**Chapter 3.5**). This effect is, at least in part, due to a negative cooperativity upon binding due to steric crowding, so might be expected to be more pronounced for linker **18** than for the smaller catechols employed in **Chapter 3**.

$$[HG] = \frac{\frac{[H]_0[G]_{0+1}}{K_a} - \sqrt{\left(\frac{[H]_0[G]_{0+1}}{K_a}\right)^2 - 4[H]_0[G]_0}}{2}$$

Equation 4.1

An instructive parameter is the proportion of available nanoparticle-bound boronic acids that are converted to boronic esters, which we express here as the parameter %binding. %Binding is defined here as bound host (i.e.  $[HG]$ )/total host ( $[H]_0$ ). A constant concentration of nanoparticles, suitable for UV-vis spectroscopy and TEM analysis was employed. The nanoparticle-bound boronic acid was defined as the host, at a constant concentration of 0.036 mM. The %binding for a range of linker (guest) concentration was subsequently estimated (**Figure 4.5**).

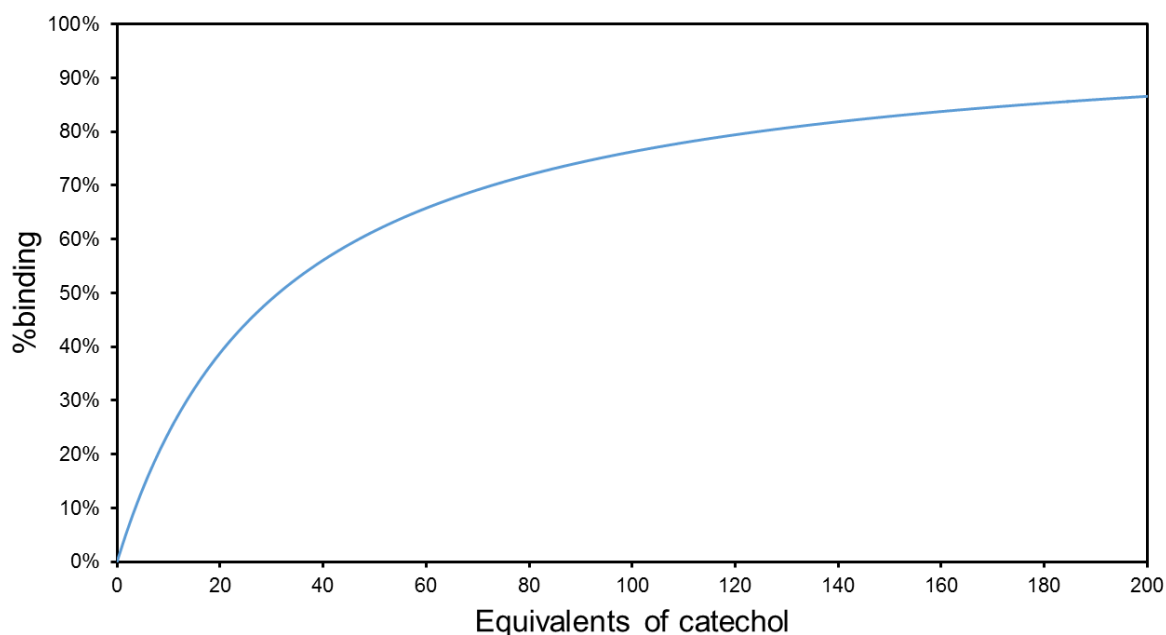


**Figure 4.5** Graph showing the extent of host–guest binding based on a  $K_a$  value of  $900 \text{ M}^{-1}$  as guest concentration increases at a constant host concentration of 0.036 mM. Calculated for a 1:1 binding isotherm (**Equation 4.1**).

A range of linker concentrations from 0.006 mM (0.17 eq.) to 2.99 mM (83 eq.) was chosen, spanning %binding from < 1%–73%. In general, samples with higher linker concentration precipitated faster, in as little as three hours, with samples at lower linker concentrations taking up to three weeks to produce completely colourless supernatants. At very low concentration (< 0.11 mM, 3.1 eq.) no precipitation was observed, even after five weeks of monitoring. Indeed, TEM imaging of the solution at these low linker concentrations did not reveal any sign of nanoparticle assembly (**Figure 4.6A**). The lowest

concentration of linker at which assembly was observed was 0.11 mM (3.1 eq.), which corresponds to 9% binding.

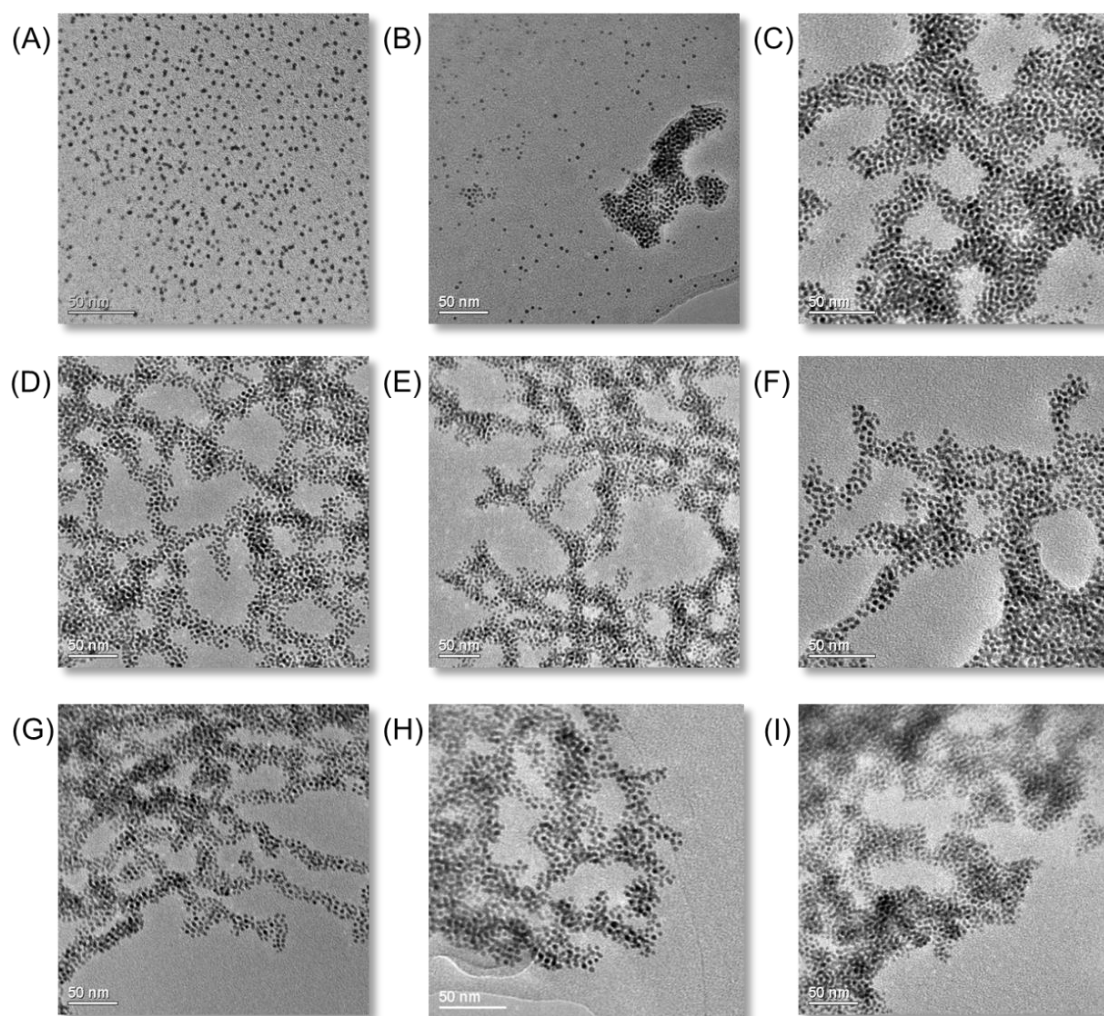


**Figure 4.6** TEM images of nanoparticle assemblies demonstrating the effect of varying linker concentration on assembly morphology. All images were obtained three weeks after mixing. AuNP-7a (0.036 mM in MeOH), *N*-methylmorpholine (105 mM) with linker **18** at (A) 0.006 mM, 0.17 eq. (sample showed no sign of precipitation), (B) 0.11 mM, 3.1 eq. (sample did not fully precipitate), (C) 0.23 mM, 6.4 eq. (sample did not fully precipitate), (D) 0.44 mM, 12.2 eq., (E) 0.55 mM, 15.3 eq., (F) 0.83 mM, 23.1 eq., (G) 1.09 mM, 30.3 eq., (H) 2.08 mM, 57.8 eq., (I) 2.99 mM, 83.1 eq.

**Table 4.1** shows the aggregation times and the predicted total binding, based on the measured  $K_a$  values of  $900 \text{ M}^{-1}$  with a model boronic acid. The assembled samples were visualised by transmission electron microscopy (TEM) (**Figure 4.6**). Varying the extent of binding results in a marked difference change in the morphology of the observed structure. Samples for TEM were prepared by briefly sonicating the precipitated nanoparticles, and immediately

placing a drop of the resulting suspension on a TEM grid, which was dried in air. At low concentrations of linker (3.1 eq., 9% binding) (**Figure 4.6B**), small isolated aggregates can be seen, alongside individual, non-aggregated nanoparticles, while the supernatant solution remained red in colour, indicating that the sample had not fully precipitated. At slightly higher linker concentrations (6.4 eq., 17% binding) (**Figure 4.6C**), extended aggregates are seen; they can be visualised only at the edges of the aggregate, where the nanoparticles lay flat on the TEM grid. The structure of these aggregates is a mixture of dense areas of extended nanoparticle coverage in two dimensions, as well as branch-like, dendritic chains of nanoparticles. These dendritic branches tend to be wide and short. At intermediate linker concentrations (12.2–15.3 eq., corresponding to 28% and 33% binding) (**Figures 4.6D** and **E**, respectively), the branched-dendritic morphology is seen throughout the sample. Interconnected chains, generally 3–4 nanoparticles wide form a relatively sparse net-like assembly. Further increasing the concentration of linker (23.1 eq., 42% binding and 30.3 eq., 49% binding) (**Figures 4.6F** and **G**) leads again to a mixed morphology, similar to 6.4 eq. (**Figure 4.6C**). Areas of dense, extended nanoparticle coverage are combined with a branched-dendritic morphology of narrow chains. Finally, at very high linker concentrations (57.8 eq., 65% binding and 83.1 eq., 73% binding) (**Figures 4.6H** and **I**), a suggestion of branched chains remain but the sample is generally densely assembled into bulky, disordered aggregates.

**Table 4.1** Summary of assembly experiments varying the linker concentration, reporting the time taken for the nanoparticle sample to fully precipitate and the calculated %binding based on an association constant of  $900 \text{ M}^{-1}$ .

Sample	[Nanoparticles] / mM <sup>a</sup>	[Linker] / mM <sup>b</sup>	Linker equivalents	%binding	Time to fully precipitate/days
A	0.036	0.006	0.2	< 1%	—
B	0.036	0.11	3.1	9%	—
C	0.036	0.23	6.4	17%	—
D	0.036	0.44	12.2	28%	7
E	0.036	0.55	15.3	33%	5
F	0.036	0.83	23.1	42%	5
G	0.036	1.09	30.3	49%	4
H	0.036	2.08	57.8	65%	3
I	0.036	2.99	83.1	73%	0.1

<sup>a</sup> In terms of boronic acid ligands

<sup>b</sup> [Catechol] =  $\frac{1}{2}$  [Linker]

The branched-dendritic morphology seen in sample (E), 15.3 eq., 33% binding (Figures 4.6D and 4.7) displayed an unusually high level of order, not commonly seen for covalently assembled nanoparticles. Therefore more detailed investigation was undertaken to analyse these assemblies. Throughout the remainder of this chapter, the conditions employed for these assemblies will be referred to as the standard conditions.

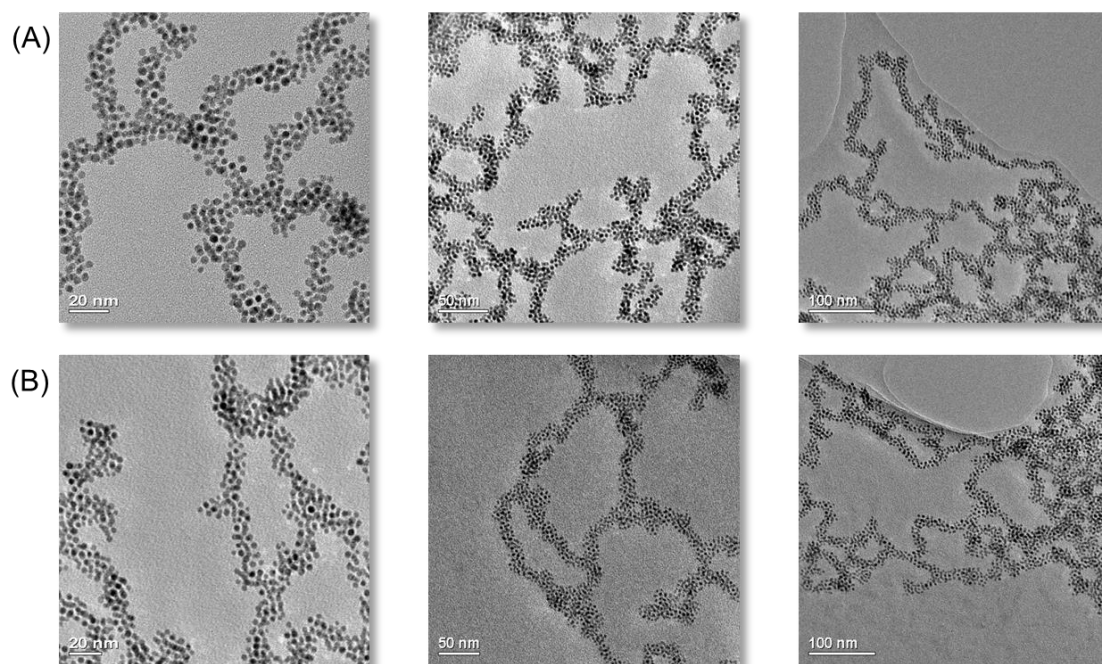


**Figure 4.7** TEM images of aggregates prepared under optimised conditions: AuNP-7a (0.036 mM in terms of boronic acids), linker **18** (0.55 mM, 15.3 eq.) and *N*-methylmorpholine (105 mM, 2692 eq.) in methanol. TEM images were obtained from two independently assembled batches (**A**) and (**B**), and show areas of the grid where the chains of nanoparticles can be seen to lie flat on the grid in a single layer, allowing structure visualisation, which reveals a branched-dendritic, net-like assembly.

TEM images from several independently assembled samples revealed that the branched-dendritic morphology was obtained reproducibly (**Figure 4.7**). This assembly structure is most clearly visible at the edges of large aggregates, where the assembled nanoparticles lie flat in a single layer. TEM images of the precipitated nanoparticles away from the edges of the large aggregates reveal that the net-like structure continues throughout the aggregate, although it is harder to visualise this where the nanoparticles lie several layers deep on the grid (**Figure 4.8**).

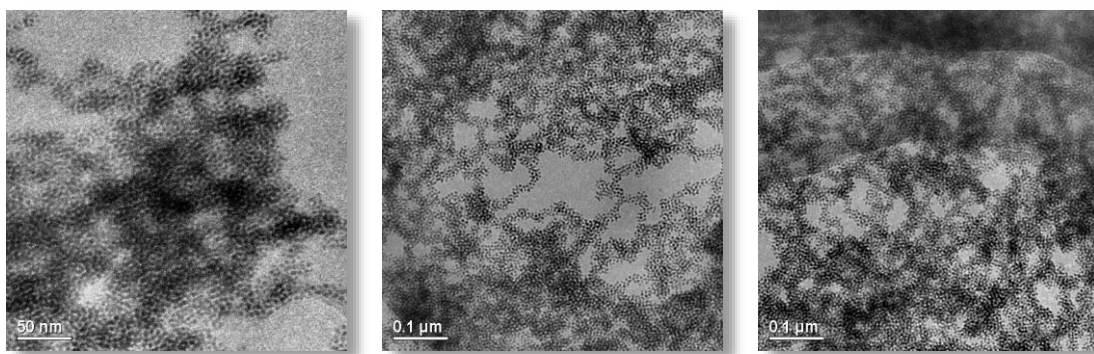


**Figure 4.8** TEM images of aggregates assembled under standard conditions: AuNP-7a (0.036 mM in terms of boronic acids), linker **18** (0.55 mM, 15.3 eq.) and *N*-methylmorpholine (105 mM, 2692 eq.) in methanol. These TEM images show the areas where aggregates several layers deep are deposited. The right-hand picture in particular shows that the same net-like structure (seen at the edge of aggregates in the TEM images in **Figure 4.7**) extends through the entire aggregate.

Scanning electron microscopy (SEM) images provide better visualisation of the denser aggregates, as SEM provides a much greater depth of focus and field of depth than TEM. However, the resolution is too low to see individual nanoparticles. The images again show the branched net-like structure and, interestingly, the larger superstructural features appear to similarly display a branched-dendritic morphology.

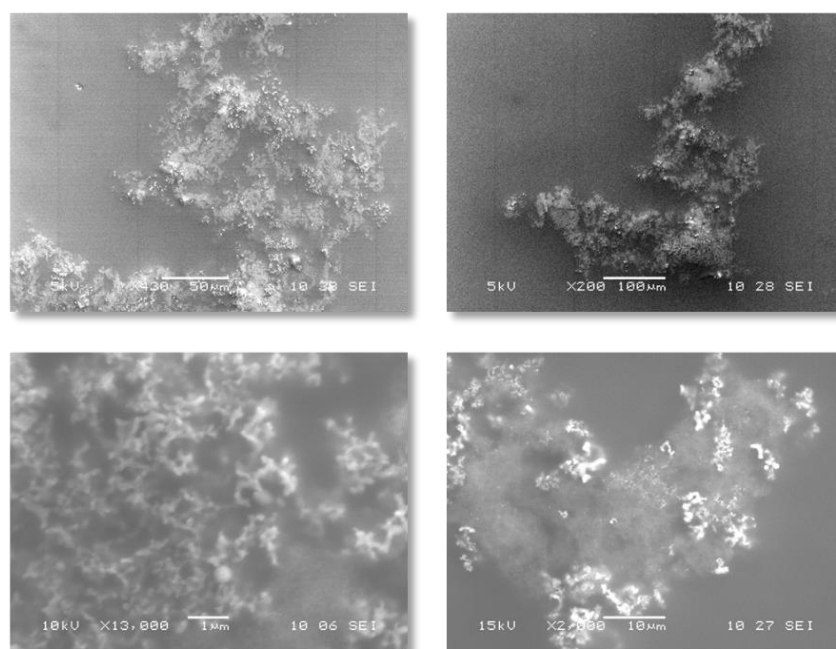


**Figure 4.9** SEM images of aggregates assembled under standard conditions: AuNP-7a (0.036 mM in terms of boronic acids), linker **18** (0.55 mM, 15.3 eq.) and *N*-methylmorpholine (105 mM, 2692 eq.) in methanol.

It is possible to also vary the extent of binding by changing the nanoparticle concentration. However, in practice, the sensitivity and range of UV-vis spectroscopy restricts direct monitoring of aggregation to starting nanoparticle concentrations in the range from 0.018 mM to 0.072 mM (in terms of boronic acid), half and double the nanoparticle concentration used thus far. At these nanoparticle concentrations, the same linker concentration (0.55 mM) was added to induce nanoparticle assembly. There is no noticeable change in the observed morphology (**Figure 4.10**).

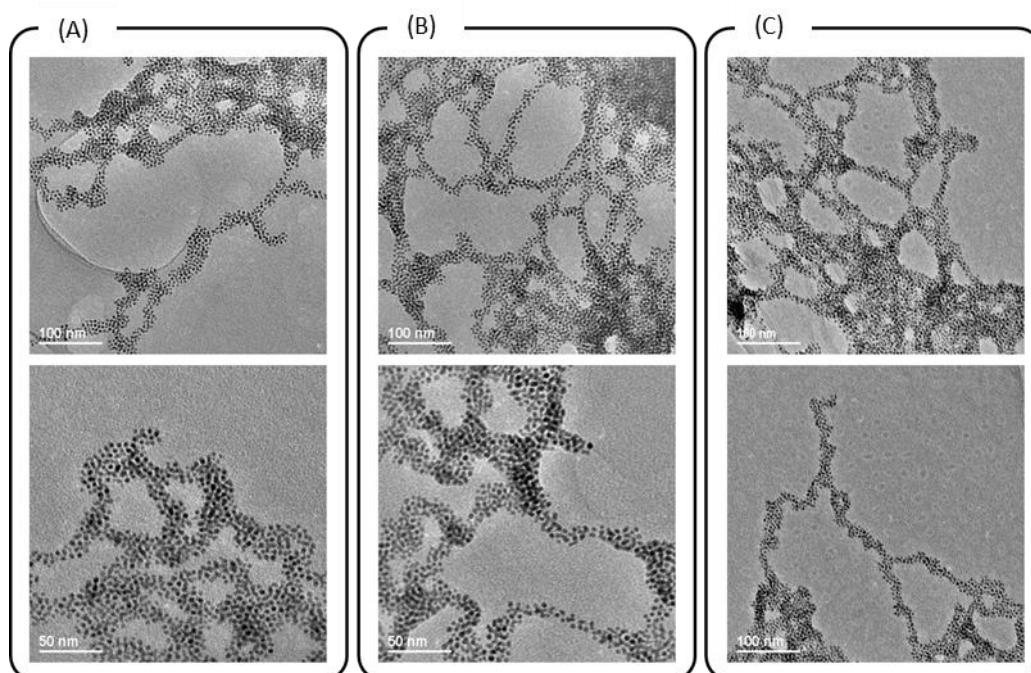


**Figure 4.10** TEM images of nanoparticle aggregates formed from different initial concentrations of AuNP-7a, maintaining a constant linker concentration. (A) 0.019 mM ( $\frac{1}{2}$  standard concentration), (B) 0.039 mM (standard concentration), (C) 0.078 (2  $\times$  standard concentration). Concentration of *N*-methylmorpholine was kept constant (105 mM, 2692 eq.) in methanol.

The similarity across the observed morphologies is perhaps unsurprising as the %binding based on the estimated  $K_a$  value of  $900 \text{ M}^{-1}$  remains unchanged at 33%. The fact that varying %binding as a function of linker concentration affects the observed assembly morphology is strongly suggestive that dynamic covalent boronic ester formation is involved in the assembly. Studies presented in **Chapter 3** confirm that boronic ester formation with monotopic binding partners does occur on nanoparticles under basic conditions, while the colloidal stability of AuNP-7b has already been verified in methanol containing *N*-

methylmorpholine, ruling out the possibility of the assembly resulting merely from precipitation due to a loss of colloidal stability over time.

It was necessary to also rule out non-specific binding between the linker and the nanoparticles. Methyl ether-coated AuNP-**8** (**Chapter 2**) was subjected to the same assembly conditions as AuNP-**7a**. AuNP-**8** was selected as a nanoparticle sample of similar size to AuNP-**7a** ( $\approx 3$  nm), and coated with a structurally similar ligand, minimising differences based on ligand packing or intra-monolayer interactions, such as hydrogen bonding through the amide. No evidence of precipitation could be detected by eye even after several weeks. After two weeks, the sample was visualised by TEM microscopy and no presence of aggregates could be seen (**Figure 4.11**).

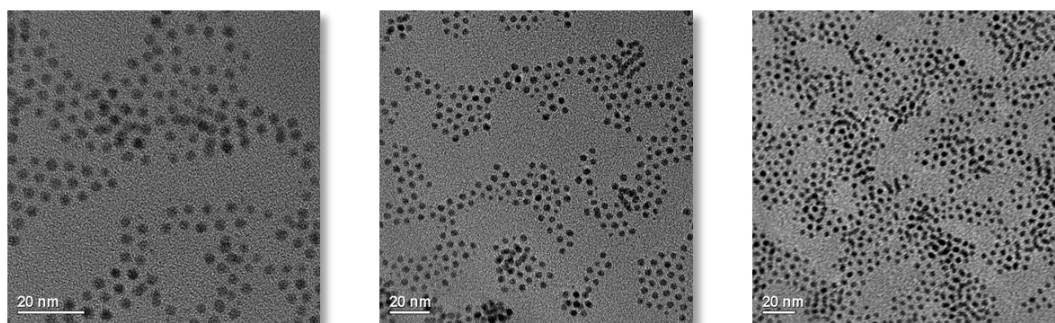


**Figure 4.11** TEM images of a control assembly experiment, combining AuNP-**8** ( $0.1 \text{ mg mL}^{-1}$ ), linker **18** ( $0.55 \text{ mM}$ ,  $15.3 \text{ eq.}$ ) and *N*-methylmorpholine ( $105 \text{ mM}$ ,  $2692 \text{ eq.}$ ) in methanol.

#### 4.4 Reversible boronic ester-mediated nanoparticle assembly: Disassembly

Although the precipitation of boronic ester-linked assemblies is an irreversible process, as demonstrated in **Chapter 3.4**, boronic ester formation on AuNP-**7a** is reversible. The reversible nature of the dynamic covalent boronic ester linkages can be exploited by providing an appropriate change in conditions or stimulus in order to disassemble the aggregates. Addition of a competing binding unit, such as 1,2-dihydroxybenzene should out-compete the linker,

leading to disassembly. To a sample of nanoparticle assemblies, aggregated under the optimum conditions with flexible linker **18**, a large excess of 1,2-dihydroxybenzene (250 eq. relative to linker molecules) was added. As the assembled nanoparticle structure was fully precipitated, the competitive binding of the 1,2-dihydroxybenzene capping molecule proceeded initially as a heterogeneous process, and was therefore very slow. Frequent agitation of the sample by sonication, eventually (after five weeks) led to a visible re-suspension of all precipitated material. After this initial five-week period, only partial disassembly was observed by TEM, with small spherical aggregates formed. However, after a further week, TEM images revealed complete disassembly with only isolated nanoparticles visible in all images (**Figure 4.12**). The disassembly process is very slow. This is likely due to the heterogeneous nature of the process and the non-continuous agitation of the process. Repeating the disassembly experiment with continuous sonication might be expected to speed up the process to a similar timeframe as the assembly.

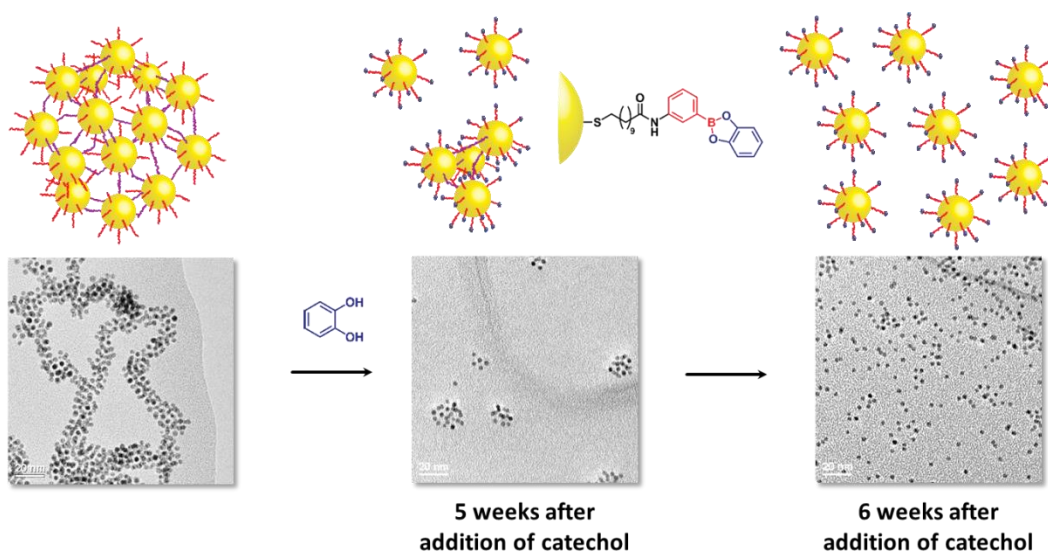


**Figure 4.12** Disassembly of boronic ester-linked nanoparticles by addition of a competing binding unit.

Instead of a competitive catechol binding unit, a competitive boronic acid binding unit might also lead to disassembly. However, on adding phenyl boronic acid (250 eq.) to an aggregated sample, and agitating over a period of six weeks, no disassembly was observed. It is possible that a greater excess of

these competitive binders may be required, as there is significantly more linker than nanoparticle-bound boronic acid present in the aggregated sample.

## 4.5 Mechanism of boronic ester-mediated nanoparticle assembly

The disassembly through addition of a competitive catechol binder provides further strong evidence that the assembly process is driven by dynamic covalent boronic ester formation. The importance of thermodynamic control for nanoparticle assembly has been stressed throughout this thesis so far. However, the assembly processes seen here are not purely thermodynamically controlled. The precipitation is effectively an irreversible process. This, coupled with the timeframe of the assembly, gives some clues as to the mechanistic detail. From NMR experiments in **Chapter 3**, boronic ester formation on AuNP-**7a** was shown to be very rapid, reaching equilibrium within a matter of seconds. However, the timeframe for the formation of the nanoparticle assemblies reported in this chapter occurs over several days. Throughout the assembly process, TEM analysis of the supernatant did not provide any evidence of nanoparticle assemblies in solution. While individual binding events occur quickly, permanently linked assemblies under these conditions occur only when driven by an irreversible precipitation event. A probable explanation of the assembly process involves the formation of small clusters of nanoparticles until eventually, by chance, one of these clusters becomes large enough that it is no longer colloiddially stable, leading to precipitation. Subsequently, the assembly proceeds in a heterogeneous manner, with linker and nanoparticle attachment to the initial nucleation point, akin to molecular crystal growth. It should be noted, however, that direct evidence for the formation of such small aggregates prior to extended nanoparticle assembly has not been observed.

The overall assembly and precipitation process may be monitored by UV-vis spectroscopy, through the decrease in intensity of the SPR band, which is

proportional to the concentration of nanoparticles in solution. Monitoring the change in the extinction at 507 nm ( $\lambda_{\max}$  (SPR) of AuNP-7a) over time gives a kinetic profile of the assembly process (**Figure 4.13**). Under the standard conditions, initially a slight decrease in nanoparticle concentration is seen, but this levels out after 10 hours. This initial decrease corresponds to a drop to  $\approx 95\%$  of the starting absorbance and possibly corresponds to a small population of less stable nanoparticles. The subsequent slight increase in absorbance is attributed to the oxidation of the catechol linker, which slowly occurs under these conditions giving rise to oxidative decomposition products that absorb in the same region of the spectrum as the nanoparticle SPR band.<sup>213</sup> At about 100 hours after addition of the linker, a sudden rapid precipitation of the nanoparticles is observed. This rapid precipitation event takes about 20 hours to complete, slowing as the nanoparticle concentration decreases. At 120 hours, the nanoparticles have fully precipitated, resulting in no further change in the absorbance. The precipitation has been visually observed in a number of samples to occur consistently between four and five days (100–120 hours).

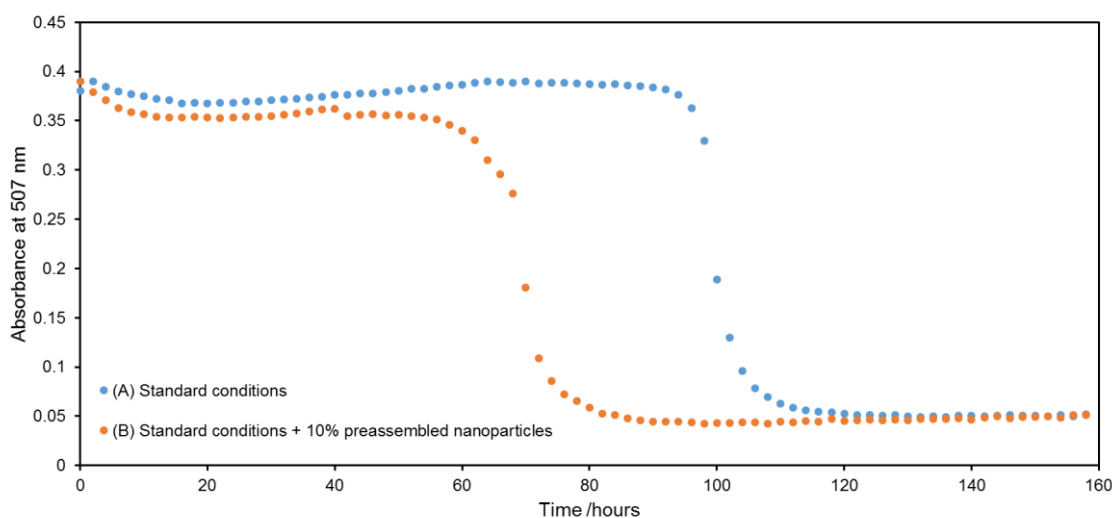


**Figure 4.13** Kinetic profiles for nanoparticle assembly under the (A) standard conditions: AuNP-7a (0.036 mM in terms of boronic acids), linker **18** (0.55 mM, 15.3 eq.) and *N*-methylmorpholine (105 mM, 2692 eq.) in methanol) and (B) standard conditions + 10% pre-assembled nanoparticles.

These kinetic observations fit a hypothesis of an initial slow nucleation event, during which individual nanoparticle–nanoparticle links are rapidly forming and

breaking, followed by a more rapid growth phase, driven by precipitation which slows as the concentration of nanoparticles decreases (**Figure 4.14**). In order to test the hypothesis of a slow initial nucleation event, a small quantity of pre-assembled nanoparticles was added. Addition of 10% of pre-assembled nanoparticles prior to addition of linker causes the rapid growth phase to occur after about 60 hours. This is again consistent with the proposed mechanism, as the pre-assembled nanoparticles act as a pre-formed nucleation point.

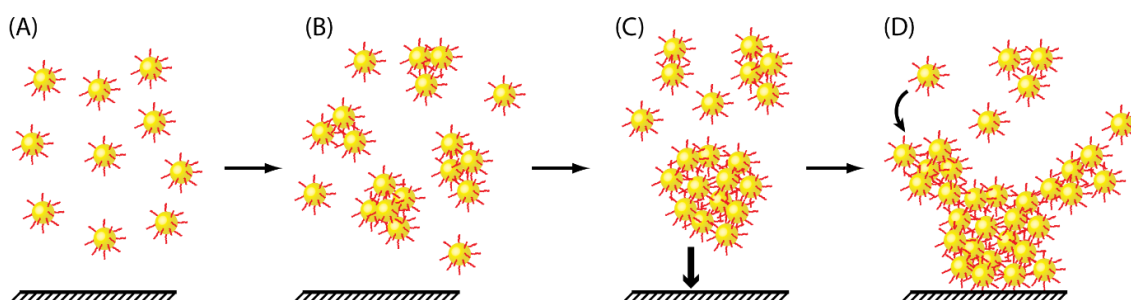


**Figure 4.14** Schematic representation of the assembly mechanism. (A) Boronic acid nanoparticles in solution prior to addition of linker. (B) Linker added and random nucleation of small colloiddally stable clusters. (C) Eventually larger clusters precipitate. (D) Growth on reactive surfaces of precipitates leads to formation of branched-dendritic assemblies.

There are a number of parallels between the assembly process described here and supramolecular polymerisation, where molecules assembly non-covalently to form large molecular assemblies, such as polymers or gels.<sup>212a,212b</sup> There are a number of models that describe the growth of supramolecular polymers. Isodesmic supramolecular polymerisation describes processes where monomers may dimerise or attach to oligomers, by the formation of identical non-covalent bonds.<sup>212a</sup> Factors such as concentration and association strength have been well explored in such systems. With the acquisition of further kinetic data for the boronic-ester mediated assembly of nanoparticles presented here, and a better understanding of the implication of nanoparticle-surface-confinement on dynamic covalent processes, such models and principles from supramolecular polymerisation may be applied to better understanding and developing this dynamic-covalent assembly of nanoparticles.

## 4.6 Analysis and molecular-level control of assembly morphology

While some qualitative morphological differences between samples assembled at different linker concentrations are readily evident, a more rigorous and systematic approach to characterising the assemblies is desirable. Inter-particle distance is a key structural parameter, important for controlling a range of electronic and optical properties in nanoparticle assemblies.<sup>204</sup>

The branched-dendritic nature of some of the assemblies is reminiscent of fractals. It is possible to analyse the deposits as fractals, to extract a numerical value for the dimensionality of the observed aggregate.<sup>214</sup> A fractal dimension describes how a shape of  $N$  dimensions occupies a space of  $N+1$  dimensions. For example, a straight line is a one-dimensional object, as it does not occupy any area. However, if a curved, wiggly line is placed in a two-dimensional space, it will occupy some of that space. This suggests that it can now be categorised as a two-dimensional object. The concept of classical Euclidean dimensions breaks down, as described in different ways, the line seems to be classifiable as both a one-dimensional and a two-dimensional object. Fractal dimensions allow an object to be classified as having any fractal dimension ( $D_f$ ), where  $D_f \geq 0$ , allowing an object's dimension to be any (real) non-negative number. This allows objects to have dimensions which lie in between the classical Euclidean dimensions, for example the squiggly line can be considered as having a dimension somewhere between 1D and 2D (for example, 1.2). The fractal dimension of objects may be determined by image analysis.

Fractal analysis is commonly used to characterise electrochemically deposited metal structures,<sup>215</sup> and more recently has been applied in analysis of nanoparticle deposits.<sup>217–219</sup> Particle deposition is a well-studied phenomenon, widespread in nature. Particle deposition occurs when particles lose their colloidal stability, leading to their deposition and sedimentation or gel formation. The resulting assemblies can be analysed in a number of ways, including small-angle X-ray scattering to provide ensemble information about short-range order

in the sample, or by microscopy sampling methods. A fractal analysis of the resulting 2D microscopy images of the assemblies can provide information about the assembly process. Although generally applied to describe the deposition of larger particles, many of the principles may be applied to nanoparticle assembly. The boronic ester-mediated assembly described here consists of a thermodynamically controlled reaction coupled to an irreversible kinetically controlled precipitation event, such as in particle deposition. Aggregate growth processes, particle deposition or 3D assembly in colloidal suspension can be described by diffusion-limited and reaction-limited models, two idealised models which contribute to varying amounts in the real world. In the case of diffusion-limited aggregation, all particle collisions lead to aggregation, whereas reaction-limited aggregation is limited by the attractive forces between the particles, which means that relatively few particle collisions result in particle assembly. The deposits produced by either of these mechanisms are statistically self-similar, examples of naturally occurring fractals. Under idealised conditions, diffusion-limited assembly gives lower fractal dimensions. This is because the structure produces results from all particle collisions, leading to sparse structures.<sup>220</sup> Reaction-limited aggregation gives rise to denser structures with higher fractal dimensions, in the limit corresponding to energy minimised close-packed aggregates.

**Table 4.2** Summary of a fractal dimensions determined by the box-counting method using ImageJ (**Chapter 7.5.3**) for a series of assemblies obtained with linker **18**. AuNP-7a (0.036 mM in terms of boronic acids), *N*-methylmorpholine (105 mM) in methanol.

[Linker] / mM	Ratio	%binding	$D_f$
0.11	3.1	9%	1.875
0.23	6.4	17%	1.816
0.44	12.2	28%	1.719
0.55	15.3	33%	1.670
0.80	22.2	42%	1.676
1.05	29.2	49%	1.705
1.92	53.3	65%	1.770
2.65	73.6	73%	1.786

Analysis of several images taken from assembled nanoparticle samples (listed in **Table 4.2**) allows for quantitative analysis of the observed morphologies. Fractal dimensions for a minimum of three images at each set of conditions were determined by the box-counting method using ImageJ software (**Chapter 7.5.3**). A minimum fractal dimension of  $D_f = 1.67$  is seen for the sample assembled at a linker concentration of 0.55 mM (15.3 eq.) (**Figure 4.15**). At either lower or higher concentrations, higher fractal dimensions were measured. This reflects the more sparse, branched/net-like structure of the assemblies at optimum conditions. However, the results of this technique are prone to subject bias and sample variation. The image analysis assumes that all assemblies are lying flat with the nanoparticles only one layer deep. Furthermore, prior to fractal analysis, images need to be converted to binary black-and-white images, which is a further source of error/subject bias, as all images have different initial contrast, and the threshold for the binary conversion must be manually selected. Therefore the results should be viewed with caution.

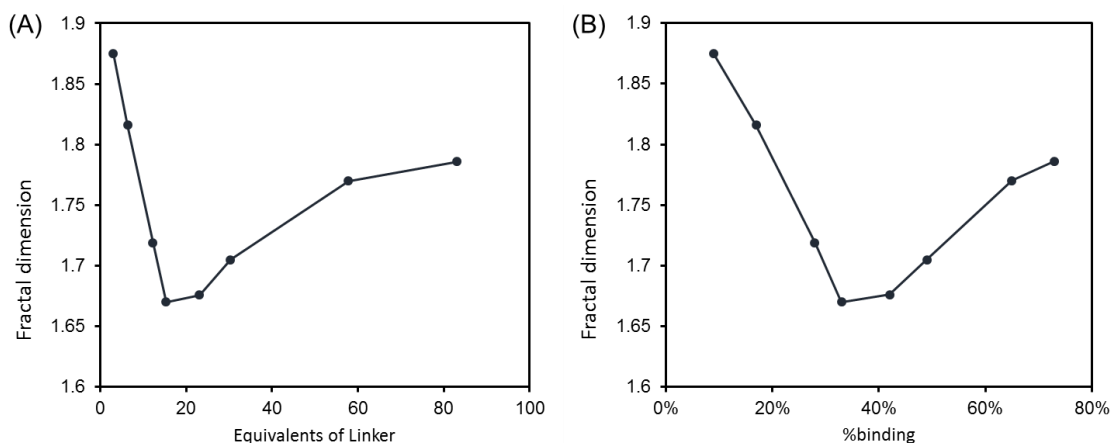


**Figure 4.15** Plots of (A) equivalents of linker against fractal dimension and (B) %binding against fractal dimension. Fractal dimensions were determined by the box-counting method using ImageJ (**Chapter 7.5.3**)

The appearance of a minimum at intermediate %binding reflects the assembly mechanism. At low linker concentrations, few particle collisions lead to a stable nanoparticle–nanoparticle link. As linker concentration increases, more particle collisions lead to the formation of a stable nanoparticle–nanoparticle link. At high linker concentrations, where the equilibrium now sits strongly towards boronic ester formation, the boronic acids of colliding particles may already be blocked by additional linker molecules, again leading to few collisions that result in assembly-stable linkage being formed. At the highest linker concentrations, a further mechanism which may also be at play might be loss of colloidal stability for nanoparticles with a high number of linker molecules **18** attached. At intermediate concentrations, an optimum is achieved with a balance between the favourable equilibrium position for boronic ester formation, and sufficiently high availability of complementary functionality. This means that a high proportion of particle collisions result in assembly, which gives rise to an assembly process where diffusion limited aggregation dominates. This is reflected in the lower fractal dimension, corresponding to a more diffusion-limited aggregation process.

Qualitatively, and quantitatively with the parameterisation of the assembly morphologies, a simple change in the amount of linker has been demonstrated to have an observable effect on the assembly morphology. This strongly indicates molecular control over the dynamic covalent assembly of

nanoparticles. One advantage of using small, simple molecules to achieve dynamic covalent nanoparticle assembly is the rich structural diversity that may be accessed through simple synthetic organic chemistry. Structural changes in the nature of the linker can tune the binding strength and introduce different structural properties (for example length, steric bulk, rigidity and solvophilicity) and therefore have the potential to affect the observed morphology.

A range of linkers were prepared (**Figure 4.16**). Rigid linker **19**, rigid salicylic acid linker **20** and trigonal linker **21**. The rigidity of linker **19** might be expected to change the assembly, although it must be noted that the boronic acid ligands on the nanoparticles have multiple rotatable bonds. Salicylic acid linker **20** replaces the catechol functionality with a salicylic acid, which, as discussed in **Chapter 3**, is also expected to form boronate esters, but with a different equilibrium constant.

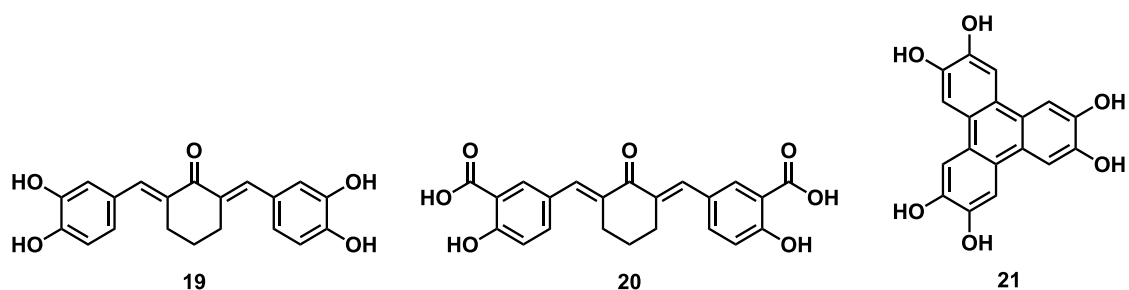


**Figure 4.16** Structures of a range of alternative linker molecules.

As with flexible linker **18**, an estimate of the association constant for the binding of the nanoparticle-bound boronic acid with the linker could be estimated by NMR spectroscopy measurements with a model compound. The association constants determined were  $5200 \text{ M}^{-1}$  for rigid linker **19** and  $1800 \text{ M}^{-1}$  for salicylic acid linker **20** (**Chapter 7.4.1, Table 7.6**).

Each of the three new linkers was applied under the standard conditions of AuNP-**7b** ( $0.1 \text{ mg mL}^{-1}$ ,  $0.039 \text{ mM}$  in terms of boronic acids), linker ( $0.559 \text{ mM}$ ,  $14.7 \text{ eq.}$ ) and *N*-methylmorpholine ( $105 \text{ mM}$ ,  $2692 \text{ eq.}$ ) in methanol. Due to the intense colour of these highly conjugated linkers, it was not possible to tell if the

samples had fully precipitated, or if nanoparticles remained in solution as the solution colour was dominated by the linker. This also made UV-vis analysis of these samples not possible. However, after about a week, some precipitate was seen in the samples containing rigid linker **19** and rigid salicylic acid linker **20**. No precipitate was observed in the sample containing trigonal linker **21** until about 20 days after addition of the linker. The assembly structures with the rigid linkers were all analysed by TEM microscopy (**Figure 4.17**) after three weeks.

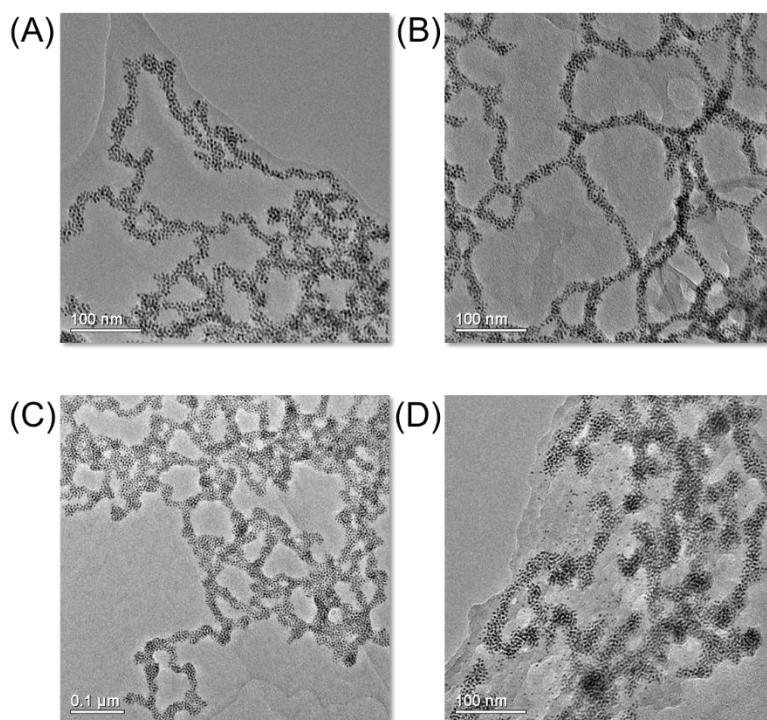


**Figure 4.17** TEM images obtained three weeks after AuNP-7a assembly was initiated under the standard conditions. AuNP-7a (0.036 mM in terms of boronic acids), linker (0.55 mM, 15.3 eq.) and *N*-methylmorpholine (105 mM, 2692 eq.) in methanol. (A) Flexible linker **18**, (B) rigid linker **19**, (C) rigid salicylic acid linker **20**, (D) trigonal linker **21**.

As seen above, flexible linker **18** (**Figure 4.17A**), rigid linker **19** (**Figure 4.17B**) and rigid salicylic acid linker **20** (**Figure 4.17C**) give rise to branched-dendritic assemblies. In comparison with flexible linker **18**, rigid linker **19** gives rise to narrower chains and greater distances between branch points. The structure assembled with trigonal linker **21** (**Figure 4.17D**) consists of small branched assemblies, and some unassembled, free nanoparticles are observed even after three weeks.

A range of linker concentrations were employed for assembly with both rigid catechol linker **19** and rigid salicylic acid linker **20**. At all ratios with both linkers, a branched-dendritic morphology was observed, and no distinct morphological differences were observed. The %binding could be estimated from association constants measured with model boronic acid **10**, and, as with flexible catechol linker **18**, the fractal dimensions of the assemblies were measured.

**Table 4.3** Summary of assembly experiments using rigid linker **19** and salicylic acid linker **20**. AuNP-7a (0.036 mM in terms of boronic acids), *N*-methylmorpholine (105 mM) in methanol.

[NP] / mM	[Linker] / mM	Ratio	Rigid linker <b>19</b>		Salicylic acid linker <b>20</b>	
			%binding	$D_f$	%binding	$D_f$
0.036	0.11	3.1	34%	1.743	16%	1.618
0.036	0.23	6.4	52%	1.634	28%	1.635
0.036	0.44	12.2	68%	1.585	43%	1.608
0.036	0.55	15.3	73%	1.548	49%	1.601
0.036	0.80	22.2	80%	1.607	58%	1.591
0.036	1.05	29.2	84%	1.596	65%	1.499
0.036	1.92	53.3	91%	1.612	77%	1.684
0.036	2.65	73.6	93%	1.619	83%	1.775

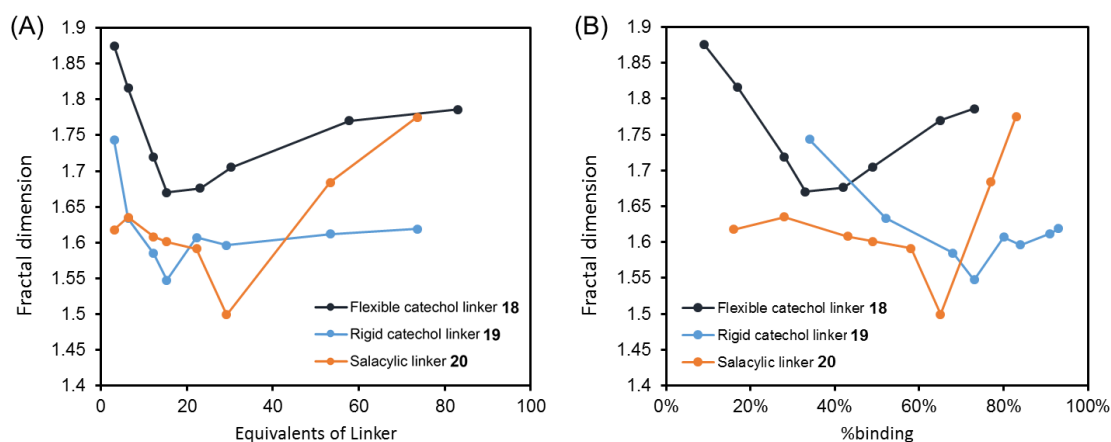


**Figure 4.18** Plots of (A) equivalents of linker against fractal dimension (B) %binding against fractal dimension for rigid linker **19** and rigid salicylic acid linker **20** (data for flexible linker **18** reproduced from **Figure 4.15**). Fractal dimensions were determined by the box-counting method using ImageJ (**Chapter 7.5.3**).

The fractal dimension is plotted against the equivalents of linker and the %binding in **Figure 4.18**. As with flexible linker **18**, the assembly with both rigid linker **19** and rigid salicylic acid linker **20** displays a minimum  $D_f$  at intermediate linker concentrations. For rigid linker **19**, the minimum appears at 15.3 eq. whereas for rigid salicylic acid linker **20**, the minimum fractal dimension is observed at 29.2 eq. Interestingly, although a minimum  $D_f$  for salicylic acid linker **20** is seen at almost twice the number of equivalents as for rigid linker **19**, the %binding with these ligands is at the minimum  $D_f$  is much more similar, 65% and 73%, respectively.

The overall lower fractal dimensions seen with the rigid linkers reflect the stronger binding. This stronger binding means that boronic ester formation is favoured, leading to assembly being more likely when particles collide. This shows a level of molecular control over the assembly whereby increasing the binding strength can predictably influence the assembly.

Finally, although a minimum  $D_f$  is observed at similar %binding for rigid linker **19** (73%) and rigid salicylic acid linker **20** (65%), these values are very different from that for flexible linker **18** (33%), contrary to the hypothesis. However, this could be down to deficiencies in the estimation of the association constants for the linkers, as the effect of steric crowding (**Chapter 3.5**) has not been accounted for. As rigid linker **19** and rigid salicylic acid linker **20** are isostructural, the effects of steric crowding on the binding constant might be expected to be similar in both cases. This is reflected well in the similarity in the %binding at minimum  $D_f$  for both these linkers.

## 4.7 Towards reconfigurable nanoparticle assemblies

During the disassembly experiment, before full disassembly had been achieved, small, spherical assemblies were observed by TEM (**Figure 4.12**). Such relatively small assemblies are colloidally stable, and therefore genuine examples of covalently-linked nanoparticles assembled under thermodynamic

control. It was thought that the balance between linker and competing capping agent resulted in this structure, leading to assemblies cross-linked internally, but capped externally by the capping molecule. In an attempt to access such a morphology directly from the initial unassembled nanoparticles, flexible linker **18** (at the standard 15.3 eq.) was combined with 1,2-dihydroxybenzoic acid (30.6 eq.) as a capping agent and added to AuNP-7a. While small, spherical aggregates were not observed, the assembly morphology produced under these conditions was different, globular in nature (**Figure 4.19**). It is possible to speculate that this is due to the formation of spherical assemblies, as predicted, but at this specific ratio, these assemblies are insufficiently stabilised and become linked and precipitate. It is also necessary to balance the thermodynamic assembly size against the colloidal stability of the small aggregates.

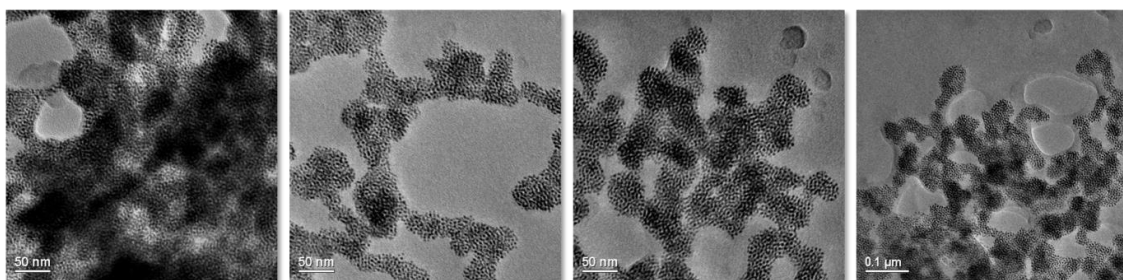


**Figure 4.19** TEM images of aggregates obtained under standard conditions (AuNP-7a (0.036 mM in terms of boronic acids), linker **18** (0.55 mM, 15.3 eq.) and *N*-methylmorpholine (105 mM, 2692 eq.) in methanol), in the presence of 2 eq. (relative to linker **18**) of 3,4-dihydroxybenzoic acid. This gives rise to globular assemblies, almost spherical in nature.

Ongoing and future work seeks to further explore this nanoparticle assembly with a mixture of linker and stopper, with the goal to develop conditions for the assembly of colloidally stable thermodynamic assemblies by boronate ester formation.

## 4.8 Conclusions and future work

Nanoparticle assemblies have been created by dynamic covalent bonds (boronic esters). Kinetic analysis reveals a nucleation–growth assembly process

comprising a thermodynamically driven nucleation and kinetic trapping by precipitation. Nevertheless the reversibility of the dynamic covalent linkages can still be activated by providing an appropriate chemical stimulus which can break apart the assemblies by out-competing the ditopic linker (**Figure 4.20A**). The evidence for boronic ester formation driving the assembly is not merely phenomenological, but draws on the molecular work in **Chapter 3**, which demonstrated boronic ester formation on nanoparticles and confirmed the reversibility of the process. Variation of molecular parameters, such as linker concentration, rigidity and boronic ester formation constant, can all result in changes in aggregate morphology. Qualitatively, “optimal” branched-dendritic assemblies are observed at intermediate linker concentrations, indicative of a diffusion-limited aggregation process, with assemblies more characteristic of reaction-limited aggregation processes observed at both lower and higher linker concentrations. Quantitative analysis of aggregate morphology confirms that it should be possible to directly correlate assembly structural characteristics with molecular parameters. However, more accurate/representative characterisation of parameters such as equilibrium constants in the nanoparticle-bound environment are required in order to achieve this.

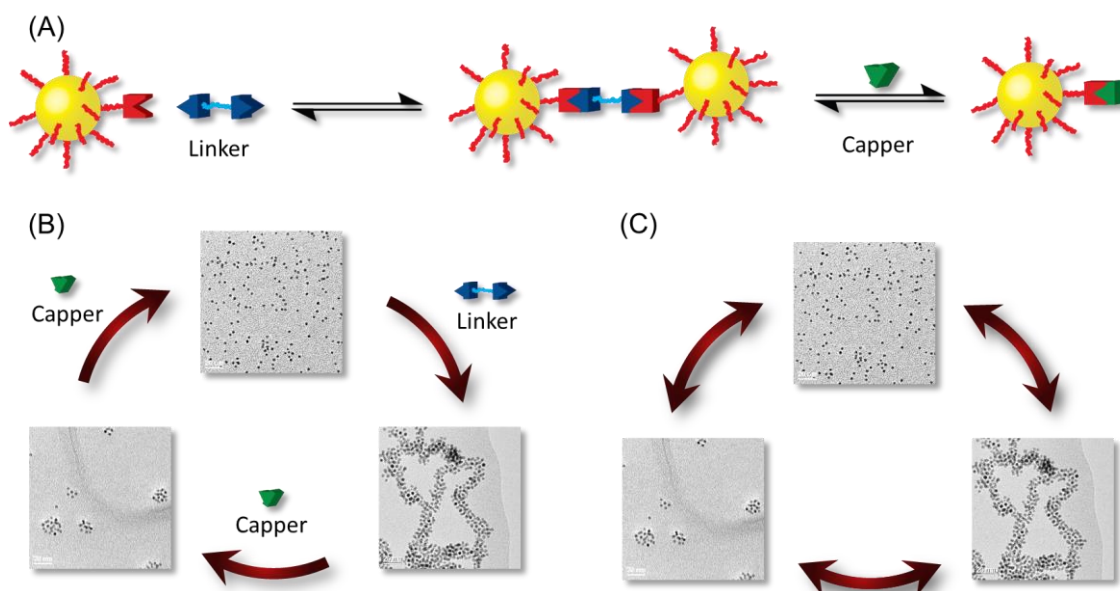


**Figure 4.20** (A) Schematic representation of nanoparticle assembly and disassembly through use of a molecular linker and stopper. (B) Boronic ester-mediated assembly, reconfiguration and disassembly of nanoparticles, as reported in this chapter. (C) Future work seeks to complete the cycle in the opposite direction, initially forming small colloidal stable aggregates through addition of a mixture

of linker and stopper, reconfiguration by addition of excess linker and subsequent full disassembly by addition of stopper.

A basic level of reconfiguration of boronic ester assembly structure has been demonstrated (**Figure 4.20B**). Future work will seek to further develop an understanding of how molecular input affects assembly morphology, leading, ultimately, to the creation of systems that are truly reconfigurable by simply tuning the molecular input (**Figure 4.20C**).

# Chapter 5:

## Noncovalent planet–satellite nanoparticle assembly

This chapter focuses on the formation of discrete nanoparticle assemblies composed of a core ‘planet’ nanoparticle coated with several smaller ‘satellite’ nanoparticles, to give a planet–satellite three-dimensional architecture.

A highly multivalent hydrogen bonding interaction, afforded by dense, single component monolayer coverage, controls the assembly of 1,2-diol-coated ‘satellite’ nanoparticles with citrate-stabilised ‘planet’ nanoparticles. The aqueous assembly process is operationally simple and rapid, giving rise to complete isotropic coverage of the large ‘planet’ nanoparticle with small ‘satellite’ nanoparticles, which could be easily purified from excess satellite nanoparticles by a precipitation–washing–redispersion process. The planet–satellite assemblies were found to display remarkable colloidal stability which was imparted by the satellites. The versatility of this noncovalent approach was demonstrated by varying the ‘planet’ building block, successfully assembling building blocks of different sizes, shapes and materials, leading to a wide array of structures.

The multitude of field enhancement ‘hotspots’ located at inter-nanoparticle gaps of the planet–satellite assemblies offered the opportunity for surface-enhanced Raman spectroscopy (SERS). Simply mixing the pre-formed planet–satellite assemblies with a thiophenol SERS reporter (at 100 nM concentration) led to incorporation of the receptor to the hotspots and a SERS signal was detected.

The level of control achieved in the formation of planet–satellite assemblies is highly encouraging, and offers potential to develop a generalisable nanoparticle building block toolkit for the predictable formation of robust and structurally diverse nanoparticle assemblies.

*I gratefully acknowledge the contribution of Sarah Flook to this chapter, who carried out experiments for the optimisation of preparation of planet–satellite assemblies and investigated their scope and stability, contributing to data for **Figures 5.5–5.8, 5.9, 5.15–5.21, 5.25, 5.27–5.29** during her Summer Project (June 2014 – August 2014). Furthermore, I gratefully acknowledge the contribution of Dr Steven Asiala at the University of Strathclyde for collaboration and assistance in obtaining Zetapotential measurements and Raman spectra.*

## 5.1 Introduction

Although resulting in covalent bond formation, the boronic ester chemistry discussed in **Chapters 3** and **4** is very similar to host-guest chemistry mediated by noncovalent interactions, sharing similar binding strengths and rapid kinetics of equilibration, and resulting in relatively kinetically labile bonds. Host–guest interactions have been applied in numerous cases to direct nanoparticle assembly.<sup>98,101,102</sup> There are a number of examples where a host–guest system, comprising of a macrocyclic host and a complementary guest, has been employed for nanoparticle assembly. Combining a polymer-supported macrocycle with nanoparticles functionalised with an appropriate guest can give rise to the formation of a pseudorotaxane complex between the nanoparticle and polymer, thus leading to a polymer-linked nanoparticle assembly (**Figure 5.1**).<sup>98,102</sup> This type of assembly strategy has been used to assemble nanorods<sup>221</sup> as well as spherical particles.

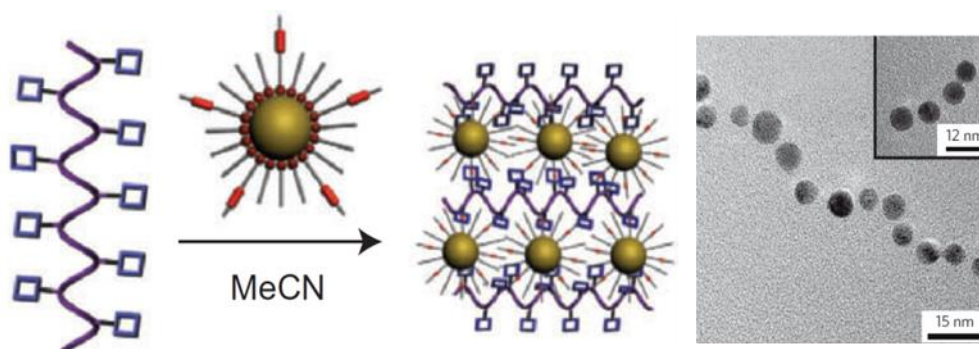


**Figure 5.1** Schematic representation of polymer-supported nanoparticle assembly by a pseudorotaxane host–guest interaction. Left is a TEM image of the obtained nanoparticle assembly (Figure reproduced from **ref. 98**).

The complexity of the host–guest structures used is such that nanoparticles are functionalised with mixed monolayers, with only a few active ligands per nanoparticle, resulting in only a few relatively strong interactions per particle. However, the abundance of ligands per nanoparticle, and the fact that when two nano-sized surfaces come together, several ligands on each nanoparticle are brought into close proximity, presenting the opportunity for much larger numbers of interactions per nanoparticle in a cooperative manner. This potential for highly multivalent interactions between nanoparticles means that very weak

interactions can in fact play a significant (or the major) role in directing nanoparticle assembly, and thus can become significant in the field of nanoparticle assembly.

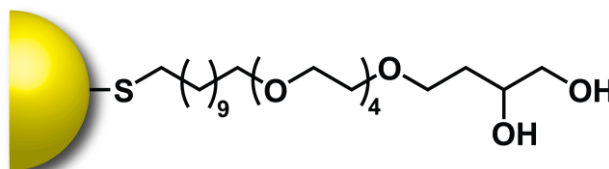
Nanoparticle assemblies consisting of a core nanoparticle ‘planet’ coated with several smaller nanoparticle ‘satellites’ give a planet–satellite assembly an attractive 3D architecture. When bringing together noble metal nanoparticles, the surface plasmon resonances of the individual nanoparticles interact, leading to strong near-field coupling.<sup>212,222–224</sup> These unique optoelectronic effects have been widely investigated, both from a fundamental perspective, and for a range of applications including colorimetric sensors,<sup>120,225</sup> surface-enhanced spectroscopies,<sup>226–228</sup> and nanometrology.<sup>210</sup> Such planet–satellite structures bear a multitude of field enhancement ‘hotspots’ located within precisely controlled inter-nanoparticle gaps.<sup>224</sup>

Combining two different building blocks to achieve discrete assemblies of this sort can lead to a diverse range of well-defined colloiddally stable superstructures. There are a number of desirable features of such planet–satellite assemblies. Bulk approaches may produce molar quantities of planet–satellite assemblies. Production of planet–satellite assemblies should be rapid and operationally simple to facilitate this.

Previously, such structures have been achieved using oligonucleotide-directed self-assembly.<sup>124,208,225–237</sup> However, this strategy is restricted to relatively large inter-nanoparticle distances (hence weak plasmon coupling) and to a narrow window of environmental conditions. Additionally, oligonucleotide-directed structures collapse on drying. Alternatively, manipulation of solution ionic strength can lead to aggregation of charge-stabilised nanoparticles,<sup>238</sup> but this demands very careful control of conditions in order to achieve – and subsequently maintain – a desired aggregate architecture. More recently, covalently-linked strategies have produced some exciting results, yet it has proven challenging to produce uniform structures,<sup>87</sup> without requiring preparation of complex macromolecular linkers,<sup>88</sup> or undertaking multi-step assembly,<sup>90</sup> stabilisation/encapsulation<sup>238</sup> and purification protocols.<sup>89,90</sup>

Hydrogen bonding in water is an inherently weak interaction due to the competitive binding of water both as a donor and as an acceptor. Many biomolecular examples make extensive use of hydrogen bonding, but this is usually the result of the hydrogen bonding units being placed in a relatively hydrophobic environment. Oligonucleotide duplex formation is a notable example of hydrogen bonding determining supramolecular assembly in an aqueous environment. The multivalency arising from multiple hydrogen bonding interactions leads to the formation of aqueous stable supramolecular structures held together solely by the hydrogen bond. The presence of thousands of ligands per nanoparticle results in the potential to exploit such weak hydrogen bonding in a highly multivalent manner to direct assembly.<sup>241</sup>

## 5.2 Synthesis and characterisation of planet–satellite assemblies



AuNP-5

**Figure 5.2** 1,2-diol-functionalised gold nanoparticles (AuNP-5).

AuNP-5 (**Figure 5.2**) ( $5.73 \pm 0.85$  nm), the synthesis of which is discussed in **Chapter 2.2**, was found to be soluble in water as a result of the tetra(ethylene glycol) region of the ligand. AuNP-5 was dissolved in water as a  $0.1 \text{ mg mL}^{-1}$  solution. When an aqueous solution of AuNP-5 was added to a solution of commercial 40 nm citrate-stabilised nanoparticles (sized by TEM imaging as  $39.09 \pm 3.31$  nm), an unexpected immediate colour change from red to purple was observed. This could be the result of plasmon coupling, potentially indicating nanoparticle aggregation. TEM images of the resultant purple solution revealed the appearance of planet–satellite assemblies (**Figure 5.3**), with

satellite nanoparticles not only seen around the edges of the planet nanoparticles, but also on top, suggesting a genuine inter-nanoparticle interaction rather than a drying effect.

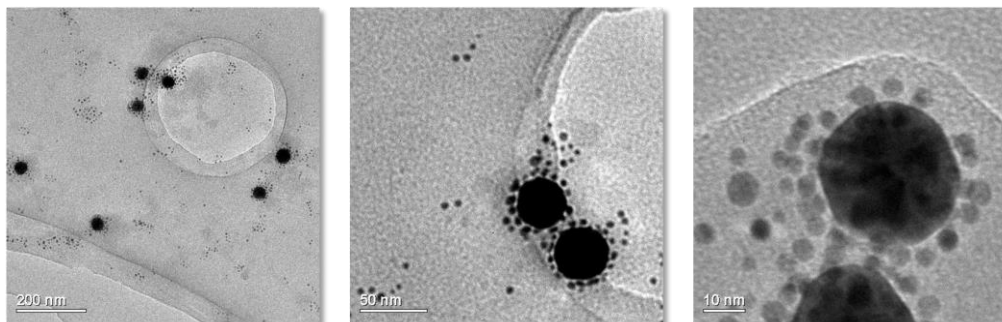


**Figure 5.3** TEM images of the purple solution resulting from mixing a solution of AuNP-5 with commercial 40 nm citrate-stabilised nanoparticles. Planet–satellite assemblies are seen, as well as an excess of AuNP-5. It is possible to see that the smaller nanoparticles lie on top of the larger nanoparticles.

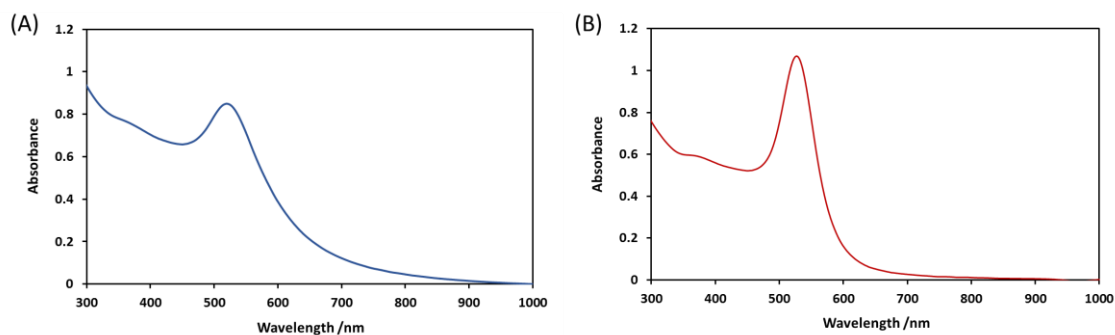


**Figure 5.4** Extinction spectra ( $\text{H}_2\text{O}$ ,  $20\text{ }^\circ\text{C}$ , path length = 1 cm) of (A) AuNP-5, showing  $\lambda_{\text{max}}$  (SPR) = 519 nm ( $A = 0.8841$ ) and (B) 40 nm commercial citrate-stabilised nanoparticles, showing  $\lambda_{\text{max}}$  (SPR) = 526 nm ( $A = 1.0775$ ).

In order to optimise planet–satellite formation, starting concentrations of the two component nanoparticle solutions were determined by UV-vis spectroscopy (Figure 5.4) in order to determine the nanoparticle concentration. Extinction coefficients ( $\epsilon$ ) at  $\lambda_{\text{max}}$  (SPR) for the nanoparticles could be calculated using Equation 5.1,<sup>242</sup> where  $d$  is the mean particle diameter in nm,  $k = 3.32111$  and  $a = 10.80505$ . This empirically derived relationship has been derived for both organic and aqueous dispersions of nanoparticles across a relatively wide range of sizes.

$$\ln \varepsilon = k \ln d + a \quad \text{Equation 5.1}$$

These extinction coefficients could then be used to calculate nanoparticle concentrations using the Beer–Lambert equation (**Equation 5.2**), where  $A$  is the measured absorbance at  $\lambda_{\max}$  (SPR),  $l$  is the path length of the cell (1 cm for all measurements) and  $c$  is the nanoparticle concentration.

$$A = \varepsilon cl \quad \text{Equation 5.2}$$

This gave the concentrations shown in **Table 5.1**.

**Table 5.1** Extinction coefficients ( $\varepsilon$ ) and nanoparticle concentrations calculated from the UV-vis spectra.

Sample	$\varepsilon / \text{M}^{-1} \text{cm}^{-1}$	Concentration / nM
AuNP-5	$1.624 \times 10^7$	54.4
40 nm commercial citrate-stabilised nanoparticles	$9.550 \times 10^{10}$	0.112

In order to establish the optimum stoichiometric ratio for planet–satellite assembly, the component nanoparticles were mixed in different ratios, ranging from 14:1 to 2800:1 AuNP-5:citrate-NP. Monitoring the resulting assembly by UV-vis spectroscopy revealed a maximum red shift in the SPR maximum at around 280:1 (**Figure 5.5**). The initial increase in  $\lambda_{\max}$  (SPR) with increasing satellite nanoparticles is ascribed to increased coverage of the planet nanoparticles leading to a larger average SPR shift. After reaching complete coverage around the 280:1 mixing ratio, the subsequent decrease in the  $\lambda_{\max}$  (SPR) can be ascribed to the presence of increasing amounts of free AuNP-5 in solution, which begins to dominate the spectrum.

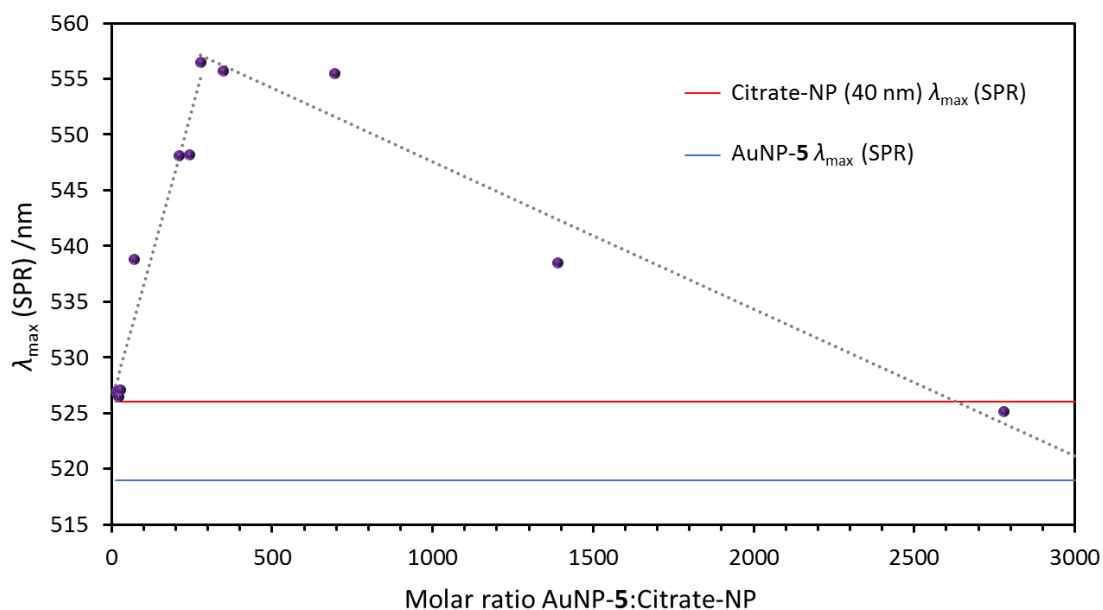


**Figure 5.5** Plot of  $\lambda_{\max}$  (SPR) observed for colloidal dispersions with varying AuNP-5:citrate-NP (40 nm) ratio ( $\text{H}_2\text{O}$ , 20 °C). The maximum shift at a ratio of 280:1 reveals the optimum mixing ratio for planet–satellite formation. The solid red and blue lines indicate  $\lambda_{\max}$  (SPR) of the component NPs in isolation; the dotted lines provide a guide for the eye.

TEM images (**Figure 5.6**) revealed that at low ratios (30:1) of AuNP-5:citrate-NP, incomplete coverage of planet surface by satellites. At high ratios (1390:1), complete planet–satellite formation was observed, along with a large excess of AuNP-5. At 280 equivalents (the ratio corresponding to the maximum red shift in SPR maximum) complete satellite formation was observed and there was only a small excess of unbound AuNP-5.

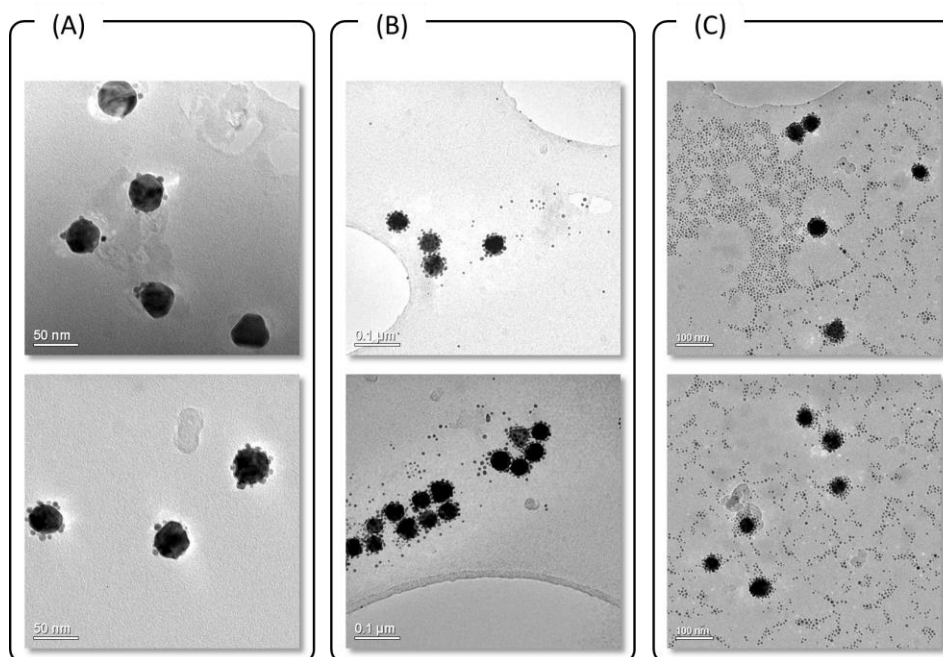


**Figure 5.6** Representative TEM images of unpurified planet–satellite assembly samples at (A) low (30:1), (B) optimum (280:1) and (C) high (1390:1) ratios of AuNP-5:citrate-NP, revealing incomplete satellite coverage at low ratios, and a high excess of satellites at high ratios. At the optimum ratio, complete satellite coverage is observed with only a small excess of AuNP-5.

Under optimum conditions (AuNP-5:citrate-NP, 280:1), excess satellite nanoparticles were present. Therefore a purification protocol was established which would lead to the formation of pure solutions of planet–satellite assemblies, leading to an overall two-step process for achieving pure planet–satellite assemblies (**Figure 5.7**).

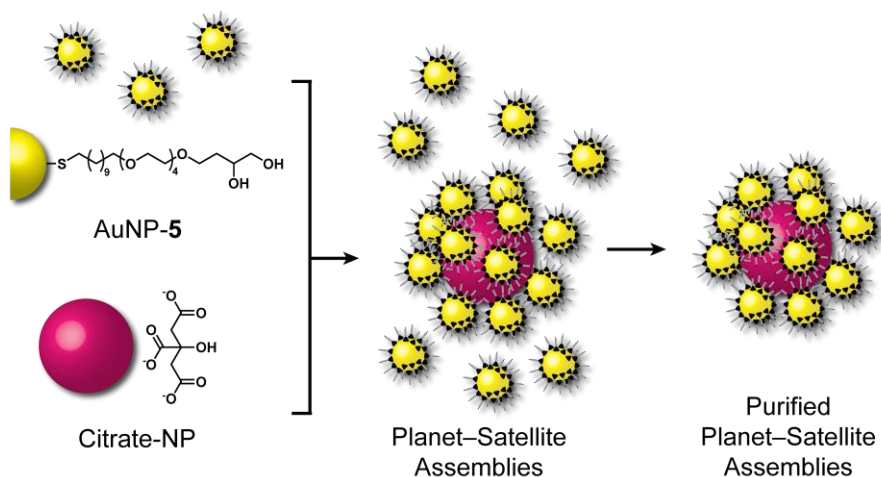


**Figure 5.7** Schematic representation of the planet–satellite assembly. Component nanoparticles are mixed at the optimum ratio of AuNP-5:citrate-NP, 280:1, followed by removal of the excess satellite nanoparticles to give pure solutions of planet–satellite assemblies.

The excess satellite nanoparticles could be easily removed by a centrifugation process. Centrifugation caused the large, planet–satellite assemblies to precipitate. The supernatant was decanted and the residual nanoparticle pellet was resuspended in the same volume of water. Two rounds of this purification process were required for complete removal of the free satellite nanoparticles, centrifuging at 5600 rcf the first time, and 2900 rcf the second time. This process was readily scalable, and was limited only by the capacity of the centrifuge.

As seen in **Figure 5.8**, after the first round of purification, the position of  $\lambda_{\max}$  (SPR) shifted from 555 nm for the unpurified planet–satellite assemblies to 561 nm, consistent with the removal of unbound AuNP-5. TEM images revealed that some free AuNP-5 still remained in solution at this stage. After the second round of purification, the  $\lambda_{\max}$  (SPR) was further redshifted to 564 nm, and free AuNP-5 could no longer be observed by TEM.

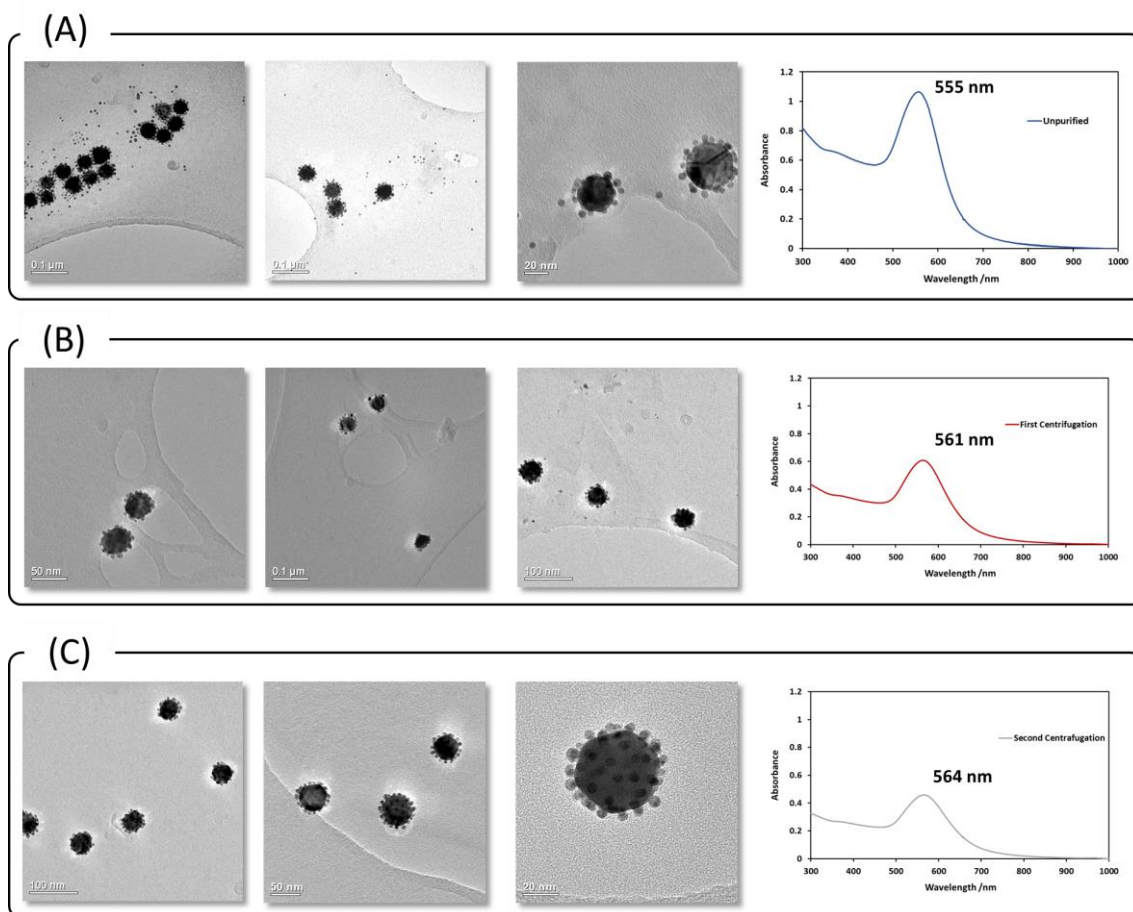


**Figure 5.8** Representative TEM images and UV-vis spectra (H<sub>2</sub>O, 20 °C) of samples at each stage of the purification procedure: (A) unpurified, (B) centrifuged–redispersed once, (C) centrifuged–redispersed twice, revealing the progressive removal of excess AuNP-5.

The absolute absorbance values at  $\lambda_{\max}$  (SPR) decrease during the purification process, consistent with the loss of nanoparticles. However, TEM images (Figure 5.9) of the supernatant discarded at each stage revealed very few planet–satellite assemblies, indicating that the majority of the loss in absorbance was due to the removal of free AuNP-5 from the solution, reflecting a highly efficient purification process.

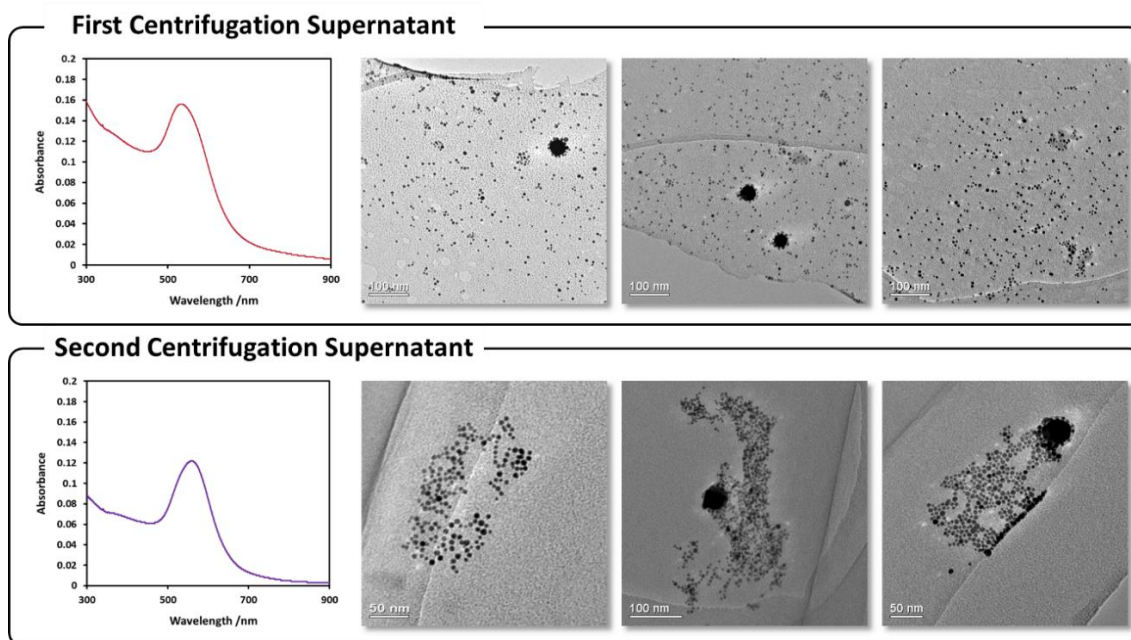


**Figure 5.9** UV-vis spectra (H<sub>2</sub>O, 20 °C) and representative TEM images of the supernatant solution removed after centrifugation at each stage of purification. At both stages, very few planet–satellite assemblies were removed, suggesting an efficient purification process.

Pure solutions of planet–satellite assemblies were obtained readily and the production of planet–satellite assemblies was easily scaled. The redshifted UV-vis spectrum (**Figure 5.10A**) and DLS measurements (**Figure 5.10B**) confirmed that the planet–satellite assemblies existed in solution, as opposed to forming upon evaporation of the solution on the TEM grid. DLS shows a single, symmetrical peak, suggesting that assemblies are intact and uniform in size in colloidal suspension.

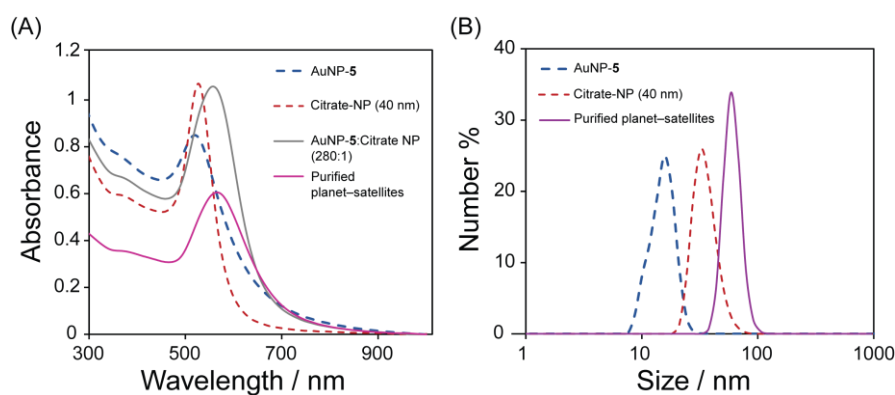


**Figure 5.10** Component nanoparticles and planet–satellite assemblies: **(A)** UV-vis spectra and **(B)** DLS measurements of component nanoparticles and planet–satellite assemblies.

The DLS measurements gave a hydrodynamic diameter of the planet–satellite assemblies of 54 nm, which is in good agreement with the expected size of the assemblies. The diameter of the assemblies should correspond to the sum of the nanoparticles plus the organic components. The extended chain conformation of diol ligand ( $5^{\text{thiol}}$ ) was modelled (**Figure 5.11**), giving a distance of 3.53 nm from the thiol sulfur atom to the terminal oxygen of the diol. The maximum possible diameter of the planet–satellite assembly should therefore correspond to one planet nanoparticle (39 nm), two planet nanoparticles ( $2 \times 5.7$  nm) and four ligands ( $4 \times 3.5$  nm) (**Figure 5.12**).

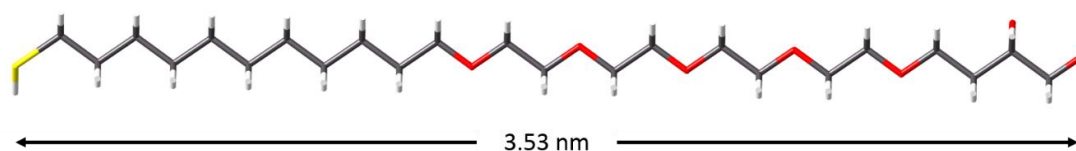


**Figure 5.11** Straight chain conformation model of the ligand coating AuNP-5 (Maestro 2012). The distance is the sulfur to terminal oxygen distance, representing the maximum possible ligand length.

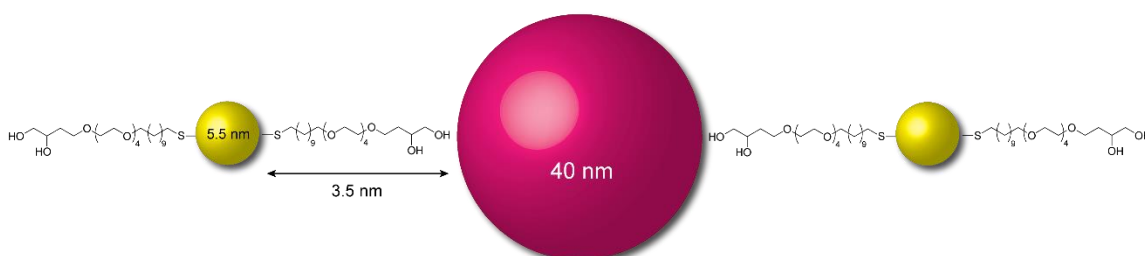


**Figure 5.12** Theoretical maximum diameter of a planet–satellite assembly calculated as  $4 \times 3.5$  nm +  $2 \times 5.5$  nm + 40 nm = 65 nm. This assumes fully extended conformations and does not account for the tilt-angle of the ligands to the nanoparticle surface; therefore the measured actual radius is expected to be lower. This is consistent with the DLS data.

In addition to the dimensions illustrated in **Figure 5.12**, the depth of the stabilising citrate monolayer should be considered ( $2 \times 0.66$  nm).<sup>11</sup> This gives a total diameter of 65 nm, which is greater than that measured by DLS (54 nm). The discrepancy between the modelled and measured diameter is due to not accounting for the tilt angle of the ligand ( $\approx 30^\circ$ )<sup>243</sup> and more significantly result

from the highly unfavoured fully extended conformation of the tetraethylene glycol section of the ligand.

The uniformity of the planet–satellite assemblies was further examined by counting the number of satellite nanoparticles observed on a given planet in TEM images. To account for the fact that TEM produces a two-dimensional image of one side of the assembly, the unseen side must be assumed to be the same as the observed side. For four representative assemblies (**Figure 5.13**), taken from images of purified samples, prepared at the optimised ratio of 280:1 (AuNP-5:citrate-NP), satellite coverage was estimated, revealing a consistent coverage of around 70 satellites per planet (**Figure 5.13**). The estimated coverage for samples prepared at higher ratios of AuNP-5:citrate-NP gave the same result.

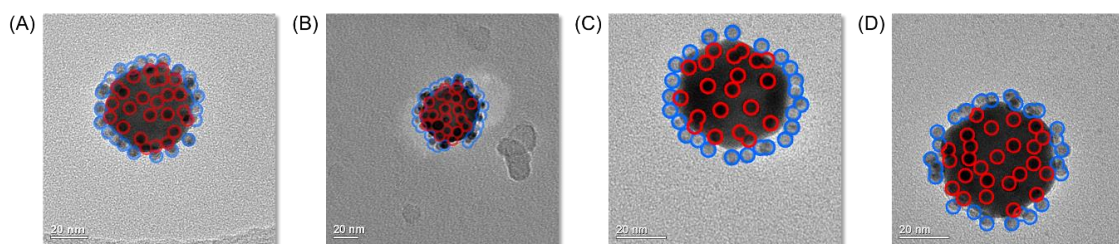


**Figure 5.13** Visualisation of satellite nanoparticles on top of the planet is possible by TEM, with all visible satellite nanoparticles highlighted. The edge satellites (blue) and the face satellites (red) were counted to give an indication of the satellite coverage. It is assumed that the unseen face has the same number of satellite nanoparticles on it; therefore, the number of face satellites (red) is doubled. **(A)** (face: 25; edge: 23) → 73 satellites. **(B)** (face: 20; edge: 23) → 63. **(C)** (face: 20, edge: 24) → 64. **(D)** (face: 25; edge: 25) → 75.

### 5.3 Colloidal stability of planet–satellite assemblies

The planet–satellite assemblies displayed remarkable stability, remaining colloiddially stable for more than a year. The stability of the assemblies was further probed in response to a variety of conditions. An aqueous planet–satellite solution (1 mL) was heated to 80 °C for three hours. A UV-vis spectrum obtained once the solution had cooled to room temperature revealed no change from the starting spectrum (**Figure 5.14**). In a separate experiment, UV-vis spectra were recorded at 20, 30, 40 and 50 °C. The value of  $\lambda_{\text{max}}$  (SPR) remained unchanged at 564 nm throughout, and the overlaid spectra were found to be indistinguishable, indicating the thermal stability of the planet–satellite assemblies.

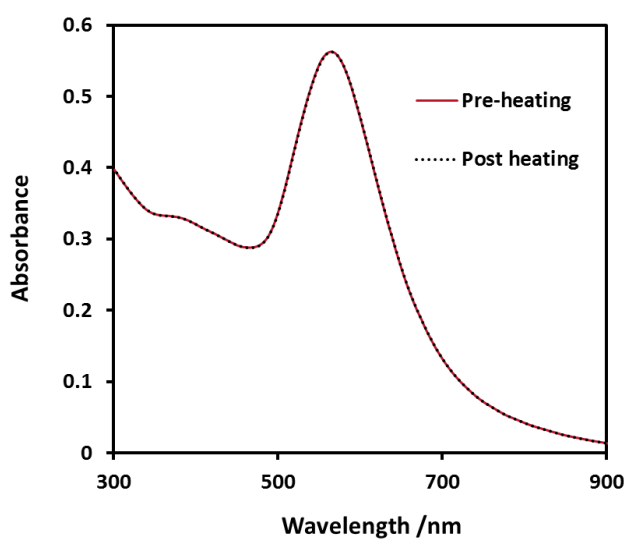


**Figure 5.14** UV-vis spectrum ( $\text{H}_2\text{O}$ , 20 °C) of planet–satellite assemblies prior to and after heating to 80 °C for three hours, revealing no change in the spectrum.

Solvent can be removed from the planet–satellite assemblies without disrupting the assembly structure. This may be achieved either by centrifugation (5600 rfc, 5 mins) to induce nanoparticle precipitation and subsequent decanting of the supernatant or by evaporation (either under vacuum or under a stream of air). The assemblies may be redispersed in both cases with no apparent change in the assembly structure by both UV-vis and TEM. Following centrifuge-induced

precipitation, the supernatant was carefully removed from the resulting pellet. The pellet remained moist after this process, and was subsequently redispersed in fresh water with no loss of material (**Figure 5.15A**). Following solvent evaporation, redispersion in the same volume of water showed no shift in the SPR band of the assemblies; however a decrease in absorbance was observed (**Figure 5.15B**), attributable to irreversible adsorption of assemblies to the walls of the glass container.

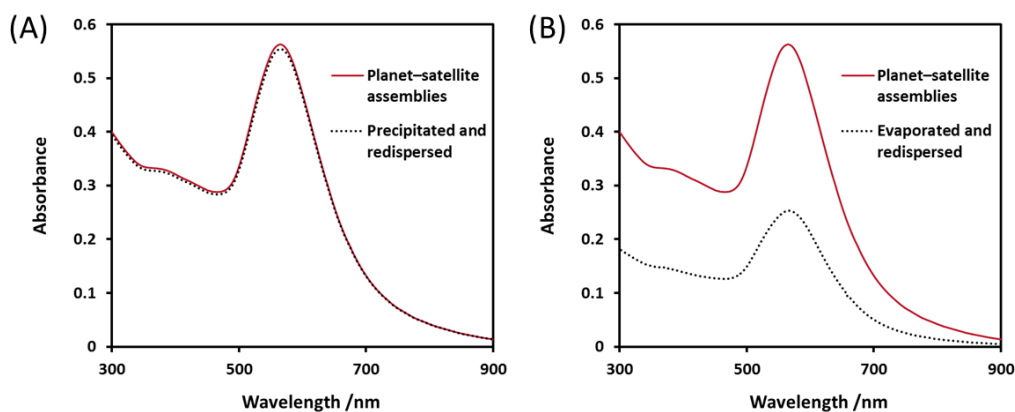


**Figure 5.15** UV-vis spectra ( $\text{H}_2\text{O}$ , 20 °C) of planet–satellite assemblies before solvent removal and after redispersion. **(A)** Redispersion of planet–satellite assemblies in water after centrifuge-induced (5600 rfc, 5 mins) nanoparticle precipitation and decanting of original solvent. **(B)** Redispersion of planet–satellite assemblies in water after solvent evaporation under airflow.

Redispersion after centrifugation-induced precipitation could be achieved not only in water, but also in organic solvent. A solution of satellites was centrifuged at 5600 rcf for five minutes to induce complete precipitation. The solvent was decanted. Addition of the same volume of MeCN followed by sonication led to complete redispersion of the assemblies, again with no apparent loss of material (**Figures 5.16** and **5.17**).

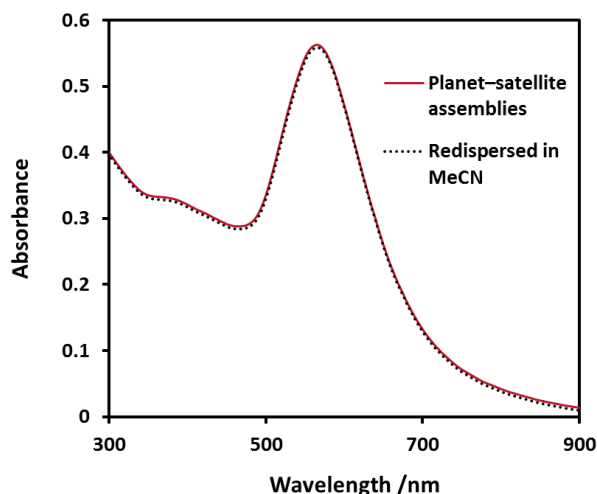


**Figure 5.16** UV-vis spectra ( $\text{H}_2\text{O}$ , 20 °C) of planet–satellite assemblies after redispersion in MeCN.

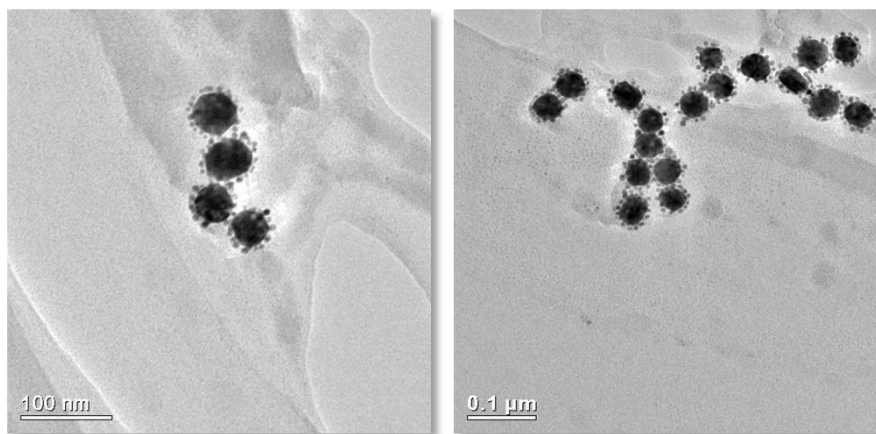


**Figure 5.17** Representative TEM images of planet–satellite assemblies after redispersion in MeCN.

The colloidal stability of the planet–satellite assemblies was also assessed with respect to increasing ionic strength. Citrate-stabilised nanoparticles, stabilised by charge–charge interactions, show very poor tolerance to increases in ionic strength. A simple visual experiment demonstrated the superior stability of the planet–satellite assemblies over citrate-stabilised nanoparticles to an increase in the concentration of NaCl. Citrate-stabilised nanoparticles were unstable at NaCl concentrations above 0.05 M, whereas the planet–satellite assemblies remained stable even up to 2.50 M, as evidenced by visual analysis (**Figure 5.18**).

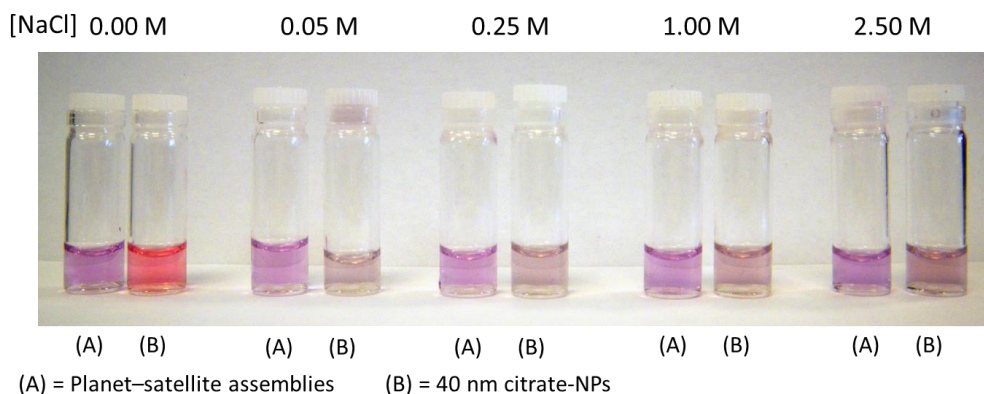


**Figure 5.18** Stability to NaCl. Visual comparison of colloidal stability under conditions of increasing ionic strength for planet–satellite assemblies (**A**) compared to citrate-stabilised nanoparticles and (**B**) on increasing solution ionic strength. Images were taken 30 minutes after adjusting salt concentrations to the stated values. In all samples up to  $[\text{NaCl}] = 2.50 \text{ M}$ , planet–satellite assemblies appeared stable, whereas the citrate-stabilised nanoparticles were unstable even to low (0.05 M) salt concentrations.

The stability of the planet–satellite assemblies to increasing concentration of NaCl was confirmed by UV-vis spectroscopy (**Figure 5.19**). The planet–satellite assemblies showed no change in the position of the SPR band, indicating both their structural and colloidal stability to high NaCl concentrations (the variation in absolute absorption is not systematic and is attributed to scattering). By comparison, the spectra of citrate-stabilised nanoparticles show the emergence of a new peak at 800 nm even at  $[\text{NaCl}] = 0.05 \text{ M}$ . The disappearance of this peak at very high salt concentrations suggests precipitation of large aggregates from solution.

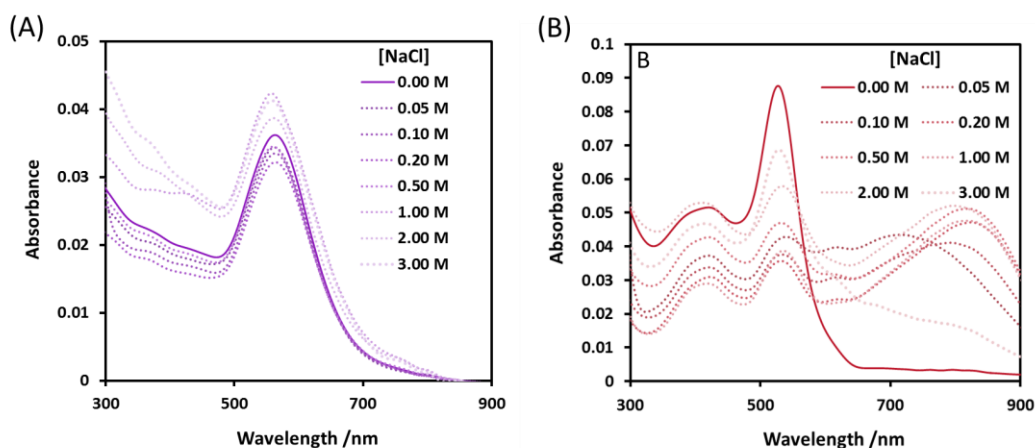


**Figure 5.19** UV-vis spectra ( $\text{H}_2\text{O}$ , 20 °C) of planet–satellite assemblies (A) and citrate-stabilised nanoparticles (B) in aqueous solution with  $[\text{NaCl}]$  ranging from 0.00 M to 3.00 M (all spectra recorded within three minutes of NaCl addition).

The stability of planet–satellite assemblies in the presence of divalent salts was also investigated. In the presence of increasing concentrations of  $\text{MgCl}_2$ , no change in the position of the SPR band (**Figure 5.20A**) was observed (the variation in absolute absorption is not systematic and is attributed to scattering). By comparison, the spectra of citrate-stabilised nanoparticles show the emergence of a new peak at 800 nm, even at  $[\text{MgCl}_2] = 0.05 \text{ M}$  (**Figure 5.20B**).

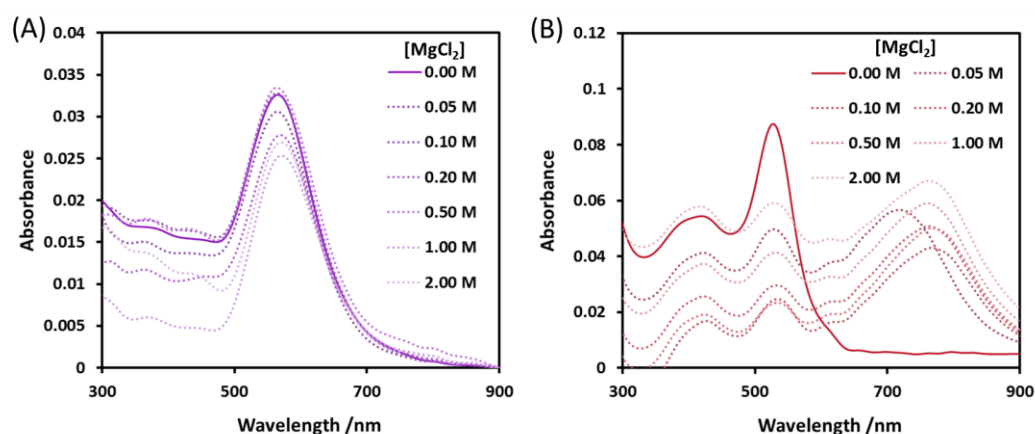


**Figure 5.20** UV-vis spectra ( $\text{H}_2\text{O}$ , 20 °C) of planet–satellite assemblies (A) and citrate-stabilised nanoparticles (B) in aqueous solution with  $[\text{MgCl}_2]$  ranging from 0.00 M to 2.00 M (all spectra recorded within three minutes of addition of  $\text{MgCl}_2$ ).

Planet–satellite assembly stability was also examined visually at pH values between pH 0 and 14. The assemblies appeared stable by eye at all pH values

between pH 0 and 14 (**Figure 5.21**). By comparison, the citrate-stabilised nanoparticles were unstable at both low ( $\leq 4$ ) and high ( $\geq 11$ ) pH values. At low values, protonation of the stabilising citrate layer reduced the electrostatic stabilisation of the citrate-stabilised nanoparticles, causing a loss of colloidal stability, leading to aggregation and precipitation. The instability at high pH values was likely a result of increased solution ionic strength.

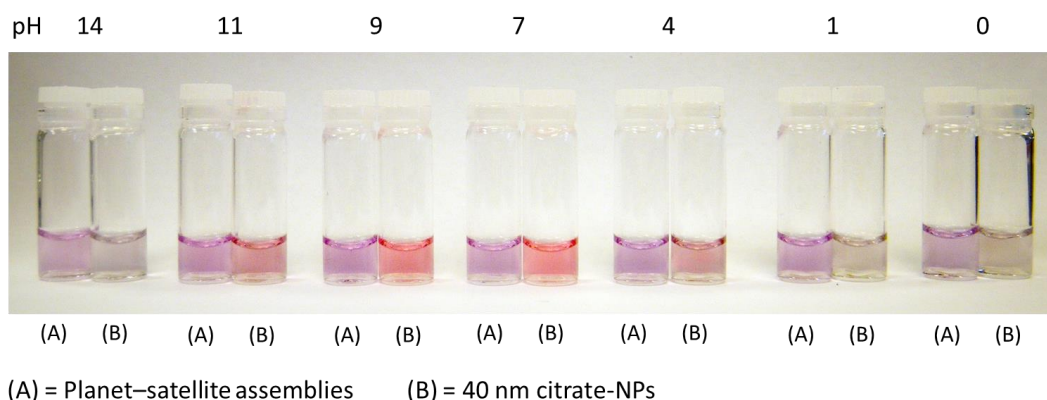


**Figure 5.21** Stability to pH. A visual experiment showing the superior stability of the planet–satellite assemblies (**A**) compared to citrate-stabilised nanoparticles (**B**) on varying pH. Images were taken one hour after adjusting the pH from pH 7 using either HCl or NaOH.

The stability of the planet–satellite assemblies can most likely be attributed to the inherent stability of satellite AuNP-5. AuNP-5 are stable to varying conditions of both ionic strength and pH (**Figure 5.22**). Coating the relatively unstable charge-stabilised citrate-stabilised nanoparticles with stable ligand-coated AuNP-5 masks the stability properties of the citrate nanoparticles, transferring instead the stability of AuNP-5 to the much larger assembled structures.

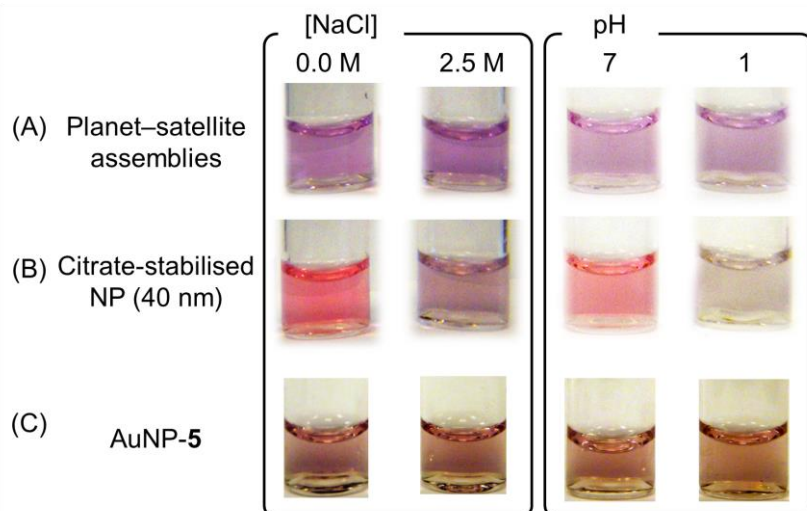


**Figure 5.22** Images of aqueous dispersions of planet–satellites (A), citrate-stabilised nanoparticles (B) and AuNP-5 (C) demonstrating the transfer of the stability properties of AuNP-5 to the binary assemblies under conditions of increased ionic strength and decreased pH.

As well as the colloidal stability of the planet–satellite assemblies, the assemblies also display remarkable structural stability, suggesting a strong interaction between the diol satellite nanoparticles and the citrate-stabilised, planet nanoparticle. None of the conditions which the assemblies were subjected to led to their disassembly; indeed addition of an excess of competing molecular diol (glycerol) had no effect on the assemblies, indicating either that the structures are kinetically trapped or that the concentration of glycerol added was not thermodynamically able to out-compete the highly multivalent interaction between the nanoparticles. Van der Waals attractions between the nanoparticles may also provide a significant contribution to the structural stability of the assemblies.

## 5.4 Probing the planet–satellite interaction

Electrostatic attraction is a possible reason for the interaction between the nanoparticles. Electrostatics have been used previously in nanoparticle assembly,<sup>241,244</sup> even for the formation of planet–satellite assemblies.<sup>238</sup> Zeta-

potential measurements (**Table 5.2**) of the binary assemblies, as well as the two components were obtained.

**Table 5.2** Zeta potential measurements of the planet–satellite assemblies, and the two component nanoparticle solutions.

Nanoparticles	Zeta potential / mV
AuNP-5	$-1.23 \pm 10.3$
40 nm commercial citrate-stabilised nanoparticles	$-52.9 \pm 20.9$
Planet–satellite assemblies	$-16.5 \pm 14.4$

The citrate-stabilised nanoparticles are strongly negatively charged, as expected due to the stabilising layer of triply negatively charged citrate. 1,2-Diol-coated AuNP-5 are neutral, as expected, as they are stabilised by neutral ligands. This indicates that an electrostatic interaction is not responsible for the nanoparticle assembly. The planet–satellite assemblies are slightly negatively charged. The negative charge of the planet, citrate-stabilised nanoparticle is partially screened by the neutral diol nanoparticles. This is consistent with the observations for the stability of the planet–satellite assemblies, which display stability behaviour that is similar to the diol satellite nanoparticles, rather than the citrate-stabilised planet core.

A control experiment followed the same procedure as for formation of planet–satellite assemblies (**Section 5.2**), but with AuNP-5 replaced by AuNP-4 (**Figure 5.23**), where the diol functionality was replaced by a single alcohol. No nanoparticle aggregation was observed, either in solution (UV-vis) or by TEM (**Figure 5.24**). The TEM images reveal no planet–satellite formation, showing only randomly associated structures formed during the drying process. The absence of aggregates in solution is confirmed by UV-vis analysis, which shows extinction spectra of the mixtures as simple superpositions of the two component spectra, with no shift in the position of the SPR band. The absence of assembly when replacing the diol with a single alcohol suggests that the self-assembly process appears to be governed by a highly specific interaction

between the 1,2-dihydroxy functionality on AuNP-5 and the citrate-stabilised nanoparticles.

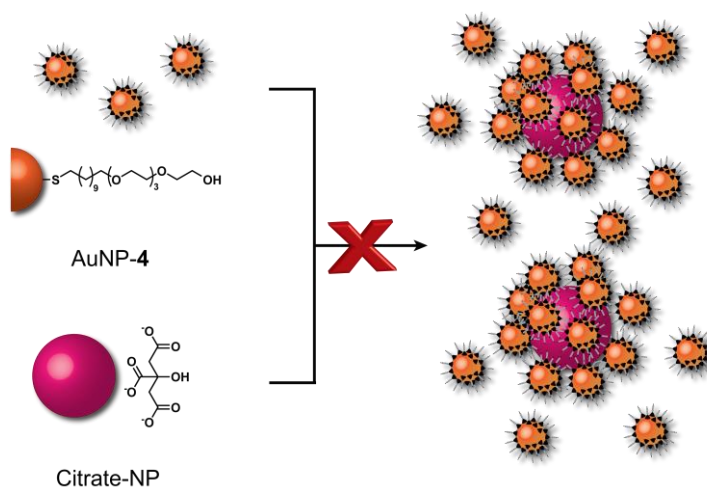


**Figure 5.23** Schematic representation of a control experiment using monohydroxy-functionalised AuNP-4.

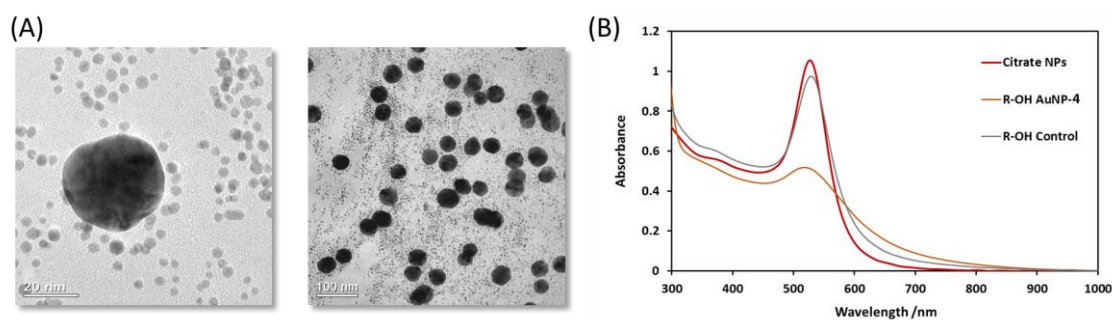


**Figure 5.24** (A) Representative TEM images and (B) UV-vis spectra ( $\text{H}_2\text{O}$ ,  $20^\circ\text{C}$ ) for control experiment, where hydroxyl-functionalised AuNP-4 was used in place of dihydroxy-functionalised AuNP-5. No assembly could be detected either by TEM or UV-vis spectroscopy.

As 40 nm citrate-stabilised nanoparticles from a commercial source had been exclusively used in the development of the planet–satellite assembly and purification protocols, it was important to also ensure that the formation could be successful with citrate-stabilised nanoparticles in general, as opposed to being induced by some minor component present in the commercial nanoparticle samples. As such, 30 nm citrate-stabilised nanoparticles were

prepared by a literature method.<sup>245</sup> These home-made nanoparticles, which were known to be free of any stabilisers other than citrate, were substituted for the commercial nanoparticles, with no effect on the assembly process.

An explanation for the nanoparticle assembly could involve a direct interaction between the 1,2-diols and the Au surface. Studies under ultrahigh vacuum conditions suggest that alcohols can adsorb weakly on noble metal surfaces at low temperatures,<sup>246,247</sup> but it is clear from the results with monohydroxy-functionalised AuNP-4 that such a process alone is not sufficient to achieve nanoparticle self-assembly. A chelate interaction between the 1,2-diols of AuNP-5 and metal surface atoms may of course enhance this interaction, yet would still require penetration and displacement of the surface-bound citrate monolayer and a significant Au–diol binding energy, which does not seem to be preceded by other solution phase results on either flat or nanoparticle surfaces.

A more likely explanation would involve interaction of the 1,2-diols with the citrate monolayer through hydrogen bonding. Investigations to elucidate the structure of the charge stabilising layer of citrate-stabilised nanoparticles have suggested that citrate binds to AuNP surfaces through two carboxylate–Au interactions. This leaves one free carboxylate which is involved in hydrogen bonding to a weakly associated citric acid adlayer.<sup>11</sup> Despite the inherently limited stabilisation provided by hydroxyl-based hydrogen bonds in aqueous environments,<sup>239</sup> a cooperative multi-point interaction between the 1,2-dihydroxy motif on AuNP-5 and a nanoparticle-bound carboxylate may be sufficient to displace the secondary citric acid layer.<sup>248–253</sup>

An NMR titration between model 1,2-diol **22** and sodium citrate in water indicated a very weak interaction between the diol and the citrate (**Figure 5.25**). Fluorinated molecular 1,2-diol **22** was kept at constant concentration, and trisodium citrate was added, resulting in a shift in the position of the <sup>19</sup>F resonance of the 1,2-diol, indicating an interaction with the citrate. The titration data was fitted to a 1:1 binding isotherm to give an association constant of 4.7 M<sup>-1</sup>. Fitting to a 1:1 binding isotherm is assumed because citrate is in a

large excess, even at early stages of the titration, though 2:1 and 3:1 complexes are possible too. It should be noted that the titration had relatively few data points and the interaction was very weak, so the absolute value should be viewed as tentative. Nonetheless, a small but measurable association constant for a single interaction of a diol with citrate supports the theory that a highly multivalent interaction between 1,2-diol-coated AuNP-5 and the citrate-stabilised nanoparticles could be responsible for the assembly.

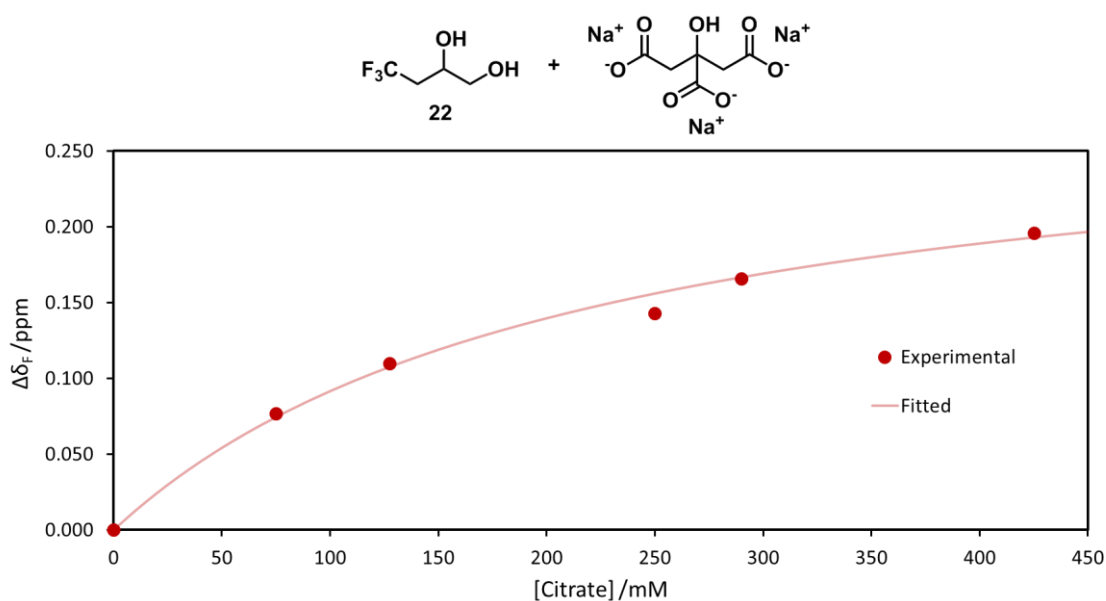


**Figure 5.25** NMR titration data of fluorinated 1,2-diol **22** (8.56 mM) with trisodium citrate. The shift in the  $^{19}\text{F}$  resonance of 1,2-diol **22** was fitted to a 1:1 binding isotherm, giving  $K_a = 4.7 \text{ M}^{-1}$ .

The cumulative multivalence of several such interactions between the two densely functionalised nanoparticle surfaces could then explain the robust planet–satellite nanoparticle association. Alternatively, once the nanoparticles have been brought together initially, van der Waals interactions between the two relatively large surfaces may also contribute to assembly stability.

With the exception of biomolecule-based systems,<sup>23,212</sup> multivalent hydrogen bonding under aqueous conditions has previously been invoked in only a handful of cases to explain nanoparticle aggregation.<sup>248–253</sup> Each of these cases involves only a single nanoparticle building block and achieves limited structural control and stability.

## 5.5 Modifying the ‘planet’ nanoparticle

Assembly of 1,2-diol-coated AuNP-5 with citrate-stabilised nanoparticles to form planet–satellite assemblies was observed using either commercial 40 nm citrate-stabilised nanoparticles or home-made 30 nm citrate-stabilised nanoparticles. In both cases planet–satellite assemblies were obtained and could be purified. Modification of the size of the planet nanoparticle was extended by substituting 150 nm citrate-stabilised cores. Again, assembly occurred as previously (**Figure 5.26**), and the resultant planet–satellite assemblies could be purified by precipitation–redispersion as before.

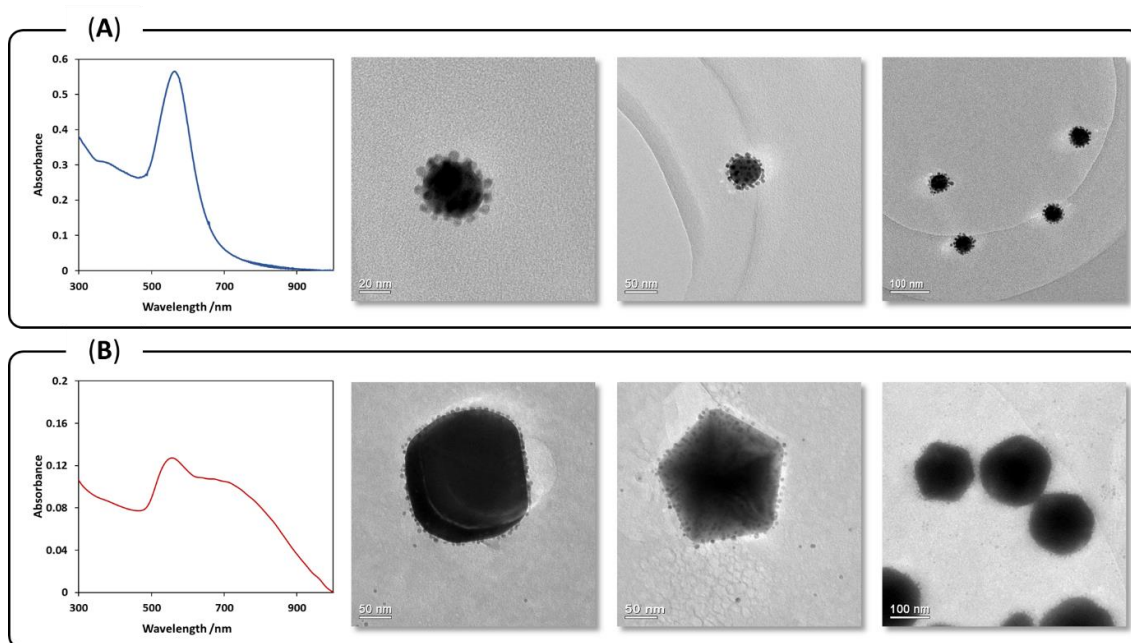


**Figure 5.26** UV-vis ( $\text{H}_2\text{O}$ , 20 °C) and representative TEM images of planet–satellite assemblies with different planet nanoparticle sizes: (A) 30 nm and (B) 150 nm. The synthesis and purification procedure was as described for the 40 nm core planet–satellite assemblies.

In addition to modifications of the planet size, the shape of the planet nanoparticle was also varied. A solution of citrate-stabilised nanoparticles was prepared, consisting of a variety of shapes and sizes (**Chapter 7.3.2**). The shapes of the nanoparticles were generally spherical, triangular prismatic or rod-like. Upon mixing with AuNP-5, planet–satellite assembly was again observed, with all nanoparticles, regardless of shape or size, being uniformly

coated by AuNP-5. It was again possible to remove excess AuNP-5 by centrifugation–precipitation (**Figure 5.27**).

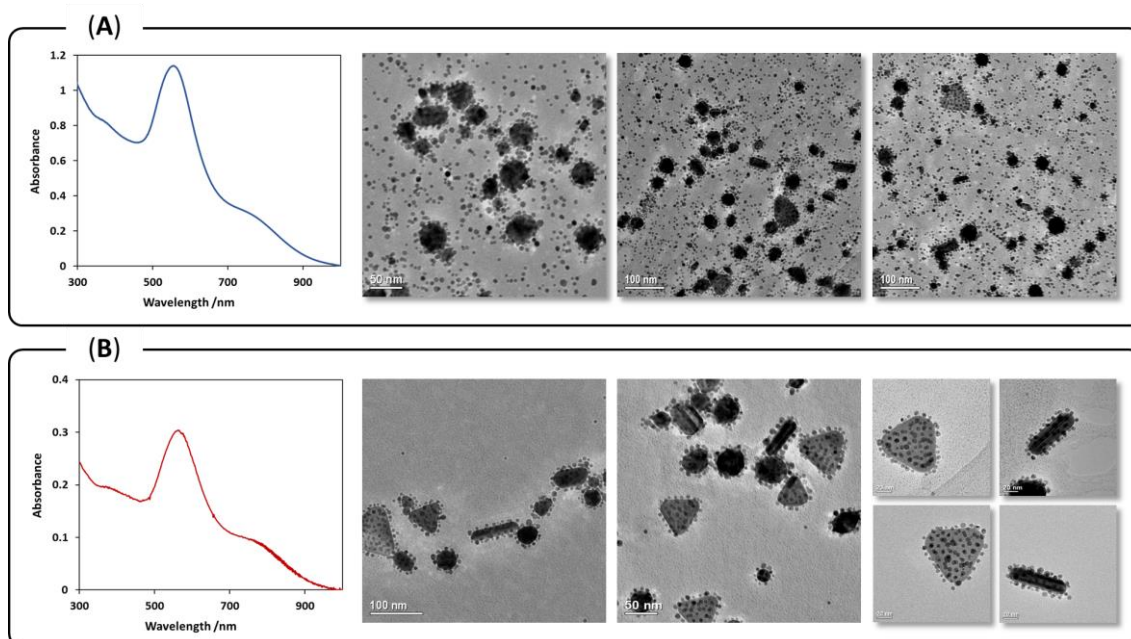


**Figure 5.27** UV-vis ( $\text{H}_2\text{O}$ , 20 °C) and representative TEM images of planet–satellite assemblies with planet nanoparticles of varying shapes and sizes. Synthesis and purification of the sample was carried out as described for the 40 nm planet–satellite assemblies.

It may be desirable for certain applications to change the nanoparticle material. For this reason, 40 nm commercial silver citrate-stabilised nanoparticles were investigated as potential planet nanoparticles for planet–satellite assembly. As with the 40 nm gold nanoparticles, the concentration of the silver nanoparticles was first determined.

Extinction coefficients ( $\epsilon$ ) at  $\lambda_{\text{max}}$  (SPR) could be estimated for the silver nanoparticles using **Equation 5.3**,<sup>254</sup> where  $d$  is the mean particle diameter in nm,  $A = 4.20 \times 10^8$  and  $\gamma = 0.77$ .

$$\epsilon = Ad^{\gamma}$$

**Equation 5.3**

This gave a value for the extinction coefficient of 40 nm commercial silver citrate-stabilised nanoparticles as  $7.19 \times 10^9$  and a nanoparticle concentration of 0.0949 nM.

As for the gold nanoparticles, in order to establish the optimum stoichiometric ratio for planet–satellite assembly with silver nanoparticles, the component nanoparticles were mixed in different ratios, ranging from 10:1 to 1000:1 AuNP-5:silver citrate-NP. Monitoring the resulting assembly by UV-vis spectroscopy revealed an optimum mixing ratio at 250:1 (**Figure 5.28**), very similar to the gold planets, which is consistent with the maximal shift being determined solely by the geometrical dimensions of the two nanoparticle components.

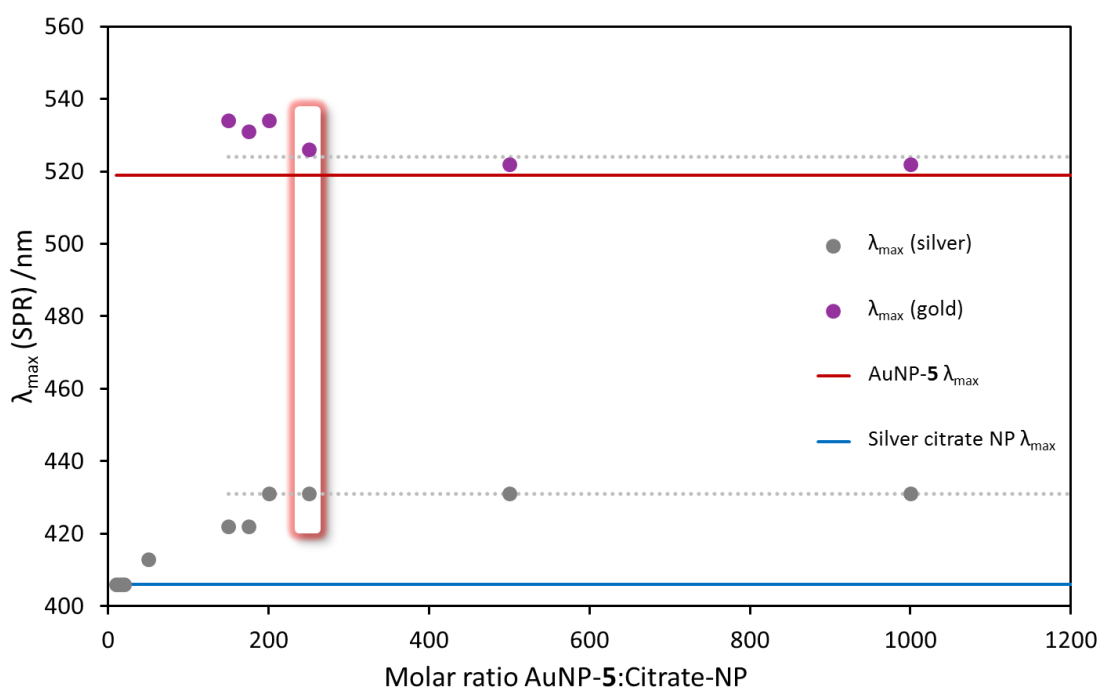


**Figure 5.28** Plot of  $\lambda_{\max}$  (SPR) observed for colloidal dispersions with varying AuNP-5:silver-citrate-NP (40 nm) ratio (H<sub>2</sub>O, 20 °C). The plateau in the shifts of both the silver and gold SPR bands is at a ratio of 250:1, revealing the optimum mixing ratio for planet–satellite formation. The solid red and blue lines indicate  $\lambda_{\max}$  (SPR) of the component nanoparticles in isolation; the dotted lines provide a guide for the eye.

In the case of gold planets, an increase in the wavelength of  $\lambda_{\max}$  (SPR) was observed as more planet–satellite assemblies were formed, followed by a decrease as unbound AuNP-5 started to dominate the spectra. Silver nanoparticles have an SPR band at much shorter wavelengths, around 400 nm as opposed to 500 nm for gold; therefore the SPR bands for the two component nanoparticles do not overlap, allowing the observation of an increase of the

silver SPR band wavelength, and a corresponding decrease of the gold SPR wavelength. Both SPR bands then reach a plateau, at a mixing ratio of 250:1. Higher mixing ratios do not result in a change in the position of the SPR bands of either the gold or the silver. The silver has by this stage formed isotropic, fully coated planet–satellite assemblies, therefore no further plasmon coupling can occur, whereas for the gold peak, the spectrum is now dominated by the unbound AuNP-5.

The purification protocol for the silver-planet assemblies has not been optimised to the same degree as with the gold-planet assemblies, but a similar centrifugation-induced precipitation–redispersion process was employed, centrifuging the samples first at 1500 rcf for four minutes, then at 1800 rcf for four minutes to give near-pure solutions of planet–satellite assemblies (**Figure 5.29**).

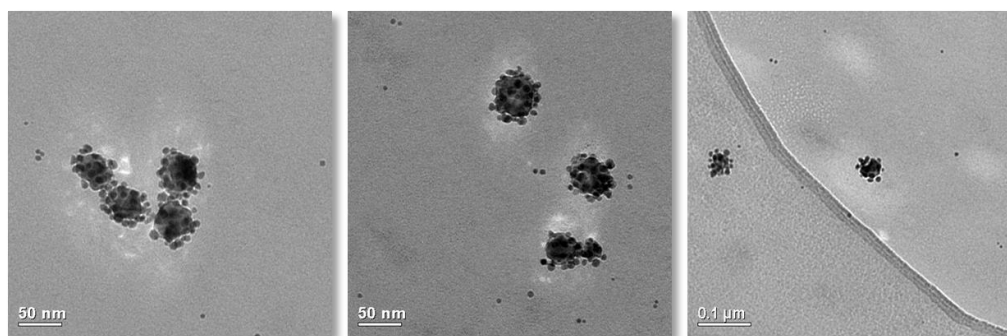


**Figure 5.29** Representative TEM images showing planet–satellite assemblies composed of 1,2-diol-coated AuNP-5 and a 40 nm silver citrate-stabilised planet core.

## 5.6 Planet–satellite assemblies for surface-enhanced Raman spectroscopy

One attractive feature of nanoparticle assemblies such as these is the multitude of field enhancement ‘hotspots’ located at inter-nanoparticle gaps,<sup>224</sup> offering the potential for surface-enhanced Raman spectroscopy (SERS). SERS relies on the incorporation of an analyte in a ‘hotspot’. Hotspots are formed at nanoscale gaps, for example between nanoparticles. The strongest hotspots

are formed where the plasmon coupling of the component nanoparticles is highest. The planet–satellite assemblies presented here have a number of features which make them attractive for SERS uses. The large SPR red shifts seen for the planet–satellite assemblies suggest that the hotspots will be suitable for SERS uses. The assemblies' aqueous solubility, uniform structure, and temporal colloidal and structural stability also lends itself to potential biological SERS applications. Planet–satellite assemblies previously used for SERS applications often involve assembly of the planet–satellite structure around the reporter.<sup>87,90,226,238</sup> The molecular simplicity of the planet–satellite assemblies presented here and their structural simplicity give rise to the potential for incorporating an SERS-active probe within the nanoparticle gaps and evaluating the SERS enhancement.

Thiophenol is a SERS reporter which shows a distinctive peak at  $1000\text{ cm}^{-1}$ . An ethanolic solution of thiophenol was mixed with as-made planet–satellite assemblies to give three solutions resulting in a final thiophenol concentration ranging from  $10^{-5}\text{ M}$  to  $10^{-7}\text{ M}$ . These solutions were incubated for 30 minutes, and then centrifuged at 1500 rcf for 20 minutes to induce nanoparticle precipitation. The solvent was decanted to remove excess thiophenol and ethanol, and the nanoparticles were resuspended in water. Raman spectra were acquired using an excitation wavelength of 638 nm (**Figure 5.30**).

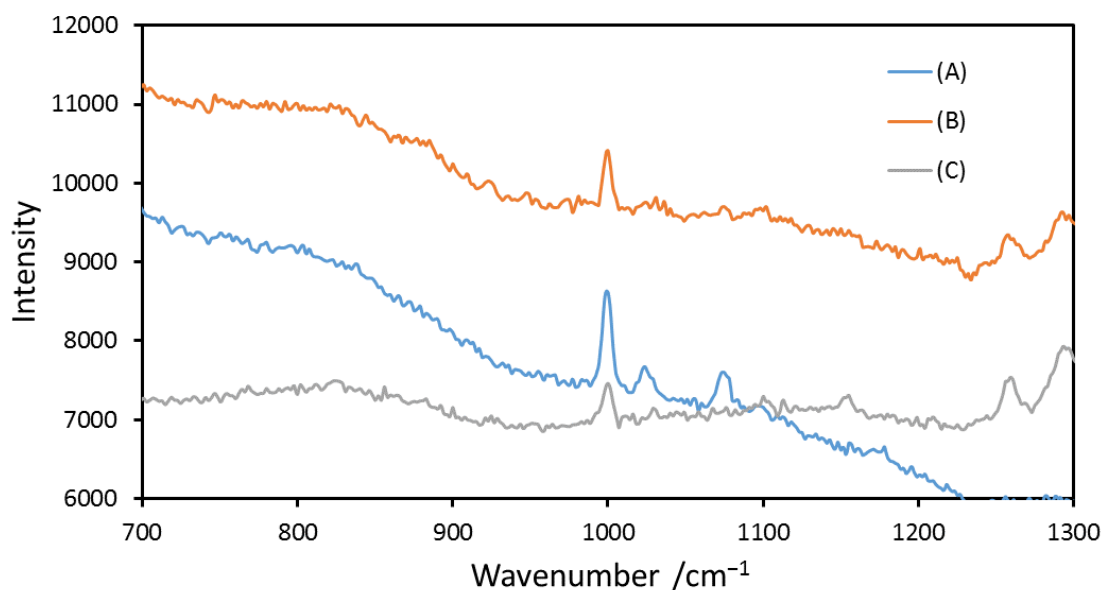


**Figure 5.30** Partial Raman spectra of planet–satellite assemblies mixed with (A)  $10^{-5}$  M thiophenol, (B)  $10^{-6}$  M thiophenol and (C)  $10^{-7}$  M thiophenol. Spectra were acquired using an excitation wavelength of 638 nm, with a 10 second acquisition. Each spectrum is the result of averaging three scans. The thiophenol peak is seen at  $1000\text{ cm}^{-1}$ .

The resultant Raman spectra all contained signals corresponding to the thiophenol probe, indicating that for all samples the thiophenol was incorporated into the hotspots of the planet–satellite assemblies. The thiophenol could be easily detected at all concentrations simply by mixing with the pre-formed planet–satellite assemblies. It can also be noted that while the signal intensity did decrease as the concentration of thiophenol was decreased, the decrease in signal intensity did not drop by an order of magnitude (**Table 5.3**).

**Table 5.3** Peak height analysis of the thiophenol peak at  $1000\text{ cm}^{-1}$  in Raman spectra of planet–satellite assemblies mixed with thiophenol.

[Thiophenol] / M	Peak height
$10^{-5}$	1176
$10^{-6}$	573
$10^{-7}$	462

The peak height decreases only by approximately half, despite a one hundred-fold decrease in the thiophenol concentration. If all the thiophenol were incorporated into uniform hotspots, the decrease in peak height would be expected to be in proportion to the thiophenol concentration. As this is not the case, it is likely that the decrease is due to the difference in the incorporation of thiophenol into the hotspots on the planet–satellite assemblies, which would be expected to occur faster when the thiophenol concentration is higher. This suggests that if longer incubation times were used, the signal intensity may have ended up the same for all samples, as the hotspots were saturated with receptor. By further extension, it might be expected that much lower concentrations of thiophenol would still give good Raman signals, if incubation times were long enough to allow good incorporation of the reporter molecule into the hotspots.

## 5.7 Conclusions and future work

A robust, simple, and versatile solution-phase approach has been developed for the formation of planet–satellite nanoparticle assemblies in a predictable manner, giving rise to reproducible three-dimensional structures. The rapid, one-step assembly procedure does not require careful control of environmental conditions, eliminates the need for complex biological, supramolecular or macromolecular nanoparticle ligands, and is readily scalable. Dense isotropic coverage of the planet nanoparticles can be achieved, irrespective of surface area, through optimisation of building block stoichiometry using simple spectroscopic measurements.

The highly stable characteristics of the satellite nanoparticles are conferred on the binary assemblies, which are dispersible in either aqueous or organic media. This allows rapid and efficient purification via standard techniques, without recourse to additional capping or stabilising steps.<sup>90</sup> The use of small molecules to direct assembly, as opposed to oligonucleotides, gives rise to short inter-nanoparticle distances, which produce large SPR red shifts for the

resulting planet–satellite assemblies, producing intense electromagnetic field enhancements at hotspots between the neighbouring nanoparticle surfaces.

Preliminary investigations into harnessing the field enhancement of the planet–satellite assemblies for SERS applications have been conducted, simply by mixing the pre-formed nanoparticle architectures with a Raman reporter, to simply generate Raman signals even at very low ( $< 10^{-7}$  M) receptor concentrations. The simplicity of the approach is very attractive. Other planet–satellite assemblies employed for SERS applications tend to require assembly around the reporter.<sup>90,238</sup> Being able to simply mix the pre-formed nanoparticle architecture with a reporter in order to obtain SERS enhancement is a highly attractive prospect. The colloidal stability of the assemblies is also highly attractive: the assemblies remained stable in solution for  $> 24$  hours after mixing with the thiophenol Raman reporter, whereas mixing the reporter with citrate-stabilised nanoparticles induced particle aggregation and a loss of colloidal stability within 30 minutes, necessitating immediate acquisition of solution-phase SERS measurements.

The level of control achieved here is highly encouraging in the quest to develop a generalisable nanoparticle building block toolkit that can rival the pre-eminent oligonucleotide approaches by exploiting the stability and structural diversity of nonbiomolecular synthetic chemistry. Thus far, only two components have been employed in the assemblies. One way to increase the sophistication of nanoparticle architectures is to introduce a third building block. The surface of the planet–satellite assemblies is coated in the same 1,2-diol ligands as component AuNP-5. Mixing pre-formed planet–satellite assemblies with another citrate-stabilised nanoparticle is expected to give rise to further assembly in a hierarchical manner, where smaller component nanoparticles are used to build larger building blocks, which are in turn combined to give larger structures (**Figure 5.31**).

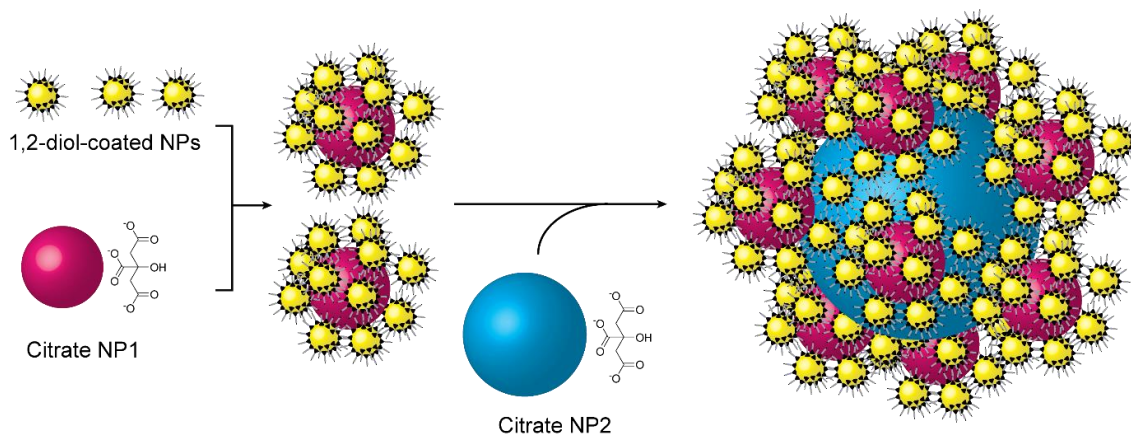


**Figure 5.31** Schematic representation of the hierarchical assembly of extended nanostructures. Planet–satellite assemblies are formed initially as discussed, and then subsequently used as building blocks for coating another nanoparticle.

Initial experiments in which the pre-formed planet–satellite assemblies were simply mixed with 150 nm citrate-stabilised nanoparticles in a 1:1 v/v ratio showed some promise. TEM images revealed that the pre-formed planet–satellite assemblies were indeed attaching to the new, larger citrate-stabilised nanoparticles (**Figure 5.32**). However, complete isotropic coverage was not observed, with generally just a few planet–satellite assemblies attached to each 150 nm citrate-stabilised nanoparticle. A large excess of free planet–satellite assemblies unattached to the 150 nm citrate-stabilised nanoparticles was also observed.

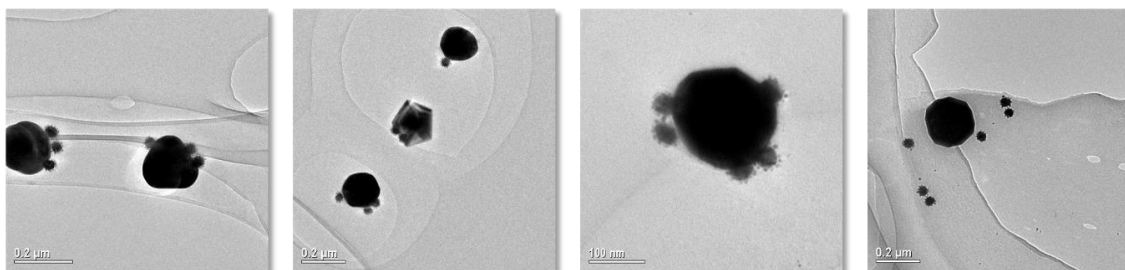


**Figure 5.32** TEM images of a solution where planet–satellite assemblies were mixed in a 1:1 v/v ratio with commercially purchased 150 nm citrate-stabilised nanoparticles resulting in the hierarchical assembly of three-nanoparticle component structures.

It is likely that the poor coverage is due to electrostatic repulsions. Zeta-potential measurements (**Table 5.2**) revealed that although the negative charge of the citrate-stabilised planet nanoparticle is screened by the satellite nanoparticles, the overall assembly still carries a negative charge. If this can be

addressed through charge-screening, then the potential for hierarchical bottom–up assembly of multi-component structures from these simple nanoparticle building blocks is a distinct, exciting possibility.

# Chapter 6:

## General conclusions

This thesis presents research pertaining to the vision of developing a toolkit of nanoparticle building blocks, which may be assembled in a predictable and controlled way, governed by relatively simple and easily optimised abiotic molecular systems. The interesting and often unique properties defined by nanoparticle chemical composition, size and shape, also crucially depend on assembly structure when several nanoparticles are brought together. Simple, nonbiomolecular assembly strategies have so far failed to deliver a precise level of control over nanoparticle assembly. This thesis develops the use of simple, small organic molecules for the control of nanoparticle functionalisation and assembly.

Using gold nanoparticles as a prototypical monolayer-stabilised nanoparticle systems, the synthesis of functionalised nanoparticles has been explored through the use of a single-phase method. This operationally simple approach has been applied to the synthesis of a range of functionalised nanoparticles, offering access to both organic and water-soluble nanoparticles with a narrow size distribution. Furthermore, control over nanoparticle size has been demonstrated in a ligand-nonspecific manner, whereby a slower rate of addition of the reducing agent results in a larger nanoparticle size, crucially, with no detrimental effect on the nanoparticle size distribution. Previously, identically functionalised nanoparticles of different sizes could only be accessed through ligand exchange procedures. The slow addition approach for tuning nanoparticle size developed here offers a general approach to the size-controlled synthesis of functionalised nanoparticles, resulting in easy access to nanoparticle building blocks in a range of sizes.

The reversibly dynamic covalent properties of boronic ester formation presents a highly desirable route to the functionalisation and assembly of nanoparticles. Boronic acid functionalised gold nanoparticles have been synthesised and fully

characterised. Detailed molecular-level characterisation revealed the peroxide-induced oxidation of boronic acids to the corresponding phenol during the synthesis. This phenomenon was suppressed by the addition of an antioxidant, establishing a robust route to boronic acid functionalised nanoparticles in high purity and with control of nanoparticle size. The oxidation of nanoparticle-bound boronic acids has significant implications for a variety of other functionalised nanoparticle systems that seek to exploit boronic acid chemistry but for which molecular-level characterisation has not to this point been achieved.

Boronic ester formation has been investigated, and catechol, salicylic acid and salicylamide have been established as a range of isostructural binding partners for boronic acids, exhibiting a range of association constants across an order of magnitude for the molecular processes in freely-dissolved solution. Direct molecular evidence from  $^{19}\text{F}$  NMR spectroscopy of nanoparticle-bound boronic ester formation has been demonstrated for the first time. Dynamic boronic ester exchange has been demonstrated in a reversible manner, confirming the equilibrium control of the process on nanoparticle-bound monolayers.  $^{19}\text{F}$  NMR spectroscopy has further allowed the characterisation of nanoparticle-bound boronic ester formation in a quantitative manner, allowing association constants to be measured for the process within the nanoparticle-bound monolayer. The association constants for boronic ester formation on nanoparticle-bound boronic acids are lower than for corresponding isostructural freely soluble model compounds. This is attributed to a negative cooperativity on nanoparticle-bound boronic ester formation due to steric crowding. Initial experiments indicate that even minor structural changes of the binding partner can strongly influence the extent of this steric effect.

Having established the thermodynamic control of nanoparticle-bound boronic ester formation, boronic ester-mediated assembly of nanoparticles was investigated. A bis-catechol linker was shown to induce nanoparticle assembly by covalently linking nanoparticles. Covalently linked nanoparticles precipitated as large aggregates. Remarkably, these covalently linked aggregates could be entirely disassembled and re-suspended by addition of a molecular stimulus to break the inter-nanoparticle covalent boronic ester linkages. Varying the

nanoparticle/linker ratio resulted in a quantifiable change in assembly morphology. Chemical changes in the linker structure demonstrated the link between molecular input and assembly morphology further, demonstrating in turn, for the first time, molecular control over dynamic covalently-linked nanoparticle assemblies. This establishes the presence of fundamental links between the molecular details of nanoparticle-bound dynamic covalent processes with the resulting assembly structure upon formation of dynamic covalently-linked assemblies.

Boronic ester mediated nanoparticle assembly offers a combination of kinetic lability and covalent bond strength. Much weaker noncovalent interactions which also present kinetic lability offer the prospect for sufficient bond strength are employed in a highly multivalent fashion. An unanticipated observation of assembly between 1,2-diol-functionalised nanoparticle and citrate-stabilised nanoparticles to form planet–satellite nanoparticle architectures presented an alternative assembly strategy based on highly multivalent hydrogen bonding. The resulting assemblies were shown to be both highly structurally and colloidal stable, with the colloidal stability properties of the 1,2-diol satellite nanoparticles transferred to the assembly as a whole. The rapid, operationally simple one-step assembly procedure – which, unlike existing methods, does not require careful control of environmental conditions and eliminates the need for complex biological, supramolecular or macromolecular nanoparticle ligands – is readily scalable. The shape, size and material of the planet nanoparticle were varied, resulting in predictable isotropic coverage of the planet nanoparticle. The resulting nanoparticle assemblies have shown SERS enhancement of a small-molecule probe, simply by mixing the preassembled planet–satellites with the receptor, which contrasts existing methods which require assembly of the planet–satellite structure around the probe.

In this thesis, the development of a general strategy for the assembly of dynamic molecularly controlled building blocks has been pursued. Further investigations to better understand the implications of molecular confinement within a nanoparticle-bound monolayer are certainly key to developing molecular control over nanoparticle assembly. The influence of features such as

nanoparticle size, shape, ligand length and reactive ligand surface concentration is not well understood. As demonstrated by the boronic ester-mediated nanoparticle assembly, the molecular detail of binding strength determines the nanoparticle assembly structure. Many of the fundamental principles of reactivity of nanoparticle-bound boronic acids should apply to a range of dynamic covalent reactions (for example, hydrazones, imines and acetals), further emphasising the urgent need for a better understanding of these processes at the molecular level.

Despite the inherent challenges of studying nanoparticle-bound systems, the links between molecular structure and assembly properties demonstrated in this thesis highlight the importance of future work in this field. A better understanding of the reactivity of nanoparticle-bound molecular species will pave the way for accessing the full potential for the rational design of predictable, reconfigurable dynamic nanoparticle assembly systems, and therefore allow access to new nanomaterials and nanodevices.

# Chapter 7: Experimental and synthetic procedures

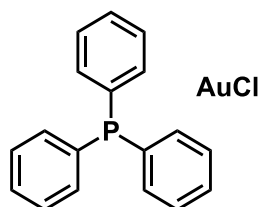
## 7.1 General experimental procedures

Unless stated otherwise, all reagents were purchased from commercial sources (Sigma Aldrich UK, Alfa Aesar UK, Acros UK, TCI UK, Fluorochem or Apollo Scientific) and used without further purification. Commercial citrate-stabilized nanoparticle (NP) samples were purchased from BBI Scientific and used as supplied. Dry solvents were obtained by means of a MBBRAUN MB SPS-800TM solvent purification system, where solvents were passed through filter columns and dispensed under an argon atmosphere. Nanopure water from an Elga PURELAB Classic system was used throughout for all NP work. Organic compounds were purified by trituration, recrystallisation or flash column chromatography. Flash column chromatography was performed using Geduran® Si60 (40-63  $\mu\text{m}$ , Merck, Germany) as the stationary phase, and thin-layer chromatography (TLC) was performed on pre-coated silica gel plates (0.25 mm thick, 60F254, Merck, Germany) and observed under UV light ( $\lambda_{\text{max}}$  254 nm), or visualized by staining with a basic potassium permanganate solution, followed by heating. Compounds containing boronic acids or catechols could not be analysed by TLC (or purified by column chromatography) due to streaking and irreversible adsorption of boronic acids or oxidation of catechols on silica. AuNP micrographs were obtained using a JEM 2010 TEM on samples prepared by deposition of one drop of nanoparticle suspension on Holey Carbon Films on 300 mesh Cu grids (Agar Scientific®). Nanoparticle diameters were measured automatically using the software ImageJ. The images were first converted to black and white images using the “Threshold” function. The area of the nanoparticles was measured using the “Analyze particles” function. Particles on edges were excluded. UV-vis spectroscopy was performed using a Thermo Scientific Evolution Array UV-Visible Spectrophotometer or a Thermo Scientific

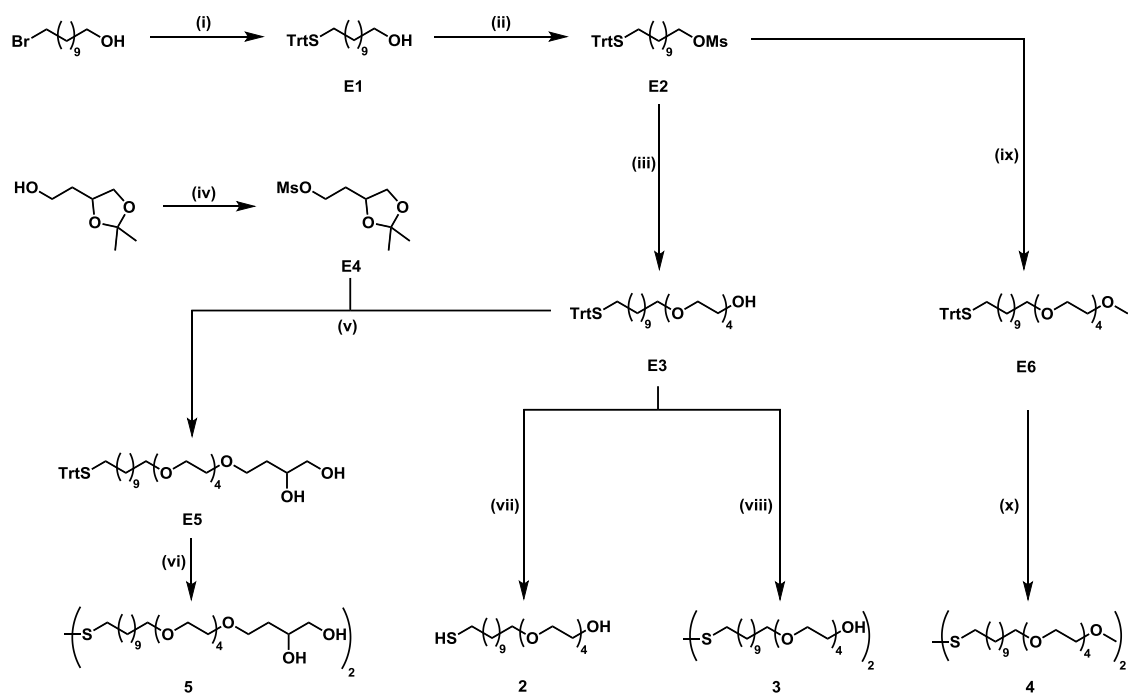
Evolution 220 UV-Visible Spectrophotometer.  $^1\text{H}$ ,  $^{13}\text{C}$ ,  $^{19}\text{F}$  and  $^{31}\text{P}$  NMR spectra were recorded on Bruker Avance II 300, 400 and 500 instruments, at a constant temperature of 25 °C.  $^1\text{H}$  and  $^{13}\text{C}$  chemical shifts are reported in parts per million (ppm) from low to high field and referenced to the literature values for chemical shifts of residual non-deuterated solvent, with respect to tetramethylsilane.  $^{19}\text{F}$  NMR chemical shifts are referenced to  $\text{CFCl}_3$  (0.00 ppm) as external standard.  $^{31}\text{P}$  NMR chemical shifts are referenced to  $\text{PPh}_3$  (–6.00 ppm) as external standard. Standard abbreviations indicating multiplicity are used as follows: bs (broad singlet), bm (broad multiplet), d (doublet), dd (doublet of doublets), m (multiplet), q (quartet), s (singlet), t (triplet), tt (triplet of triplets), J (coupling constant). Spectra were analyzed using MestReNova (Version 9.0.0). Quantitative NMR experiments were run with a pulse delay time  $> 5 \times T_1$  for the slowest relaxing signal present. Melting points were determined using a Stuart SMP30 Melting Point Apparatus and are reported uncorrected. Mass spectrometry was also carried out at the EPSRC National Mass Spectrometry Facility on a Thermo Scientific LTQ Orbitrap XL. DLS measurements were performed on a Malvern Zetasizer  $\mu\text{V}$  instrument, with three replicates of 10–15 runs used throughout. The number of runs was determined automatically. Zetapotential measurements were performed on a Malvern Zetasizer ZS instrument. Raman spectra were obtained using a Snowy Range Sierra instrument with a 638 nm laser.

## 7.2 Synthesis of organic compounds

### Compound 1: Chloro(triphenylphosphine)gold(I)

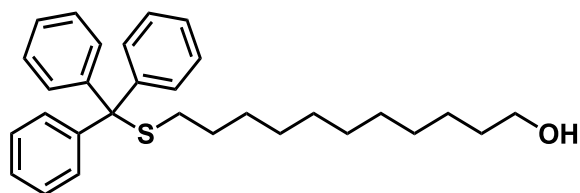


A solution of PPh<sub>3</sub> (735 mg, 2.80 mmol) in diethyl ether (10 mL) was added dropwise to a solution of HAuCl<sub>4</sub>·3H<sub>2</sub>O (500 mg, 1.47 mmol) in diethyl ether (30 mL). The reaction mixture was stirred at 0 °C for three hours, and then allowed to warm to RT. The resulting white precipitate was filtered and washed with cold Et<sub>2</sub>O to give an off-white solid. This solid was recrystallised from CH<sub>2</sub>Cl<sub>2</sub>/hexane to give the desired gold complex **1** as a crystalline white solid (500 mg, 1.01 mmol, 69%); M.p.: 236–237 °C (In agreement with literature values<sup>255a</sup>); <sup>1</sup>H NMR (300.1 MHz, CDCl<sub>3</sub>): δ 7.55–7.45 (15H, m, ArH); <sup>13</sup>C NMR (125.8 MHz, CDCl<sub>3</sub>): δ 134.4–134.1 (d, *J* = 14 Hz), 132.3–132.0 (d, *J* = 3 Hz), 129.5–129.3 (d, *J* = 12 Hz), 129.1–128.4 (d, *J* = 97 Hz); <sup>31</sup>P NMR (121.5 MHz, CDCl<sub>3</sub>): δ 33.5 (1P, s); HRMS (ES<sup>+</sup>) *m/z* calculated for [M+Na]<sup>+</sup> C<sub>18</sub>H<sub>15</sub>AuClNaP 517.0158, found 517.0162.



**Scheme 7.1** Reagents and conditions for synthesis of thiol/disulfide ligands **5**, **2**, **3** and **4**. (i) NaOH/H<sub>2</sub>O, Ph<sub>3</sub>CSH, EtOH, PhMe, 5 h, RT, 99%. (ii) MsCl, Et<sub>3</sub>N, CH<sub>2</sub>Cl<sub>2</sub>, 3 h, 0 °C, 99%. (iii) NaOH/H<sub>2</sub>O, tetraethylene glycol, 100 °C, 24 h, 81%. (iv) MsCl, Et<sub>3</sub>N, CH<sub>2</sub>Cl<sub>2</sub>, 18 h, 0 °C, 99%. (v) 1. NaH, THF, 96 h, reflux; 2. HCl/H<sub>2</sub>O, MeOH, RT, 3 h, 15%. (vi) I<sub>2</sub>, MeOH, 4 h, RT, 82%. (vii) CF<sub>3</sub>CO<sub>2</sub>H, <sup>3</sup>Pr<sub>3</sub>SiH, CH<sub>2</sub>Cl<sub>2</sub>, 5 h, RT, 84%. (viii) I<sub>2</sub>, MeOH, 4 h, RT, 74%. (ix) NaH, tetraethylene glycol monomethyl ether, THF, reflux, 18 h, 40%. (x) I<sub>2</sub>, MeOH, 4 h, RT, 53%.

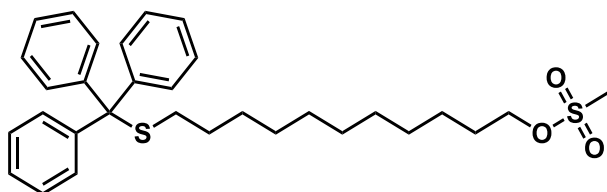
### Compound E1: 11-(tritylthio)undecan-1-ol



A solution of NaOH (2.67 g, 66.8 mmol) in H<sub>2</sub>O (25 mL) was added to a solution of triphenylmethanethiol (12.3 g, 44.5 mmol) in a mixture of EtOH/PhMe (1:1 v/v, 100 mL). 11-Bromo-1-undecanol (11.2 mg, 44.5 mmol) was dissolved in a second solution of EtOH/PhMe (1:1 v/v, 100 mL), which was then added to the triphenylmethanethiol mixture in one portion. The reaction mixture was stirred for 18 hours at RT. The mixture was poured into a saturated solution of NaHCO<sub>3</sub> (50 mL) and extracted with Et<sub>2</sub>O (3 × 40 mL). The combined organic layers were washed with brine (3 × 40 mL), dried over MgSO<sub>4</sub> and solvent was

removed under vacuum to give a pale yellow oil. The crude product was purified by flash column chromatography (SiO<sub>2</sub>, hexane/EtOAc, 8:1 → 1:1) to give the desired product **E1** as a pale yellow oil (17.4 g, 39.0 mmol, 88%, spectral data in agreement with the literature<sup>256</sup>); <sup>1</sup>H NMR (500.1 MHz, CDCl<sub>3</sub>): δ 7.46–7.43 (6H, dd, *J* = 9.0 Hz, *J* = 1.5 Hz, Ar*H*), 7.19–7.34 (9H, m, Ar*H*), 3.66 (2H, t, *J* = 7.5 Hz, CH<sub>2</sub>OH), 2.16 (2H, t, *J* = 7.5 Hz, CH<sub>2</sub>S), 1.59 (2H, qn, *J* = 7.5 Hz, CH<sub>2</sub>), 1.44–1.20 (16H, m, CH<sub>2</sub>); <sup>13</sup>C NMR (125.8 MHz, CDCl<sub>3</sub>): δ 145.2 (ArC), 129.7 (ArCH), 127.9 (ArCH), 126.6 (ArCH), 66.4 (C<sub>q</sub>), 63.1 (CH<sub>2</sub>O), 34.2 (CH<sub>2</sub>S), 32.9 (CH<sub>2</sub>), 32.1 (CH<sub>2</sub>), 29.7 (CH<sub>2</sub>), 29.6 (CH<sub>2</sub>), 29.5 (CH<sub>2</sub>), 29.3 (CH<sub>2</sub>), 29.1 (CH<sub>2</sub>), 28.7 (CH<sub>2</sub>), 25.8 (CH<sub>2</sub>).

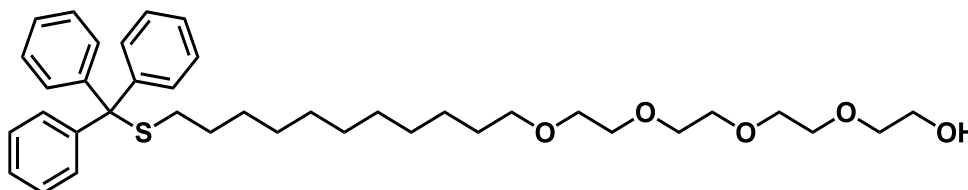
### Compound E2: 11-(tritylthio)undecyl methanesulfonate



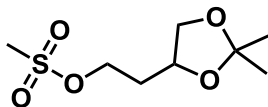
A solution of 11-(tritylthio)undecan-1-ol **E1** (17.4 g, 39.0 mmol) and triethylamine (6.70 g, 58.5 mmol) in dry CH<sub>2</sub>Cl<sub>2</sub> (100 mL) was cooled to 4 °C and stirred under argon. Methanesulfonyl chloride (7.89 g, 78.0 mmol) in dry CH<sub>2</sub>Cl<sub>2</sub> (50 mL) was added dropwise, while maintaining the temperature below 5 °C. The reaction mixture was stirred for 30 minutes at 4 °C and then allowed to warm to RT and stirred for a further 2 hours. Solvent was then removed under reduced pressure. The resulting residue was redissolved in CH<sub>2</sub>Cl<sub>2</sub> (30 mL) and washed with 0.1 M HCl (2 × 20 mL), saturated NaHCO<sub>3</sub> solution (3 × 20 mL), and brine (2 × 20 mL). The organic layer was dried over Na<sub>2</sub>SO<sub>4</sub> and concentrated under reduced pressure to give the desired product **E2** as a yellow oil (19.4 g, 36.9 mmol, 95%, spectral data in agreement with the literature<sup>256</sup>); <sup>1</sup>H NMR (500.1 MHz, CDCl<sub>3</sub>): δ 7.44 (6H, dd, *J* = 6.0 Hz, *J* = 1.5 Hz, Ar*H*), 7.33–7.20 (9H, m, Ar*H*), 4.24 (2H, t, *J* = 6.0 Hz, CH<sub>2</sub>O), 3.02 (3H, s, CH<sub>3</sub>), 2.16 (2H, t, *J* = 7.5 Hz, CH<sub>2</sub>S), 1.77 (2H, qn, *J* = 6.0 Hz, CH<sub>2</sub>), 1.44–1.20 (16H, m, CH<sub>2</sub>); <sup>13</sup>C NMR (125.8 MHz, CDCl<sub>3</sub>): δ 145.2 (ArC), 129.7 (ArCH),

127.9 (ArCH), 126.6 (ArCH), 70.3 (CH<sub>2</sub>O), 66.5 (C<sub>q</sub>), 52.7 (CH<sub>3</sub>), 37.5 (CH<sub>2</sub>S), 32.1 (CH<sub>2</sub>), 29.5 (CH<sub>2</sub>), 29.5 (CH<sub>2</sub>), 29.3 (CH<sub>2</sub>), 29.2 (CH<sub>2</sub>), 29.1 (CH<sub>2</sub>), 29.1 (CH<sub>2</sub>), 28.7 (CH<sub>2</sub>), 25.5 (CH<sub>2</sub>).

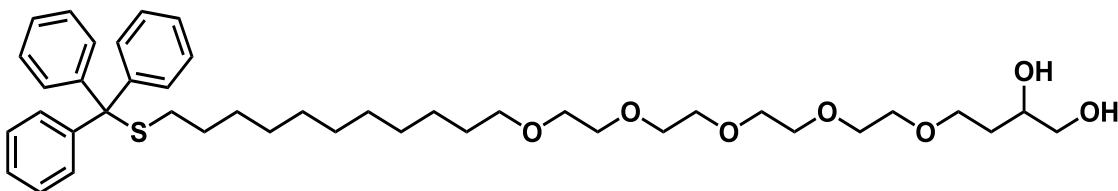
**Compound E3: 1,1,1-triphenyl-14,17,20,23-tetraoxa-2-thiapentacosan-25-ol**



NaOH (1.90 g, 47.4 mmol) in H<sub>2</sub>O (2 mL) was added to tetraethylene glycol (140 g, 720 mmol) and stirred for 1 hour at 90 °C. 11-(tritylthio)undecyl methanesulfonate **E2** (22.6 g, 43.1 mmol) was added to the reaction mixture and stirred for 24 hours at 90 °C (monitored by TLC, hexane/EtOAc, 1:2). After cooling to RT, the reaction mixture was poured into H<sub>2</sub>O (200 mL) and extracted with Et<sub>2</sub>O (5 × 100 mL), washed with saturated NaHCO<sub>3</sub> (3 × 50 mL) and brine (3 × 50 mL), dried over MgSO<sub>4</sub> and evaporated under vacuum to give the desired product **E3** as a yellow oil (20.3 g, 32.5 mmol, 76%, spectral data in agreement with the literature<sup>256</sup>); <sup>1</sup>H NMR (300.1 MHz, CDCl<sub>3</sub>): δ 7.42 (6H, dd, *J* = 6.9 Hz, *J* = 1.5 Hz, ArH), 7.32–7.18 (9H, m, ArH), 3.74 (2H, t, *J* = 4.4 Hz, CH<sub>2</sub>OH), 3.69–3.57 (14H, m, OCH<sub>2</sub>CH<sub>2</sub>O), 3.45 (2H, t, *J* = 6.9 Hz, CH<sub>2</sub>O), 2.13 (2H, t, *J* = 7.5 Hz, CH<sub>2</sub>S), 1.62–1.53 (2H, m, CH<sub>2</sub>), 1.43–1.11 (16H, m, CH<sub>2</sub>); <sup>13</sup>C NMR (75.5 MHz, CDCl<sub>3</sub>): δ 145.2 (ArC), 129.7 (ArCH), 127.9 (ArCH), 126.6 (ArCH), 72.7 (CH<sub>2</sub>O), 71.7 (CH<sub>2</sub>O), 70.8 (CH<sub>2</sub>O), 70.8 (CH<sub>2</sub>O), 70.7 (CH<sub>2</sub>O), 70.7 (CH<sub>2</sub>O), 70.5 (CH<sub>2</sub>O), 70.2 (CH<sub>2</sub>O), 66.5 (C<sub>q</sub>), 61.9 (CH<sub>2</sub>O), 32.2 (CH<sub>2</sub>S), 29.7 (CH<sub>2</sub>), 29.7 (CH<sub>2</sub>), 29.6 (CH<sub>2</sub>), 29.6 (CH<sub>2</sub>), 29.5 (CH<sub>2</sub>), 29.3 (CH<sub>2</sub>), 29.2 (CH<sub>2</sub>), 28.7 (CH<sub>2</sub>), 26.2 (CH<sub>2</sub>); MS (ES<sup>+</sup>) *m/z* 644.93 ([M+Na]<sup>+</sup>, 100).

**Compound E4: 2-(2,2-dimethyl-1,3-dioxolan-4-yl)ethyl methanesulfonate**

To a solution of 4-(2-hydroxyethyl)-2,2-dimethyl-1,3-dioxolane (5.00 g, 30.5 mmol) and Et<sub>3</sub>N (3.69 g, 36.5 mmol) in CH<sub>2</sub>Cl<sub>2</sub> (60 mL) at 0 °C was added dropwise a solution of methanesulfonyl chloride (4.18 g, 36.5 mmol) in CH<sub>2</sub>Cl<sub>2</sub> (20 mL). The reaction mixture was stirred at 0 °C for 1.5 hours, then H<sub>2</sub>O (20 mL) was added. The organic layer was separated, washed with saturated Na<sub>2</sub>CO<sub>3</sub> (2 × 30 mL) and brine (2 × 30 mL), dried over MgSO<sub>4</sub> and concentrated under reduced pressure to give compound **E4** as a yellow oil (5.86 g, 26.1 mmol, 91%, spectral data in agreement with the literature<sup>257</sup>); <sup>1</sup>H NMR (300.1 MHz, CDCl<sub>3</sub>): δ 4.43–4.30 (2H, m, CH<sub>2</sub>O), 4.27–4.18 (1H, m, CH), 4.10 (1H, dd, *J* = 8.1 Hz and *J* = 6.0 Hz, CH<sub>2</sub>), 3.60 (1H, dd, *J* = 8.1 Hz, *J* = 6.5 Hz, CH<sub>2</sub>), 3.02 (3H, s, CH<sub>3</sub>), 2.08 – 1.89 (2H, m, CH<sub>2</sub>), 1.41 (3H, s, CH<sub>3</sub>), 1.35 (3H, s, CH<sub>3</sub>); <sup>13</sup>C NMR (CDCl<sub>3</sub>, 75.5 MHz): δ 109.7 (C<sub>q</sub>), 72.3 (CH), 69.3 (CH<sub>2</sub>), 67.2 (CH<sub>2</sub>), 37.5 (SCH<sub>3</sub>), 33.6 (CH<sub>2</sub>), 27.1 (CH<sub>3</sub>), 25.7 (CH<sub>3</sub>).

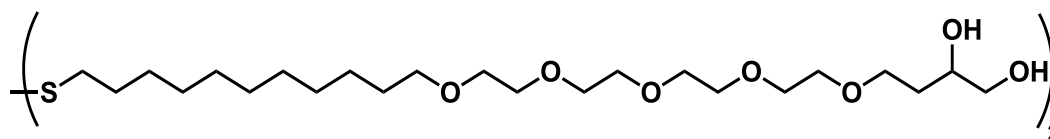
**Compound E5: 1,1,1-triphenyl-14,17,20,23,26-pentaoxa-2-thiatriacontane-29,30-diol**

NaH (0.732 g, 60% dispersion in mineral oil, 18.3 mmol) was added to a solution of trityl protected hydroxythiol **E3** (7.60 g, 12.2 mmol) in dry THF (100 mL) and stirred for 1 hour at 50 °C under argon. To this reaction mixture, methanesulfonate **E4** (3.00 g, 13.4 mmol) was added and refluxed for 18 hours (monitored by TLC, hexane/EtOAc, 1:2). The reaction mixture was quenched

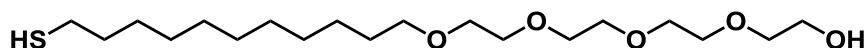
with saturated ammonium chloride, and the volume of solvent was reduced to about 10 mL under vacuum. The residue was diluted with EtOAc (50 mL) and washed with sat. NaHCO<sub>3</sub> (3 × 20 mL) and brine (2 × 30 mL), dried over MgSO<sub>4</sub> and solvent removed under vacuum. The residue was partially purified by column chromatography (hexane/EtOAc, 1:2) to give the intermediate acetal as a pale yellow oil. <sup>1</sup>H NMR (500.1 MHz, CDCl<sub>3</sub>): δ 7.42–7.40, (6H, m, ArH), 7.29–7.26, (6H, m, ArH), 7.21–7.18, (3H, m, ArH), 4.21–4.16 (1H, m, CH), 4.07–4.05 (1H, m, CH<sub>2</sub>), 3.82–3.77 (1H, m, CH<sub>2</sub>'), 3.65 – 3.50, (18H, m, CH<sub>2</sub>O), 3.44 (2H, t, *J* = 7.5 Hz, CH<sub>2</sub>O) 2.12 (2H, t, *J* = 7.5 Hz, CH<sub>2</sub>S), 1.59–1.53 (4H, m, CH<sub>2</sub>), 1.43–1.08 (2H, m, CH<sub>2</sub>), 1.43 (16H, m, CH<sub>2</sub>), 1.40 (3H, s, CH<sub>3</sub>), 1.35 (3H, s, CH<sub>3</sub>).

The oil was dissolved in MeOH (100 mL) and conc. HCl (10 mL) was added. The mixture was stirred at RT for one hour and then neutralised with NaHCO<sub>3</sub>. The volume of solvent was reduced to approximately 20 mL under vacuum, and subsequently the remaining cloudy solution was diluted with water (20 mL) and extracted with CH<sub>2</sub>Cl<sub>2</sub> (3 × 50 mL). The combined organic layers were washed with brine (3 × 30 mL) and dried over MgSO<sub>4</sub>. Solvent was removed under vacuum to give **E5** as a pale yellow oil. (1.95 g, 2.75 mmol, 15%); R<sub>f</sub> = 0.20 (Hexane/EtOAc, 1:2); <sup>1</sup>H NMR (300.1 MHz, CDCl<sub>3</sub>): δ 7.43–7.39, (6H, m, ArH), 7.32–7.26, (6H, m, ArH), 7.26–7.18, (3H, m, ArH), 3.96–3.88 (1H, m, CH), 3.76–3.57, (18H, m, CH<sub>2</sub>O), 3.47–3.42 (4H, m, CH<sub>2</sub>O) 2.13 (2H, t, *J* = 7.5 Hz, CH<sub>2</sub>S), 1.78–1.70 (2H, m, CH<sub>2</sub>), 1.62–1.53 (2H, m, CH<sub>2</sub>), 1.43 (16H, m, CH<sub>2</sub>); <sup>13</sup>C NMR (CDCl<sub>3</sub>, 75.5 MHz): δ 145.2 (ArC), 129.7 (ArCH), 127.9 (ArCH), 126.6 (ArCH), 71.7 (CH<sub>2</sub>O), 70.9 (CHO), 70.9 (CH<sub>2</sub>O), 70.7 (CH<sub>2</sub>O), 70.7 (CH<sub>2</sub>O), 70.7 (CH<sub>2</sub>O), 70.7 (CH<sub>2</sub>O), 70.5 (CH<sub>2</sub>O), 70.3 (CH<sub>2</sub>O), 70.1 (CH<sub>2</sub>O), 68.9 (CH<sub>2</sub>O), 66.7 (C<sub>q</sub>), 32.9 (CH<sub>2</sub>S), 32.2 (CH<sub>2</sub>), 29.7 (CH<sub>2</sub>), 29.7 (CH<sub>2</sub>), 29.6 (CH<sub>2</sub>), 29.6 (CH<sub>2</sub>), 29.5 (CH<sub>2</sub>), 29.3 (CH<sub>2</sub>), 29.2 (CH<sub>2</sub>), 28.7 (CH<sub>2</sub>), 26.2 (CH<sub>2</sub>); MS (ES<sup>+</sup>) *m/z* 733.24 ([M+Na]<sup>+</sup>, 100), (ES<sup>-</sup>) *m/z* 745.29 ([M+<sup>35</sup>Cl]<sup>-</sup>, 100), 747.34 ([M+<sup>37</sup>Cl]<sup>-</sup>, 30); HRMS (ES<sup>+</sup>) *m/z* calculated for [M+Na]<sup>+</sup> C<sub>42</sub>H<sub>62</sub>NaO<sub>7</sub>S<sup>+</sup> 733.4108, found 733.4116.

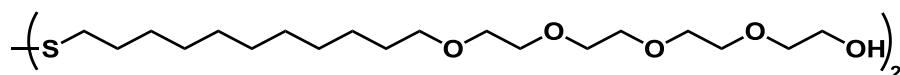
**Compound 5: 5,8,11,14,17,42,45,48,51,54-decaoxa-29,30-dithiaoctapentacontane-1,2,57,58-tetraol**



Trityl protected thiol **E5** (200 mg, 0.281 mmol) was dissolved in MeOH (8 mL) and I<sub>2</sub> (143 mg, 0.563 mmol) was added. The reaction was stirred at RT for 4 hours. The solution was then decolorized by addition of an aqueous sat. sodium sulfite solution until no brown color persisted. Solvent was removed under reduced pressure, and the residue was redissolved in CH<sub>2</sub>Cl<sub>2</sub> (20 mL), washed with sat. NaHCO<sub>3</sub> (3 × 25 mL) and brine (3 × 25 mL). The resulting oil was dissolved in hexane/EtOAc (1:2) and loaded onto a short plug of silica, washing with more of the same solvent. The desired pure product was eluted using methanol and dried under vacuum to give **5** as a pale yellow oil. (108 mg, 0.230 mmol, 82%); R<sub>f</sub> = 0.30 (EtOAc/MeOH 1:1); <sup>1</sup>H NMR (500.1 MHz, CDCl<sub>3</sub>): δ 3.95–3.87 (2H, m, CHOH), 3.71–3.55 (36H, m, CH<sub>2</sub>O), 3.51–3.41 (8H, m, CH<sub>2</sub>O), 2.76 (8H, bs, OH), 2.67 (4H, t, J = 7.5 Hz, CH<sub>2</sub>O), 1.76–1.52, (4H, m, CH<sub>2</sub>), 1.38–1.19, (28H, m, CH<sub>2</sub>); <sup>13</sup>C NMR (CDCl<sub>3</sub>, 125.8 MHz): δ 71.7 (CH<sub>2</sub>O), 70.9 (CHO), 70.9 (CH<sub>2</sub>O), 70.7 (CH<sub>2</sub>O), 70.7 (CH<sub>2</sub>O), 70.7 (CH<sub>2</sub>O), 70.7 (CH<sub>2</sub>O), 70.5 (CH<sub>2</sub>O), 70.3 (CH<sub>2</sub>O), 70.1 (CH<sub>2</sub>O), 68.9 (CH<sub>2</sub>O), 66.7 (CH<sub>2</sub>O), 39.3 (CH<sub>2</sub>S), 32.9 (CH<sub>2</sub>), 29.7 (CH<sub>2</sub>), 29.7 (CH<sub>2</sub>), 29.7 (CH<sub>2</sub>), 29.6 (CH<sub>2</sub>), 29.6 (CH<sub>2</sub>), 29.4 (CH<sub>2</sub>), 29.3 (CH<sub>2</sub>), 28.7 (CH<sub>2</sub>), 26.2 (CH<sub>2</sub>); MS (ES<sup>+</sup>) m/z 952.64 ([M+NH<sub>4</sub>]<sup>+</sup>, 100), 957.60 ([M+Na]<sup>+</sup>, 100), (ES<sup>-</sup>) m/z 969.51 ([M+<sup>35</sup>Cl]<sup>-</sup>, 100), 971.63 ([M+<sup>37</sup>Cl]<sup>-</sup>, 30); HRMS (ES<sup>+</sup>) m/z calculated for [M+NH<sub>4</sub>]<sup>+</sup> C<sub>46</sub>H<sub>94</sub>O<sub>14</sub>S<sub>2</sub>NH<sub>4</sub><sup>+</sup> 952.6423, found 952.6422, calculated for [M+Na]<sup>+</sup> C<sub>46</sub>H<sub>94</sub>O<sub>14</sub>S<sub>2</sub>Na<sup>+</sup> 957.5977, found 957.5971.

**Compound 2: 23-mercapto-3,6,9,12-tetraoxatricosan-1-ol**

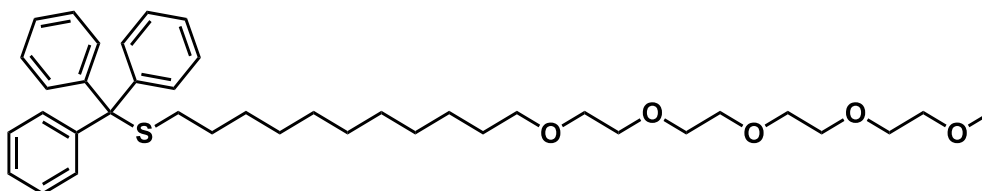
Trityl protected thiol **E3** (2.00 g, 3.21 mmol) was dissolved in dry  $\text{CH}_2\text{Cl}_2$  (30 mL) and an excess of trifluoroacetic acid (7.32 g, 64.20 mmol) was added. Subsequently triisopropylsilane (0.61 g, 3.85 mmol) was added and the reaction was stirred at room temperature under argon for 5 hours. Solvent and most of the  $\text{CF}_3\text{CO}_2\text{H}$  and  $i\text{Pr}_3\text{SiH}$  was distilled off at atmospheric pressure. The crude product was purified by column chromatography (hexane/EtOAc, 3:1  $\rightarrow$  1:8) to give the desired product as a colorless oil (1.03 g, 2.71 mmol, 84%, spectral data in agreement with the literature<sup>257</sup>);  $^1\text{H}$  NMR (300.1 MHz,  $\text{CDCl}_3$ ):  $\delta$  4.51–4.48 (2H, m,  $\text{CH}_2\text{O}$ ), 3.81–3.78 (2H, m,  $\text{CH}_2\text{O}$ ), 3.68 – 3.56 (12H, m,  $6 \times \text{CH}_2\text{O}$ ), 3.45 (2H, t,  $J = 7.4$  Hz,  $\text{CH}_2\text{OH}$ ), 2.51 (2H, dd,  $J = 7.5$  Hz,  $J = 7.5$  Hz,  $\text{CH}_2\text{SH}$ ), 1.65–1.52 (4H, m,  $2 \times \text{CH}_2$ ), 1.39 – 1.23 (14H, m,  $7 \times \text{CH}_2$ ), 1.33 (1H, t,  $J = 7.8$  Hz,  $\text{SH}$ );  $^{13}\text{C}$  NMR (75.5 MHz,  $\text{CDCl}_3$ ):  $\delta$  71.7 ( $\text{CH}_2\text{O}$ ), 70.9 ( $\text{CH}_2\text{O}$ ), 70.8 ( $\text{CH}_2\text{O}$ ), 70.7 ( $\text{CH}_2\text{O}$ ), 70.7 ( $\text{CH}_2\text{O}$ ), 70.7 ( $\text{CH}_2\text{O}$ ), 70.1 ( $\text{CH}_2\text{O}$ ), 68.3 ( $\text{CH}_2\text{O}$ ), 67.1 ( $\text{CH}_2\text{OH}$ ), 34.2 ( $\text{CH}_2\text{S}$ ), 29.7 ( $\text{CH}_2$ ), 29.7 ( $\text{CH}_2$ ), 29.7 ( $\text{CH}_2$ ), 29.6 ( $\text{CH}_2$ ), 29.6 ( $\text{CH}_2$ ), 29.2 ( $\text{CH}_2$ ), 28.5 ( $\text{CH}_2$ ), 26.2 ( $\text{CH}_2$ ), 24.8 ( $\text{CH}_2$ ); MS ( $\text{ES}^+$ )  $m/z$  403.25 ( $[\text{M}+\text{Na}]^+$ , 100).

**Compound 3: 3,6,9,12,37,40,43,46-octaoxa-24,25-dithiaoctatetracontane-1,48-diol**

Trityl protected thiol **E3** (3.03 g, 7.71 mmol) was dissolved in MeOH (150 mL) and  $\text{I}_2$  (3.91 g, 15.4 mmol) was added. The reaction was stirred at RT for 4 hours. After which a sat. aqueous sodium sulfite solution was added to decolour the solution. Solvent was removed under reduced pressure and the residue was redissolved in EtOAc (100 mL), washing with sat.  $\text{NaHCO}_3$  ( $3 \times 25$  mL) and brine ( $3 \times 25$  mL). The organic layer was dried over  $\text{MgSO}_4$  and

solvent was removed under vacuum to give an off-white oil. The oil was redissolved in the minimum volume of hexane/EtOAc (1:2 v/v) and charged onto a short plug of silica. After washing with hex/EtOAc (1:2), the product was stripped off the plug using MeOH and dried under vacuum to give compound **3** as a white solid. (1.37 g, 1.80 mmol, 74%, spectral data in agreement with the literature<sup>258</sup>); <sup>1</sup>H NMR (300.1 MHz, CDCl<sub>3</sub>): δ 3.74 (4H, t, *J* = 4.8 Hz, CH<sub>2</sub>OH), 3.68–3.55 (28H, m, CH<sub>2</sub>O), 3.45 (2H, t, *J* = 6.9 Hz, CH<sub>2</sub>O), 2.66 (2H, t, *J* = 7.4 Hz, CH<sub>2</sub>S), 1.70–1.52 (4H, m, CH<sub>2</sub>), 1.41–1.19 (14H, m, CH<sub>2</sub>); <sup>13</sup>C NMR (75.5 MHz, CDCl<sub>3</sub>): δ 71.7 (CH<sub>2</sub>O), 70.9 (CH<sub>2</sub>O), 70.8 (CH<sub>2</sub>O), 70.8 (CH<sub>2</sub>O), 70.7 (CH<sub>2</sub>O), 70.7 (CH<sub>2</sub>O), 70.7 (CH<sub>2</sub>O), 70.1 (CH<sub>2</sub>O), 68.3 (CH<sub>2</sub>O), 67.1 (CH<sub>2</sub>OH), 34.2 (CH<sub>2</sub>S), 29.7 (CH<sub>2</sub>), 29.7 (CH<sub>2</sub>), 29.7 (CH<sub>2</sub>), 29.6 (CH<sub>2</sub>), 29.6 (CH<sub>2</sub>), 29.2 (CH<sub>2</sub>), 28.5 (CH<sub>2</sub>), 26.2 (CH<sub>2</sub>), 24.8 (CH<sub>2</sub>); MS (ES<sup>+</sup>) *m/z* 781.35 ([M+Na]<sup>+</sup>, 100).

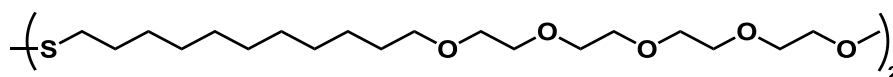
**Compound E6: 27,27,27-triphenyl-2,5,8,11,14-pentaoxa-26-thiaheptacosane**



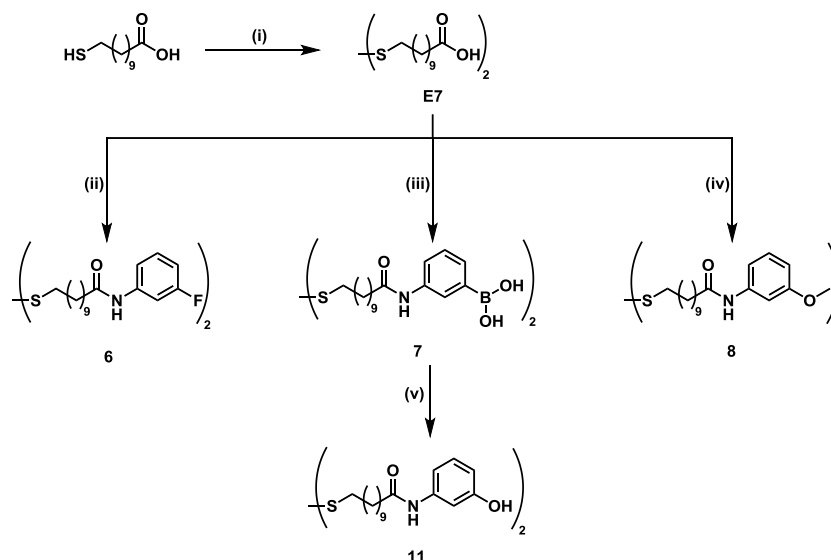
NaH (as a 60% dispersion in mineral oil) (70.0 mg, 2.90 mmol) was added to a solution of tetraethylene glycol mono-methyl ether (791 mg, 3.80 mmol) in dry THF (10 mL) under argon and stirred at RT for 0.5 h. To this, a solution of 11-(tritylthio)undecyl methanesulfonate **3** (1.00 g, 1.90 mmol) in dry THF (10 mL) was added. The mixture was heated to reflux under argon for 18 h. The reaction was poured into dilute HCl (20 mL) and extracted with CH<sub>2</sub>Cl<sub>2</sub> (3 × 20 mL). The combined organic layers were washed with saturated NaHCO<sub>3</sub> (2 × 10 mL) and brine (2 × 10 mL). The organic layer was dried over MgSO<sub>4</sub> and solvent was removed under vacuum to give a brown oil. The residue was purified by column chromatography (SiO<sub>2</sub>, hex/EtOAc, 3:1 → 1:8) to give the desired product **E6** as a colourless oil (490 mg, 0.762 mmol, 40%); <sup>1</sup>H NMR (300.1 MHz, CDCl<sub>3</sub>): δ =

7.42 (6H, dd,  $J = 6.9$  Hz,  $J = 1.5$  Hz, ArH), 7.43–7.28 (6H, m, ArH), 7.22 – 7.17 (3H, m, ArH), 3.66–3.62 (12H, m, CH<sub>2</sub>O), 3.59–3.53 (4H, m, CH<sub>2</sub>O), 3.44 (2H, t,  $J = 7.5$  Hz, CH<sub>2</sub>O), 2.13 (2H, t,  $J = 7.5$  Hz, CH<sub>2</sub>S), 1.61–1.52 (2H, m, CH<sub>2</sub>), 1.43 1.09 (16H, m, CH<sub>2</sub>); <sup>13</sup>C NMR (75.5 MHz, CDCl<sub>3</sub>): δ 145.2 (C), 129.7 (6 × ArC), 127.9 (6 × ArC), 126.6 (3 × ArC), 72.1 (CH<sub>2</sub>O), 71.7 (CH<sub>2</sub>O), 70.7 (6 × CH<sub>2</sub>O), 70.2 (CH<sub>2</sub>O), 59.2 (OCH<sub>3</sub>), 32.2 (CH<sub>2</sub>S), 29.8 (CH<sub>2</sub>), 29.7 (CH<sub>2</sub>), 29.6 (2 × CH<sub>2</sub>), 29.5 (CH<sub>2</sub>), 29.3 (CH<sub>2</sub>), 29.2 (CH<sub>2</sub>), 28.7 (CH<sub>2</sub>), 26.2 (CH<sub>2</sub>). HRMS (ES<sup>+</sup>)  $m/z$  calculated for [M+Na]<sup>+</sup> C<sub>39</sub>H<sub>56</sub>O<sub>5</sub>SNa<sup>+</sup> 659.3741, found 569.3725.

**Compound 4: 3,6,9,12,37,40,43,46-octaoxa-24,25-dithiaoctatetracontane-1,48-diol**

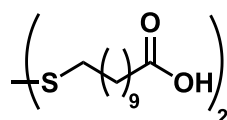


Trityl protected thiol **E6** (2.97 g, 4.66 mmol) was dissolved in MeOH (150 mL) and I<sub>2</sub> (2.37 g, 9.33 mmol) was added. The reaction was stirred at RT for 4 hours. After which a sat. aqueous sodium sulfite solution was added to decolor the solution. Solvent was then removed and the residue was redissolved in CH<sub>2</sub>Cl<sub>2</sub> (100 mL), washing with sat. NaHCO<sub>3</sub> (3 × 25 mL) and brine (3 × 25 mL). The organic layer was dried over MgSO<sub>4</sub> and solvent was removed under vacuum to give an yellow oil. The oil was purified by column chromatography (SiO<sub>2</sub>, hex/EtOAc, 1:2) to give the desired product **4** as an off-white oil. (0.970 g, 1.23 mmol, 53%); <sup>1</sup>H NMR (300.1 MHz, CDCl<sub>3</sub>): δ 3.74 (4H, t,  $J = 4.8$  Hz, CH<sub>2</sub>OH), 3.68–3.55 (28H, m, CH<sub>2</sub>O), 3.45 (2H, t,  $J = 6.9$  Hz, CH<sub>2</sub>O), 2.66 (2H, t,  $J = 7.4$  Hz, CH<sub>2</sub>S), 1.70–1.52 (4H, m, CH<sub>2</sub>), 1.41–1.19 (14H, m, CH<sub>2</sub>); <sup>13</sup>C NMR (75.5 MHz, CDCl<sub>3</sub>): δ 71.7 (CH<sub>2</sub>O), 70.9 (CH<sub>2</sub>O), 70.8 (CH<sub>2</sub>O), 70.8 (CH<sub>2</sub>O), 70.7 (CH<sub>2</sub>O), 70.7 (CH<sub>2</sub>O), 70.7 (CH<sub>2</sub>O), 70.1 (CH<sub>2</sub>O), 68.3 (CH<sub>2</sub>O), 67.1 (CH<sub>2</sub>OH), 34.2 (CH<sub>2</sub>S), 29.7 (CH<sub>2</sub>), 29.7 (CH<sub>2</sub>), 29.7 (CH<sub>2</sub>), 29.6 (CH<sub>2</sub>), 29.6 (CH<sub>2</sub>), 29.2 (CH<sub>2</sub>), 28.5 (CH<sub>2</sub>), 26.2 (CH<sub>2</sub>), 24.8 (CH<sub>2</sub>); HRMS (ES<sup>+</sup>)  $m/z$  calculated for [M+Na]<sup>+</sup> C<sub>40</sub>H<sub>82</sub>O<sub>10</sub>S<sub>2</sub>Na<sup>+</sup> 809.5242, found 809.5202.

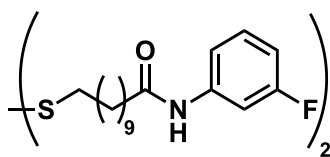


**Scheme 7.2** Reagents and conditions for synthesis of benzamide ligands **6**, **7**, and **8**. (i)  $\text{SO}_2\text{Cl}_2$ ,  $\text{CH}_2\text{Cl}_2$ ,  $0\text{ }^\circ\text{C}$ , 0.1 h, 99%. (ii) EDC·HCl, HOBT, *N,N*-diisopropylethylamine, MeCN/THF, RT, 18 h, 88%. (iii) EDC·HCl, HOBT, *N,N*-diisopropylethylamine, MeCN/THF, RT, 18 h, 82%. (iv) EDC·HCl, HOBT, *N,N*-diisopropylethylamine, MeCN/THF, RT, 18 h, 77%. (v)  $\text{H}_2\text{O}_2$ , NaOH, MeOH, RT, 0.1 h, 99%.

### Compound E7: 11,11'-disulfanediyldiundecanoic acid

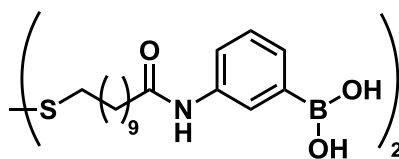


A solution of sulfuryl chloride (1.24 g (0.77 mL), 9.16 mmol) in dry  $\text{CH}_2\text{Cl}_2$  (30 mL) was added to a solution of 11-mercaptoundecanoic acid (4.00 g, 18.3 mmol) in dry  $\text{CH}_2\text{Cl}_2$  (60 mL) at  $0\text{ }^\circ\text{C}$ . Solvent was removed under vacuum to give the desired product as an off-white solid (3.99 g, 9.18 mmol, 99%, spectral data in agreement with the literature<sup>259</sup>); M.p.:  $97\text{--}100\text{ }^\circ\text{C}$ .  $^1\text{H}$  NMR (300.1 MHz;  $\text{DMSO-}d_6$ ):  $\delta$  = 2.68 (4H, t,  $J$  = 6.0,  $\text{CH}_2\text{S}$ ), 2.18 (4H, t,  $J$  = 7.5,  $2 \times \text{CH}_2\text{CO}_2\text{H}$ ), 1.65–1.55 (4H, m,  $2 \times \text{CH}_2\text{CH}_2\text{S}$ ), 1.52–1.43 (4H, m,  $\text{CH}_2$ ), 1.38–1.20 (24H, m,  $12 \times \text{CH}_2$ );  $^{13}\text{C}$  NMR (75.5 MHz;  $\text{DMSO-}d_6$ ):  $\delta$  = 174.5 (C), 37.8 ( $\text{CH}_2$ ), 33.6 ( $\text{CH}_2$ ), 28.8 ( $\text{CH}_2$ ), 28.8 ( $\text{CH}_2$ ), 28.8 ( $\text{CH}_2$ ), 28.7 ( $\text{CH}_2$ ), 28.5 ( $\text{CH}_2$ ), 28.5 ( $\text{CH}_2$ ), 27.7 ( $\text{CH}_2$ ), 24.5 ( $\text{CH}_2$ ).

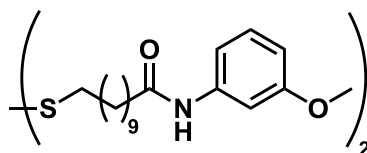
**Compound 6: 11,11'-disulfanediylbis(N-(3-fluorophenyl)undecanamide)**

11,11'-disulfanediylundecanoic acid (**E7**) (1.00 g, 2.30 mmol), 3-fluoroaniline (0.853 g, 5.50 mmol) and EDC•HCl (1.10 g, 5.75 mmol) were dissolved in THF (10 mL) and MeCN (5 mL). *N,N*-diisopropylethylamine (1.49 g, 11.5 mmol) was added and the reaction was stirred at room temperature for 16 hours. The solution was poured into a mixture of EtOAc and 1 M HCl. The organic layer was washed with 1 M HCL, sat. NaHCO<sub>3</sub> and brine, dried over MgSO<sub>4</sub>. Solvent was removed under vacuum to give pale yellow solid. This solid was sonicated in MeOH and filtered to give the desired product **6** as a white solid. (1.26 g, 2.03 mmol, 88%); <sup>1</sup>H NMR (500.1 MHz; CDCl<sub>3</sub>): δ = 9.93 (2H, br s, NH), 7.39 (2H, d, *J* = 11.5, ArH), 7.17–7.11 (4H, m, ArH), 6.71–6.64 (2H, m, ArH), 2.59 (4H, t, *J* = 7.5, CH<sub>2</sub>S), 2.25 (4H, t, *J* = 7.5, CH<sub>2</sub>CO) 1.63–1.52 (8H, m, CH<sub>2</sub>), 1.34–1.16 (24H, m, CH<sub>2</sub>); <sup>13</sup>C NMR (125.8 MHz; CDCl<sub>3</sub>): δ = 178.2 (C), 172.9–170.9 (d, *J* = 252 Hz, CF), 139.1 (C), 129.9–129.8 (d, *J* = 13 Hz, CH), 115.0 (d, *J* = 2 Hz, CH), 110.5–110.4 (d, *J* = 21 Hz, CH), 107.2–107.0 (d, *J* = 25 Hz, CH), 39.1 (CH<sub>2</sub>), 39.1 (CH<sub>2</sub>), 29.4 (CH<sub>2</sub>), 29.4 (CH<sub>2</sub>), 29.4 (CH<sub>2</sub>), 29.3 (CH<sub>2</sub>), 29.2 (CH<sub>2</sub>), 29.1 (CH<sub>2</sub>), 28.4 (CH<sub>2</sub>), 25.6 (CH<sub>2</sub>); <sup>19</sup>F NMR (470.4 MHz, DMSO-*d*<sub>6</sub>): δ = –108.67. HRMS (ES<sup>+</sup>) *m/z* calculated for [M+H]<sup>+</sup> C<sub>34</sub>H<sub>51</sub>F<sub>2</sub>N<sub>2</sub>O<sub>2</sub>S<sub>2</sub><sup>+</sup> 612.3355, found 612.3345.

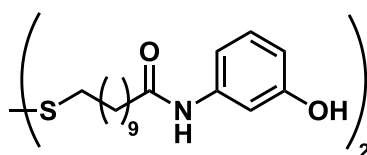
**Compound 7: (((11,11'-disulfanediyldiundecanoyl))bis(azanediyl))bis(3,1-phenylene)diboronic acid**



11,11'-disulfanediyldiundecanoic acid (**E7**) ((1.00 g, 2.30 mmol), 3-aminophenylboronic acid monohydrate (0.891 g, 5.75 mmol) and EDC•HCl (1.10 g, 5.75 mmol) were dissolved in THF (10 mL) and MeCN (10 mL). *N,N*-diisopropylethylamine (1.49 g, 11.5 mmol) was added and the reaction was stirred at room temperature for 16 hours. The solution was poured into a mixture of EtOAc and 1 M HCl, and allowed to stand for 2 hours, during which time a white solid precipitated at the phase-boundary. The solid was filtered, washed with 1M HCl and CH<sub>2</sub>Cl<sub>2</sub> and dried to afford the desired product **7** as an off white solid. (1.26 g, 1.88 mmol, 82%); M.p.: 204 – 209 °C (dec.). <sup>1</sup>H NMR (500.1 MHz; DMSO-*d*<sub>6</sub>): δ = 9.78 (2H, s, NH), 7.81 (2H, s, ArH), 7.71 (2H, d, *J* = 8.2, ArH), 7.45 (2H, d, *J* = 7.2, 2 × ArH), 7.23 (2H, t, *J* = 9.0, ArH), 2.67 (4H, t, *J* = 7.2, CH<sub>2</sub>S), 2.27 (4H, t, *J* = 7.4, CH<sub>2</sub>CO) 1.64 – 1.51 (8H, m, CH<sub>2</sub>), 1.38 – 1.19 (24H, m, CH<sub>2</sub>); <sup>13</sup>C NMR (125.8 MHz; DMSO-*d*<sub>6</sub>): δ = 171.3 (C), 138.6 (C), 132.5 (C), 128.9 (CH), 127.8 (CH), 125.2 (CH), 121.2 (CH), 37.9 (CH<sub>2</sub>), 36.5 (CH<sub>2</sub>), 29.0 (CH<sub>2</sub>), 29.0 (CH<sub>2</sub>), 28.9 (CH<sub>2</sub>), 28.8 (CH<sub>2</sub>), 28.7 (CH<sub>2</sub>), 28.6 (CH<sub>2</sub>), 27.8 (CH<sub>2</sub>), 25.3 (CH<sub>2</sub>). HRMS (ES<sup>+</sup>) *m/z* calculated for dimethoxy-derivative [M+2CH<sub>2</sub>+H]<sup>+</sup> C<sub>36</sub>H<sub>58</sub>B<sub>2</sub>N<sub>2</sub>O<sub>6</sub>S<sub>2</sub><sup>+</sup> 723.3815, found 723.3802.

**Compound 8: 11,11'-disulfanediylbis(N-(3-methoxyphenyl)undecanamide)**

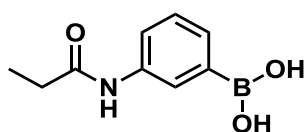
11,11'-disulfanediylundecanoic acid (**E7**) ((1.00 g, 2.30 mmol), 3-methoxyaniline (0.708 g, 5.75 mmol) and EDC•HCl (1.10 g, 5.75 mmol) were dissolved in THF (10 mL) and MeCN (10 mL). *N,N*-diisopropylethylamine (1.49 g, 11.5 mmol) was added and the reaction was stirred at room temperature for 16 hours. The solution was poured into a mixture of EtOAc and 1 M HCl. A white solid precipitated instantaneously at the phase-boundary. The solid was filtered, washed with 1M HCl and CH<sub>2</sub>Cl<sub>2</sub> and dried to afford the desired product **8** as a white solid. (1.14 g, 1.77 mmol, 77%); <sup>1</sup>H NMR (500.1 MHz; DMSO-*d*<sub>6</sub>): δ = 9.83 (s, 2H, NH), 7.30 (t, *J* = 2.2 Hz, 2H, ArH), 7.17 (t, *J* = 8.1 Hz, 2H, ArH), 7.10 (dt, *J* = 8.3, 1.2 Hz, 2H, ArH), 6.59 (ddd, *J* = 8.1, 2.5, 1.0 Hz, 2H, ArH), 3.71 (s, 6H, CH<sub>3</sub>), 2.67 (t, *J* = 7.2 Hz, 4H, CH<sub>2</sub>), 2.27 (t, *J* = 7.4 Hz, 4H, CH<sub>2</sub>), 1.58 (dq, *J* = 16.0, 8.3, 7.7 Hz, 8H, CH<sub>2</sub>), 1.32–1.22 (m, 24H, CH<sub>2</sub>). HRMS (ES<sup>+</sup>) *m/z* calculated for [M+Na]<sup>+</sup> C<sub>36</sub>H<sub>56</sub>N<sub>2</sub>O<sub>4</sub>S<sub>2</sub>Na<sup>+</sup> 667.3574, found 767.3601.

**Compound 9: 11,11'-disulfanediylbis(N-(3-hydroxyphenyl)undecanamide)**

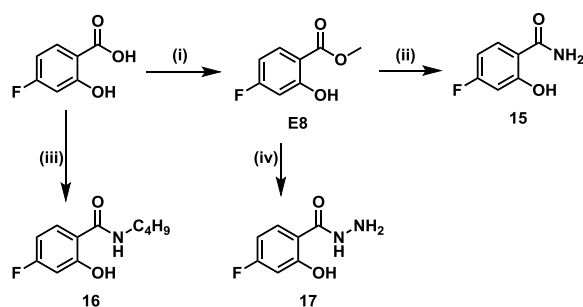
Boronic acid disulfide **7** (50.0 mg, 0.0745 mmol) was dissolved in MeOH (5 mL), to this was added 1 M aqueous, NaOH (0.5 mL) and H<sub>2</sub>O<sub>2</sub> (30% w/v solution in water) (0.5 mL). The reaction was stirred for 10 minutes, and poured into water (20 mL). A white solid precipitate. The precipitate was washed and dried to afford the desired product **9** as a white solid (45 mg, 1.77 mmol, 99%); <sup>1</sup>H NMR (500.1 MHz; CD<sub>3</sub>OD): δ = 6.98 (t, *J* = 8.1 Hz, 2H, ArH), 6.78 (m, 4H), 6.46 (d,

$J = 8.2$  Hz, 2H), 2.65 (t,  $J = 7.2$  Hz, 4H,  $\text{CH}_2$ ), 2.32 (t,  $J = 7.5$  Hz, 2H,  $\text{CH}_2$ ), 1.68–1.62 (m, 8H,  $\text{CH}_2$ ), 1.47–1.13 (m, 24H).;  $^{13}\text{C}$  NMR (125.8 MHz;  $\text{CD}_3\text{OD}$ ):  $\delta = 178.5$  (C), 156.7 (C), 140.1 (C), 130.0 (CH), 115.5 (CH), 111.0 (CH), 105.3 (CH), 39.6 ( $\text{CH}_2$ ), 37.9 ( $\text{CH}_2$ ), 30.2 ( $\text{CH}_2$ ), 30.2 ( $\text{CH}_2$ ), 30.1 ( $\text{CH}_2$ ), 30.0 ( $\text{CH}_2$ ), 29.9 ( $\text{CH}_2$ ), 29.8 ( $\text{CH}_2$ ), 29.1 ( $\text{CH}_2$ ), 26.9 ( $\text{CH}_2$ ). HRMS ( $\text{ES}^+$ )  $m/z$  calculated for  $[\text{M}+\text{H}]^+$   $\text{C}_{34}\text{H}_{53}\text{N}_2\text{O}_4\text{S}_2\text{H}^+$  617.3441, found 617.3450.

### Compound 10: (3-propionamidophenyl)boronic acid

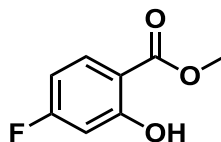


3-Aminophenylboronic acid monohydrate (0.500 g, 3.65 mmol) was dissolved in water (30 mL) and EDCI·HCl (1.05 g, 5.48) was added. To this solution, propanoic acid (2.76 mL, 36.51 mmol) was added. The mixture was stirred at room temperature for 24 h and extracted with  $\text{Et}_2\text{O}$  (3 × 35 mL). Solvent was removed under reduced pressure and the residue was recrystallised from water to yield the desired product **10** as white crystals (0.360 g, 1.87 mmol, 47%).  $^1\text{H}$  NMR (500.1 MHz,  $\text{DMSO}-d_6$ ):  $\delta = 9.77$  (1H, s, NH), 7.99 (2H, s, OH), 7.81 (1H, s, ArH), 7.71 (1H, d,  $J = 9.0$  Hz, ArH), 7.44 (1H, d,  $J = 7.5$  Hz, ArH), 7.24 (1H, s, ArH), 2.30 (2H, q,  $J = 7.5$  Hz,  $\text{CH}_2$ ), 1.07 (3H, t,  $J = 7.5$  Hz,  $\text{CH}_3$ );  $^{13}\text{C}$  NMR (75.5 MHz,  $\text{DMSO}-d_6$ ):  $\delta = 171.8$  (C), 138.51 (C), 132.6 (C), 128.7 (CH), 127.6 (CH), 125.1 (CH), 121.1 (CH), 29.5 ( $\text{CH}_2$ ), 9.8 ( $\text{CH}_3$ ). HRMS ( $\text{ES}^+$ )  $m/z$  calculated for monomethoxy-derivative  $[\text{M}+\text{CH}_2+\text{H}]^+$   $\text{C}_{10}\text{H}_{15}\text{BNO}_3^+$  208.1140, found 208.1147.

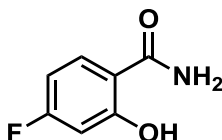


**Scheme 7.3** Reagents and conditions for synthesis of salicylic acid derivatives 15, 16, and 17. (i)  $\text{H}_2\text{SO}_4$ , MeOH, reflux, 10 days, 64%. (ii)  $\text{NH}_3$  (aq), 50 °C, 72 h, 78%. (iii) EDC•HCl, HOBT, *N,N*-diisopropylethylamine, MeCN/THF, RT, 72 h, 30%. (iv)  $\text{N}_2\text{H}_4\cdot\text{H}_2\text{O}$ , MeOH, reflux, 18 h, 90%.

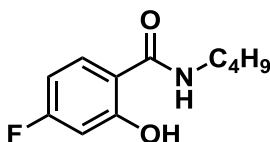
### Compound E8: methyl 4-fluoro-2-hydroxybenzoate



Conc.  $\text{H}_2\text{SO}_4$  (0.26 mL) was added to a solution of 4-fluorosalic acid (1.00 g, 6.41 mmol) in MeOH (15 mL). The solution was stirred at reflux for 10 days. Solvent was removed under reduced pressure and the residue was dissolved in water (1 mL).  $\text{K}_2\text{CO}_3$  was added until effervescing stopped and a precipitate formed. The precipitate was filtered and washed with water to yield the desired product **E8** as a cream solid (0.700 g, 4.11 mmol, 64%, spectral data in agreement with the literature<sup>260</sup>);  $^1\text{H}$  NMR (500.1 MHz,  $\text{CDCl}_3$ ):  $\delta$  = 11.00 (1H, s, OH), 7.84 (1H, dd,  $J$  = 8.5, 6.5 Hz, ArH), 6.67 (1H, dd,  $J$  = 10.5, 2.5 Hz, ArH), 6.60 (1H, ddd,  $J$  = 8.5, 8.0, 2.5 Hz, ArH), 3.95 (3H, s,  $\text{OCH}_3$ );  $^{13}\text{C}$  NMR (75.5 MHz,  $\text{CDCl}_3$ ):  $\delta$  = 170.1 (C), 167.3 (d,  $J$  = 229.3 Hz, CF), 163.8 (d,  $J$  = 12.6 Hz, COH), 132.2 (d,  $J$  = 12.6 Hz, CH), 109.2 (C), 107.4 (d,  $J$  = 22.7 Hz, CH), 105.4 (d,  $J$  = 25.2 Hz, CH), 52.5 ( $\text{CH}_3$ ); HRMS ( $\text{ES}^+$ )  $m/z$  calculated for  $[\text{M}+\text{H}]^+$   $\text{C}_8\text{H}_8\text{FO}_3$  170.0452, observed 170.0480.

**Compound 15: 4-fluoro-2-hydroxybenzamide**

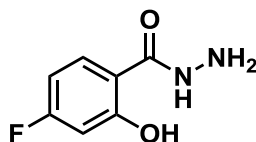
Methyl 4-fluorosalicylate **E8** (0.300 g, 1.76 mmol) was dissolved in aqueous ammonia (10 mL). The solution was heated to 50 °C and stirred for 72 h. The solvent was removed under reduced pressure and the residue was dissolved in water (10 mL). The aqueous layer was extracted with CH<sub>2</sub>Cl<sub>2</sub> (3 × 15 mL). The combined organic layers were dried over MgSO<sub>4</sub>. Solvent was removed under reduced pressure to yield the desired product **15** as a white crystalline solid (0.210 g, 1.35 mmol, 78%, spectral data in agreement with the literature<sup>260</sup>); <sup>1</sup>H NMR (500.1 MHz, DMSO): δ = 8.41 (1H, s, NH), 7.97 (1H, s, NH), 7.95–7.89 (1H, m, ArH), 6.76–6.70 (2H, m, ArH); <sup>13</sup>C NMR (75.5 MHz, DMSO-*d*<sub>6</sub>): δ = 171.5 (C), 165.3 (d, *J* = 250.7 Hz, CF), 163.4 (d, *J* = 13.9 Hz, COH), 130.4 (d, *J* = 11.3 Hz, CH), 111.3 (C), 106.0 (d, *J* = 22.7 Hz, CH), 103.9 (d, *J* = 24 Hz, CH); <sup>19</sup>F NMR (470.4 MHz, DMSO-*d*<sub>6</sub>): δ = -105.0; HRMS (EI<sup>+</sup>) *m/z* calculated for C<sub>7</sub>H<sub>7</sub>FNO<sub>2</sub> [M]<sup>+</sup> 156.0455, observed 156.0453.

**Compound 16: *N*-butyl-4-fluoro-2-hydroxybenzamide**

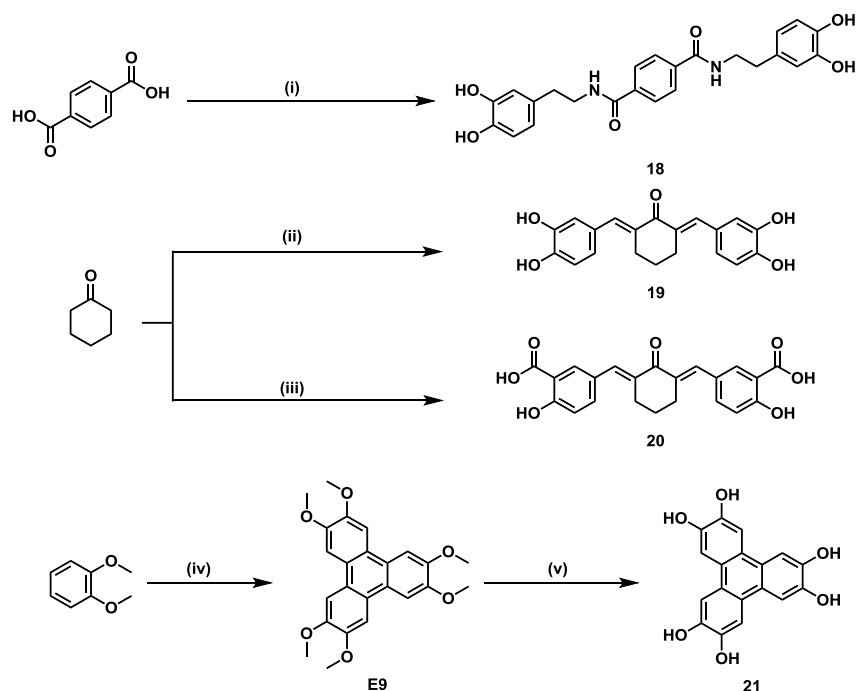
4-Fluorosalicylic acid (0.50 g, 3.20 mmol), amine (0.469 g, 6.41 mmol), EDCI·HCl (0.92 g, 4.81 mmol) and HOBt (0.65 g, 4.80 mmol) were dissolved in THF/MeCN (10 mL, 1:1 *v/v*). *N,N*-Diisopropylethylamine (1.67 mL, 9.61 mmol) was added and the reaction mixture was stirred under an argon atmosphere for 72 h. The reaction mixture was poured into 1 M aqueous HCl (25 mL) and

extracted with EtOAc (25 mL). The organic layer was washed with 1 M aqueous HCl (2 × 20 mL), sat. NaHCO<sub>3</sub> (1 × 20 mL), brine (3 × 20 mL), dried over MgSO<sub>4</sub> and the solvent was removed under vacuum. To give the desired product as an orange crystalline solid (0.192 g, 8.99 mmol, 30%); <sup>1</sup>H NMR (500.1 MHz, DMSO-*d*<sub>6</sub>): δ = 12.75 (1H, s, OH), 7.32 (1H, dd, *J* = 6.0, 9.0 Hz, ArH), 6.67 (1H, dd, *J* = 2.5, 10.5 Hz, ArH), 6.55 (1H, ddd, *J* = 2.5, 6.0, 8.5 Hz, ArH), 6.18 (1H, s, NH), 3.44 (2H, dt, *J* = 6.0, 7.0 Hz, CH<sub>2</sub>) 1.61 (2H, tt, *J* = 6.0, 7.5 Hz, CH<sub>2</sub>), 1.41 (2H, tdd, *J* = 7.0, 7.5, 7.5 Hz, CH<sub>2</sub>), 0.97 (3H, t, *J* = 7.0 Hz, CH<sub>3</sub>); <sup>13</sup>C NMR (75.5 MHz, DMSO-*d*<sub>6</sub>): δ = 169.4 (d, *J* = 289.8 Hz, CF), 165.2 (C), 163.9 (d, *J* = 13.9 Hz, COH), 127.1 (d, *J* = 11.2 Hz, CH), 111.1 (C), 106.6 (d, *J* = 22.9 Hz, CH), 105.4 (d, *J* = 23.6 Hz, CH), 39.6 (CH<sub>2</sub>), 31.7 (CH<sub>2</sub>), 20.3 (CH<sub>2</sub>), 13.9 (CH<sub>3</sub>); <sup>19</sup>F NMR (470.4 MHz, DMSO): δ = -104.0; HRMS (NSI<sup>+</sup>) *m/z* calculated for C<sub>11</sub>H<sub>16</sub>FNO<sub>2</sub> [M+H]<sup>+</sup> 212.2081, observed 212.1083.

#### Compound 17: 4-fluoro-2-hydroxybenzohydrazide

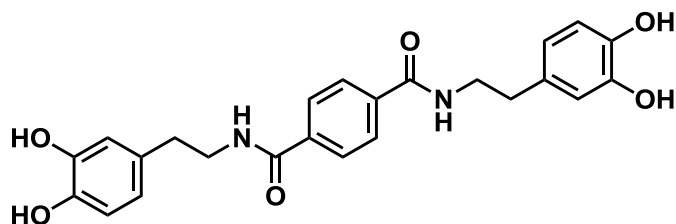


Hydrazine hydrate (0.17 mL, 3.53 mmol, 3 eq) was added to methyl 4-fluorosalicylate **E8** (0.20 g, 1.18 mmol) dissolved in MeOH (5 mL). The solution was heated under reflux for 18 h. Volatiles were removed under reduced pressure and the yellow residue was redissolved in EtOAc (10 mL). The organic phase was washed with brine (3 × 10 mL), dried over MgSO<sub>4</sub> and the solvent was removed under vacuum to yield the desired product **17** as a white solid (0.18 g, 1.06 mmol, 90% spectral data in agreement with the literature<sup>261</sup>); <sup>1</sup>H NMR (500.1 MHz, DMSO-*d*<sub>6</sub>): δ = 10.08 (1H, s, NH), 7.89–7.83 (1H, m, ArH), 6.75–6.70 (2H, m, ArH), 4.65 (2H, s, NH<sub>2</sub>); <sup>13</sup>C NMR (75.5 MHz, DMSO-*d*<sub>6</sub>): δ = 166.7 (C), 130.6 (d, *J* = 11.3 Hz, CH), 111.2 (C), 107.6 (d, *J* = 22.8 Hz, C), 105.0 (d, *J* = 25.2 Hz, C), 2 × C<sub>q</sub> not detected; <sup>19</sup>F NMR (470.4 MHz, DMSO): δ = -105.9; HRMS (NSI<sup>+</sup>) *m/z* calculated for C<sub>7</sub>H<sub>8</sub>FN<sub>2</sub>O<sub>2</sub> [M+H]<sup>+</sup> 171.0564, observed 171.0560.



**Scheme 7.4** Reagents and conditions for synthesis of linkers 18, 19, 20 and 21. (i) Dopamine hydrochloride, EDC·HCl, HOBT, *N,N*-diisopropylethylamine, DMF, RT, 16 h, 94%. (ii) 5-formyl-2-hydroxybenzoic acid, HCl, AcOH, 50 °C, 3 h, 38%. (iii)  $\text{FeCl}_3$ ,  $\text{H}_2\text{SO}_4$ ,  $\text{CH}_2\text{Cl}_2$ , RT, 4 h, 83%. (iv)  $\text{BBr}_3$ ,  $\text{CH}_2\text{Cl}_2$ ,  $-70\text{ }^\circ\text{C} \rightarrow \text{RT}$ , 8 h, 90%.

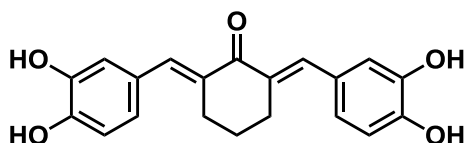
### Compound 18: *N,N'*-bis(3,4-dihydroxyphenethyl)terephthalamide



Terephthalic acid (500 mg, 3.01 mmol), dopamine hydrochloride (1490 mg, 7.52 mmol), EDC.HCl (1442 mg, 7.52 mmol) and HOBT (1016 mg, 7.52 mmol) were dissolved in DMF (20 mL) under argon. *N,N*-diisopropylethylamine (2917 mg, 22.6 mmol) was added and the reaction was stirred at room temperature for 16 hours. The reaction mixture was poured into 1 M HCl (100 mL) and left to stand for 1 hour. After 1 hour a white solid had precipitated. The solid was filtered, washed with 1M HCl and dried to give the desired product **18** as a white

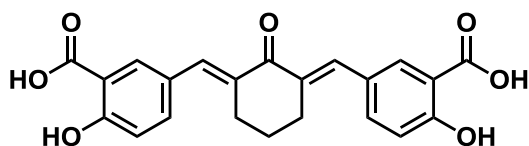
solid (1.24 g, 2.83 mmol, 94%); M.p.: 230–232 °C;  $^1\text{H}$  NMR (300.1 MHz; DMSO- $d_6$ ):  $\delta$  = 8.64 (t,  $J$  = 5.6 Hz, 1H), 7.88 (s, 2H), 6.68 – 6.58 (m, 2H), 6.47 (dd,  $J$  = 8.0, 2.1 Hz, 1H), 3.39 (dt,  $J$  = 8.6, 6.2 Hz, 2H), 2.65 (dd,  $J$  = 8.7, 6.4 Hz, 2H);  $^{13}\text{C}$  NMR (75.5 MHz;  $\text{CDCl}_3$ ):  $\delta$  = 164.4 (2C), 145.1 (2C), 143.6 (2C), 136.8 (2C), 130.2 (2C), 127.1 (4CH), 119.3 (2CH), 116.0 (2CH), 115.5 (2CH), 41.4 (2C), 34.6 (2C); HRMS (NSI $^+$ )  $m/z$  calculated for  $\text{C}_{24}\text{H}_{25}\text{N}_2\text{O}_6$   $[\text{M}+\text{H}]^+$  437.1707, observed 437.1706.

**Compound 19: 2,6-bis((E)-3,4-dihydroxybenzylidene)cyclohexan-1-one**



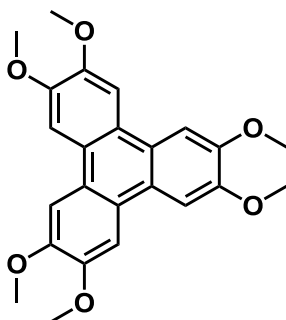
3,4-dihydroxybenzaldehyde (464 mg, 3.36 mmol) and cyclohexanone (150 mg, 1.53 mmol) were dissolved in acetic acid (20 mL). Conc. HCl (2 mL) was added and the mixture was stirred at 50 °C for 3 hours. The solution turned dark red. Water (100 mL) was added and a black solid precipitated and was filtered off. The product was recrystallised from MeOH/ $\text{H}_2\text{O}$  to give the desired product **19** a fine golden crystalline solid (158 mg, 0.467 mmol, 31%); M.p.: 242–246 °C (dec.);  $^1\text{H}$  NMR (300.1 MHz; DMSO- $d_6$ ):  $\delta$  = 9.45 (s, 2H, OH), 9.15 (s, 2H, OH), 7.45 (s, 2H, CH), 6.98 (d,  $J$  = 2.0 Hz, 2H, ArH), 6.93–6.75 (m, 4H, ArH), 2.85 (t,  $J$  = 5.8 Hz, 4H,  $\text{CH}_2$ ), 1.71 (m, 2H,  $\text{CH}_2$ );  $^{13}\text{C}$  NMR (75.5 MHz;  $\text{CDCl}_3$ ):  $\delta$  = 188.5 (C), 146.8 (2C), 145.1 (2C), 136.1 (2CH), 133.1 (2C), 126.9 (2C), 123.4 (2CH), 117.6 (2CH), 115.7 (2CH), 28.1 (2 $\text{CH}_2$ ), 22.5 ( $\text{CH}_2$ ); HRMS (ES $^-$ )  $m/z$  calculated for  $\text{C}_{20}\text{H}_{17}\text{O}_5$   $[\text{M}-\text{H}]^-$  337.1081, observed 337.1080.

**Compound 20: 5,5'-((1E,1'E)-(2-oxocyclohexane-1,3-diyliidene)bis(methanylylidene))bis(2-hydroxybenzoic acid)**



5-Formyl-2-hydroxybenzoic acid (635 mg, 3.83 mmol) and cyclohexanone (150 mg, 1.53 mmol) were suspended in acetic acid (20 mL). Conc. HCl (2 mL) was added and the mixture was stirred at 50 °C for 3 hours. The solution turned bright pink. Water (100 mL) was added and a purple solid precipitated. The solid was recrystallised from EtOH/H<sub>2</sub>O to give the desired product as a dark green solid (230 mg, 0.583 mmol, 38%); <sup>1</sup>H NMR (300.1 MHz; DMSO-*d*<sub>6</sub>): δ = 7.96 (d, *J* = 2.3 Hz, 2H, CH), 7.71 (dd, *J* = 8.8, 2.3 Hz, 2H, ArH), 7.57 (s, 2H ArH), 7.03 (d, *J* = 8.6 Hz, 2H), 2.87 (dd, *J* = 12.5, 2.1 Hz, 4H, CH<sub>2</sub>), 1.72 (qn, *J* = 6.3 Hz, 2H, CH<sub>2</sub>); <sup>13</sup>C NMR (75.5 MHz; CDCl<sub>3</sub>): δ = 188.4 (C), 171.5 (2C), 161.3 (2C), 137.8 (2CH), 134.9 (2C), 134.7 (2CH), 132.4 (2CH), 126.6 (2C), 117.6 (2CH), 113.3 (2C), 27.8 (2CH<sub>2</sub>), 22.4 (CH<sub>2</sub>); HRMS (ES<sup>-</sup>) *m/z* calculated for C<sub>22</sub>H<sub>17</sub>O<sub>7</sub> [M-H]<sup>-</sup> 393.0980, observed 393.0982.

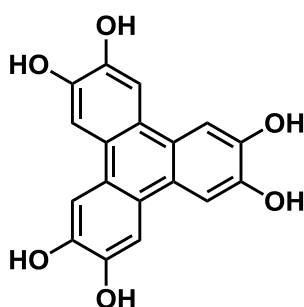
**Compound E9: 2,3,6,7,10,11-hexamethoxytriphenylene**



A solution of 1,2-dimethoxybenzene (1.38 g, 10.0 mmol) in CH<sub>2</sub>Cl<sub>2</sub> (15 ml) was added dropwise to a suspension of FeCl<sub>3</sub>·H<sub>2</sub>O (5.407 g, 30.0 mmol) and concentrated sulfuric acid (0.07 ml) in CH<sub>2</sub>Cl<sub>2</sub> (30 ml). After complete addition (15 min), the reaction mixture was further stirred for 3 h at room temperature,

then 40 ml of methanol were slowly added with vigorous stirring. The resulting mixture was further stirred for a further 30 minutes and precipitate was filtered, washed with methanol (5 × 20 ml) and dried under reduced pressure to give the desired product **E9** as a slightly beige powder (1.13 g, 2.77 mmol, 83%, spectral data in agreement with the literature<sup>262</sup>); <sup>1</sup>H NMR (300.1 MHz; CDCl<sub>3</sub>): δ = 4.05 (s, 18H, CH<sub>3</sub>), 7.80 (s, 6H, ArH).

### Compound 21: triphenylene-2,3,6,7,10,11-hexaol



Hexamethoxytriphenylene **E9** (1.02 g, 2.50 mmol) was dissolved in dichloromethane (20 ml) and the obtained solution was cooled to  $-70\text{ }^{\circ}\text{C}$  and maintained under a nitrogen atmosphere. A solution of BBr<sub>3</sub> (1 M, CH<sub>2</sub>Cl<sub>2</sub>, 30 ml) was then added dropwise to the reaction mixture over a period of 30 min. After complete addition, the reaction temperature was gradually allowed to reach room temperature and stirring was continued for 8 h. The reaction mixture was then slowly poured into crushed ice (100 g) and the obtained mixture was stirred vigorously until the ice melted. The reaction mixture was then extracted with diethyl ether (6 × 150 ml) and the combined organic extracts were washed with half-saturated NaCl solution (200 ml), dried over magnesium sulfate and dried under reduced pressure. The purple/green solid was recrystallised from EtOH/H<sub>2</sub>O to give the desired product **21** as a light grey solid. (0.729 g, 2.25 mmol, 90%); <sup>1</sup>H NMR (500.1 MHz; DMSO-*d*<sub>6</sub>): δ = 9.29 (s, 6H, OH), 7.60 (s, 6H, ArH); <sup>13</sup>C NMR (125.5 MHz; CDCl<sub>3</sub>): δ = 145.2 (6C), 121.8 (6C), 107.7 (6CH); HRMS (ES<sup>-</sup>) *m/z* calculated for C<sub>16</sub>H<sub>11</sub>O<sub>6</sub> [M-H]<sup>-</sup> 323.0561, observed 323.0565.

## 7.3 Nanoparticle synthesis and characterisation

### 7.3.1 Synthesis and characterisation of ligand-functionalised nanoparticles

#### General nanoparticle synthesis procedure

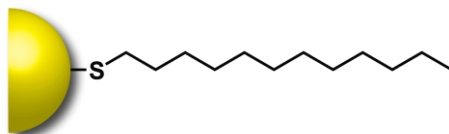
ClAuPPh<sub>3</sub> **1** (200 mg, 0.40 mmol, 1 eq.) and the appropriate thiol (or disulfide) (0.48 mmol, 1.2 eq. (in terms of sulfur atoms)) was dissolved in a suitable solvent (40 mL) and heated to 55 °C. To this, borane *tert*-butylamine complex (TBAB) (4.04 mmol, 10 eq.) was added in the form of a powder. The mixture was stirred at 55 °C for 2 hours. After 2 hour the solution was allowed to cool to room temperature and stirred for a further 3 hours. A non-solvent (200 mL) was added to this and the mixture was kept in the freezer to induce precipitation. If precipitation did not occur, or the precipitate was not visibly a fine powder, solvent was removed under vacuum. The residue was redissolved in the minimum volume of a suitable solvent, and then precipitated with a suitable non-solvent. The supernatant was decanted from the precipitate, which was then washed and sonicated with a suitable non-solvent (10 × 50 mL), or until no free ligand could be detected by TLC. The procedure could be scaled from 50 mg – 1000 mg of gold salt.

#### General slow-addition nanoparticle synthesis procedure

The general nanoparticle synthesis procedure was followed, but the TBAB was dissolved in the same solvent mixture as was being used for the synthesis (100 mg mL<sup>-1</sup>), and added to the reaction mixture by syringe pump. The total reaction time remained 2 h at 55 °C and 3 h at room temperature, regardless of the rate of TBAB addition.

**1-Dodecanethiol-coated nanoparticles**

AuNP-**9**-CHCl<sub>3</sub> (3.14 ± 0.55 nm) (**Figure 2.11**)

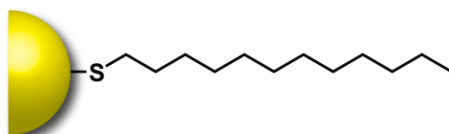


The general procedure was followed on a 400 mg scale with respect to AuPPh<sub>3</sub>Cl **1**. Ligand: 1-dodecanethiol **9**. Solvent: CHCl<sub>3</sub>. Non-solvent EtOH.

Yield: 155 mg of pure nanoparticles. <sup>1</sup>H NMR (400.1 MHz; CDCl<sub>3</sub>): δ = 2.1–1.5 (br s, CH<sub>2</sub>), 1.5–1.0 (br s, CH<sub>2</sub>), 1.0–0.6 (br s, CH<sub>3</sub>).

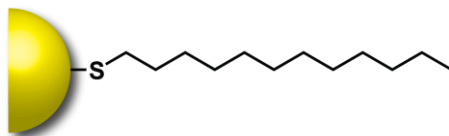
**1-Dodecanethiol-coated nanoparticles**

AuNP-**9**-CHCl<sub>3</sub>-slow (5.14 ± 0.95 nm) (**Figure 2.11**)



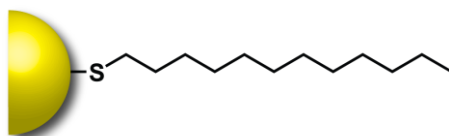
The general slow addition procedure was followed on a 20 mg scale with respect to AuPPh<sub>3</sub>Cl **1**. Reductant added over 2 hours. Ligand: 1-dodecanethiol **9**. Solvent: CHCl<sub>3</sub>. Non-solvent EtOH.

Yield: 10 mg of pure nanoparticles.

**1-Dodecanethiol-coated nanoparticles**AuNP-9-PhMe ( $5.70 \pm 0.51$  nm) (**Figure 2.12**)

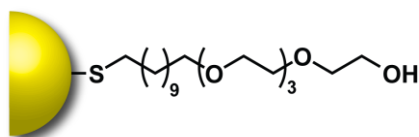
The general procedure was followed on a 20 mg scale with respect to AuPPh<sub>3</sub>Cl **1**. Ligand: 1-dodecanethiol **9**. Solvent: CHCl<sub>3</sub>. Non-solvent EtOH.

Yield: 9 mg of pure nanoparticles. <sup>1</sup>H NMR (400.1 MHz; CDCl<sub>3</sub>):  $\delta$  = 2.1–1.5 (br s, CH<sub>2</sub>), 1.5–1.0 (br s, CH<sub>2</sub>), 1.0–0.6 (br s, CH<sub>3</sub>).

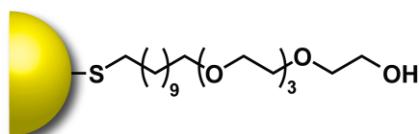
**1-Dodecanethiol-coated nanoparticles**AuNP-9-PhMe-slow ( $6.17 \pm 0.77$  nm) (**Figure 2.12**)

The general slow addition procedure was followed on a 20 mg scale with respect to AuPPh<sub>3</sub>Cl **1**. Reductant added over 2 hours. Ligand: 1-dodecanethiol **9**. Solvent: CHCl<sub>3</sub>. Non-solvent EtOH.

Yield: 10 mg of pure nanoparticles.

**23-mercapto-3,6,9,12-tetraoxatricosan-1-ol-coated nanoparticles**AuNP-2 ( $5.70 \pm 0.51$  nm) (**Figures 2.3 and 2.15**)

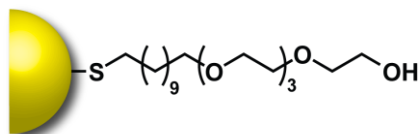
The general procedure was followed on a 200 mg scale with respect to AuPPh<sub>3</sub>Cl **1**. Ligand: alkyl tetra(ethyleneglycol) **2**. Solvent: MeCN/THF, 1:1 v/v. Non-solvent Et<sub>2</sub>O. Nanoparticles washed with CH<sub>2</sub>Cl<sub>2</sub> once precipitated. Yield: 82 mg of pure nanoparticles. <sup>1</sup>H NMR (300.1 MHz; D<sub>2</sub>O):  $\delta = 4.0\text{--}3.3$  (bs, CH<sub>2</sub>O),  $2.0\text{--}0.8$  (bs CH<sub>2</sub>).

**23-mercapto-3,6,9,12-tetraoxatricosan-1-ol-coated nanoparticles**AuNP-2-slow ( $11.23 \pm 1.48$  nm) (**Figure 2.15**)

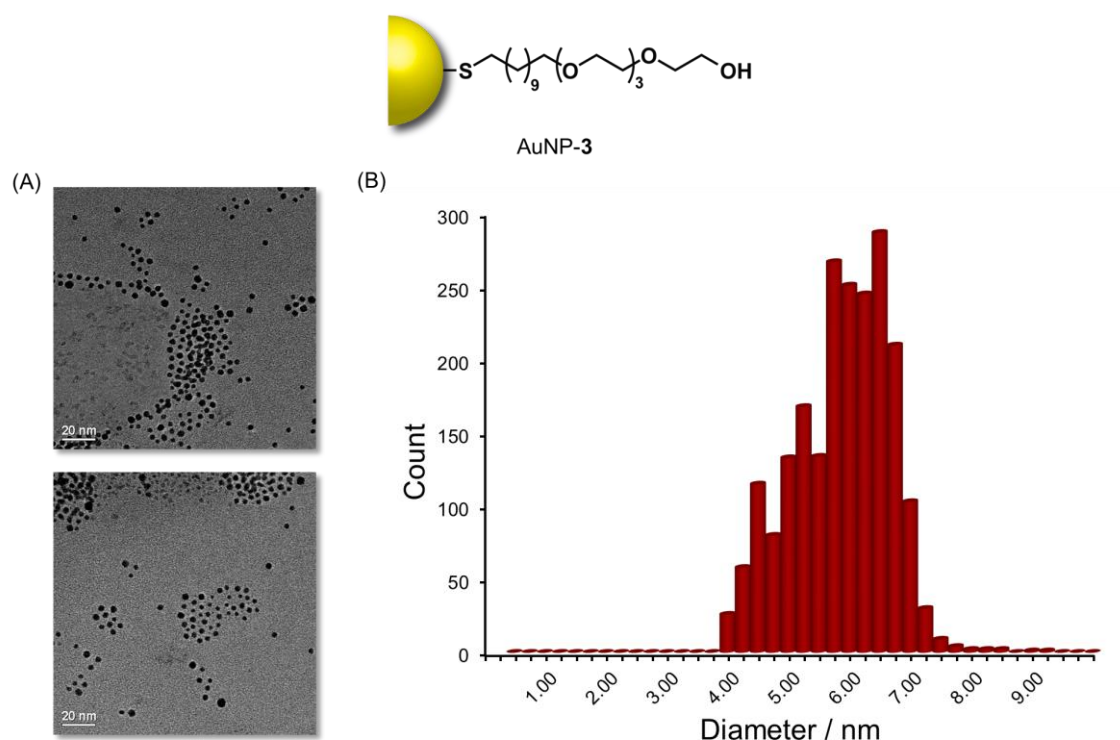
The general slow addition procedure was followed on a 20 mg scale with respect to AuPPh<sub>3</sub>Cl **1**. Reductant added over 2 hours. Ligand: alkyl tetra(ethyleneglycol) **2**. Solvent: MeCN/THF, 1:1 v/v.. Non-solvent Et<sub>2</sub>O. Yield: 6 mg of pure nanoparticles.

### 3,6,9,12,37,40,43,46-octaoxa-24,25-dithiaoctatetracontane-1,48-diol-coated nanoparticles

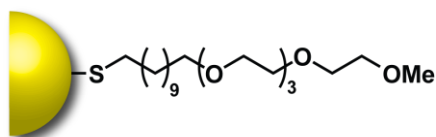
AuNP-3 ( $5.49 \pm 0.82$  nm)



The general procedure was followed on a 50 mg scale with respect to AuPPh<sub>3</sub>Cl **1**. Ligand: alkyl tetra(ethyleneglycol) disulfide **3**. Solvent: MeCN/THF, 1:1 v/v. Non-solvent Et<sub>2</sub>O. Nanoparticles washed with CH<sub>2</sub>Cl<sub>2</sub> once precipitated. Yield: 27 mg of pure nanoparticles. <sup>1</sup>H NMR (300.1 MHz; D<sub>2</sub>O):  $\delta$  = 4.0–3.3 (bs, CH<sub>2</sub>O), 2.0–0.8 (bs CH<sub>2</sub>).



**Figure 7.1** (A) TEM images of AuNP-3 and (B) histogram of size distribution of nanoparticles as found through analysis of TEM images. AuNP-3 were found to have a size of  $5.49 \pm 0.82$  nm, constituting a dispersity of 15%.

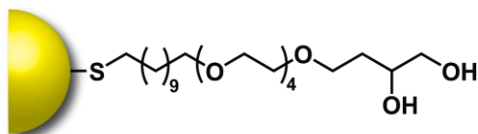
**2,5,8,11,14-pentaoxapentacosane-25-thiol-coated nanoparticles**AuNP-4 ( $4.23 \pm 0.65$  nm) (**Figure 2.4**)

The general procedure was followed on a 100 mg scale with respect to AuPPh<sub>3</sub>Cl **1**. Ligand: alkyl tetra(ethyleneglycol) methyl ether disulfide **4**. Solvent: MeCN/THF, 1:1 v/v. Non-solvent Et<sub>2</sub>O. Nanoparticles washed with CH<sub>2</sub>Cl<sub>2</sub> once precipitated.

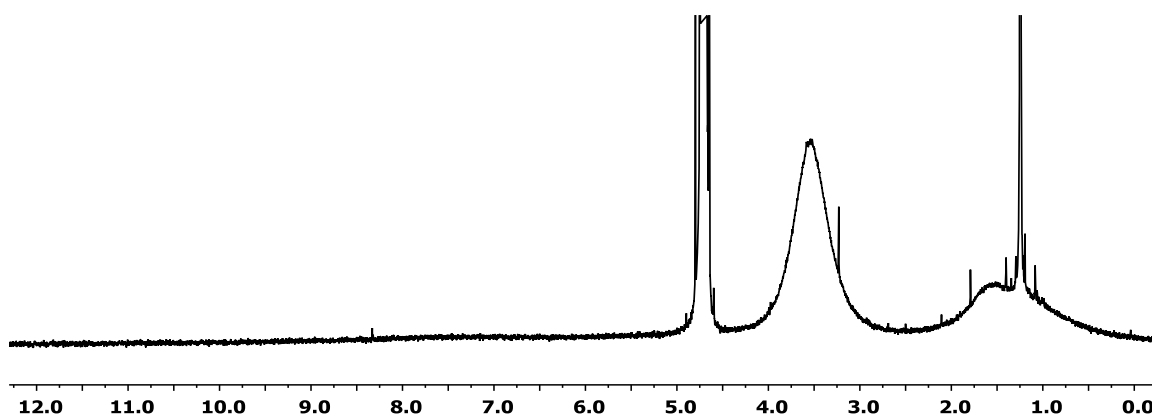
Yield: 56 mg of pure nanoparticles. <sup>1</sup>H NMR (400.1 MHz; D<sub>2</sub>O): δ = 4.0–3.2 (br s, CH<sub>2</sub>, CH<sub>3</sub>), 1.8–1.3 (br s CH<sub>2</sub>).

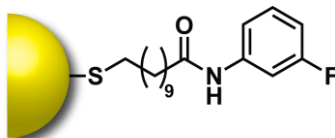
**5,8,11,14,17,42,45,48,51,54-decaoxa-29,30-dithiaoctapentacontane-1,2,57,58-tetrao-coated nanoparticles**

AuNP-5 (5.73 ± 0.85 nm) (Figure 2.5, Chapter 5)



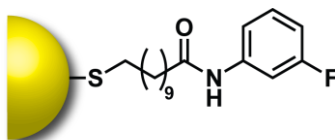
The general procedure was followed on a 400 mg scale with respect to AuPPh<sub>3</sub>Cl **1**. Ligand: alkyl tetra(ethyleneglycol) diol-disulfide **5**. Solvent: MeCN/THF, 1:1 v/v.. Non-solvent Et<sub>2</sub>O. Nanoparticles washed with CH<sub>2</sub>Cl<sub>2</sub> once precipitated. Yield: 112 mg of pure nanoparticles. <sup>1</sup>H NMR (400.1 MHz; D<sub>2</sub>O): 4.1–3.0 (bs, CH<sub>2</sub>O), 2.0–0.5 (bs CH<sub>2</sub>).

**Figure 7.2** <sup>1</sup>H NMR spectrum (400.1 MHz, D<sub>2</sub>O, 298 K) of AuNP-5.

**11,11'-disulfanediylbis(N-(3-fluorophenyl)undecanamide)-coated nanoparticles**AuNP-6 ( $3.86 \pm 0.39$  nm) (Figure 2.6 and 2.13)

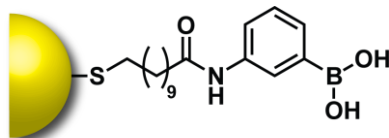
The general procedure was followed on a 100 mg scale with respect to AuPPh<sub>3</sub>Cl **1**. Ligand: fluorine-tagged benzamide **6**. Solvent: THF/MeOH, 10:1 v/v. Non-solvent H<sub>2</sub>O. Nanoparticles were purified by gel permeation chromatography stationary phase Bio-Beads™ S-X1 (200–400 mesh, mobile phase THF).

Yield: 37 mg of pure nanoparticles. <sup>1</sup>H NMR (500.1 MHz; CDCl<sub>3</sub>): δ = 10.0–9.2 (bs, NH), 7.7–6.4 (bm, ArH), 2.9–0.7 (bs CH<sub>2</sub>); <sup>19</sup>F NMR (470.4 MHz, CDCl<sub>3</sub>): δ = –111.7 (bs).

**11,11'-disulfanediylbis(N-(3-fluorophenyl)undecanamide)-coated nanoparticles**AuNP-6-slow ( $5.64 \pm 1.05$  nm) (Figure 2.13)

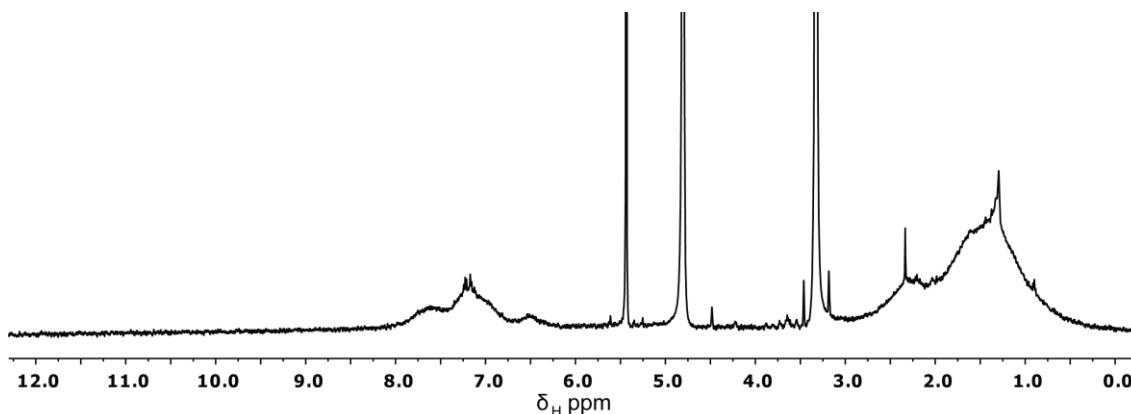
The general slow addition procedure was followed on a 20 mg scale with respect to AuPPh<sub>3</sub>Cl **1**. Reductant added over 2 hours. Ligand: fluorine-tagged benzamide **6**. Solvent: THF/MeOH, 10:1 v/v. Non-solvent H<sub>2</sub>O.

Yield: 13 mg of pure nanoparticles.

**(((11,11'-disulfanediylbis(undecanoyl))bis(azanediyl))bis(3,1-phenylene))diboronic acid-coated nanoparticles**AuNP-7a ( $3.10 \pm 0.42$  nm) (**Figures 2.10 and 2.14, Chapters 2.5 and 4**)

The general procedure was followed on a 500 mg scale with respect to AuPPh<sub>3</sub>Cl **1**. Ligand: boronic acid benzamide **7**. Solvent: THF/MeOH, 10:1 v/v. Non-solvent Et<sub>2</sub>O. Nanoparticles were washed with THF, 0.1 M HCl and CH<sub>2</sub>Cl<sub>2</sub>. Nanoparticles were resuspended in THF/MeOH, 10:1 v/v three times and precipitated three times with Et<sub>2</sub>O to ensure complete removal of free ligand.

Yield: 230 mg of nanoparticles.

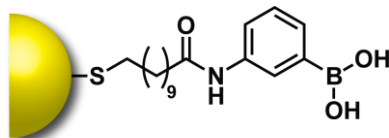


**Figure 7.3** <sup>1</sup>H NMR spectrum (400.1 MHz, CD<sub>3</sub>OD/CD<sub>2</sub>Cl<sub>2</sub>, 99:1, 298 K) of AuNP-7a.

**ICP-OES** of AuNP-7a: Sample dissolved in *aqua regia* (1.2 mL) (freshly made from analytical grade HCl and HNO<sub>3</sub>). Once the nanoparticles had fully dissolved, sample was diluted with water (10 mL) to give a total volume of 11.2 mL. Two blank samples were prepared in the same way. Absolute gold, sulfur and boron concentrations were determined in ppm by subtracting the blank from the measured sample. Blank values were < ppm for each element.

**Table 7.1** ICP-OES data for AuNP-7a.

	Sample A	Sample B
Mass of NPs /mg	3.79	1.70
Volume of sample /mL	11.2	11.2
Au /ppm	253.92	113.57
S /ppm	6.27	2.91
B /ppm	1.31	0.59
Au absolute mass /mg	2.84	1.27
S absolute mass /mg	0.07	0.032
B absolute mass /mg	0.015	0.0067
[Au] /mmoles	0.014	0.0065
[S] /mmoles	0.0022	0.0010
[B] /mmoles	0.0014	0.00062
Au:S:B molar ratio	6.6 : 1.0 : 0.62	6.3 : 1.0 : 0.61
'Molar mass' per boronic acid /g mol <sup>-1</sup>	2793	2761

**(((11,11'-disulfanediy)bis(undecanoyl))bis(azanediyl))bis(3,1-phenylene))diboronic acid-coated nanoparticles**AuNP-7b (3.41 ± 0.43 nm) (**Chapters 2.5 and 3**)

The general procedure was followed on a 500 mg scale with respect to AuPPh<sub>3</sub>Cl **1**. Ligand: boronic acid benzamide **7**. Solvent: THF/MeOH, 10:1 v/v. Non-solvent Et<sub>2</sub>O. Nanoparticles were resuspended in THF/MeOH, 10:1 v/v three times and precipitated three times with Et<sub>2</sub>O to ensure complete removal of free ligand. THF used for both synthesis and purification contained 15 mM BHT.

Yield: 246 mg of pure nanoparticles.

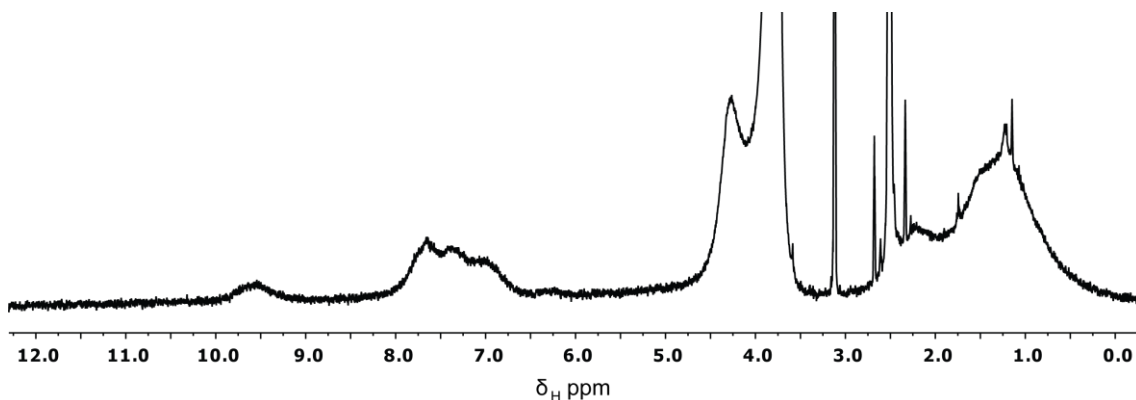


**Figure 7.4** <sup>1</sup>H NMR spectrum (500.1 MHz, DMSO-*d*<sub>6</sub>/H<sub>2</sub>O, 99:1, 298 K) of AuNP-7b.

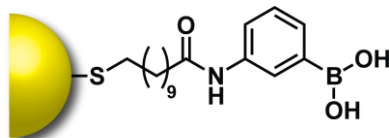
**ICP-OES** of AuNP-7b: Sample dissolved in *aqua regia* (1.2 mL) (freshly made from analytical grade HCl and HNO<sub>3</sub>). Once the nanoparticles had fully dissolved, sample was diluted with water (10 mL) to give a total volume of 11.2 mL. Two blank samples were prepared in the same way. Absolute gold, sulfur and boron concentrations were determined in ppm by subtracting the blank from the measured sample. Blank values were < ppm for each element.

**Table 7.2** ICP-OES data for AuNP-7b.

	Sample A	Sample B
Mass of NPs /mg	1.99	2.60
Volume of sample /mL	11.2	11.2
Au /ppm	120.31	156.16
S /ppm	2.74	3.45
B /ppm	0.89	1.13
Au absolute mass /mg	1.35	1.75
S absolute mass /mg	0.031	0.039
B absolute mass /mg	0.010	0.013
[Au] /mmoles	0.0068	0.0089
[S] /mmoles	0.00096	0.00120
[B] /mmoles	0.00092	0.0012
Au:S:B molar ratio	7.2 : 1.0 : 0.97	7.4 : 1.0 : 0.97
'Molar mass' per boronic acid /g mol <sup>-1</sup>	2196	1907

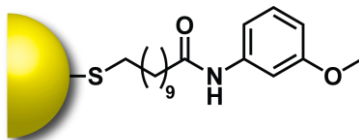
**(((11,11'-disulfaneyldiylbis(undecanoyl))bis(azanediyl))bis(3,1-phenylene))diboronic acid-coated nanoparticles**

AuNP-7-slow ( $4.95 \pm 0.66$  nm) (Figure 2.14)

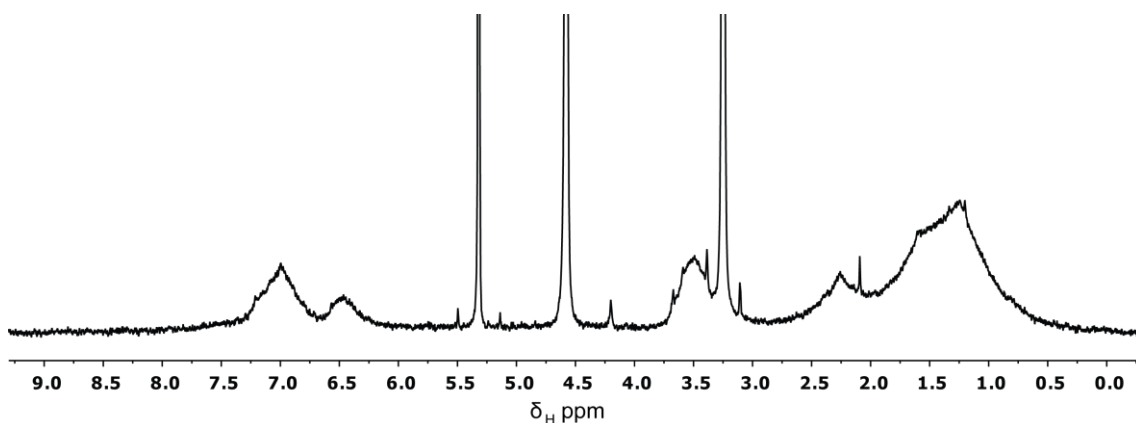


The general slow addition procedure was followed on a 100 mg scale with respect to AuPPh<sub>3</sub>Cl **1**. Reductant added over 2 hours. Ligand: boronic acid benzamide **7**. Solvent: THF/MeOH, 10:1 v/v. Non-solvent H<sub>2</sub>O.

Yield: 39 mg of pure nanoparticles. <sup>1</sup>H NMR (500.1 MHz; CDCl<sub>3</sub>):  $\delta$  = 8.0–6.0 (bm, ArH), 3.0–1.0 (bm CH<sub>2</sub>).

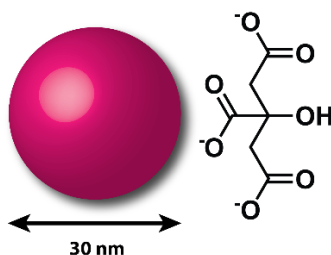
**11,11'-disulfanediylbis(N-(3-methoxyphenyl)undecanamide)-coated nanoparticles**AuNP-8 (3.48 ± 0.49 nm) (**Figure 2.10**)

The general procedure was followed on a 50 mg scale with respect to AuPPh<sub>3</sub>Cl **1**. Ligand: methyl ether benzamide **8**. Solvent: THF/MeOH, 10:1 v/v. Non-solvent Et<sub>2</sub>O. Nanoparticles were washed with CH<sub>2</sub>Cl<sub>2</sub> and 0.1 M HCl. Yield: 21 mg of nanoparticles.

**Figure 7.5** <sup>1</sup>H NMR spectrum (400.1 MHz, CD<sub>2</sub>Cl<sub>2</sub>, 298 K) of AuNP-8.

### 7.3.2 Synthesis and characterisation of citrate-stabilised nanoparticles

#### 30 nm Citrate-stabilised nanoparticles (Chapter 5.5)



#### Synthetic procedure<sup>245</sup>

Prior to synthesis, all glassware was cleaned rigorously with aqua regia, or, alternatively, new vials were used.

Three stock solutions were made up: **solution A**, H<sub>AuCl<sub>4</sub>·3H<sub>2</sub>O</sub> (25.0 mg, 0.0635 mmol) in H<sub>2</sub>O (5 mL), **solution B**, silver nitrate (5.00 mg, 0.0294 mmol) in H<sub>2</sub>O (5 mL), and **solution C**, trisodium citrate dihydrate (50.0 mg, 0.170 mmol) in H<sub>2</sub>O (5 mL). Gold **solution A** (1000 μL) and silver **solution B** (43 μL) were added to citrate **solution C** (200 μL). Water (1260 μL) was subsequently added to give a total volume of 2.5 mL). The final quantities of each reagent were H<sub>AuCl<sub>4</sub>·3H<sub>2</sub>O</sub> (5.00 mg, 12.7 μmol), silver nitrate (0.0425 mg, 0.250 μmol) and trisodium citrate dihydrate (2.00 mg, 6.80 μmol). The combined solution was added to vigorously stirring boiling water (47.5 mL). The solution was heated to reflux for 1 hour, after which it was allowed to cool to RT and stored directly with no further work up.

## Characterisation

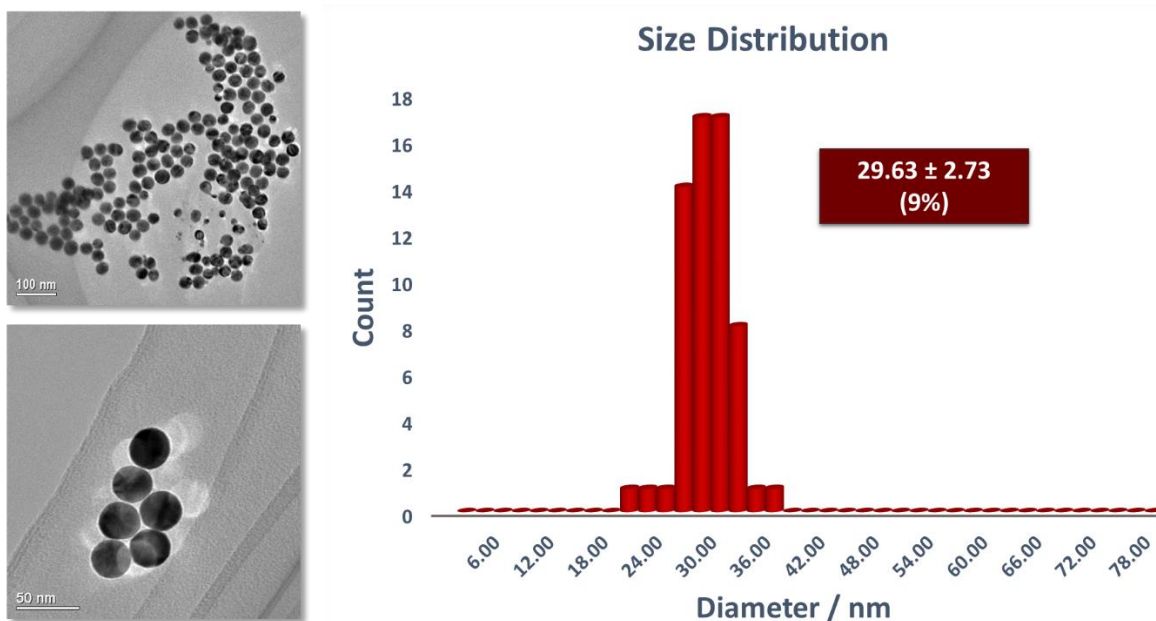


**Figure 7.6** Representative TEM images of 30 nm citrate stabilized nanoparticle and histogram of nanoparticle size distribution as found through analysis of TEM images using *ImageJ* software, as described in the general methods section. nanoparticles were found to have a size of  $29.63 \pm 2.73$  nm, corresponding to a dispersity of 10%.

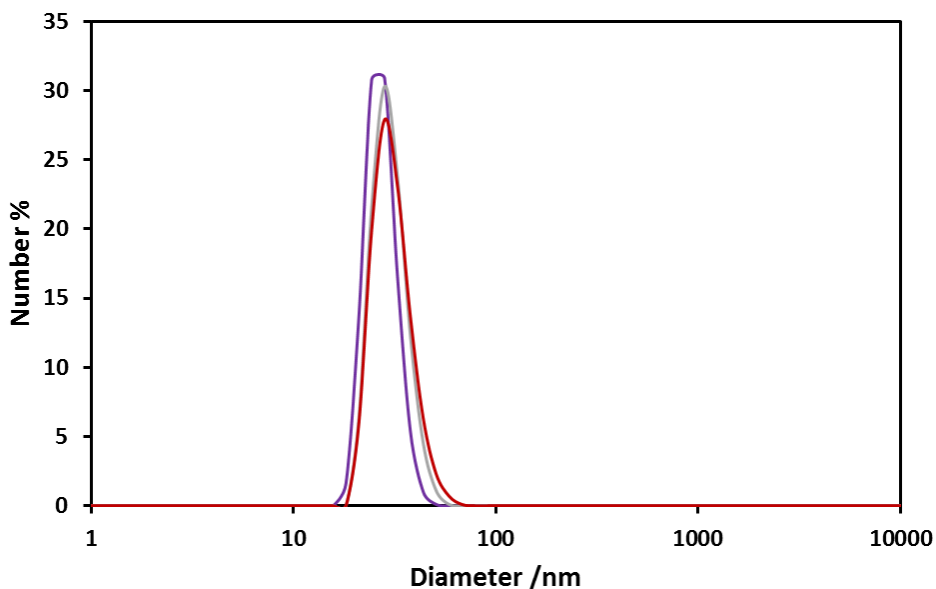


**Figure 7.7** Dynamic light scattering measurements ( $\text{H}_2\text{O}$ ,  $25.0$  °C) of 30 nm citrate-stabilised nanoparticles. Three replicate measurements gave an average hydrodynamic diameter of 31.2 nm.

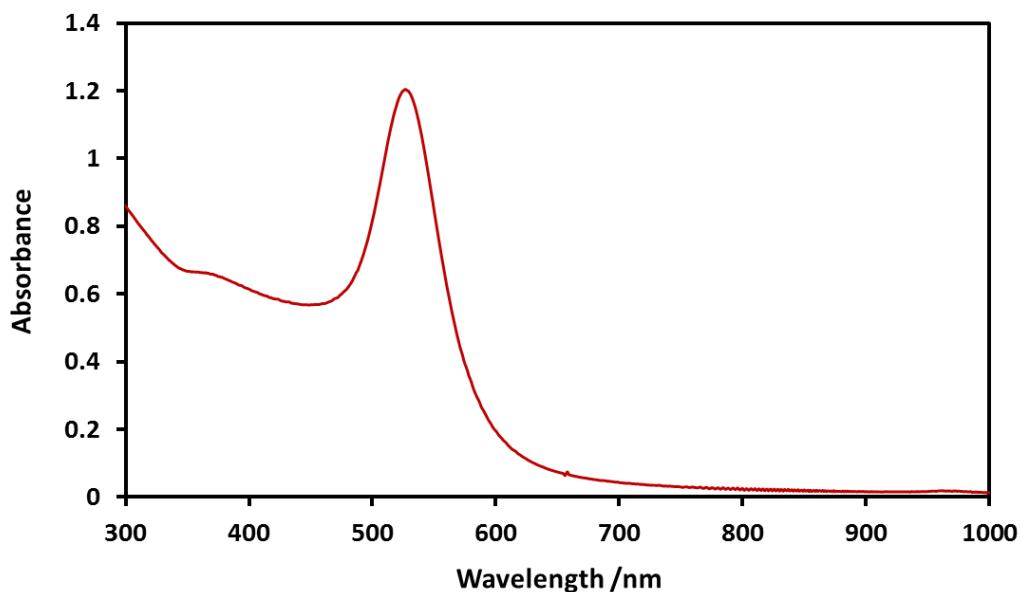
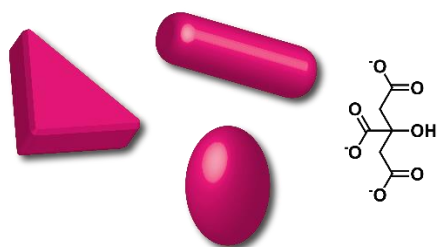


**Figure S7.8** Extinction spectrum ( $\text{H}_2\text{O}$ , 20 °C) of 30 nm citrate-stabilised nanoparticles, showing  $\lambda_{\text{max}}$  (SPR) = 529 nm.

### Mixed shape citrate-stabilised nanoparticles (Chapter 5.5)



#### Synthetic procedure

Prior to synthesis, all glassware was cleaned rigorously with aqua regia, or, alternatively, new vials were used.

$\text{HAuCl}_4 \cdot 3\text{H}_2\text{O}$  (21.6 mg, 0.050 mmol) was dissolved in  $\text{H}_2\text{O}$  (100 mL) and heated to reflux. Trisodium citrate dihydrate (113 mg, 0.384 mmol) was dissolved in  $\text{H}_2\text{O}$  (10 mL) and quickly added to the gold solution. The solution was heated for a further 10 minutes, when it initially turned black, and then gradually a deep red color. The reaction mixture was allowed to cool to RT. The

solution contained 10 nm seed nanoparticles, which were stored without further purification.

$\text{HAuCl}_4 \cdot 3\text{H}_2\text{O}$  (9.80 mg, 9.80  $\mu\text{mol}$ ) was dissolved in  $\text{H}_2\text{O}$  (100 mL). 10 nm seed nanoparticle solution (1 mL) was mixed with the  $\text{HAuCl}_4 \cdot 3\text{H}_2\text{O}$  solution (9 mL) and stirred at room temperature for 7 hours, resulting in a disperse mixture of nanoparticles, containing significant populations of rods and prisms.

### Characterisation

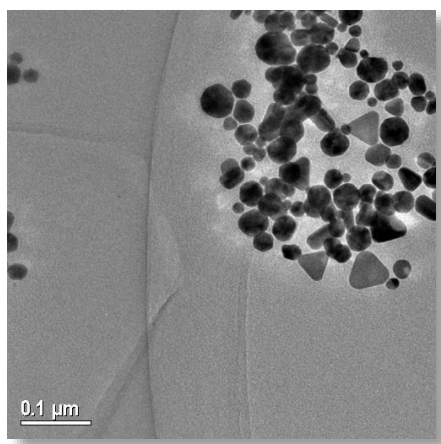


**Figure 7.9** Representative TEM image of the solution of mixed shapes and sizes of citrate-stabilised nanoparticles, including spheres, rods and triangular prisms.

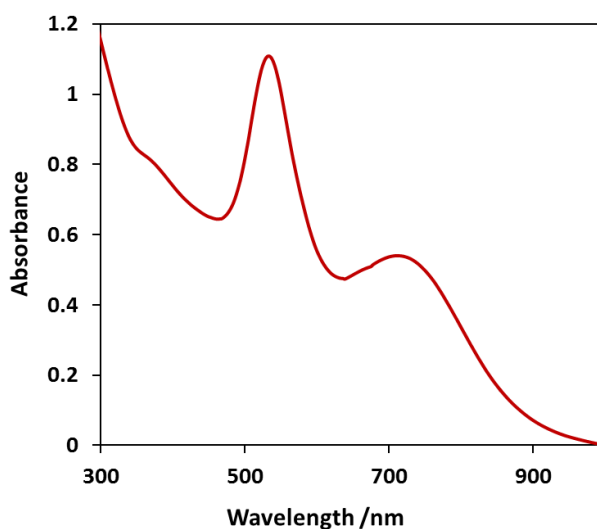


**Figure 7.10** Extinction spectrum ( $\text{H}_2\text{O}$ , 20  $^{\circ}\text{C}$ ) of mixed shapes and sizes of citrate-stabilised nanoparticles.

## 7.4 NMR experiments

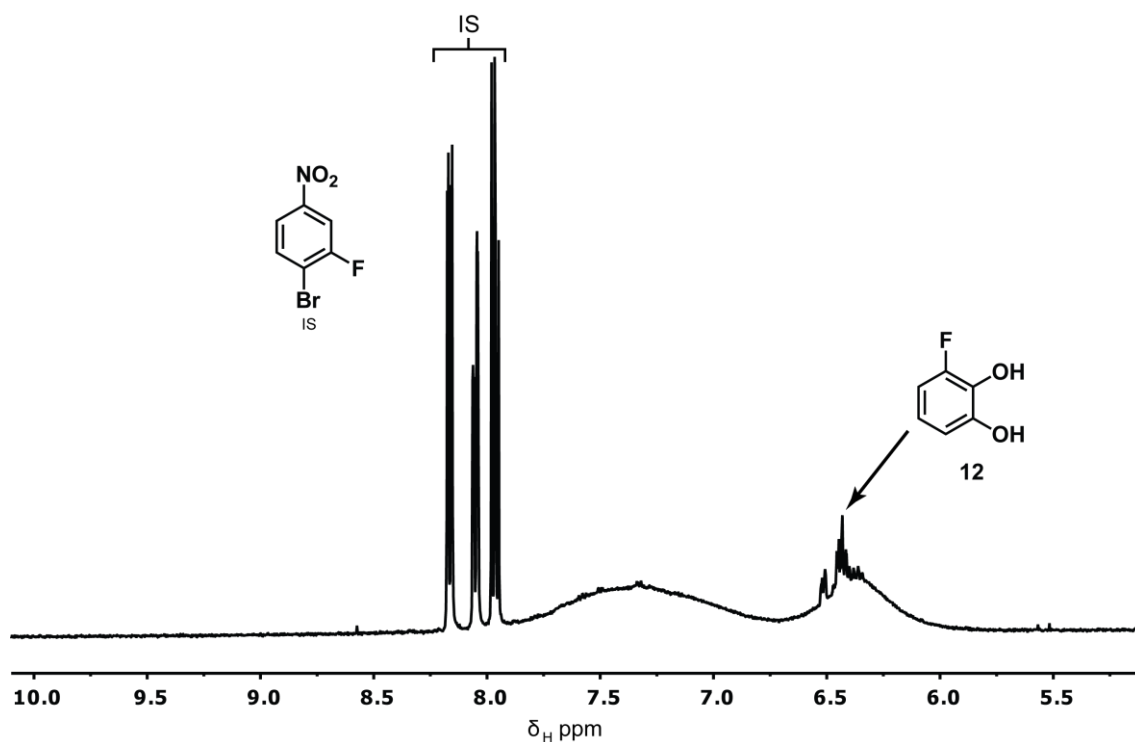


**Figure 7.11** Partial  $^1\text{H}$  NMR (500.1 MHz,  $\text{CD}_3\text{OD}$ , 298 K) of equilibrium mixtures of 3-fluorocatechol **12** and AuNP-**7b** in the presence of *N*-methylmorpholine (100 eq.) and 4-bromo-3-fluoronitrobenzene internal standard. The broad peak centred around 7.4 ppm arises from the nanoparticle-bound boronic acid (in both its acid and ester forms), and the broad peak centred around 6.4 ppm (partially obscured by the sharp resonances of unbound 3-fluorocatechol **12**) arises from 3-fluorocatechol part of the nanoparticle bound boronic ester.

### 7.4.1 $T_1$ measurements

$T_1$  times were measured using an inversion recovery method and analysed using Mestrenova. All quantitative experiments were carried out in CD<sub>3</sub>OD, as such  $T_1$  times of all components measured were at approximately 5–10 mM in CD<sub>3</sub>OD.

**Table 7.3** Measure  $T_1$  values for all compounds and complexes studies in **Chapter 3**.

Species	$T_1$ time /s
3-fluoro-4-bromonitrobenzene <b>IS</b>	3.8
3-fluorocatechol <b>12</b>	2.1
4-fluorocatechol <b>13</b>	2.7
4-fluorosalicilyc acid <b>14</b>	0.9
4-fluorosalicylamide <b>15</b>	2.2
4-fluorosalacylhydrazide <b>16</b>	0.5
3-fluorocatechol ester [ <b>10•12</b> ]	1.2
4-fluorocatechol ester [ <b>10•13</b> ]	1.4
4-fluorosalicilyc acid ester [ <b>10•14</b> ]	3.7
4-fluorosalicylamide ester [ <b>10•15</b> ]	0.9
4-fluorosalicilyc acid ester [ <b>10•16</b> ]	0.9
3-fluorocatechol NP-ester [AuNP- <b>7•12</b> ]	1.0
4-fluorocatechol NP-ester [AuNP- <b>7•13</b> ]	0.9
4-fluorosalicilyc acid NP-ester [AuNP- <b>7•14</b> ]	2.4

### 7.4.2 Single-point measurement of association constants

4-Bromo-3-fluoronitrobenzene (internal standard **IS**) (5 mM), binding partner (5 mM) and model boronic acid **10** (5 mM) or nanoparticle-bound boronic acid AuNP-**7b** were dissolved in the deuterated solvent (1 mL). <sup>19</sup>F NMR (32 scans,  $D_1 = 20$  s) were recorded before and after the addition of base (100 eq). Equilibrium concentrations could be measured by integrating signals relative to the internal standard.

## Nanoparticle-bound association constants

**Table 7.4** Association constants derived from equilibrium mixtures of 3-fluorocatechol **12** and AuNP-**7b** by  $^{19}\text{F}$  NMR spectroscopy (470.4 MHz,  $\text{CD}_3\text{OD}$ , 298 K, 8 scans,  $D_1 = 20$  s) in the presence of *N*-methylmorpholine (100 eq.) and 4-Bromo-3-fluoronitrobenzene internal standard. Concentrations were measured by integration relative to the internal standard.

Experiment	[ <b>12</b> ] /mM	[AuNP- <b>7b</b> · <b>12</b> ] /mM	[AuNP- <b>7b</b> ] /mM <sup>a</sup>	$K_a$ /M <sup>-1</sup>
A	2.38	4.42	1.52	1263
B	2.26	4.52	1.42	1411
C	2.26	4.29	1.65	1152

<sup>a</sup> Nanoparticle concentrations in terms of boronic acid, [AuNP-**7b**] determined by subtracting [AuNP-**7b**·**12**] from initial total [AuNP-**7b**]<sub>0</sub> (calculated from ICP-OES)

**Table 7.5** Association constants derived from equilibrium mixtures of 4-fluorocatechol **13** and AuNP-**7b** by  $^{19}\text{F}$  NMR spectroscopy (470.4 MHz,  $\text{CD}_3\text{OD}$ , 298 K, 8 scans,  $D_1 = 20$  s) in the presence of *N*-methylmorpholine (100 eq.) and 4-Bromo-3-fluoronitrobenzene internal standard. Concentrations were measured by integration relative to the internal standard.

Experiment	[ <b>13</b> ] /mM	[AuNP- <b>7b</b> · <b>13</b> ] /mM	[AuNP- <b>7b</b> ] /mM <sup>a</sup>	$K_a$ /M <sup>-1</sup>
A	2.24	3.73	2.59	644
B	2.28	3.58	2.74	574
C	2.23	3.66	2.66	618

<sup>a</sup> Nanoparticle concentrations in terms of boronic acid, [AuNP-**7b**] determined by subtracting [AuNP-**7b**·**12**] from initial total [AuNP-**7b**]<sub>0</sub> (calculated from ICP-OES)

**Table 7.6** Association constants derived from equilibrium mixtures of 4-fluorosalicic acid **14** and AuNP-**7b** by  $^{19}\text{F}$  NMR spectroscopy (470.4 MHz,  $\text{CD}_3\text{OD}$ , 298 K, 8 scans,  $D_1 = 20$  s) in the presence of *N*-methylmorpholine (100 eq.) and 4-Bromo-3-fluoronitrobenzene internal standard. Concentrations were measured by integration relative to the internal standard.

Experiment	[ <b>14</b> ] /mM	[AuNP- <b>7b</b> • <b>14</b> ] /mM	[AuNP- <b>7b</b> ] /mM <sup>a</sup>	$K_a$ /M <sup>-1</sup>
A	2.32	2.15	2.59	358
B	2.39	2.26	2.48	381
C	2.34	2.47	2.27	465

<sup>a</sup> Nanoparticle concentrations in terms of boronic acid, [AuNP-**7b**] determined by subtracting [AuNP-**7b**•**12**] from initial total [AuNP-**7b**]<sub>0</sub> (calculated from ICP-OES)

### Model boronic acid and linker association constants

Association constants for model boronic acid **10** and linker molecules **18**, **19** and **20** were determined by single point  $^1\text{H}$  NMR spectroscopy. Binding events at either end of the linker were assumed to be independent of each other, as such a 1:1 binding model was assumed. Association constants and concentrations are quoted for individual boronic ester formation events.

**Table 7.7** Association constants derived from equilibrium mixtures of linkers **18**, **19** and **20** with model boronic acid **10** by  $^1\text{H}$  NMR spectroscopy (500.1 MHz,  $\text{CD}_3\text{OD}$ , 298 K, 16 scans,  $D_1 = 5$  s) in the presence of *N*-methylmorpholine (100 eq.) and 4-Bromo-3-fluoronitrobenzene internal standard. Concentrations were measured by integration relative to the internal standard.

Linker	[linker] /mM <sup>a</sup>	[ <b>10</b> •linker] /mM <sup>a</sup>	[ <b>10</b> ] /mM	$K_a$ /M <sup>-1</sup>
<b>18</b>	1.85	7.05	4.27	900
<b>19</b>	0.46	10.60	4.43	5200
<b>20</b>	1.64	9.00	3.06	1800

<sup>a</sup> Linker and complex concentration in terms of functional groups, I.E. [linker] = 2 × [linker]<sub>molecules</sub>

### 7.4.3 Titrations

$K_{\text{base}}$  values of salicylic acid **14** and salicylamide **15** with *N*-methylmorpholine (**Figure 3.8**)

4-Bromo-3-fluoronitrobenzene (5 mM) and salicylic acid **14** or salicylamide **15** (5 mM) were dissolved in CD<sub>3</sub>OD (3 mL) (**Solution A**). *N*-methylmorpholine (300 mM) was added to 2 mL of **Solution A** to make **Solution B**. **Solution B** (5–100  $\mu$ L per addition) was titrated into **Solution A**. The resultant shift in the <sup>19</sup>F resonance of salicylic acid **14** or salicylamide **15** was monitored by <sup>19</sup>F NMR spectroscopy (470.4 MHz, CD<sub>3</sub>OD, 298 K, 8 scans,  $D_1 = 20$  s). Titration data was fitted to a 1:1 binding isotherm by an iterative process using Microsoft Excel or Matlab.

Dependence of boronic ester formation on concentration of base

(**Figure 3.9**)

4-Bromo-3-fluoronitrobenzene (5 mM), 4-fluorocatechol **13** or salicylic acid **14** (5 mM) and model boronic acid **10** (5 mM) were dissolved in CD<sub>3</sub>OD (3 mL) (**Solution A**). *N*-methylmorpholine (150 mM) was added to 2 mL of **Solution A** to make **Solution B**. **Solution B** (5–100  $\mu$ L per addition) was titrated into **Solution A**. The resultant increase in the <sup>19</sup>F resonance of the boronic ester was monitored by <sup>19</sup>F NMR spectroscopy, integrating relative to the internal standard (470.4 MHz, CD<sub>3</sub>OD, 298 K, 8 scans,  $D_1 = 20$  s).

Boronic ester formation on nanoparticle-bound boronic acids, titration to establish equivalents required for saturation binding

4-Bromo-3-fluoronitrobenzene ( $\approx 5$  mM) and AuNP-7 (5 mM, in terms of boronic acid) and *N*-methylmorpholine (70 mM) were dissolved in CD<sub>3</sub>OD (3 mL) (**Solution A**). 3-fluorocatechol **12** or 4-fluorocatechol **13** (300 mM) was added to 2 mL of **Solution A** to make **Solution B**. **Solution B** (5–100  $\mu$ L per addition) was titrated into **Solution A**. The resultant increase in the <sup>19</sup>F resonance of the boronic ester was monitored by <sup>19</sup>F NMR spectroscopy, integrating relative to the internal standard (470.4 MHz, CD<sub>3</sub>OD, 298 K, 8 scans,  $D_1 = 20$  s).

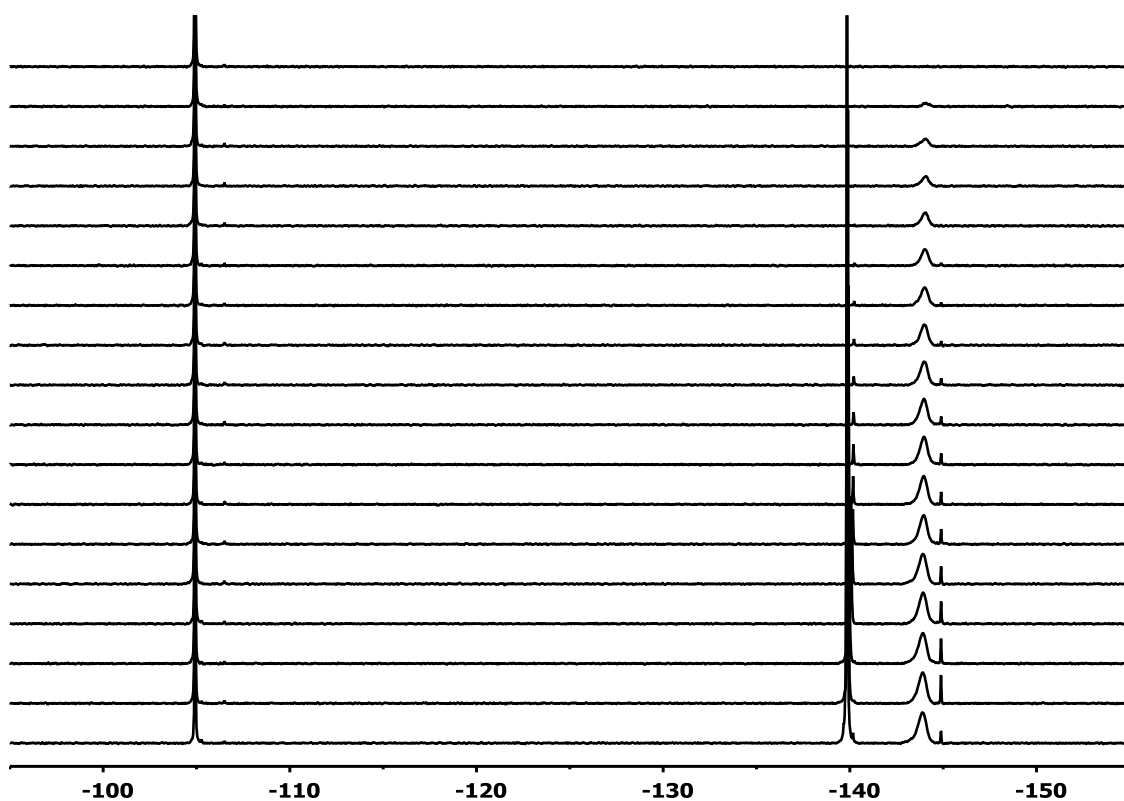


**Figure 7.12** Partial  $^{19}\text{F}$  NMR (470.4 MHz,  $\text{CD}_3\text{OD}$ , 298 K, 8 scans,  $D_1 = 20$  s). Example stack plot from an NMR titration of 3-fluorocatechol **12** with AuNP-7 to establish at how many equivalents of catechol no more boronic ester is formed.

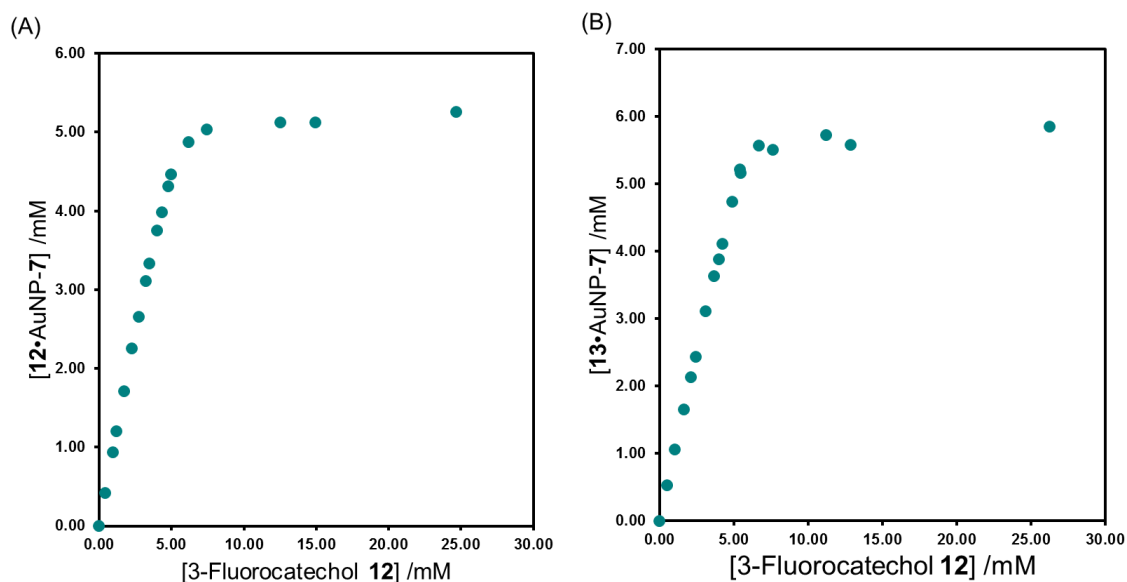


**Figure 7.13** Titration curves for (A) 3-fluorocatechol **12** and (B) 4-fluorocatechol **13** with AuNP-7 (approx. 5 mM), as determined by  $^{19}\text{F}$  NMR (470.4 MHz,  $\text{CD}_3\text{OD}$ , 298 K, 8 scans,  $D_1 = 20$  s).

## 7.5 Boronic ester-mediated nanoparticle assembly

### 7.5.1 Stability of AuNP-7

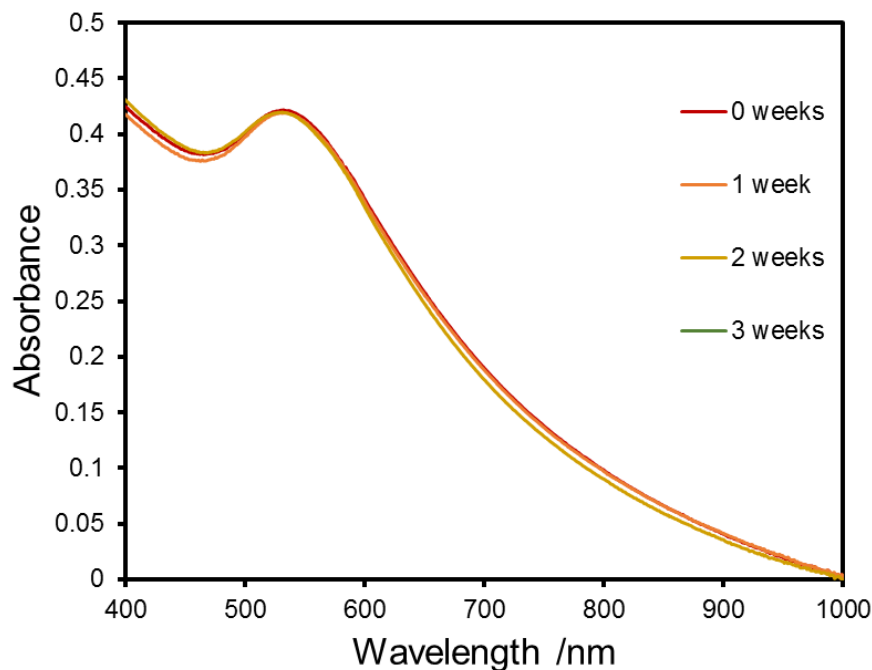


**Figure 7.14** UV-vis spectra (MeOH, 20 °C) showing the colloidal stability of AuNP-7a.

### 7.5.2 Interparticle distance modelling

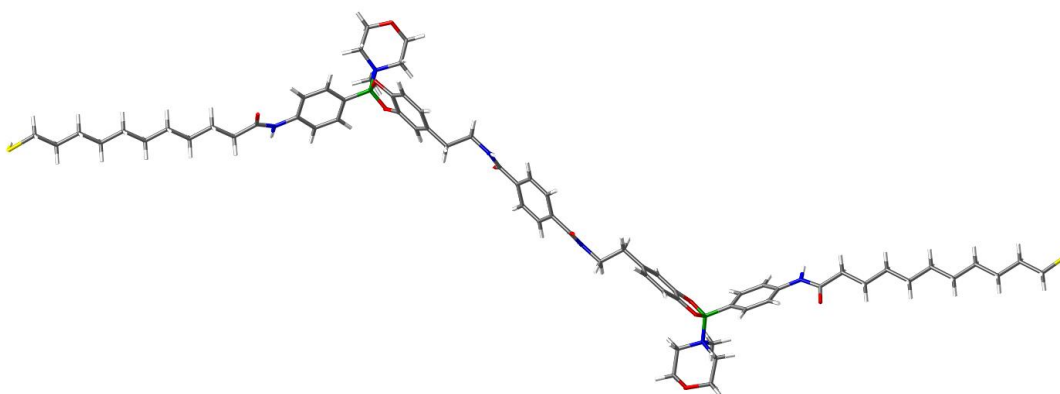


**Figure 7.15** Extended model of nanoparticle-bound boronic ester linkage (Maestro 2012). The sulfur–sulfur distance was measured as 6.09 nm.

### 7.5.3 Fractal dimension determination

The fractal dimension was calculated by a box counting method<sup>214</sup> using ImageJ. Nanoparticle assembly images where nanoparticles lay flat, I.E. only one layer deep, were selected and converted to binary by the 'Threshold' function. The image was analysed using the 'Fractal Box Count' function, using box sizes of 2, 4, 8, 16, 32 and 64. The fractal dimension was determined from the gradient of a plot of log (box size) against log (count) (count of boxes containing the fractal).

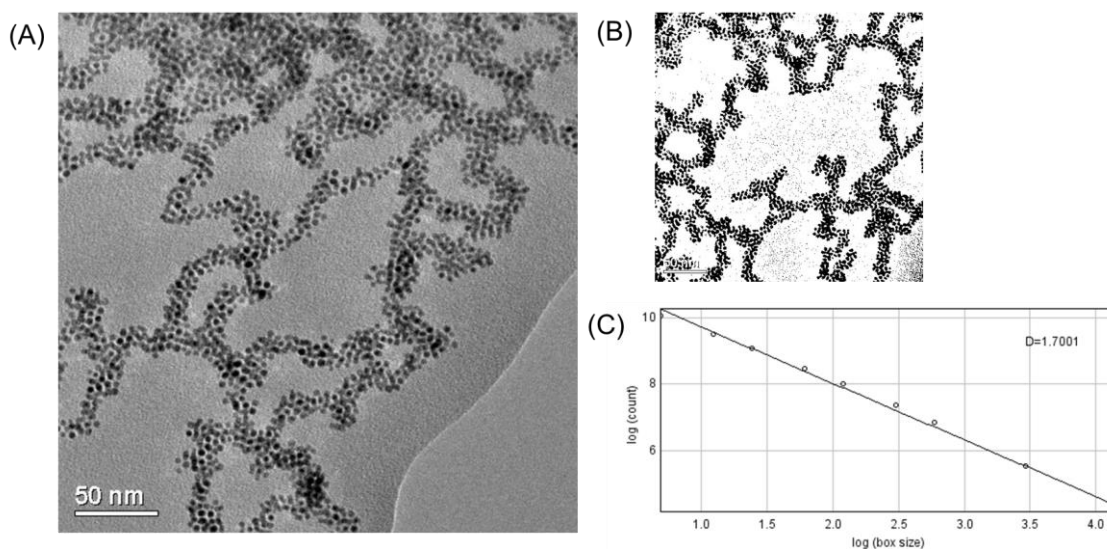


**Figure 7.16** Example of fractal image analysis. (A) the original TEM image. (B) the image converted to binary and (C) a plot of log (box size) against log (count) as determined by the 'Fractal Box count' function in ImageJ.

# References

- 1 M.-C. Daniel and D. Astruc, *Chem. Rev.* **2004**, *104*, 293–346.
- 2 H. Goesmann and C. Feldmann, *Angew. Chem. Int. Ed.* **2010**, *49*, 1362–1395.
- 3 S. E. Lohse and C. J. Murphy, *J. Am. Chem. Soc.* **2012**, *134*, 15607–15620.
- 4 I. Ojea-Jiménez, F. M. Romero, N. G. Bastús and V. Puentes, *J. Phys. Chem. C* **2010**, *114*, 1800–1804.
- 5 C. Wanawongthai, A. Pongpeerapat, K. Higashi, Y. Tozuka, K. Moribe and K. Yamamoto, *Int. J. Pharm.* **2009**, *376*, 169–175.
- 6 A. Gutsch, H. Mühlenweg and M. Krämer, *Small* **2005**, *1*, 30–46.
- 7 V. K. LaMer and R. H. Dinegar, *J. Am. Chem. Soc.* **1950**, *72*, 4847–4854.
- 8 J. Turkevich, P. C. Stevenson and J. Hillier, *Discuss. Faraday Soc.* **1951**, *11*, 55–75.
- 9 G. Frens, *Nature–Phys. Sci.* **1973**, *241*, 20–22.
- 10 P. Zhao, N. Li and D. Astruc, *Coord. Chem. Rev.* **2013**, *257*, 638–665.
- 11 J.-W. Park and J. S. Shumaker-Parry, *J. Am. Chem. Soc.* **2014**, *136*, 1907–1921.
- 12 S. Kumar, K. S. Gandhi and R. Kumar, *Ind. Eng. Chem. Res.* **2007**, *46*, 3128–3136.
- 13 R. Sardar, A. M. Funston, P. Mulvaney and R. W. Murray, *Langmuir* **2009**, *25*, 13840–13851.
- 14 P. J. G. Goulet and R. B. Lennox, *J. Am. Chem. Soc.* **2010**, *132*, 9582–9584.
- 15 K. Saha, S. S. Agasti, C. Kim, X. Li and V. M. Rotello, *Chem. Rev.* **2012**, *112*, 2739–2779.

- 16 T. G. Schaaf, M. N. Shafigullin, J. T. Khoury, I. Vezmar, R. L. Whetten, W. G. Cullen, P. N. First, C. Gutiérrez-Wing, J. Ascencio and M. J. Jose-Yacamán, *J. Phys. Chem. B* **1997**, *101*, 7885–7891.
- 17 J. Park, J. Joo, S. G. Kwon, Y. Jang and T. Hyeon, *Angew. Chem. Int. Ed.* **2007**, *46*, 4630–4660.
- 18 N. Zheng, J. Fan and G. D. Stucky, *J. Am. Chem. Soc.* **2006**, *128*, 6550–6551.
- 19 J. Song, D. Kim and D. Lee, *Langmuir* **2011**, *27*, 13854–13860.
- 20 R. L. Whetten, J. T. Khoury, M. M. Alvarez, S. Murthy, I. Vezmar, Z. L. Wang, P. W. Stephens, C. L. Cleveland, W. D. Luedtke and U. Landman, *Adv. Mater.* **1996**, *8*, 428–433.
- 21 C. L. Cleveland, U. Landman, M. N. Shafigullin, P. W. Stephens and R. L. Whetten, *Z. Phys. D* **1997**, *40*, 503–508.
- 22 F. Li, D. P. Josephson and A. Stein, *Angew. Chem. Int. Ed.* **2011**, *50*, 360–388.
- 23 C. L. Choi and A. P. Alivisatos, *Annu. Rev. Phys. Chem.* **2010**, *61*, 369–389.
- 24 K. C. Nicolaou and E. J. Sorensen, *Classics in Total Synthesis: Targets, Strategies, Methods*, Wiley-VCH, **1996**.
- 25 C. Burda, X. Chen, R. Narayanan and M. A. El-Sayed, *Chem. Rev.* **2005**, *105*, 1025–1102.
- 26 M. Brust, M. Walker, D. Bethell, D. J. Schiffrin and R. Whyman, *J. Chem. Soc., Chem. Commun.* **1994**, 801–802.
- 27 Y. Xue, X. Li, H. Li and W. Zhang, *Nat. Commun.* **2014**, *5*, 4348.
- 28 K. L. Kelly, E. Coronado, L. L. Zhao and G. C. Schatz, *J. Phys. Chem. B* **2003**, *107*, 668–677.
- 29 M. Haruta, N. Yamada, T. Kobayashi and S. Ijima, *J. Catal.* **1989**, *115*, 301–309.
- 30 P. Zhao, N. Li and D. Astruc, *Coord. Chem. Rev.* **2013**, *257*, 638–665.
- 31 E. Gaffet, M. Tachikart, O. El Kedim and R. Rahouadj, *Mater. Charact.* **1996**, *36*, 185–190.
- 32 J. S. Bradley, *Clusters and Colloids*, VCH, **1994**.

- 
- 33 D. Steinigeweg, M. Schütz, M. Salehi and S. Schlücker, *Small* **2011**, *7*, 2443–2448.
- 34 B. Kowalczyk, I. Lagzi and B. A. Grzybowski, *Nanoseparations, Curr. Opin. Colloid Interface Sci.* **2011**, *16*, 135–148.
- 35 N. T. K. Thanh, N. Maclean and S. Mahiddine, *Chem. Rev.* **2014**, *114*, 7610–7630.
- 36 F. Wang, V. N. Richards, S. P. Shields and W. E. Buhro, *Chem. Mater.* **2014**, *26*, 5–21.
- 37 G. Frens, *Nat.–Phys. Sci.* **1973**, *241*, 20–22.
- 38 M. J. Hostetler, J. E. Wingate, C.-J. Zhong, J. E. Harris, R. W. Vachet, M. R. Clark, J. D. Londono, S. J. Green, J. J. Stokes, G. D. Wignall, G. L. Glish, M. D. Porter, N. D. Evans and R. W. Murray, *Langmuir* **1998**, *14*, 17–30.
- 39 G. Canzi, A. A. Morse and C. P. Kubiak, *J. Phys. Chem. C* **2011**, *115*, 7972–7978.
- 40 A. C. Templeton, M. J. Hostetler, C. T. Kraft and R. W. Murray, *J. Am. Chem. Soc.* **1998**, *120*, 1906–1911.
- 41 X. Ji, X. Song, J. Li, Y. Bai, W. Yang and X. Peng, *J. Am. Chem. Soc.* **2007**, *129*, 13939–13948.
- 42 Y. Li, O. Zaluzhna, B. Xu, Y. Gao, J. M. Modest, Y. J. Tong, *J. Am. Chem. Soc.* **2011**, *133*, 2092–2095.
- 43 N. R. Jana and X. Peng, *J. Am. Chem. Soc.* **2003**, *125*, 14280–14281.
- 44 J. R. Heath, *Science* **1997**, *277*, 1978–1981.
- 45 D. V. Leff, L. Brandt and J. R. Heath, *Langmuir* **1996**, *12*, 4723–4730.
- 46 D. E. Cliffl, F. P. Zamborini, S. M. Gross and R. W. Murray, *Langmuir* **2000**, *16*, 9699–9702.
- 47 G. Schmid and A. Lehnert, *Angew. Chem. Int. Ed.* **1989**, *28*, 780.
- 48 D. L. Van Hying, W. G. Klemperer and C. F. Zukoski, *Langmuir* **2001**, *17*, 3128–3135.
- 49 H. Zheng, R. K. Smith, Y.-w. Jun, C. Kisielowski, U. Dahmen and A. P. Alivisatos, *Science* **2009**, *5*, 1309–1312.
- 50 D. G. Duff, A. Baiker and P. P. Edwards, *Langmuir* **1993**, *9*, 2301–2309.

- 
- 51 D. Andreescu, T. K. Sau and D. V. Goia, *J. Colloid Interface Sci.* **2006**, *298*, 742–751.
- 52 H. Hiramatsu and F. E. Osterloh, *Chem. Mater.* **2004**, *16*, 2509–2511.
- 53 T. G. Clarke, N. A. Hampson, J. B. Lee, J. R. Morley and B. Scanlon, *Tetrahedron Lett.* **1968**, *54*, 5685–5688.
- 54 Y. Li, O. Zaluzhna and Y. J. Tong, *Chem. Commun.* **2011**, *47*, 6033–6035.
- 55 S. Peng, Y. Lee, C. Wang, H. Yin, S. Dai and S. Sun, *Nano Res.* **2008**, *1*, 229–234.
- 56 R. Sadar and J. S. Shumaker-Parry, *Chem. Mater.* **2009**, *21*, 1167–1169.
- 57 R. Sadar and J. S. Shumaker-Parry, *J. Am. Chem. Soc.* **2011**, *133*, 8179–8190.
- 58 W. D. Pyrz and D. J. Buttrey, *Langmuir* **2008**, *24*, 11350–11360.
- 59 J. Lim, S. P. Yeap, H. X. Che and S. C. Low, *Nanoscale Res. Lett.* **2013**, *8*, 381–394.
- 60 O. Kohlmann, W. E. Steinmetz, X.-A. Mao, W. P. Wuelfing, A. C. Templeton, R. W. Murray and C. S. Johnson, *J. Phys. Chem. B* **2001**, *105*, 8801–8809.
- 61 L. E. Marbella and J. E. Millstone, *Chem. Mater.* **2015**, *27*, 2721–2739.
- 62 W. P. Wuelfing, S. M. Gross, D. T. Miles and R. W. Murray, *J. Am. Chem. Soc.* **1998**, *120*, 12696–12697.
- 63 A. G. Kanaras, F. S. Kamounah, K. Schaumburg, C. J. Kiely and M. Brust, *Chem. Commun.* **2002**, 2294–2295.
- 64 R. S. Ingram, M. J. Hostetler and R. W. Murray, *J. Am. Chem. Soc.* **1997**, *119*, 9175–9178.
- 65 M. J. Hostetler, A. Templeton and R. Murray, *Langmuir* **1999**, *15*, 3782–3789.
- 66 A. Caragheorgheopol and V. Chechik, *Phys. Chem. Chem. Phys.* **2008**, *10*, 5029–5041.
- 67 Y. Song, T. Huang and R. Murray, *J. Am. Chem. Soc.* **2003**, *125*, 11694–11701.

- 68 C.-T. Kuo, C.-F. Chen, M.-W. Gu, M.-N. Su, J.-F. Huang, M.-J. Huang and C.-h. Chen, *Chem. Asian. J.* **2014**, *9*, 844–851.
- 69 J. Owen, *Science* **2015**, *347*, 615–616.
- 70 T. Mizuhara, K. Saha, D. F. Moyano, C. S. Kim, B. Yan, Y.-K. Kim and V. M. Rotello, *Angew. Chem. Int. Ed.* **2015**, *54*, 6567–6570.
- 71 P. P. Pillai, S. Huda, B. Kowalczyk and B. A. Grzybowski, *J. Am. Chem. Soc.* **2013**, *135*, 6392–6395.
- 72 R. J. Macfarlane, M. N. O'Brien, S. H. Petrosko and C. A. Mirkin, *Angew. Chem. Int. Ed.* **2013**, *52*, 5688–5698.
- 73 U. Drechsler, B. Erdogan and V. M. Rotello, *Chem. Eur. J.* **2004**, *10*, 5570–5579.
- 74 V. Montes-Garcia, J. Perez-Juste, I. Pastoriza-Santos and L. M. Liz-Marzán, *Chem. Eur. J.* **2014**, *20*, 10874–10883.
- 75 Y.-W. Yang, Y.-L. Sun and N. Song, *Acc. Chem. Res.* **2014**, *47*, 1950–1960.
- 76 E. R. Kay, J. Lee, D. G. Nocera and M. G. Bawendi, *Angew. Chem. Int. Ed.* **2013**, *52*, 1165–1169.
- 77 R. Klajn, J. F. Stoddart and B. A. Grzybowski, *Chem. Soc. Rev.* **2010**, *39*, 2203–2237.
- 78 A. C. Fahrenbach, S. C. Warren, J. T. Incorvati, A.-J. Avestro, J. C. Barnes, J. F. Stoddart and B. A. Grzybowski, *Adv. Mater.* **2013**, *25*, 331–348.
- 79 K. E. Sapsford, W. R. Algar, L. Berti, K. B. Gemmill, B. J. Casey, E. Oh, M. H. Stewart and I. L. Medintz, *Chem. Rev.* **2013**, *113*, 1904–2074.
- 80 I. Kosif, M. Cui, T. P. Russell and T. Emrick, *Angew. Chem. Int. Ed.* **2013**, *52*, 6620–6623.
- 81 F. della Sala and E. R. Kay, *Angew. Chem. Int. Ed.* **2015**, *54*, 4187–4191.
- 82 P. Nowak, V. Saggiomo, F. Salehian, M. Colomb-Delsuc, Y. Han and S. Otto, *Angew. Chem. Int. Ed.* **2015**, *54*, 4192–4197.
- 83 Z. H. Nie, A. Petukhova and E. Kumacheva, *Nat. Nanotechnol.* **2010**, *5*, 15–25.

- 
- 84 T. Wang, D. LaMontagne, J. Lynch, J. Zhuang and Y. C. Cao, *Chem. Soc. Rev.* **2013**, *42*, 2804–2823.
- 85 M. Grzelczak, J. Vermant, E. M. Furst and L. M. Liz-Marzán, *ACS Nano* **2011**, *4*, 3591–3605.
- 86 L. Xu, W. Ma, L. Wang, C. Xu, H. Kuang, N. A. Kotov, *Chem. Soc. Rev.* **2013**, *42*, 3114–3126.
- 87 N. Gandra and S. Singamaneni, *Chem. Commun.* **2012**, *48*, 11540–11542.
- 88 C. Rossner and P. Vana, *Angew. Chem. Int. Ed.* **2014**, *53*, 12639–12642.
- 89 Y. Wang, G. Chen, M. Yang, G. Silber, S. Xing, L. H. Tan, F. Wang, Y. Feng, X. Liu, S. Li and H. Chen, *Nat. Commun.* **2010**, *1*, 87.
- 90 J. H. Yoon, J. Lim and S. Yoon, *ACS Nano* **2012**, *6*, 7199–7208.
- 91 Y. Min, M. Akbulut, K. Kristiansen, Y. Golan and J. Israelachvili, *Nat. Mater.* **2008**, *7*, 527–538.
- 92 R. Klajn, K. J. M. Bishop and B. A. Grzybowski, *Proc. Natl. Acad. Sci. U.S.A.* **2007**, *104*, 10305–10309.
- 93 M. Quintiliani, M. Bassetti, C. Pasquini, C. Battocchio, M. de Rossi, F. Mura, R. Matassa, L. Fontana, M. V. Russo and I. Fratoddi, *J. Mater. Chem. C* **2014**, *2*, 2517
- 94 M. Orbach, M. Lahav, P. Milko, S. G. Wolf and M. E. van der Boom, *Angew. Chem. Int. Ed.* **2012**, *51*, 7142–7145.
- 95 L. Beverina, *ChemPhysChem* **2010**, *11*, 2075–2077.
- 96 A. K. Boal, F. Ilhan, J. E. DeRouchey, T. Thurn-Albrecht, T. P. Russell and V. M. Rotello, *Nature* **2000**, *404*, 746–748.
- 97 T. Shirman, T. Arad, M. E. van der Boom, *Angew. Chem. Int. Ed.* **2010**, *49*, 926–929.
- 98 R. Klajn, M. A. Olson, P. J. Wesson, L. Fang, A. Coskun, A. Trabolsi, S. Soh, J. F. Stoddart and B. A. Grzybowski, *Nat. Chem.* **2009**, *1*, 733–738.
- 99 G. Pieters, C. Pezzato and L. J. Prins, *J. Am. Chem. Soc.* **2012**, *134*, 15289–15292.
- 100 C. Pezzato, P. Scrimin and L. J. Prins, *Angew. Chem. Int. Ed.* **2014**, *53*, 2104–2109.
-

- 
- 101 D. Ryan, S. N. Rao, H. Rensmo, D. Fitzmaurice, J. A. Preece, S. Wenger, J. F. Stoddart and N. Zaccheroni, *J. Am. Chem. Soc.* **2000**, *122*, 6252–6257.
- 102 R. J. Coulston, S. T. Jones, T.-C. Lee, E. A. Appel and O. A. Scherman, *Chem. Commun.* **2011**, *47*, 164–166.
- 103 C. A. Mirkin, R. L. Letsinger, R. C. Mucic and J. J. Storhoff, *Nature* **1996**, *389*, 607–609.
- 104 A. P. Alivisatos, K. P. Johnsson, X. Peng, T. E. Wilson, C. J. Loweth, M. P. Bruchez Jr. and P. G. Schultz, *Nature* **1996**, *382*, 609–611.
- 105 S. Y. Park, A. K. R. Lytton-Jean, B. Lee, S. Weigand, G. C. Schatz and C. A. Mirkin, *Nature* **2008**, *451*, 553–556.
- 106 R. J. Macfarlane, B. Lee, H. D. Hill, A. J. Senesi, S. Seifert and C. A. Mirkin, *Proc. Natl. Acad. Sci. U.S.A.* **2009**, *106*, 10493–10498.
- 107 D. Nykypanchuk, M. M. Maye, D. van der Lelie and O. Gang, *Nature* **2008**, *451*, 549–552.
- 108 E. V. Shevchenko, D. V. Talapin, N. A. Kotov, S. O'Brien and C. B. Murray, *Nature* **2006**, *439*, 55–59.
- 109 C. B. Murray, C. R. Kagan and M. G. Bawendi, *Annu. Rev. Mater. Sci.* **2000**, *30*, 545–610.
- 110 A. M. Kalsin, M. Fialkowski, M. Paszewski, S. K. Smoukov, K. J. M. Bishop and B. A. Grzybowski, *Science* **2006**, *312*, 420–424.
- 111 J. Henzie, M. Grünwald, A. Widmer-Cooper, P. L. Geissler and P. Yang, *Nat. Mater.* **2012**, *11*, 131–137.
- 112 F. X. Redl, K.-S. Cho, C. B. Murray and S. O'Brien, *Nature* **2003**, *423*, 968–971.
- 113 D. A. Giljohann, D. S. Seferos, A. E. Prigodich, P. C. Patel and C. A. Mirkin, *J. Am. Chem. Soc.* **2009**, *131*, 2072–2073.
- 114 R. J. Macfarlane, B. Lee, M. R. Jones, N. Harris, G. C. Schatz, C. A. Mirkin, *Science* **2011**, *334*, 204–208.
- 115 D. Nykypanchuk, M. M. Maye, D. van der Lelie and O. Gang, *Nature* **2008**, *451*, 549–552.
- 116 D. Sun and O. Gang, *J. Am. Chem. Soc.* **2011**, *133*, 5252–5254.

- 
- 117 R. J. Macfarlane, R. V. Thaner, K. A. Brown, J. Zhang, B. Lee, S.-B. T. Nguyen and C. A. Mirkin, *Proc. Natl. Acad. Sci. U.S.A.* **2014**, *111*, 14995–15000.
- 118 C. Zhang, R. J. Macfarlane, K. L. Young, C. H. J. Choi, L. L. Hao, E. Auyeung, G. L. Liu, X. Z. Zhou and C. A. Mirkin, *Nat. Mater.* **2013**, *12*, 741–746.
- 119 J. I. Cutler, E. Auyeung, C. A. Mirkin, *J. Am. Chem. Soc.* **2012**, *134*, 1376–1391.
- 120 R. Elghanian, J. J. Storhoff, R. C. Mucic, R. L. Letsinger and C. A. Mirkin, *Science* **1997**, *277*, 1078–1081.
- 121 D. A. Giljohann, D. S. Seferos, W. L. Daniel, M. D. Massich, P. C. Patel and C. A. Mirkin, *Angew. Chem. Int. Ed.* **2010**, *49*, 3280–3294.
- 122 D. Zheng, D. S. Seferos, D. A. Giljohann, P. C. Patel and C. A. Mirkin, *Nano Lett.* **2009**, *9*, 3258–3261.
- 123 M. P. Busson, B. Rolly, B. Stout, N. Bonod, E. Larquet, A. Polman and S. Bidault, *Nano Lett.* **2011**, *11*, 5060–5065.
- 124 F. Huo, A. K. R. Lytton-Jean and C. A. Mirkin, *Adv. Mater.* **2006**, *18*, 2304–2306.
- 125 M. M. Maye, M. T. Kumara, D. Nykypanchuk, W. B. Sherman and O. Gang, *Nat. Nanotechnol.* **2010**, *5*, 116–120.
- 126 D. Zanchet, C. M. Micheel, W. J. Parak, D. Gerion, S. C. Williams and A. P. Alivisatos, *J. Phys. Chem. B* **2002**, *106*, 11758–11763.
- 127 G. Chen, Y. Wang, L. H. Tan, M. Yang, L. S. Tan, Y. Chen and H. Chen, *J. Am. Chem. Soc.* **2009**, *131*, 4218–4219.
- 128 L. Bai, X. Ma, J. Liu, X. Sun, D. Zhao and D. G. Evans, *J. Am. Chem. Soc.* **2010**, *132*, 2333–2337.
- 129 G. Gasparini, M. Dal Molin, A. Lovato and L. J. Prins, *Dynamic Covalent Chemistry. Supramolecular Chemistry: From Molecules to Nanomaterials*, Wiley, **2012**.
- 130 Y. Jin, C. Yu, R. J. Denman and W. Zhang, *Chem. Soc. Rev.* **2013**, *42*, 6634–6654.
- 131 J. M. Lehn, *Chem. Soc. Rev.* **2007**, *36*, 151–160.
- 132 P. T. Corbett, J. Leclaire, L. Vial, K. R. West, J. L. Wietor, J. K. M. Sanders and S. Otto, *Chem. Rev.* **2006**, *106*, 3652–3711.
-

- 
- 133 F. B. L. Cougnons and J. K. M. Sanders, *Acc. Chem. Res.* **2012**, *45*, 2211–2221.
- 134 R. A. R. Hunta and S. Otto, *Chem. Commun.* **2011**, *47*, 847–858.
- 135 J. P. Lorand and J. O. Edwards, *J. Org. Chem.* **1959**, *24*, 769–774.
- 136 H. G. Kuivila, A. H. Keough and E. J. Soboczenski, *J. Org. Chem.* **1953**, *19*, 780–783.
- 137 R. Pizer & C. Tihal, *Inorg. Chem.* **1992**, *31*, 3243–3247.
- 138 X. Feng, X. Ding and D. Jiang, *Chem. Soc. Rev.* **2012**, *41*, 6010–6022.
- 139 A. P. Cote, A. I. Benin, N. W. Ockwig, M. O’Keeffe, A. J. Matzger and O. M. Yaghi, *Science* **2005**, *310*, 1166–1170.
- 140 E. L. Spitler and W. R. Dichtel, *Nat. Chem.* **2010**, *2*, 672–677.
- 141 E. L. Spitler, J. W. Colson, F. J. Uribe-Romo, A. R. Woll, M. R. Giovino, A. Saldivar and W. R. Dichtel, *Angew. Chem. Int. Ed.* **2012**, *51*, 2623–2627.
- 142 X. Wu, Z. Li, X.-X. Chen, J. S. Fossey, T. D. James and Y.-B. Jiang *Chem. Soc. Rev.* **2013**, *42*, 8032–8048.
- 143 T. D. James, M. D. Phillips and S. Shinkai, *Boronic Acids in Saccharide Recognition*, Royal Society of Chemistry, **2006**.
- 144 S. D. Bull, M. G. Davidson, J. M. H. van den Elsen, J. S. Fossey, A. Toby, A. Jenkins, Y.-B. Jiang, Y. Kubo, F. Marken, K. Sakurai, J. Zhao and T. D. James, *Acc. Chem. Res.* **2013**, *46*, 312–326.
- 145 C. R. Wade, A. E. J. Broomsgrove, S. Aldridge and F. P. Gabbaï, *Chem. Rev.* **2010**, *110*, 3958–3984.
- 146 M. Li, W. H. Zhu, F. Marken and T. D. James, *Chem. Commun.* **2015**, *51*, 14562–14573.
- 147 D. E. Prasuhn, J. B. Blanco-Canosa, G. J. Vora, J. B. Delehanty, K. Susumu, B. C. Mei, P. E. Dawson and I. L. Medintz. *ACS Nano* **2010**, *4*, 267–278.
- 148 J. B. Blanco-Canosa, I. L. Medintz, D. Farrell, H. Mattoussi, P. E. Dawson, *J. Am. Chem. Soc.* **2010**, *132*, 10027–10033.
- 149 T. Q. Huy, R. V. Chung, N. T. Thuy, C. Blanco-Andujar and N. T. K. Thanh, *Faraday Discuss.* **2014**, *175*, 73–82.
- 150 S. S. Banerjee and D.-H. Chen, *Nanotechnology* **2008**, *19*, 505104.
-

- 
- 151 Q. Yuan, R. Venkatasubramanian, S. Hein and R. D. K. Misra, *Acta Biomater.* **2008**, *4*, 1024–1037.
- 152 S. Aryal, J. J. Grailer, S. Pilla, D. A. Steeber and S. Gong, *J. Mater. Chem.* **2009**, *19*, 7879–7884.
- 153 M. Prabakaran, J. J. Grailer, S. Pilla, D. A. Steeber and S. Gong, *Biomaterials* **2009**, *30*, 6065–6075.
- 154 S. Aryal, C.-M. J. Hu and L. Zhang, *ACS Nano* **2010**, *4*, 251–258.
- 155 K. Aslan, J. Zhang, J. R. Lakowicz and C. D. Geddes, *J. Fluoresc.* **2004**, *14*, 391–400.
- 156 J. Zhang, C. D. Geddes and J. R. Lakowicz, *Anal. Biochem.* **2004**, *332*, 253–260.
- 157 S. Mohapatra, N. Panda and P. Pramanik, *Mater. Sci. Eng. C* **2009**, *29*, 2254–2260.
- 158 J. Ye, Y. Chen and Z. A. Liu, *Angew. Chem. Int. Ed.* **2014**, *53*, 10386–10389.
- 159 G. Xu, W. Zhang, L. Wei, H. Lu and P. Yang, *Analyst* **2013**, *138*, 1876–1885.
- 160 P. Dou and Z. Liu, *Anal. Bioanal. Chem.* **2011**, *399*, 3423–3429.
- 161 H. Wang, Z. Bie, C. Lü and Z. Liu, *Chem. Sci.* **2013**, *4*, 4298–4303.
- 162 L. Lin, X. Tian, S. Hong, P. Dai, Q. You, R. Wang, L. Feng, C. Xie, Z.-Q. Tian and X. Chen, *Angew. Chem. Int. Ed.* **2013**, *52*, 7266–7271.
- 163 D. Zhang and R. Pelton, *Langmuir* **2012**, *28*, 3112–3119.
- 164 N. Xia, D. Deng, L. Zhang, B. Yuan, M. Jing, J. Du and L. Liu, *Biosens. Bioelectron.* **2013**, *43*, 155–159.
- 165 Z.-A. Lin, J.-N. Zheng, F. Lin, L. Zhang, Z. Cai and G.-N. Chen, *J. Mater. Chem.* **2011**, *21*, 518.
- 166 G. Yao, H. Zhang, C. Deng, H. Lu, X. Zhang and P. Yang, *Rapid Commun. Mass Spectrom.* **2009**, *23*, 3493–3500.
- 167 K. Sparbier, A. Asperger, A. Resemann, I. Kessler, S. Koch, T. Wenzel, L. Vorweg, D. Suckau and M. J. Kostrzewa, *Biomol. Tech.* **2007**, *18*, 252–258.
- 168 W. Zhou, N. Yao, G. Yao, C. Deng, X. Zhan and P. Yang, *Chem. Commun.* **2008**, *43*, 5577–5579.
-

- 
- 169 K. Sparbier, S. Koch, I. Kessler, T. Wenzel and M. J. Kostrzewa, *Biomol. Tech.* **2005**, *16*, 405–411.
- 170 L. Liang and Z. Liu, *Chem. Commun.* **2011**, *47*, 2255–2257.
- 171 S. Liu, Z. Du, P. Li and F. Li, *Biosens. Bioelectron.* **2012**, *35*, 443–446.
- 172 L. Borlido, A. M. Azevedo, A. C. Roque and M. R. Aires-Barros, *J. Chromatogr. A* **2011**, *1218*, 7821–7827.
- 173 S. Li, L. Mao, Y. Tian, J. Wang and N. Zhou, *Analyst* **2012**, *137*, 823–825.
- 174 B. Kong, A. Zhu, Y. Luo, Y. Tian, Y. Yu and G. Shi, *Angew. Chem. Int. Ed.* **2011**, *50*, 1837–1840.
- 175 W. Scarano, H. T. T. Duong, H. Lu, P. L. De Souza and M. H. Stenzel, *Biomacromolecules* **2013**, *14*, 962–975.
- 176 E. Aznar, M. D. Marcos, R. Martínez-Máñez, F. Sancenón, J. Soto, P. Amorós and C. Guillem, *J. Am. Chem. Soc.* **2009**, *131*, 6833–6843.
- 177 Y. Zhao, B. G. Trewyn, I. I. Slowing and V. S.-Y Lin, *J. Am. Chem. Soc.* **2009**, *131*, 8398–8400.
- 178 K. P. Browne and B. A. Grzybowski, *Langmuir* **2011**, *27*, 1246–1250.
- 179 V. Chechik, R. M. Crooks and C. J. M. Stirling, *Adv. Mater.* **2000**, *12*, 1161–1171.
- 180 S. Guo, L. Lu and H. Cai, *Synlett* **2013**, *24*, 1712–1714.
- 181 A. N. Cammidge, V. H. M. Goddard, C. P. J. Schubert, H. Gopee, D. L. Hughes and D. Gonzalez-Lucas, *Org. Lett.* **2011**, *13*, 6034–6037.
- 182 M. Conte, H. Miyamura, S. Kobayashi and V. Chechik, *Chem. Commun.* **2010**, *46*, 145–147.
- 183 C. Marsden, E. Taarning, D. Hansen, L. Johansen, S. K. Klitgaard, K. Egeblad and C. H. Christensen, *Green Chem.* **2008**, *10*, 168–170.
- 184 S. Biella, L. Prati and M. Rossi, *J. Mol. Catal. A: Chem.* **2003**, *197*, 207–212.
- 185 M. Teranishi, S.-i. Naya and H. Tada, *J. Am. Chem. Soc.* **2010**, *132*, 7850–7851.
- 186 E. H. Cordes and W. P. Jenks, *J. Am. Chem. Soc.* **1962**, *84*, 826–831.
- 187 R. Pizer and C. Tihal, *Inorg. Chem.* **1992**, *31*, 3243–3247.
-

- 
- 188 L. K. Mohler and A. W. Czarnik, *J. Am. Chem. Soc.* **1993**, *115*, 7037–7038.
- 189 E. P. Serjeant and B. Dempsey, *Ionisation Constants of Organic Acids in Aqueous Solution*, Pergamon Press, **1979**.
- 190 J. Havel, L. Havelková and M. Bartušek, *Chem. Zvesti* **1969**, *23*, 582–588.
- 191 M. Mikešova and M. Bartušek, *Chem. Zvesti* **1978**, *32*, 472–477.
- 192 D. W. Tanner and T. C. Bruice, *J. Am. Chem. Soc.* **1967**, *89*, 6954–6971.
- 193 M. L. Stolowitz, C. Ahlem, K. A. Hughes, R. J. Kaiser, E. A. Kesicki, G. Li, K. P. Lund, S. M. Torkelson and J. P. Wiley, *Bioconjug. Chem.* **2001**, *12*, 229–239.
- 194 M. Arzt, C. Seidler, D. Y. W. Ng and T. Weil, *Chem. Asian. J.* **2014**, *9*, 1994–2003.
- 195 M. C. Roberts, M. C. Hanson, A. P. Massey, E. A. Karren and P. F. Kiser, *Adv. Mater.* **2007**, *19*, 2503–2507.
- 196 M. C. Roberts, A. Mahalingam, M. C. Hanson and P. F. Kiser, *Macromolecules* **2008**, *41*, 8832–8840.
- 197 D. D. Perrin, *Dissociation Constants of Organic Acids and Bases*, Butterworths, **1965**; Supplement **1972**.
- 198 J. Corse and L. L. Ingraham, *J. Am. Chem. Soc.* **1951**, *73*, 5706–5707.
- 199 D. Nematollahi and M. Rafiee, *J. Electroanal. Chem.* **2004**, *566*, 31–37.
- 200 H. K. Hall Jr., *J. Am. Chem. Soc.* **1957**, *79*, 5441–5444.
- 201 M. T. Cuberes, R. R. Schlitter and K. Gimzewski, *J. Appl. Phys. Lett.* **1996**, *69*, 3016.
- 202 D. Dietzel, T. Mönninghoff, L. Jansen, H. Fuchs, C. Ritter, U. D. Schwarz and A. Schirmeisen, *J. Appl. Phys.* **2007**, *102*, 084306.
- 203 K. Mougin, E. Gnecco, A. Rao, M. T. Cuberes, S. Jayaraman, E. W. McFarland, H. Haidara and E. Meyer, *Langmuir* **2008**, *24*, 1577–1581.
- 204 D. V. Talapin, J.-S. Lee, M. V. Kovalenko and E. V. Shevchenko, *Chem. Rev.* **2010**, *110*, 389–458.
-

- 
- 205 H. Zhang, E. W. Edwards, D. Wang and H. Möhwald, *Phys. Chem. Chem. Phys.* **2006**, *8*, 3288–3299.
- 206 X. Ye, J. Chen, B. T. Diroll and C. B. Murray, *Nano. Lett.* **2013**, *13*, 1291–1297.
- 207 B. A. Korgel, *Nat. Mater.* **2010**, *9*, 701–703.
- 208 D. S. Sebba, J. J. Mock, D. R. Smith, T. H. LaBean and A. A. Lazarides, *Nano Lett.* **2008**, *8*, 1803–1808.
- 209 D. S. Sebba, T. H. LaBean and A. A. Lazarides, *Appl. Phys. B* **2008**, *93*, 69–78.
- 210 C. Sönnichsen, B. M. Reinhard, J. Liphardt and A. P. Alivisatos, *Nat. Biotechnol.* **2005**, *6*, 741–745.
- 211 B. Nickel and T. Liedl, *Nat. Mater.* **2015**, *14*, 746–749.
- 212 S. J. Tan, M. J. Campolongo, D. Luo and W. Cheng, *Nat. Nanotechnol.* **2011**, *6*, 268–276.
- 212a T. F. A. De Greef, M. M. J. Smulders, M. Wolffs, A. P. H. J. Schenning, R. P. Sijbesma, and E. W. Meijer, *Chem. Rev.* **2009**, *109*, 5687–5754.
- 212b G. Armstrong and M. Buggy, *J. Mater. Sci.* **2005**, *40*, 547–559.
- 213 G. Albarran, W. Boggess, V. Rassolov and R. H. Schuler, *J. Phys. Chem. A*, **2010**, *114*, 7470–7478.
- 214 K. Falconer, *Fractal Geometry*, Wiley, **2003**.
- 215 T. R. Ní Mhíocháin and J. M. D. Coey, *Phys. Rev. E* **2004**, *69*, 061404.
- 216 K. Manthiram, Y. Surendranath and A. P. Alivisatos, *J. Am. Chem. Soc.* **2014**, *136*, 7237–7240.
- 217 S. China, C. Mazzoleni, K. Gorkowski, A. C. Aiken and M. K. Dubey, *Nat. Comm.* **2013**, *4*, 2122.
- 218 P. Sandkühler, M. Lattuada, H. Wu, J. Sefcik and M. Morbidelli, *Adv. Colloid Interface Sci.* **2005**, *113*, 65–146.
- 219 H. Wu, M. Lattuada and M. Morbidelli, *Adv. Colloid Interface Sci.* **2013**, *195–196*: 41–49.
- 220 P. Meakin, *Ann. Rev. Phys. Chem.* **1988**, *39*, 237–267.

- 
- 221 S. T. Jones, J. M. Zayed and O. A. Scherman, *Nanoscale* **2013**, *5*, 5299–5302.
- 222 N. J. Halas, S. Lal, W.-S. Chang, S. Link and P. Nordlander, *Chem. Rev.* **2011**, *111*, 3913–3961.
- 223 S. K. Ghosh and T. Pal, *Chem. Rev.* **2007**, *107*, 4797–4862.
- 224 J. M. Romo-Herrera, R. A. Alvarez-Puebla and L. M. Liz-Marzán, *Nanoscale* **2011**, *3*, 1304.
- 225 N. L. Rosi and C. A. Mirkin, *Chem. Rev.* **2005**, *105*, 1547–1562.
- 226 S. M. Nie and S. R. Emory, *Science* **1997**, *275*, 1102–1106.
- 227 K. Kneipp, Y. Wang, H. Kneipp, L. T. Perelman, I. Itzkan, R. R. Dasari and M. S. Feld, *Phys. Rev. Lett.* **1997**, *78*, 1667.
- 228 L. Guerrini and D. Graham, *Chem. Soc. Rev.* **2012**, *41*, 7085–7107.
- 229 R. C. Mucic, J. J. Storhoff, C. A. Mirkin and R. L. Letsinger, *J. Am. Chem. Soc.* **1998**, *120*, 12674–12675.
- 230 X. Xu, N. L. Rosi, Y. Wang, F. Huo and C. A. Mirkin, *J. Am. Chem. Soc.* **2006**, *128*, 9286–9287.
- 231 H. Yao, C. Yi, C.-H. Tzang, J. Zhu and M. Yang, *Nanotechnology* **2007**, *18*, 015102.
- 232 M. M. Maye, D. Nykypanchuk, M. Cuisinier, D. van der Lelie and O. Gang, *Nat. Mater.* **2009**, *8*, 388–391.
- 233 S.-Y. Chen and A. A. Lazarides, *J. Phys. Chem. C*, **2009**, *113*, 12167–12175.
- 234 S. Pal, J. Sharma, H. Yan and Y. Liu, *Chem. Commun.* **2009**, 6059–6061.
- 235 L. G. Xu, H. Kuang, C. L. Xu, W. Ma, L. B. Wang and N. A. Kotov, *J. Am. Chem. Soc.* **2012**, *134*, 1699–1709.
- 236 L. H. Tan, H. Xing, H. Chen and Y. Lu, *J. Am. Chem. Soc.* **2013**, *135*, 17675–17678.
- 237 L. Y. T. Chou, K. Zagorovsky and W. C. W. Chan, *Nat. Nanotechnol.* **2014**, *9*, 148–155.
- 238 N. Gandra, A. Abbas, L. Tian and S. Singamaneni, *Nano Lett.* **2012**, *12*, 2645.
- 239 C. A. Hunter, *Angew. Chem. Int. Ed.* **2004**, *43*, 5310–5324.

- 
- 240 M. Li, S. Johnson, H. Guo, E. Dujardin and S. Mann, *Adv. Funct. Mater.* **2011**, *21*, 851–859.
- 241 Z. Nie, D. Fava, E. Kumacheva, S. Zou, G. C. Walker and M. Rubinstein, *Nat. Mater.* **2007**, *6*, 609–614.
- 242 X. Liu, M. Atwater, J. Wang and Q. Huocoll, *Colloids Surf. B* **2007**, *58*, 3–7.
- 243 L. Ramin and A. Jabbarzadeh, *Langmuir* **2011**, *27*, 9748–9759.
- 244 M. Sethi, G. Joung and M. R. Knecht, *Langmuir* **2009**, *25*, 1572–1581.
- 245 H. Xia, S. Bai, J. Hartmann and D. Wang, *Langmuir* **2010**, *26*, 3585–3589.
- 246 B. Xu, X. Liu, J. Haubrich, R. J. Madix and C. M. Friend, *Angew. Chem. Int. Ed.* **2009**, *48*, 4206–4209.
- 247 X. Liu, B. Xu, J. Haubrich, R. J. Madix and C. M. Friend, *J. Am. Chem. Soc.* **2009**, *131*, 5757–5759.
- 248 J. Simard, C. Briggs, A. K. Boal and V. M. Rotello, *Chem. Commun.* **2000**, 1943–1944.
- 249 K. G. Thomas, S. Barazzouk, B. I. Ipe, S. T. S. Joseph and P. V. Kamat, *J. Phys. Chem. B* **2004**, *108*, 13066–13068.
- 250 Z. Sun, W. Ni, Z. Yang, X. Kou, L. Li and J. Wang, *Small* **2008**, *4*, 1287–1292.
- 251 I.-I. S. Lim, D. Mott, W. Ip, P. N. Njoki, Y. Pan, S. Zhou and C.-J. Zhong, *Langmuir* **2008**, *24*, 8857–8863.
- 252 N. Varghese, S. R. C. Vivekchand, A. Govindaraj and C. N. R. Rao, *Chem. Phys. Lett.* **2008**, *450*, 340–344.
- 253 W. H. Ni, R. A. Mosquera, J. Pérez-Juste and L. M. Liz-Marzán, *J. Phys. Chem. Lett.* **2010**, *1*, 1181–1185.
- 254 J. R. Navarro and M. H. Werts, *Analyst* **2013**, *138*, 583–592.
- 255 K. Kim, H. S. Han, I. Choi, C. Lee, S. G. Hong, S.-H. Suh, L. P. Lee and T. Kang, *Nat. Commun.* **2013**, *4*, 2182.
- 255a P. Byabartta, M. Laguna, *Inogr. Chem. Commun.* **2007**, *10*, 666–670.

- 
- 256 O. R. Miranda, H.-T. Chen, C.-C. You, D. E. Mortenson, X.-C. Yang, U. H. F. Bunz and V. M. Rotello, *J. Am. Chem. Soc.* **2010**, *132*, 5285–5289.
- 257 H. Perrier, G. Huyer and R. N. Young, *Tetrahedron Lett.* **1992**, *33*, 725–728.
- 258 P. D. Gianvincenzo, M. Marradia, O. M. Martínez-Ávila, L. M. Bedoyab, J. Alcamí and S. Penadés, *Bioorg. Med. Chem. Lett.*, **2010**, *20*, 2718–2721.
- 259 E. Locatelli, G. Ori, M. Fournelle, R. Lemor, M. Montorsi and M. Comes Franchini, *Chem. Eur. J.* **2011**, *17*, 9052–9056.
- 260 M. Woods and A. D. Sherry, *Inorg. Chem.* **2003**, *42*, 4401–4408.
- 261 N. Yi Mok, J. Chadwick, K. A. Kellett, N. M. Hooper, A. P. Johnson and C. W. Fishwick, *Bioorg. Med. Chem. Lett.* **2009**, *19*, 6770–6774.
- 262 R. Zniber, R. Achour, M. Z. Cherkaoui, B. Donnio, L. Gehringer and D. Guillon, *J. Mater. Chem.* **2002**, *12*, 2208–2213.

